UNIVERSITÉ DU QUÉBEC

THÈSE PRÉSENTÉ À

L'UNIVERSITÉ DU QUÉBEC À CHICOUTIMI

COMME EXIGENCE PARTIELLE

DU DOCTORAT EN INGÉNIERIE

PAR

CANGJI SHI

EFFETS DU ZR ET DU V SUR LA MICROSTRUCTURE ET LE COMPORTEMENT DE LA DÉFORMATION À CHAUD DES ALLIAGES D'ALUMINIUM 7150

NOVEMBRE 2014

UNIVERSITY OF QUEBEC

A DISSERTATION PRESENTED TO

THE UNIVERSITY OF QUEBEC AT CHICOUTIMI

IN PARTIAL FULFILLMENT OF THE REQUIREMENT FOR

THE DEGREE OF DOCTOR OF PHILOSOPHY IN

ENGINEERING

BY

CANGJI SHI

EFFECTS OF ZR AND V ON MICROSTRUCTURE AND HOT DEFORMATION BEHAVIOR OF 7150 ALUMINUM ALLOYS

NOVEMBER 2014

ABSTRACT

7xxx series aluminum alloys are very attractive materials for their applications in the automotive and aerospace industries due to their excellent combination of properties such as high strength-to-density ratio, high fracture toughness and resistance to stress corrosion cracking. These aluminum alloys are generally subjected to hot forming processes such as rolling, extrusion and forging. To optimize the mechanical properties and processability of hot-formed alloys, a better understanding of the effect of micro-alloying elements on deformation behavior and microstructural evolution during hot deformation is required. Therefore，in the present study, the hot deformation behavior of the 7150 aluminum alloys containing Zr ranging from 0 to 0.19 wt%, and V ranging from 0.01 to 0.19 wt% was studied using uniaxial compression tests conducted at various temperatures (300 to 450 °C) and strain rates (0.001 to 10 s^{-1}), respectively.

The hot deformation behavior and microstructural evolution of the 7150 base alloy (Zr free) were studied. A decline ratio map of flow stresses was proposed and divided into five deformation domains, in which the flow stress behavior was correlated with different microstructures and dynamic softening mechanisms. The results reveal that the dynamic recovery is the sole softening mechanism at temperatures of 300 to 400 °C with various strain rates, and at temperatures of 400 to 450 °C with strain rates between 1 and 10 s^{-1}. At the high deformation temperature of 450 °C with strain rates of 0.001 to 0.1 s^{-1}, a partially recrystallized microstructure was observed and dynamic recrystallization (DRX) provided an alternative softening mechanism. Two kinds of dynamic recrystallization (DRX) might operate at the high temperature, in which discontinuous dynamic recrystallization was involved at higher strain rates and continuous dynamic recrystallization was implied at lower strain rates.

After being alloyed with Zr from 0 to 0.19 wt%, the results show no significant variation in the peak flow stress or activation energy between the 7150 base alloy and the alloy containing 0.04 wt% Zr. With a further increase in the Zr content to 0.19 wt%, the values of peak flow stress and activation energy increased significantly. The solved constitutive equations yielded good predictions of the peak flow stress over wide temperature and strain-rate ranges for 7150 alloys with different Zr contents. The dynamic recovery level of the materials was reduced after being alloyed with Zr, which was associated with a decrease in the mean misorientation angle of boundaries and a decrease in subgrain size. The addition of Zr promoted the retardation of dynamic recovery and the inhibition of dynamic recrystallization during hot deformation due to the pinning effect of Al_3Zr dispersoids on dislocation motion and to restrained dynamic restoration.

When the material was alloyed with V from 0.01 to 0.19 wt%, the peak flow stress of the 7150 alloy significantly increased. The alloys containing 0.03-0.05 wt% V displayed higher values of peak flow stress than those with 0.11-0.19 wt% V at low temperatures, whereas they displayed comparable values at higher temperatures. The activation energy for hot deformation increased from 229 kJ/mol for the base alloy to approximately 270 kJ/mol for the alloys containing 0.03-0.05 wt% V. With further increases in V contents up to 0.19 wt%, the activation energy returned to approximately 250 kJ/mol. The vanadium-solute diffusion acted as the deformation rate-controlling mechanism for the alloys containing up to 0.05 wt% V, resulting in enhanced work hardening and improved subgrain strengthening effects. The precipitation of $Al_{21}V_2$ dispersoids in the alloys containing 0.11 to 0.19 wt% V promoted the retardation of dynamic recovery and the inhibition of dynamic recrystallization.

The effects of Zr (0.04 to 0.15 wt%) and V additions (0.05 to 0.15 wt%) on the processing map of 7150 aluminum alloys were investigated. The results reveal that the processing map for the 7150 base alloy exhibits a single domain (Domain I), associated with dynamic recovery and partially dynamic recrystallization. With increasing Zr and V additions, Domain I shrinks towards higher temperatures and higher strain rates with decreases in efficiency of power dissipation, due to a restrained level of dynamic recovery caused by the pinning effect of Al_3Zr and $Al_{21}V_2$ dispersoids. When the added Zr and V contents reach 0.15%, another domain (Domain II) is formed, corresponding to the cavity formation in microstructure. The flow instability during hot deformation of 7150 alloys is attributed to the formation of adiabatic shear bands and deformation bands. The instability region extends toward lower strain rates when alloyed with Zr and V. The optimum hot-working parameters for those alloys are determined to be the deformation temperature of 450 °C and strain rate of 0.01 s^{-1}.

Furthermore, a revised Sellars' constitutive equation was proposed, which considered the effects of the deformation temperature and strain rate on the material variables and which provided an accurate estimate of the hot deformation behavior of the 7150 aluminum alloy. The results reveal that the activation energy for the hot deformation of the 7150 aluminum alloy is not a constant value but rather varies as a function of the deformation conditions. The activation energy for hot deformation decreased with increasing deformation temperature and with increasing strain rate. The peak flow stresses under various deformation conditions were predicted by a revised constitutive equation and correlated with the experimental data with excellent accuracy.

RÉSUMÉ

Les alliages d'aluminium de la série 7xxx sont des matériaux très attractifs pour leurs applications dans les industries automobile et aéronautique en raison de leur excellente combinaison des propriétés telles que le haut rapport résistance-densité, la haute ténacité et la résistance à la fissuration par corrosion sous contraintes. Ces alliages d'aluminium sont généralement soumis à des procédés de formage à chaud tels que le laminage, l'extrusion et le forgeage. Pour optimiser les propriétés mécaniques et l'aptitude au traitement des alliages formés à chaud, une meilleure compréhension de l'effet des éléments de micro-alliage sur le comportement de déformation et de l'évolution de la microstructure durant la déformation à chaud est nécessaire. Par conséquent, dans cette étude, le comportement à la déformation à chaud des alliages d'aluminium 7150 contenant du Zr allant de 0 à 0,19% en poids, et du V allant de 0,01 à 0,19% en poids a été étudié en utilisant des essais de compression uniaxiale réalisés à différentes températures (300 à 450 ° C) et de la vitesse de déformation (0,001 à 10 s-1), respectivement.

Le comportement à la déformation à chaud et l'évolution de la microstructure de l'alliage de base 7150 ont été étudiés. Un contour du rapport diminué de contraintes a été proposé et divisée en cinq domaines de déformation dans lesquelles le comportement des contraintes d'écoulement a été mis en corrélation avec différentes microstructures et mécanismes d'adoucissement dynamiques. Les résultats révèlent que la restauration dynamique est le seul mécanisme d'adoucissement à des températures de 300 à 400°C avec différentes vitesses de déformation, et à des températures de 400 à 450°C avec des vitesses de déformation comprises entre 1 et 10 s^{-1}. A la température élevée de déformation de 450°C avec un taux de contraintes de 0,001 à 0,1s^{-1}, une microstructure partiellement recristallisée a été observée et la recristallisation dynamique (DRX) a fourni un mécanisme alternatif d'adoucissement. Deux types de recristallisation dynamique (DRX) pourraient fonctionner à la température élevée, l'une dans laquelle la recristallisation dynamique discontinue a participé à la hausse des vitesses de déformation et l'autre, la recristallisation dynamique continue qui a été impliquée à des vitesses de déformation plus faibles.

Après avoir été allié avec du Zr de 0 à 0,19% en poids, les résultats ne montrent pas de variation significative du pic de la contrainte d'écoulement ou de l'énergie d'activation entre l'alliage de base 7150 et l'alliage contenant 0,04% en poids de Zr. Avec une augmentation supplémentaire de la teneur en Zr jusqu'à 0,19% en poids, les valeurs du pic des contraintes d'écoulement et de l'énergie d'activation ont augmenté de manière significative. Les équations constitutives résolues ont donné de bonnes prédictions du pic de la contrainte d'écoulement sur des gammes de température et de vitesse de déformation plus large pour les alliages 7150 ayant différentes teneurs en Zr. Le niveau de restauration dynamique des matériaux a été réduite après avoir été allié avec le Zr, qui a été associée à une diminution de

l'angle moyen de désorientation des limites et d'une diminution de la taille des sous-grains. L'addition de Zr a favorisée le retard de la reprise dynamique et l'inhibition de la recristallisation dynamique pendant la déformation à chaud à cause de l'effet de restriction des précipités Al_3Zr sur le mouvement des dislocations et la maitrise de la restauration dynamique.

Lorsque le matériau a été allié avec du V de 0,01 à 0,19% en poids, la pic des contraintes d'écoulement de l'alliage 7150 a augmenté de manière significative. Les alliages contenant de 0,03 à 0,05% en poids de V ont montré des valeurs du pic de la contrainte à l'écoulement plus élevés que ceux qui contiennent une teneur de V de 0,11 à 0,19% en poids à basse température, alors qu'ils montraient des valeurs comparables à des températures plus élevées. L'énergie d'activation pour la déformation à chaud est passé de 229 kJ/mol pour l'alliage de base à environ 270 kJ/mol pour les alliages contenant de 0,03 à 0,05% en poids de V. Avec de nouvelles augmentations des teneurs en V jusqu'à 0,19% en poids, l'énergie d'activation est revenue à environ 250 kJ/mol. La diffusion de la solution de vanadium a agi en tant que mécanisme de contrôle de la vitesse de déformation pour les alliages contenant jusqu'à 0,05% en poids de V, ce qui améliore l'écrouissage et le renforcement des effets de sous-grains La précipitation of $Al_{21}V_2$ dans les alliages contenant de 0,11 à 0,19% en poids de V favorise la retardation de la restauration dynamique et l'inhibition de la recristallisation dynamique.

Les effets de l'addition du Zr (de 0.04 à 0.15% en poids) et du V (0.05 à 0.15% en poids) sur la déformation à chaud et la cartographie du processus des alliages d'aluminium 7150 ont été étudiés en utilisant des essais de compression uniaxiale réalisés à différentes températures (300 à 450°C) et différents vitesses de contraintes (de 0.001 à 10 s^{-1}). Les résultats révèlent que la carte de traitement de l'alliage de base 7150 présente un seul domaine (Domaine I), associé à la récupération dynamique et la recristallisation dynamique partielle. Avec l'augmentation de l'addition du Zr et du V, le domaine I rétrécit vers des températures plus élevées et des vitesses plus élevés de contrainte avec des baisses de l'efficacité de la puissance de dissipation, en raison d'un niveau restreint de la restauration dynamique provoquée par l'effet de l'épinglage des dispersoïdes Al_3Zr et $Al_{21}V_2$. Lorsque le contenu ajouté de Zr et V atteind 0.15%, un autre domaine (Domaine II) est formée, correspondant à la formation de la cavité dans la microstructure. L'instabilité de l'écoulement durant la déformation à chaud des alliages 7150 est attribuée à la formation de bandes de cisaillement adiabatiques et des bandes de déformation. La région d'instabilité s'étend vers des taux de déformation inférieurs lorsqu'il est allié avec le Zr et le V. Les paramètres optimaux du formage à chaud pour ces alliages sont déterminés comme étant la température de déformation de 450°C et la vitesse de contrainte de 0.01 s^{-1}.

L'équation constitutive révisée de Sellars a été proposée, qui a considéré les effets de la température de déformation et la vitesse de déformation sur les constantes des matériaux et qui a fourni une estimation précise du comportement de la déformation à chaud de l'alliage

7150 en aluminium. Les résultats révèlent que l'énergie d'activation de la déformation à chaud de l'alliage d'aluminium 7150 n'est pas une valeur constante, mais plutôt varie comme une fonction des conditions de déformation. L'énergie d'activation de la déformation à chaud a diminué avec l'augmentation de la température de déformation et avec l'augmentation de la vitesse de déformation. Les pics des contraintes d'écoulement sous différente conditions de déformation ont été prédits par une équation constitutive révisée et mis en corrélation avec les données expérimentales avec une excellente précision.

ACKNOWLEDGEMENT

I would like to express deep gratitude to my thesis supervisor, Professor X. Grant Chen, for his excellent guidance and constant support throughout the project. His scientific insight, invaluable suggestions, and confidence in my abilities have been extremely encouraging to me as a great source of inspiration, which are greatly appreciated.

I also would like to acknowledge financial support from the Natural Sciences and Engineering Research Council of Canada (NSERC) and from Rio Tinto Alcan through the NSERC Industrial Research Chair in Metallurgy of Aluminium Transformation at the University of Québec at Chicoutimi.

Grateful acknowledgement is attributed to Prof. Hugh J. McQueen at Concordia University and Prof. Weimin Mao at University of Science and Technology Beijing for valuable discussions and constructive suggestions on my research work; Dr. Zhan Zhang and Dr. Jing Lai at University of Québec at Chicoutimi for their help in TEM observation; and Prof. Dilip Sarkar at University of Québec at Chicoutimi for his assistance in XRD analysis.

Many thanks go to the technicians for their technical support on my research project: Mr. Martin Bouchard in alloy design and casting; Ms. Émélie Brideau in the hot compression tests performed on the Gleeble 3800 thermomechanical simulation unit; Mr. Alexandre Morin in sample machining; Mrs. Hélène Grégoire at NRC-Aluminum Technology Centre (NRC-ATC) in FE-SEM observation.

Special thanks are sent to Mounir Baiteche for the French translation of thesis abstract, and all my colleagues in the CIMTAL Industrial Research Chair at University of Québec at Chicoutimi who made my stay at Saguenay filled with friendship.

Finally, I would like to express my sincere appreciation to my wife, Ying Huang, and our son, Andrew Louie Shi, for their unconditional love and infinite encouragement.

PUBLICATIONS

JOURNAL ARTICLES

1. **C. Shi**, W.M. Mao, X.-G. Chen, Evolution of activation energy during hot deformation of 7150 aluminum alloy, *Materials Science and Engineering A,* 571 (2013) 83-91.

2. **C. Shi**, J. lai, X.-G. Chen, Microstructural evolution and dynamic softening mechanisms of Al-Zn-Mg-Cu alloy during hot compressive deformation, *Materials, 7 (*2014) 244-264.

3. **C. Shi**, X.-G. Chen, Effect of Zr addition on hot deformation behavior and microstructural evolution of 7150 aluminum alloy, *Materials Science and Engineering A,* 596 (2014) 183-193.

4. **C. Shi**, X.-G. Chen, Effect of vanadium on hot deformation and microstructural evolution of 7150 aluminum alloy, *Materials Science and Engineering A,* 613 (2014) 91-102.

5. **C. Shi**, X.-G. Chen, Hot workability and processing maps of 7150 aluminum alloys with Zr and V additions, *Journal of Materials Engineering and Performance*, 2014.

6. **C. Shi**, X.-G. Chen, Evolution of activation energy for hot deformation of 7150 aluminum alloys with Zr and V additions, *Materials Science and Engineering A*, 2014.

7. J. lai, **C. Shi**, X.-G. Chen, Effects of V addition on recrystallization resistance of 7150 aluminum alloy after simulative hot deformation, *Materials Characterization*, 96 (2014) 126-134.

CONFERENCE PAPERS

8. **C. Shi**, X.-G. Chen, Hot deformation behavior and microstructural evolution of homogenized 7150 aluminum alloys micro-alloyed with Zr and V, *13th International Conference on Aluminum Alloys (ICAA-13)*, Pittsburgh, USA, 3-7 June 2012, pp. 1599-1605.

9. **C. Shi**, X.-G. Chen, Effects or Zr and V micro-alloying on activation energy during hot deformation of 7150 aluminum alloys, *TMS 2015 144th Annual Meeting & Exhibition,* Orlando, USA, 15-19 March 2015.

SCIENTIFIC POSTERS

10. **C. Shi**, X.-G. Chen, Effect of Zr addition on hot deformation behavior of 7150 aluminum alloy, The Encyclopedia of Research on Aluminium in Quebec, 2013 edition, Les Presses de l'aluminium (PRAL), pp. 79.

11. **C. Shi**, X.-G. Chen, Hot compressive deformation behavior and microstructural evolution of 7150 aluminum alloy, The Encyclopedia of Research on Aluminium in Quebec, 2012 edition, Les Presses de l'aluminium (PRAL), pp. 62.

12. **C. Shi**, X.-G. Chen, Hot deformation behavior of homogenized 7150 aluminum alloys micro-alloyed with Zr and V, The Encyclopedia of Research on Aluminium in Quebec, 2011 edition, Les Presses de l'aluminium (PRAL), pp. 67.

TABLE OF CONTENTS

LIST OF FIGURES

LIST OF TABLES

CHAPTER I

DEFINITION OF PROBLEM

Chapter I Definition of Problem

1.1 Introduction

The 7xxx aluminum alloys with high strength-to-density ratio and excellent mechanical facture toughness have been widely used in the aircraft and aerospace industries [1]. These aluminum alloys are generally subjected to hot-forming processes such as rolling, forging and extrusion. The mechanical properties are affected by the chemical composition, strain history and microstructure resulting from the thermomechanical processing. To optimize the metal hot-forming processes, a better understanding of the hot workability, microstructural evolution and effect of micro-alloying elements during hot deformation is required.

Dynamic recovery and dynamic recrystallization are the typical softening mechanisms in metals and alloys during deformation at elevated temperatures [2, 3]. These softening mechanisms are determined by thermomechanical parameters such as deformation temperature, strain rate and strain degree. Aluminum and its alloys with high stacking fault energy exhibit a high rate of dynamic recovery, which significantly inhibits dynamic recrystallization [2, 3]. However, the formation of new grains during hot deformation of aluminum alloys has been frequently reported, while several mechanisms of dynamic recrystallization for aluminum alloys have been proposed [2], such as discontinuous dynamic recrystallization (DDRX), continuous dynamic recrystallization (CDRX) and geometric dynamic recrystallization (GDRX).

The addition of zirconium is well known to increase the recrystallization resistance of aluminum alloys by forming fine, coherent Al_3Zr dispersoids [4, 5]. The presence of the Al_3Zr dispersoids promotes the formation of a stable and refined subgrain structure during the hot working, which promotes additional substructure strengthening [6]. A vanadium addition is reported to maintain high temperature strength of the aluminum alloy by forming thermally stable dispersoids of $Al_{11}V$ [7, 8]. The $Al_{11}V$ dispersoids could retard dynamic softening and raise recrystallization temperature during hot working processes [9]. The effectiveness of the dispersoids depends on their size, number density and distribution [3].

The processing maps were developed on the basis of dynamic materials model (DMM), and have been used to design hot working schedules for a wide variety of materials [10]. The maps explicitly represent local peak efficiencies of power dissipation and regions of flow instability, which are associated with specific microstructure mechanisms [10, 11]. With the help of the processing maps, the deformation temperature and the strain rate corresponding to local peak efficiency of power dissipation in the safe domain are chosen as the optimum processing parameters for hot working. Conversely, hot deformation should not be conducted in the regions of flow instability in order to prevent the occurrence of microstructural defects [12].

To date, other's work has mainly focused on determining the Zener-Hollomon parameter, the activation energy for hot deformation, and various material constants in the constitutive equations for the deformation behavior of commercially aluminum alloys. However, a

systematical investigation of microstructural evolution in order to understand the different dynamic softening mechanisms of the 7xxx aluminum alloys at various deformation conditions has rarely been reported. Moreover, the study on the effect of different Zr and V contents on the hot deformation behavior of 7xxx aluminum alloys has not been found in the literature. The evolution of the deformed microstructure of 7xxx aluminum alloy after adding various contents of Zr and V must be understood. Furthermore, most of the recent studies have focused on the influences of temperature, strain rate and strain on the processing maps. The literature on investigation of the effects of micro-alloying elements on processing maps of the aluminum alloys during hot working is rarely found.

1.2 Objectives

The goal of the present work mainly consists of four parts, and the specific objectives are proposed as follows:

Part 1. Investigate the hot deformation behavior and microstructural evolution of 7150 aluminum alloy.

1. Study the flow stress behavior and microstructural evolution during hot deformation at various temperatures and strain rates.

2. Constitutively analyze the flow stress curves to determine the material constants and activation energies for hot deformation at different deformation conditions.

3. Investigate different dynamic softening mechanisms operating at various deformation

conditions to understand the evolution of flow stress behavior.

Part 2. Investigate the effect of zirconium on the hot deformation behavior and microstructural evolution of 7150 aluminum alloy.

1. Study the flow stress behavior and microstructural evolution of the 7150 aluminum alloys with a series of zirconium additions during hot deformation.
2. Constitutively analyze the flow stress curves to determine the material constants and the activation energies for hot deformation for the 7150 aluminum alloys with various zirconium additions.
3. Predict the flow stress behavior of the 7150 aluminum alloys containing different Zr contents using the solved constitutive equations.
4. Study the effect of zirconium addition on the dynamic softening mechanisms during hot deformation process.

Part 3. Investigate the effect of vanadium on the hot deformation behavior and microstructural evolution of 7150 aluminum alloy.

1. Study the flow stress behavior and microstructural evolution of the 7150 aluminum alloys with a series of vanadium additions during hot deformation.
2. Constitutively analyze the flow stress curves to understand the evolution of activation energies for hot deformation with different vanadium additions.

3. Investigate the effect of vanadium additions on the dynamic softening mechanisms during hot deformation process.

Part 4. Investigate the effect of Zr and V additions on processing map of 7150 aluminum alloy during hot deformation.

1. Study the evolution of processing map of the 7150 aluminum alloy after micro-alloyed with different Zr and V contents.

2. Investigate the microstructural evolution to understand the effect of Zr and V addition on the processing map and on the dynamic deformation mechanisms during hot deformation process.

3. Establish the optimum hot-working parameters for the 7150 aluminum alloys with different Zr and V additions.

References

[1] E.A. Starke, J.T. Staley, Prog. Aerosp. Sci. 32 (1996) 131-172.

[2] H.J. McQueen, S. Spigarelli, M. Kassner, E. Evangelista, Hot Deformation and Processing of Aluminum Alloys, CRC Press, Florida, 2011, pp. 87-233.

[3] F.J. Humphreys, M. Hatherly, Recrystallization and Related Annealing Phenomena, second ed., Elsevier Ltd., Oxford, 2004, pp. 169-450.

[4] J.D. Robson, Acta Mater. 52 (2004) 1409-1421.

[5] J.D. Robson, P.B. Prangnell, Acta Mater. 49 (2001) 599-613.

[6] Y.V. Milman, A.I. Sirko, D.V. Lotsko, D.B. Miracle, O.N. Senkov, Mater. Sci Forum 396-402 (2002) 1217-1222.

[7] E.F. Kazakova, Y.I. Rusnyak, Met. Sci. Heat Treat. 51 (2009) 436-439.

[8] K.E. Knipling, D.C. Dunand, D.N. Seidman, Z. Metallkd. 97 (2006) 246-265.

[9] J.R. Davis, ASM Specialty Handbook: Aluminum and Aluminum Alloys, American Society for Metals, Metals Park, OH, USA, 1993, pp. 23-58.

[10] Y.V.R.K. Prasad, S. Sasidhara, Hot working guide-a compendium of processing maps, ASM Intl., Ohio, USA, 1997, pp. 1-24.

[11] Y.V.R.K. Prasad, H.L. Gegel, S.M. Doraivelu, J.C. Malas, J.T. Morgan, K.A. Lark, D.R. Barker, Metall. Trans. A 15A (1984) 1883-1892.

[12] P.S. Robi, U.S. Dixit, J. Mater. Process. Technol. 142 (2003) 289-294.

CHAPTER II

LITERATURE REVIEW

Chapter II Literature Review

2.1 7xxx Aluminum Alloys

The 7xxx series aluminum alloys are very attractive materials to be used in the automotive and aerospace industries, due to their excellent combination of properties such as high strength-to-density ratio, high fracture toughness, and resistance to stress corrosion cracking [1]. Intermetallic phases, such as η($MgZn_2$), T($Al_2Mg_3Zn_3$), S(Al_2CuMg), θ(Al_2Cu) Al_7Cu_2Fe, Al_3Fe_4 and Mg_2Si, are commonly observed in the as-cast microstructure of 7xxx aluminum alloys [13]. In order to decrease the micro-segregation and dissolve the coarse eutectic particles, homogenization heat treatment is necessary for as-cast alloys before subsequent processing. However, some intermetallic particles may still remain in the aluminum matrix after homogenization, which might influence the formability, recrystallization behavior and the mechanical properties of the material [2]. Fan et al. [5] reported that the initial as-cast microstructure of a 7050 aluminum alloy contained α(Al), η($MgZn_2$), S(Al_2CuMg) and Al_7Cu_2Fe phases. The η($MgZn_2$) phase was completely dissolved after homogenization at 460 °C for 24 h, and the S(Al_2CuMg) and Al_7Cu_2Fe intermetallic particles remained in the aluminum matrix. Robson [4] suggested that the practical homogenization temper for 7000 series alloy is at temperatures of 460 to 480 °C and soaking time of 24 to 36 h, in which the coarse particles can be dissolved to a great extent to obtain a homogenized microstructure.

The hot forming of the 7xxx aluminum alloys is rather difficult because of the variety of precipitates along with dispersoids and constituent particles, which raise the strength and reduce the ductility. Dynamic recrystallization of those alloys during hot working process is rarely observed during hot deformation. Therefore, intermediate thermomechanical process is necessary for stimulating static recrystallization in order to facilitate the subsequent hot deformation [2].

2.2 Alloying of Trace Elements

The addition of micro-alloying elements, such as Zr, V, Sc, Sn, In, Cd and Ag, has been reported to increase the material strength of the alloys and afford reasonably high toughness by precipitation of dispersoids [7-10]. The effectiveness of the dispersoids depends on their size, spacing and distribution [3]. In the present study, the roles of Zr and V addition played during hot deformation process of 7xxx aluminum alloys are of great interest.

2.2.1 Zirconium alloying

ThermoCalc software and the TCAL2 database were utilized to calculate the binary Al-Zr phase diagram near the aluminum corner, as shown in Fig. 2.1. This phase diagram describes the possible phases that precipitate during solidification. The solubility limit of zirconium in liquid aluminum is approximately 0.09 wt%, above which the primary intermetallic compound of Al_3Zr forms. When the Zr content is less than 0.09%, the Al dendrites precipitate from liquid during the solidification. When the Zr content ranges from 0.09% to the peritectic point of 0.27%, the primary Al_3Zr intermetallic compound first precipitates

from the liquid phase, followed by a peritectic reaction to form the Al solid solution at 661 ºC. Under non-equilibrium solidification with high cooling rates, the peritectic reaction shifts towards a higher Zr concentration and more Zr solutes can enter the aluminum solid solution. The binary Al-Zr system has been extensively studied, particularly in rapidly solidified samples [12-15]. For small zirconium additions, decomposition of the supersaturated solid solution occurs firstly by the formation of a metastable $L1_2$ Al_3Zr phase. Prolonged heat treatment is usually required before the metastable phase transforms to the equilibrium DO_{23} Al_3Zr phase [13,14]. Qualitative studies of the precipitation kinetics of the metastable phase in binary alloys show that the peak transformation rate lies between 400 °C and 500 °C [15-17]. The size of the Al_3Zr dispersoids depends partially on the heating rate to the homogenization temperature, with slower heating rates apparently leading to a refinement in dispersoid size [17,18].

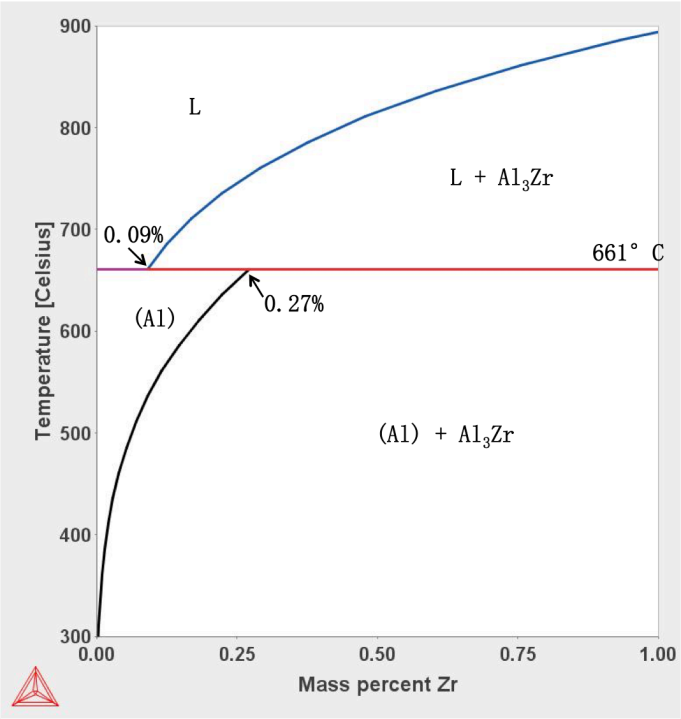

Fig. 2.1 Binary phase diagram for dilute (< 1 wt%) additions of zirconium in aluminum.

As a consequence of the peritectic solidification reaction, the Al_3Zr dispersoids are often inhomogeneously distributed within individual grains. Dispersoid free zones of Al_3Zr are observed in the interdendritic regions and in the area adjacent to the grain boundaries [19], as shown in Fig. 2.2.

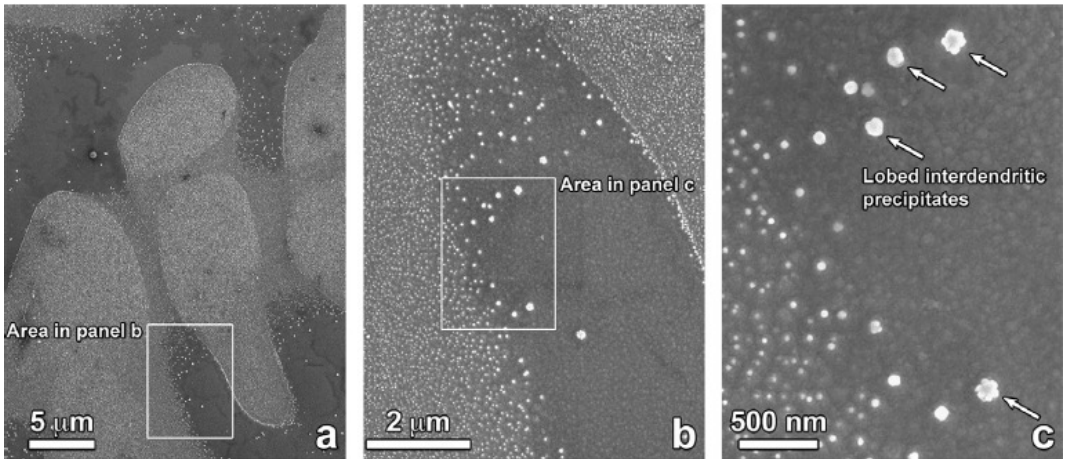

Fig. 2.2 FEG-SEM micrographs of Al_3Zr ($L1_2$) precipitates in Al-0.2% Zr aged at 425 °C for 400 h [19].

The addition of Zr is well known to increase the recrystallization resistance of aluminum alloys by forming fine, coherent Al_3Zr dispersoids [4, 5]. The presence of these dispersoids promotes the formation of a stable and refined subgrain structure during the hot deformation process, which promotes additional substructure strengthening [6]. The inhomogeneous distribution of Al_3Zr dispersoids is likely to decrease the resistance to recrystallization in dispersoid free zones, where the presence of large primary particles is also known to encourage recrystallization [22]. Several studies have focused on investigating the effect of Zr addition on the static recrystallization of aluminum alloys during solution treatment because the fracture toughness is closely related to the amount of recrystallized structure [4, 5, 14-16]. A few studies have been conducted on the hot deformation of aluminum alloys containing Zr, in which a pinning effect of Al_3Zr dispersoids on dislocations and grain boundaries has been reported [17, 18].

2.2.2 Vanadium alloying

Fig 2.3 shows the binary Al-V phase diagram near the aluminum corner, calculated by ThermoCalc software and the TCBIN database. The solubility limit of vanadium in liquid aluminum is approximately 0.16 wt%. The intermetallic phase of $Al_{10}V$ exhibits a solid solubility of 1.2 wt% in the aluminum matrix at the peritectic temperature of 665 °C. Under non-equilibrium solidification with high cooling rates, the peritectic reaction shifts towards a higher V concentration and more V solutes can enter the aluminum solid solution. Vanadium with low diffusivity and solubility in aluminum alloys is known to improve the high temperature strength of the aluminum alloy by forming thermally stable V-containing dispersoids ($Al_{11}V$) [28,29]. The presence of these dispersoids could retard the recrystallization and raise the recrystallization temperature [30]. Therefore, vanadium could be an attractive candidate to restrict the recrystallization. Some studies investigated the precipitation of $Al_{11}V$ dispersoids in the aluminum alloys containing V using rapid solidification technique [31-34]. A few of studies were conducted on the influence of V addition on the precipitation of secondary particles in aluminum alloys, such as $Al_{94}V_4Fe_2$, $Al_{18}Mg_3V_2$, AlFeVSi dispersoids, and on the mechanical properties [35-39]. Recently, Wang et al. [40] reported that the addition of 0.045 wt% V in AA5083 aluminum alloy exhibited a restriction on the growth of recrystallized grains and yielded a refined fibrous structure in the rolling sheet. With an addition of 0.15 wt% V, Cui et al. observed the precipitation of V-containing dispersoids in AA2091 (2.15Li-2.04Cu-1.5Mg-0.14Zr) alloy [41]. However,

systematical investigations of the influence of Zr and V additions on the hot deformation behavior of 7xxx aluminum alloys have not been reported in the literature.

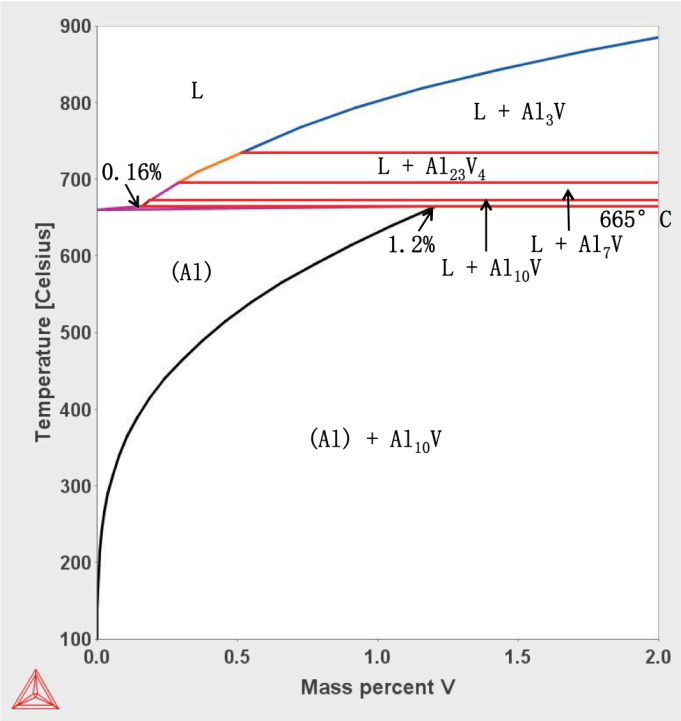

Fig. 2.3 Binary phase diagram for dilute (< 2 wt%) additions of vanadium in aluminum [12].

2.3 Plastic Deformation of Aluminum

Aluminum is a crystalline material with high stacking fault energy (SFE, 250 mJ/m^2), and its plastic deformation is carried out mainly by dislocation slipping in the lattice structure [19]. The restriction of dislocation slip through crystal defects, such as solid solution, precipitates, dispersoids and grain boundaries, leads to work hardening effect during deformation [19].

2.3.1 Slip systems

In most cases, dislocation slip takes place on the most densely packed planes and in the most densely packed directions in the crystal, which are defined as slip planes and slip directions. In aluminum and aluminum alloys, the slip plane is the plane {111} and the slip direction is the <110> direction [2, 19]. However, other slip systems may operate at high temperatures, which involves slip on {100}, {110}, {112} and {122} planes [11]. Low-temperature slip has also been reported on {111}, {110} and {122} planes [11]. Dislocation slip on several slip planes is very often activated simultaneously during deformation, which results in a multi-slip of dislocations. The deformation induces increased densities of vacancies, dislocations and grain boundaries, which act as obstacles to further movement of dislocations and lead to work hardening effect [42].

2.3.2 Work hardening effect

The work hardening effect arises when dislocations are hindered in their movement through the crystals so that a higher stress must be imposed to continue the plastic deformation. Many obstacles to dislocation movement exist, such as other dislocations, grain boundaries, solute atoms and particles of a second phase [20]. The dislocation density gradually increases as deformation proceeds. The mobile dislocations generated by the deformation do not exit through the surface, are not absorbed in grain boundaries, and do not annihilate each other, but are stored in the crystals. The stress necessary to move the later dislocations is raised due to the increase in dislocation density and the interaction between

dislocations [43].

The contribution of solid solutions to the flow stress arises from a frictional force for the movement of dislocations. The magnitude of this force is sensitive both to atomic size differences and differences in elastic properties between solute and solvent atoms [20]. When fine precipitates are formed in a material, an additional barrier to the movement of dislocations is created. The precipitate particles lie across the slip planes along which the dislocations move, so that the dislocations must behave in one of two ways: shear the particles or bypass the obstacles [20].

2.3.3 Deformation heterogeneities

Deformation heterogeneities, such as deformation, transition and shear bands, are illustrated in Fig. 2.4 [11]. During plastic deformation, dislocations are accumulated in the individual grains (Fig 2.4(a)), and eventually form dislocation boundaries, such as boundaries of cells or subgrains (Fig 2.4(b)). Regions of different orientations are formed within individual grains (Fig 2.4(c)). These are termed deformation bands and deformation on different slip systems producing different textures. The narrow regions between deformation bands are termed transition bands. Fig 2.4(d) shows a typical shear band inclined to the rolling direction passing through several grains. They are the result of plastic instability.

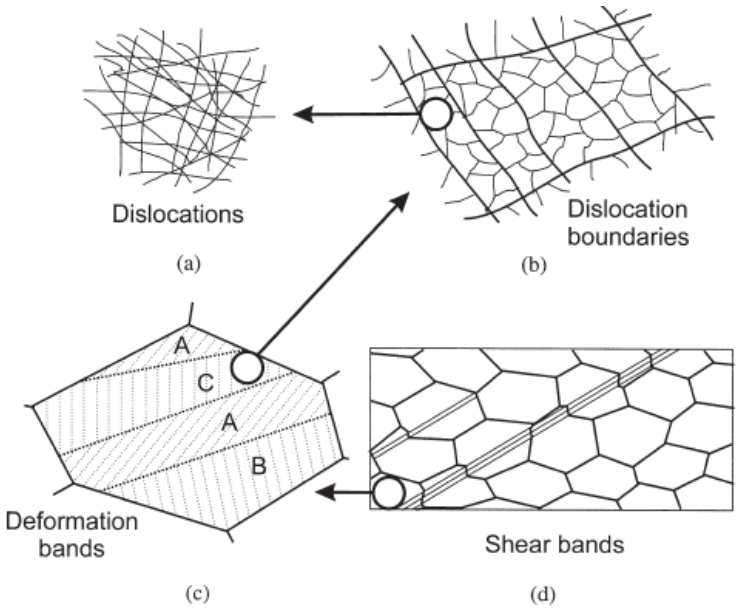

Fig. 2.4 Schematic illustrating various features in the microstructure when a metal is deformed by slip: (a) dislocations; (b) dislocation boundaries; (c) deformation and transition bands within a grain; (d) grain-scale shear bands [11].

2.4 Dynamic Softening Mechanisms

When crystalline materials are deformed at elevated temperatures, the increase of dislocation density and work hardening effect are continuously counteracted by dynamic softening processes. The principal softening mechanisms in metals and alloys during hot deformation are dynamic recovery (DRV) and dynamic recrystallization (DRX) [2, 3]. The term, dynamic, referred to the occurrence of softening processes during hot deformation. It is distinguished from the static process, which may occur in the deformed microstructure after deformation, or during post deformation annealing [11].

2.4.1 Dynamic recovery

DRV involves annihilation and rearrangement of dislocations into low energy

sub-boundaries. The recovery of dislocations consists of a series of microstructural changes which are schematically shown in Fig. 2.5 [11]. Cross-slip and climb of dislocations play an important role in DRV, and the driving force for DRV is the stored energy generated during deformation [2, 3].

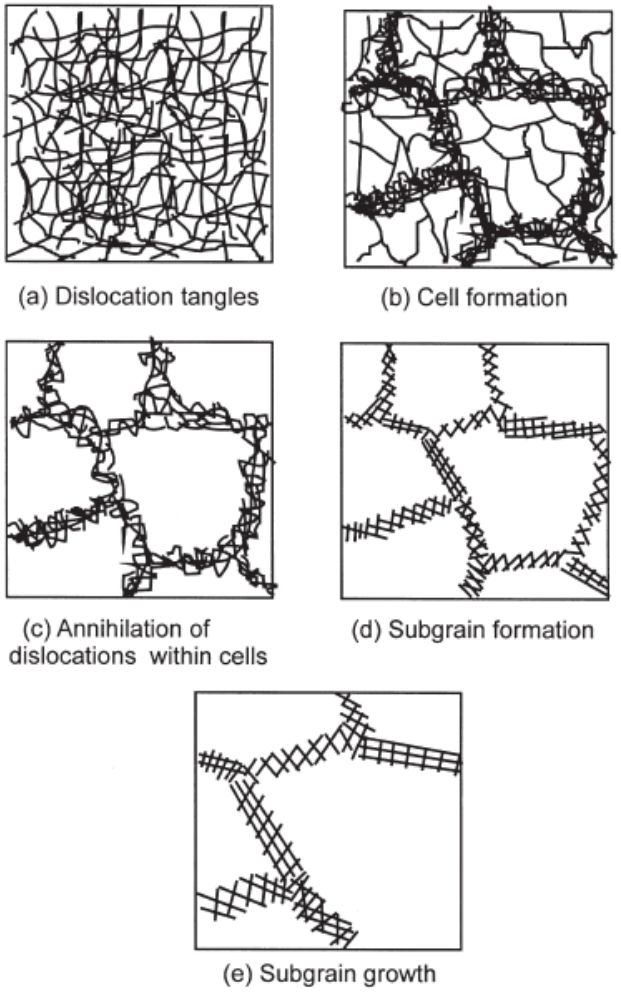

Fig. 2.5 Various stages in the recovery of a plastically deformed material [11].

2.4.2 Dynamic recrystallization

DRX is a restoration process, in which new grains containing substructures form within

the deformed structure and grow to consume the deformed grains. Several mechanisms of DRX during hot deformation have been proposed, including discontinuous dynamic recrystallization (DDRX), continuous dynamic recrystallization (CDRX), and geometric dynamic recrystallization (GDRX) [2, 3].

The DDRX involves the development of high angle grain boundaries via nucleation and growth of new grains, which typically initiates at high angle boundaries, such as original grain boundaries, boundaries of dynamically recrystallized grains and boundaries created during deformation, as well as in regions associated with large particles (>1μm) [11].

Bulging of high angle boundaries is frequently observed as a prelude to DDRX, and subsequent grain growth takes place by strain-induced boundary migration (SIBM) [11]. SIBM involves the bulging of part of a pre-existing grain boundary, leaving a region behind the migrating boundary with lower dislocation content. A characteristic feature of this mechanism is that the new grains have similar orientations to the old grains from which they have grown. Fig. 2.6 gives an example showing the recrystallized grains in aluminum, which was formed by the mechanism of SIBM [11].

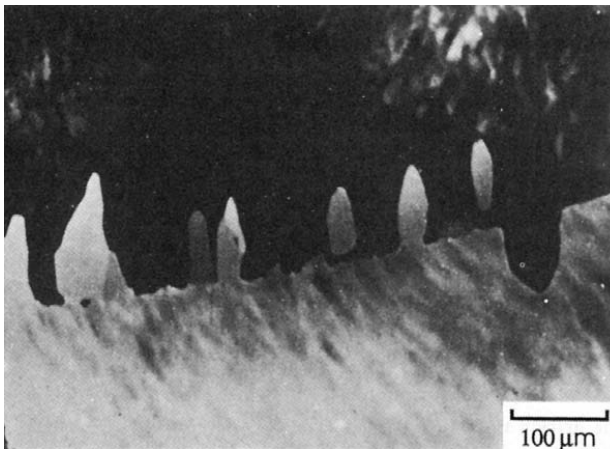

Fig. 2.6 An optical micrograph showing strain-induced grain boundary migration (SIBM) in aluminum [11].

When a material with large particles is deformed, a high stress builds up around the particles, which leads to an increased dislocation nucleation rate and thus a higher dislocation density around the particles. Subsequently, small cells with walls of high dislocation densities coalesce into nuclei, and then grow rapidly into recrystallized grains. This is known as particle stimulated nucleation (PSN) [44]. The DDRX which was attributed to PSN has been observed in aluminum alloys [6,45]. An example of fully recrystallized microstructure of Al-0.8 wt% Si alloy containing large silicon particles deformed by compression followed by annealing is shown in Fig. 2.7 [11].

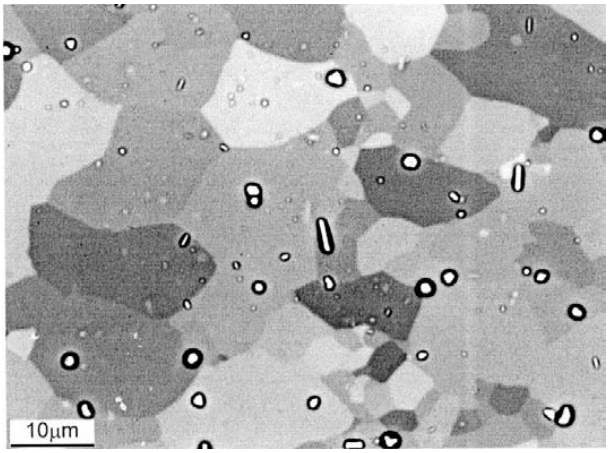

Fig. 2.7 The recrystallized microstructures in a deformed and annealed Al-0.8 wt% Si alloy containing 3μm silicon particles [11].

The CDRX occurs by the progressive accumulation of dislocations in the low angle boundaries, leading to the increase of their misorientation and the formation of large angle grain boundaries when their misorientation angles reach a critical value, approximately 15°. This mechanism has been observed in several high stacking fault energy metals, such as aluminum and aluminum alloys [46-47]. Nevertheless, there is a general agreement to consider that the transformation of low angle boundaries into high angle boundaries effectively takes place when the boundaries are pinned by fine dispersoid particles [48-51].

Moreover, Drury and Humphreys [11] reported an alternative mechanism of CDRX, which is termed rotation recrystallization. As the material is deformed, high angle boundaries develop by the progressive rotation of subgrains, which are adjacent to pre-existing grain boundaries. This mechanism involves an interaction between grain boundary deformation and the grain boundary serrations as shown in Fig. 2.8 [11]. High angle grain boundaries develop serrations due to interaction with the deformation substructure (Fig. 2.8(a)). Grain

boundary sliding can then only occur on parts of the boundary, e.g. A, while other regions (e.g. B) have to accommodate the strain by plastic deformation (Fig. 2.8(b)), leading to shear and local lattice rotation as shown in Fig. 2.8(c).

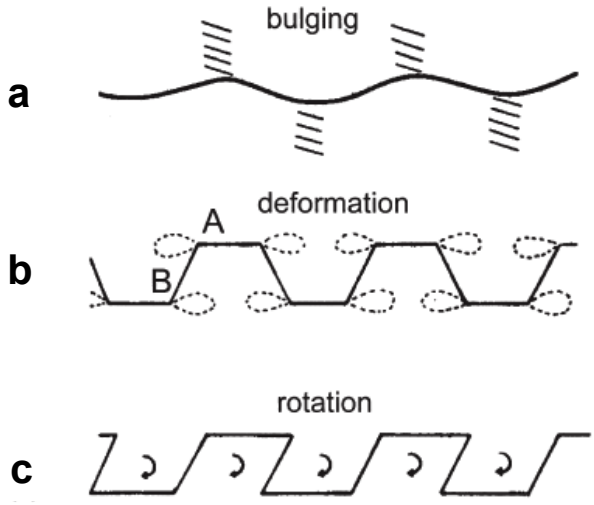

Fig. 2.8 The mechanism of dynamic recrystallization by progressive lattice rotation in Al–Mg alloys. (a) HAGB serrations form; (b) Grain boundary sliding occurs on horizontal boundaries, but slip occurs on bulged sections, leading to local lattice rotations associated with the bulges, (c) [11].

The GDRX is commonly seen at high stresses and strains in certain materials, particularly in aluminum [6,44]. At high strains, the grains of the material become flattened and elongated in the direction of the force. The grain boundaries become serrated due to surface tension effects generated by the subgrains within the grains. Eventually, the two sides of a grain will touch and annihilate each other, effectively pinching the grain into two grains, as shown in Fig. 2.9 [44].

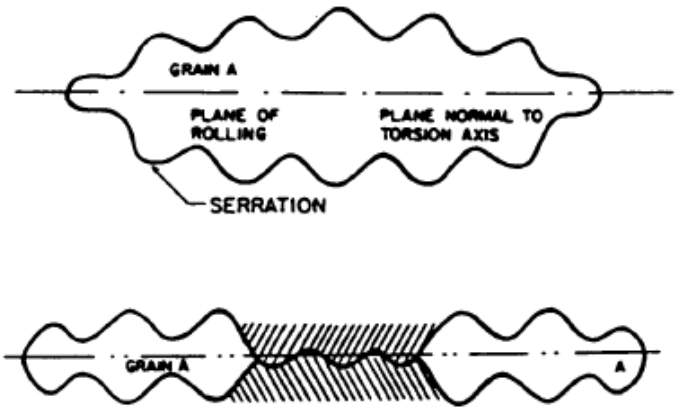

Fig. 2.9 Schematic illustration of geometric dynamic recrystallization (GDRX) [44].

Aluminum and its alloys with high stacking fault energy exhibit a high rate of DRV, which significantly inhibits DRX [6]. However, formation of new grains during hot deformation of aluminum alloys was frequently reported, while several mechanisms of DRX for aluminum alloys have been proposed, involving DDRX, CDRX and GDRX [6,11]. Moreover, during plastic deformation process, most of the deformation work is converted to heat [52]. The deformation heating may cause thermal softening of materials, which offsets the work hardening effect and result in a decrease in flow stress [53]. Furthermore, precipitation hardening alloys may alter dynamic softening behavior as a result of changes in precipitate morphology, when the material is not thoroughly over-aged. Materials pre-aged at deformation temperature have a low peak stress and exhibits a gradual softening as precipitates coalesce and subgrains form [54]. Solution-treated aluminum alloys exhibit a high peak stress due to dynamic precipitation (DPN), followed by a rapid dynamic softening as precipitates coalesce, solute depletes and DRV progresses [55].

2.5 Constitutive Analysis

2.5.1 Flow stress curve

When the hot deformation is performed at a constant temperature with a given strain rate, a true stress-true strain curve can be established, termed the flow stress curve. The flow stress curves can be divided into three typical cases, as shown in Fig. 2.10, which are closely related to different dynamic softening mechanisms. In the first case, the flow stress rises rapidly and then undergoes a continuous increase of stress with increasing strain. A progressive increase of flow stress is likely due to the fact that the rate of work hardening is higher than that of DRV [11]. In the second case, the flow stress increases to a plateau, followed by a fairly steady stress. This indicates that a dynamic equilibrium between work hardening and DRV is achieved [11]. In the third case, the flow stress exhibits a distinct peak value and then decreases significantly. In general, the decline of flow stress can be associated with the coalescence of precipitates, enhanced DRV [56-58] and DDRX [59-62]. Under conditions of low Zener-Hollomon parameter, multiple peaks may be exhibited along with a continuous flow softening, which is also as a result of DDRX [11]. Cracking may also occur during hot deformation at high strain rates that could result in a decrease in the flow stress after reaching the peak stress [63,64]. In addition, the flow stress decrease can be caused by a severe deformation heating when deformation is performed at high strain rates [6,56].

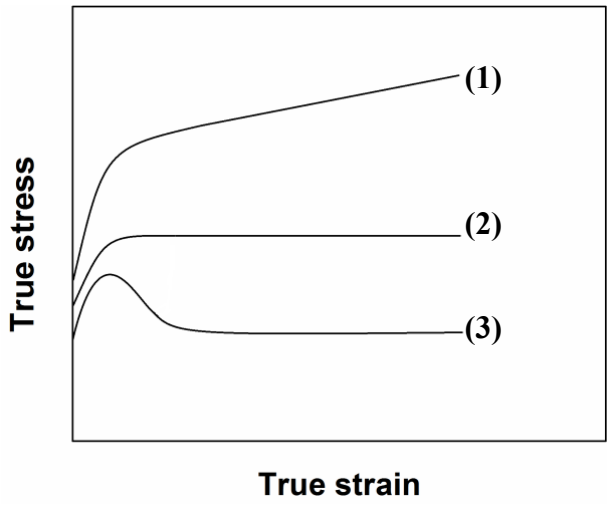

Fig. 2.10 Schematic illustration of evolution of flow stress curves in three cases [6,11].

2.5.2 Constitutive equation

A constitutive relation is generally used to describe the plastic flow properties of metals and alloys, which are correlated with the flow stress, strain rate and deformation temperature. Several models have been proposed to describe the hot deformation behavior, including physical-based, phenomenological and artificial neural network models and equations [65-74]. Sellars and McTegart [65] developed a hyperbolic-sine constitutive law to describe the hot working and creep behavior of aluminum, nickel, copper and steel materials. Johnson and Cook [66] proposed a phenomenological model, which Lin *et al.* [67] then modified to evaluate the hot compressive behavior of a 7075 aluminum alloy by considering the effects of strain rate and the deformation temperature. Chai *et al.* [68] conducted a comparative study on the capability of a back propagation neural network model and a strain-compensated, Arrhenius-type constitutive equation to represent the elevated temperature flow behavior of XC45 steel. Lin *et al.* [69] proposed a revised Arrhenius constitutive equation to describe the

effect of strain on material constants and on the flow behavior of 42CrMo steel. In addition, some researchers have applied these constitutive models and equations to evaluate the hot deformation behavior of various metals and alloys [70-74].

With various constitutive models and equations available, the hyperbolic-sine equation, proposed by Sellars and McTegart [65], is widely employed to describe the relationship between the strain rate, deformation temperature and flow stress, especially over a wide range of stresses [6,65],

$$\dot{\varepsilon} = A[\sinh(\alpha\sigma)]^n \exp(-\frac{Q}{RT}) \tag{2.1}$$

where n and A are material constants, α is the stress multiplier, σ is the flow stress (MPa), Q is the activation energy for hot deformation (kJ/mol), R is the universal gas constant (8.314 J/mol K), and T is the deformation temperature (K).

2.6 Processing Map

The processing map has been widely used to understand the hot workability of materials in terms of various microstructural mechanisms operating at different deformation conditions, which was developed on the basis of the dynamic materials model by Prasad [10, 11]. In this method, the efficiency of power dissipation, η, represents the energy dissipated through microstructural mechanisms during hot deformation and is given as,

$$\eta = \frac{2m}{2m+1} \tag{2.2}$$

where m is the strain rate sensitivity of the material given by $\frac{\partial \ln \sigma}{\partial \ln \dot{\varepsilon}}$.

The contour plot of the iso-efficiency η values as a function of temperature and strain rate constitutes the power dissipation map. Different domains in the power dissipation map imply the specific microstructural mechanisms, such as dynamic recrystallization, dynamic recovery, wedge cracking, and void formation [10, 11]. However, during the deformation process, flow instabilities may occur and lead to deformation defects in the microstructure, including flow localization, adiabatic shear deformation, flow rotation and kinking [10, 11]. The criterion to evaluate those flow instabilities is given as,

$$\xi = \frac{\partial \ln[m/(m+1)]}{\partial \ln \dot{\varepsilon}} + m < 0 \qquad (2.3)$$

The material may exhibit deformation defects when ξ is negative [10, 11]. Hence, the instability map can be generated based on the variation of ξ with the temperature and strain rate. Finally, the processing map is obtained by superimposing the instability map on the power dissipation map.

With the help of the processing maps, the deformation temperature and the strain rate corresponding to local peak efficiency of power dissipation in the safe domain is chosen as the optimum processing parameters for hot working of materials. The hot working should not be performed in the regions of flow instability in order to prevent the occurrence of microstructure defects [76]. Recently, the processing maps had been widely used to optimize the processing parameters in hot working of aluminum alloys. Luo et al. [77] developed the

processing maps of AA7050 aluminum alloy at different strains and obtained that the optimum processing parameters at a strain of 0.7 were 450 °C and 0.01 s^{-1} with an efficiency of 42%. Various microstructural defects generated during hot deformation in AA2124 aluminum alloy were studied by processing map, and the flow instability arising from adiabatic shear band and matrix cracking was observed [78]. Ganesan et al. [79] developed the processing map for AA6061 Al/15 vol.% SiCp using the flow stresses predicted from a neural network model, and the safe domains of hot working were identified and validated through microstructural investigations. A 4D process map was developed by Bhimavarapu et al. [80], which illustrates contours of power dissipation and instability with respect to strain rate, temperature, and strain. However, most of these works focused on the influences of temperature, strain rate and strain on the processing maps. Literature on investigating the effect of alloying elements on processing maps for hot working of aluminum alloys is rarely found.

References

[1] E.A. Starke, J.T. Staley, Prog. Aerosp. Sci. 32 (1996) 131-172.

[2] F.Y. Xie, X.Y. Yan, L. Ding, F. Zhang, S.L. Chen, M.G. Chu, Y.A. Chang, Mater. Sci. Eng. A, 335 (2003) 144-153.

[3] L. L. Rokhlin, T. V. Dobatkina, N. R. Bochvar, E. V. Lysova, J. Alloys Comp. 367 (2004) 10-16.

[4] J.D. Robson, Mater. Sci. Eng. A 382 (2004) 112-121.

[5] X. Fan, D. Jiang, Q. Meng, B. Zhang, T. Wang, T. Nonferr. Metal Soc. 16 (2006) 577-581.

[6] H.J. McQueen, S. Spigarelli, M. Kassner, E. Evangelista, Hot Deformation and Processing of Aluminum Alloys, CRC Press, Florida, 2011, pp. 87-233.

[7] J.D. Robson, Acta Mater. 52 (2004) 1409-1421.

[8] S. Hirosawa, T. Sato, A. Kamio, H.M. Flower, Acta Mater. 48 (2000) 1797-1806.

[9] G.B. Schaffer, S.H. Huo, J. Drennan, G.J. Auchterlonie, Acta Mater. 49 (2001) 2671-2678.

[10] J.M. Silcock, H.M. Flower, Scripta Mater. 46 (2002) 389-394.

[11] F.J. Humphreys, M. Hatherly, Recrystallization and Related Annealing Phenomena, second ed., Elsevier Ltd., Oxford, 2004, pp. 169-450.

[12] H. Okamoto, Phase Diagrams for Binary Alloys, ASM International,Materials Park, 2000.

[13] E. Nes, Acta metall. 20 (1972) 499-506.

[14] N. Ryum, Acta Metall. 17 (1969) 269-278.

[15] O. Izumi, D. Oelschlagel, Scripta Metall. 3 (1969) 619-621.

[16] S. Rystad, N. Ryum, Aluminium 53 (1977) 193-195.

[17] T. Sato, A. Kamio, G. W. Lorimer, in Proc. 5th Conf. Alumininum Alloys (ICAA-5), Vol. 2, 1996, pp 895.

[18] H. P. Deischer, G. Rumplmair, W. Lacom, F. Katner, Electron Micros. 1 (1984) 753.

[19] K.E. Knipling, D. C. Dunand, D. N. Seidman, Acta Mater. 56 (2008) 114-127.

[20] J.D. Robson, P.B. Prangnell, Acta Mater. 49 (2001) 599-613.

[21] Y.V. Milman, A.I. Sirko, D.V. Lotsko, D.B. Miracle, O.N. Senkov, Mater. Sci Forum

396-402 (2002) 1217-1222.

[22] O. Engler, E. Sachot, J.C. Ehstrom, A. Reeves, R. Shahani, Mater. Sci. Tech. 12 (1996) 717-729.

[23] B. Morere, R. Shahani, C. Maurice, J. Driver, Metall. Mater. Trans. A 32 (2001) 625-632.

[24] J.D. Robson, Mater. Sci. Eng. A 338 (2002) 219-229.

[25] A.R. Eivani, H. Ahmed, J. Zhou, J. Duszczyk, Mater. Sci. Eng. A 527 (2010) 2418-2430.

[26] Y. Li, Z. Liu, L. Lin, J. Peng, A. Ning, J. Mater. Sci. 46 (2011) 3708-3715.

[27] L. Zou, Q. Pan, Y. He, W. Liang, C. Wang, Mater. Sci. 44 (2008) 120-125.

[28] E.F. Kazakova, Y.I. Rusnyak, Met. Sci. Heat Treat. 51 (2009) 436-439.

[29] K.E. Knipling, D.C. Dunand, D.N. Seidman, Z. Metallkd. 97 (2006) 246-265.

[30] J.R. Davis, ASM Specialty Handbook: Aluminum and Aluminum Alloys, American Society for Metals, Metals Park, OH, USA, 1993, pp. 23-58.

[31] A.K. Srivastava, S. Ranganathan, J. Mater. Res. 16 (2001) 2103-2117.

[32] M. Moss, Acta Metall. 16 (1968) 321-326.

[33] Y.W. Kim, F.H. Froes, Mater. Sci. Eng. 98 (1988) 207-211.

[34] Y. Ning, Y. Li, Chin. J. Met. Sci. Technol. 6 (1990) 103-105.

[35] E.S. Humphreys, P.J. Warren, J.M. Titchmarsh, A. Cerezo, Mater. Sci. Eng. A 304-306 (2001) 844-848.

[36] C.C. Yang, Y.C. Chen, E. Chang, 34, Acta Mater. 34 (1996) 1059-1065.

[37] S. Camero, E.S. Puchi, G. Gonzalez, J. Mater. Sci. 41 (2006) 7361-7373.

[38] S. Zhu, J. Yao, L. Sweet, M. Easton, J. Taylor, P. Robinson, N. Parson, JOM 65 (2013) 584-592.

[39] A. Luo, W.V. Youdelis, Mater. Sci. Tech. 9 (1993) 781-784.

[40] S.J. Hales, T.R. McNelley, H.J. McQueen, Metal. Trans. 22A (1991) 1037-1047.

[41] R.E.D. Mann, R.L. Hexemer Jr., I.W. Donaldson, D.P. Bishop, Mater. Sci. Eng. A 528 (2011) 5476-5483.

[42] M. Rajamuthamilselvan, S. Ramanathan, J. Alloys Compd. 509 (2011) 948-952.

[43] E. Cerri, E. Evangelista, A. Forcellese and H.J. McQueen, in L. Arnberg, O. Lohne, E. Nes and N. Ryum (eds.), Aluminium Alloys, Physical and Mechanical Properties

(ICAA3), Vol. 2, NTH-SINTEF, Trondheim, 1992, pp. 139-144.

[44] X. Wang, F. Cong, Q. Zhu, J. Cui, Sci China Technol. Sci. 55 (2012) 510-514.

[45] Q. Cui, G. Itoh, M. Kanno, Y. Tsuji, K. Kobayashi, J. Japan Inst. Metals 59 (1995) 251-257.

[46] W.M. Mao, in: G.E. Totten, D.S. MacKenzie (Eds.), Handbook of Aluminum: Vol. 1: Physical Metallurgy and Processes, Marcel Dekker, Inc. New York, 2003, pp. 211-216.

[47] R.W.K. Honeycombe, The Plastic Deformation of Metals, London, E. Arnold Ltd, 1968, pp.128-176.

[48] R.D. Doherty, D.A. Hughes, F.J. Humphreys, J.J. Jonas, D.J. Jensen, A.D. Rollett, Mater. Sci. Eng. A 238 (1997) 219-274.

[49] H.J. McQueen, J.J. Jonas, J. Appl. Metalwork. 3 (1984) 233-241.

[50] C. Perdrix, M.Y. Perrin, F. Montheillet, Mem. Etud. Sci. Rev. Metall. 78 (1981) 309-320.

[51] S Gourdet, E.V Konopleva, H.J McQueen and F Montheillet, Mater. Sci. Forum, 217-227 (1996) 441-446.

[52] R.H. Bricknell, J.W. Edington, Metall. Trans. 10A (1979) 1257-1263.

[53] R.H. Bricknell, J.W. Edington, Acta Metall. 27 (1979) 1303-1311.

[54] M.T. Lyttle, J.A. Wert, J. Mater. Sci. 29 (1994) 3342–3350.

[55] H. Gudmundson, D. Brooks, J.A. Wert, Acta Metall. Mater. 39 (1991) 19–35.

[56] X. Huang, H. Zhang, Y. Han, W. Wu, J. Chen, Mater. Sci. Eng. A 527 (2010) 485-490.

[57] E. Cerri, E. Evangelista, A. Forcellese, H.J. McQueen, Mater. Sci. Eng. A 197 (1995) 181-198.

[58] G. Avramovic-Cingara, D.D. Perovic, H.J. McQueen, Met. Mat. Trans. A. 27 (1996) 3478-3490.

[59] H. Yamagata, Scripta Metall. Mater. 27 (1992) 727-732.

[60] H. Yamagata, Scripta Metall. Mater. 30 (1992) 411-416.

[61] T. Sheppard, M.G. Tutcher, Met. Sci. 14 (1980) 579-589.

[62] H.J. McQueen, E. Evangelista, J. Bowles, G. Crawford, Met. Sci. 18 (1984) 395-402.

[63] Y.V.R.K. Prasad, S. Sasidhara, Hot working guide-a compendium of processing maps, ASM Intl., Ohio, USA, 1997, pp. 1-24.

[64] H.R. Ezatpour, S.A. Sajjadi, M. Haddad-Sabzevar, G.R. Ebrahimi, Mater. Sci. Eng. A 550 (2012) 152-159.

[65] C.M. Sellars, W.J. McTegart, Mem. Sci. Rev. Met. 63 (1966) 731-746.

[66] G.R. Johnson, W.H. Cook, Eng. Fra. Mech.21 (1985), 31-48.

[67] Y. C. Lin, L.T. Li, Y.X. Fu, Y.Q. Jiang, J. Mater. Sci. 47 (2012) 1306-1318.

[68] R.X Chai, C. G, L. Yu, Mater. Sci. Eng. A 534 (2012) 101-110.

[69] Y.C. Lin, M.S. Chen, J. Zhong, Comput. Mater. Sci. 42 (2008) 470-477.

[70] S. Mandal, V. Rakesh, P.V. Sivaprasad, S. Venugopal, K.V. Kasiviswanathan,. Mater. Sci. Eng. A 500 (2009) 114-121.

[71] D. Samantaray, S. Mandal, A.K. Bhaduri, Mater. Des. 31 (2010) 981-984.

[72] Y.C. Lin, Y.C. Xia, X.M. Chen, M.S. Chen, Comput. Mater. Sci. 50 (2010) 227-233.

[73] C.L. Gan, Y.D. Xue, M.J. Wang, Mater. Sci. Eng. A 528 (2011) 4199-4203.

[74] G.L. Ji, F.G. Li, Q.H. Li, H.Q. Li, Z. Li, Mater. Sci. Eng. A 528 (2011) 4774- 4782.

[75] Y.V.R.K. Prasad, H.L. Gegel, S.M. Doraivelu, J.C. Malas, J.T. Morgan, K.A. Lark, D.R. Barker, Metall. Trans. A 15A (1984) 1883-1892.

[76] P.S. Robi, U.S. Dixit, J. Mater. Process. Technol. 142 (2003) 289-294.

[77] J. Luo, M.Q. Li, B. Wu, Mater. Sci. Eng. A 530 (2011) 559-564.

[78] S. Ramanathan, R. Karthikeyan, V. Deepak Kumar, G. Ganesan, J. Mater. Sci. Technol. 22 (2006) 611-625.

[79] G. Ganesan, K. Raghukandan, R. Karthikeyan. J. Mater. Process. Technol. 166 (2005) 423-429.

[80] S.B. Bhimavarapu, A.K. Maheshwari, D. Bhargava, S.P. Narayan, J. Mater. Sci. 46 (2011) 3191-3199.

CHAPTER III

MICROSTRUCTURAL EVOLUTION AND DYNAMIC SOFTENING MECHANISMS OF 7150 ALUMINUM ALLOY (ZR FREE) DURING HOT DEFORMATION

Chapter III Microstructural Evolution and Dynamic Softening Mechanisms of 7150 aluminum Alloy (Zr free) during Hot Deformation

Abstract

The hot deformation behavior and microstructural evolution of an Al-Zn-Mg-Cu (7150) alloy was studied during hot compression at various temperatures (300 to 450 °C) and strain rates (0.001 to 10 s^{-1}). A decline ratio map of flow stresses was proposed and divided into five deformation domains, in which the flow stress behavior was correlated with different microstructures and dynamic softening mechanisms. The results reveal that the dynamic recovery is the sole softening mechanism at temperatures of 300 to 400 °C with various strain rates, and at temperatures of 400 to 450 °C with strain rates between 1 and 10 s^{-1}. The level of dynamic recovery increases with increasing temperature and with decreasing strain rate. At the high deformation temperature of 450 °C with strain rates of 0.001 to 0.1 s^{-1}, a partially recrystallized microstructure was observed and dynamic recrystallization (DRX) provided an alternative softening mechanism. Two kinds of dynamic recrystallization (DRX) might operate at the high temperature, in which discontinuous dynamic recrystallization was involved at higher strain rates and continuous dynamic recrystallization was implied at lower strain rates.

The content of this chapter has been published as: C. Shi, J. lai, X.-G. Chen, Microstructural evolution and dynamic softening mechanisms of Al-Zn-Mg-Cu alloy during hot compressive deformation, Materials, 7 (2014) 244-264.

3.1 Introduction

The 7xxx series aluminum alloys are very attractive materials to be used in the automotive and aerospace industries, due to their excellent combination of properties such as high strength-to-density ratio, high fracture toughness, and resistance to stress corrosion cracking [1]. A good understanding of the hot deformation behavior and microstructural evolution is of primary importance for the design of hot-forming processes such as rolling, extrusion and forging. Thermomechanical factors, such as the degree of deformation, deformation temperature and strain rate are the main factors, which influence the flow stress and the associated microstructure [2,3]. Furthermore, the evolution of flow stress is correlated with different dynamic softening mechanisms during hot deformation at various deformation conditions [2,4].

Dynamic recovery (DRV) and dynamic recrystallization (DRX) are the typical softening mechanisms in metals and alloys during deformation at elevated temperatures [2,4]. Aluminum and its alloys with high stacking fault energy exhibit a high rate of DRV, which significantly inhibits DRX [2]. However, formation of new grains during hot deformation of aluminum alloys was frequently reported, while several mechanisms of DRX for aluminum alloys have been proposed [5-13]. The discontinuous dynamic recrystallization (DDRX) was observed in aluminum and aluminum alloys by many researchers [5-9]. DDRX involves the development of high angle grain boundaries via nucleation and growth of new grains, which typically initiates at high angle boundaries, such as original grain boundaries, boundaries of

dynamically recrystallized grains and boundaries created during deformation [4]. Bulging of grain boundaries is frequently observed as a prelude to DDRX, and subsequent grain growth proceeds by strain-induced boundary migration [4]. Furthermore, continuous dynamic recrystallization (CDRX) was also observed in aluminum alloys [10-13]. This mechanism differs from that of DDRX, in which new grains are formed progressively within the deformed original grains from a continuous increase of subgrain boundary misorientations, as a result of accumulation of dislocations in low angle boundaries [2,10-13].

Moreover, during plastic deformation process, most of the deformation work is converted to heat [14]. Plastic deformation performed at high strain rate conditions is essentially adiabatic, thus generating a significant deformation heat and leading to a noticeable increase in temperature [15]. The deformation heating may cause thermal softening of materials, which offsets the work hardening effect and result in a decrease in flow stress [16-18]. In addition, formation of adiabatic shear bands is usually observed at regions where deformation is localized [15]. Furthermore, precipitation hardening alloys may alter dynamic softening behavior as a result of changes in precipitate morphology, when the material is not thoroughly over-aged. Materials pre-aged at deformation temperature have a low peak stress and exhibit gradual softening as precipitates coalesce and subgrains form [19,20]. Solution-treated aluminum alloys exhibit a high peak stress due to dynamic precipitation (DPN), followed by a rapid dynamic softening as precipitates coalesce, solute depletes and DRV progresses [17,21-24].

To date, the previous studies have been mainly on determining Zener-Hollomon parameter (Z), activation energy for hot deformation, and various material constants in the constitutive equations for describing hot deformation behavior of 7xxx aluminum alloys [25,26]. The softening mechanism of these alloys is generally reported to be DRV at low temperature with high strain rate, while DRX occurs as deformed at high temperature with low strain rate [27-29]. Different dynamic recrystallization mechanisms of 7075-T6 aluminum alloy have been studied during deformation at semi-solid temperature range (450-580°C) [30]. Several researchers have studied the kinetics and rate of DRX and DRV using various models [31,32]. Jonas et al. [31] measured the kinetic of DRX using the Avrami formulation, and predicted the DRX flow curves. Mostafaei and Kazeminezhad [32] proposed a mathematical method based on hot flow curves to predict the effects of temperature and strain rate on the kinetics of DRV in the Al-Mg alloy. However, quantitative characterization of the evolution of flow stress curves at different deformation conditions has rarely been reported. The relationship between the evolution of flow stress and various dynamic softening mechanisms during hot deformation needs to be clarified. During deformation at medium temperature range (up to 450°C), a systematical investigation of different dynamic softening mechanisms at various deformation conditions for 7150 aluminum alloy is limited.

In the present paper, the hot deformation behavior of an Al-Zn-Mg-Cu alloy (7150) is studied using uniaxial compression tests performed at various temperatures and strain rates.

The microstructural evolution during the hot deformation is investigated in order to understand the various dynamic softening mechanisms at different deformation conditions. Based on the different decline levels in flow stresses with respect to peak stresses, a decline ratio map of flow stresses is proposed to correlate flow stress behavior with dynamic softening mechanisms at various deformation conditions.

3.2 Experimental

The experiments were conducted on an Al-Zn-Mg-Cu alloy. The chemical composition of the experimental alloy analyzed by an optical emission spectrometer is given in Table 3.1. The most elements of the alloy are in the range of 7150 composition designation. But no Zr is added in this study. Approximately 3 kg of materials was melted in an electrical resistance furnace and then cast into a rectangular permanent steel mold measuring 30 x 40 x 80 mm^3. The cast ingots were homogenized at 465 °C for 24 h, followed by a direct water quenching. Cylindrical samples of 10 mm in diameter and 15 mm long were machined from the homogenized ingots. Uniaxial compression tests were conducted on a Gleeble 3800 thermomechanical simulation unit at strain rates of 0.001, 0.01, 0.1, 1 and 10 s^{-1} and deformation temperatures of 300, 350, 400 and 450 °C respectively. During the tests on the Gleeble unit, the samples were heated to the desirable deformation temperature at a heating rate of 10 °C/s and held for 3 min to ensure a homogenous temperature distribution through the samples. The samples were deformed to a total true strain of 0.8 and then immediately water-quenched to maintain the microstructure at the deformation temperature. Some

selected samples were also deformed to different true strains of 0.1, 0.3 and 0.5, followed by water quenching, in order to investigate the microstructural evolution during deformation process.

The microstructures of the as-cast and as-homogenized materials were examined prior to hot deformation under an optical microscope. The intermetallic phases were identified using the electron backscattered diffraction (EBSD) technique and the energy dispersive spectroscope (EDS) with a scanning electron microscope (SEM, JEOL JSM-6480LV). All deformed samples were sectioned parallel to the compression axis along the centerline and then polished and etched in the Keller solution for optical microscope observation. Additionally, some deformed and as-homogenized samples were selected for EBSD analysis. In the EBSD analysis, the boundaries of both the grains and subgrains are defined as low angle boundaries (LABs), medium angle boundaries (MABs) and high angle boundaries (HABs) for which the misorientation angles of boundaries occur in the ranges of 1-5°, 5-15° and greater than 15°, respectively [33]. The spatial resolution for EBSD parallel to the sample tilt axis in the W-filament SEM (JEOL JSM-6480LV) is ~60 nm on aluminum, while the angular precision is 1°. The step size between the scanning points was set to 1.0 μm for the grain structure of samples. The dynamic recrystallized grains were separated from the deformed ones using the grain average misorientation (GAM) method [34,35]. A threshold value of GAM (2.5°) inside a grain was determined to distinguish a recrystallized grain from a deformed one. Grains with GAM less than 2.5° were considered as recrystallized grains.

Subsequently, the size of the recrystallized grains was measured by means of grain reconstruction method [36]. For quantitative measurement of misorientation distribution of boundaries, EBSD line scan was carried out [36,37], and a sample surface area of about 1.2 mm^2 with a scanning step size of 3.0 μm was selected. In addition, EBSD analysis was performed to measure the grain size of the as-homogenized sample using the linear intercept method [36]; a surface area of approximately 10 mm^2 with a scanning step size of 5.0 μm was selected for the sample. Samples for TEM observation were mechanically grinded to the thicknesses of 35-60 μm followed by electropolish in a twin-jet polishing unit, which were operated at 15 V and -20 °C using a 30 vol.% nitric acid and 70 vol.% methanol solution. The disks were observed in a transmission electron microscope (TEM, JEOL-JEM-2100), operated at 200 kV.

Table 3.1 Chemical composition of the experimental alloy (Zr free) (wt%).

Zn	Mg	Cu	Si	Fe	Mn	V	Ti	Al
6.44	2.47	2.29	0.16	0.15	0.002	0.01	0.009	Bal.

3.3 Results

3.3.1 Initial microstructure

Fig. 3.1a shows the initial as-cast microstructure of the alloy, which contained $MgZn_2(\eta)$, $Al_6(FeCu)$, Mg_2Si, $Al_2CuMg(S)$ and $Al_2Cu(\theta)$ intermetallic phases, distributed in the interdendritic boundaries. The Al_2CuMg phase was observed to be attached with the $MgZn_2$ phase (lamellar eutectic morphology) and Al_2Cu phase (isolated droplet morphology) in the aluminum matrix. These phases have been commonly observed in as-cast 7xxx aluminum

alloys [38,39]. After homogenization treatment at 465°C for 24 h, the $MgZn_2$ and Al_2Cu phases were completely dissolved into the aluminum matrix, while the coarse particles of $Al_6(FeCu)$, Mg_2Si and Al_2CuMg were only dissolved partially and some of them were retained in the matrix (Fig. 3.1b).

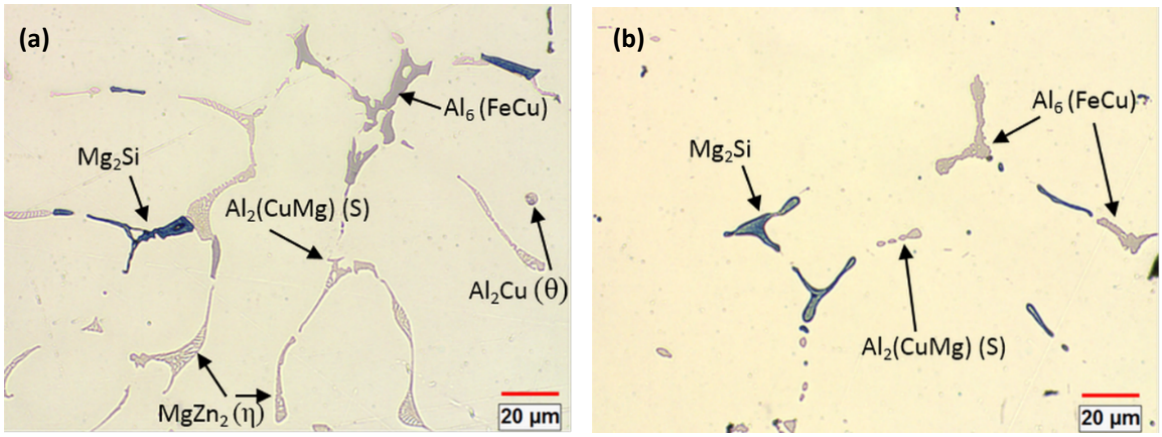

Fig. 3.1 The optical micrographs of the alloy: (a) as-cast mictrostructure and (b) as-homogenized microstructure.

3.3.2 Flow stress behavior

The hot compression tests of the alloy were carried out at deformation temperatures of 300 to 450 °C and at strain rates of 0.001 to 10 s^{-1}. A series of true stress-true strain curves under different deformation conditions are shown in Fig. 3.2. In general, the flow stress increased rapidly at the beginning of deformation and then remained fairly constant or decreased to some extent after attaining the peak stress. At the early stage of deformation, dislocations multiplied dramatically, and the work hardening process was predominant, thereby leading to a rapid increase in the flow stress [4]. As the dislocation density increased, dynamic softening occurred, which can offset the effect of work hardening [2,4]. Thus the

flow stress increased at a decreasing rate until the peak stress was reached. Subsequently, the flow stress either decreased with increasing strain or remained fairly steady. The former behavior is observed when the rate of dynamic softening is higher than that of work hardening [2,4]. The latter behavior occurs as a result of a dynamic equilibrium between work hardening and dynamic softening [2,4]. In both cases, a distinct peak stress is visible as the maximum value in the flow stress curve (see the arrow in Fig. 3.2a). Occasionally, the flow stress can continuously increase after the early stage of deformation. In this case, the peak stress was identified as the tangent point on the flow stress curve by the extension of a line along the steady-state flow stresses (see the arrow in Fig. 3.2b).

Furthermore, it is evident that the level of the flow stress decreased with increasing deformation temperature and with decreasing strain rate. As the deformation temperature rises, the thermal activation which favors overcoming an energy barrier to dislocation motion is increased, while the stress needed to deform a material decreases [40,41]. Besides, with the increase of temperature, the level of dynamic softening is improved, so that the dislocation density is reduced to facilitate the further dislocation motion [2,4]. Hence, increasing temperature could substantially reduce the resistance to dislocation movement, which results in the decline of flow stress. On the other hand, with the decrease of strain rate, the dislocation multiplication rate is reduced which leads to less tangled dislocation structures as barriers to the dislocation movement [2]. In addition, decreasing strain rate results in an increasing level of dynamic softening due to the relatively more time for proceeding of

dislocation polygonization, which facilitates the further movement of dislocation [2,4]. Therefore, decreasing strain rate is expected to lower the stress which is needed for dislocation movement, and leads to the decrease in flow stress.

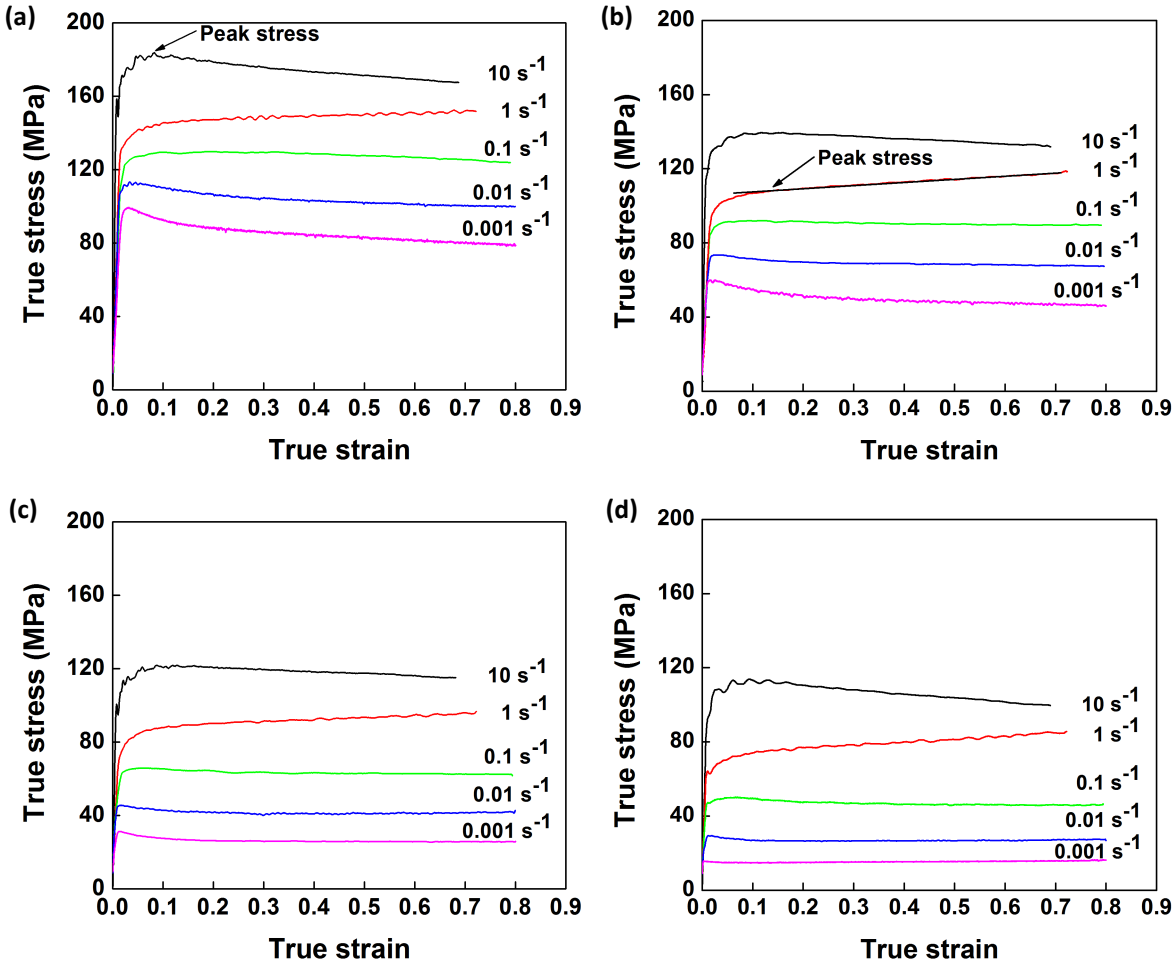

Fig. 3.2 True stress-true strain curves of the alloy during hot compression deformation: (a) T = 300 °C; (b) T = 350 °C; (c) T = 400 °C; and (d) T = 450 °C.

3.3.3 Decline ratio map of flow stresses

The flow stress curves can be divided in three typical cases, as shown in Fig 4.3a, which are closely related to different dynamic softening mechanisms. In the first case, the flow stress rises rapidly and then undergoes a continuous increase of stress with increasing strain.

A progressive increase of flow stress is likely due to that the rate of work hardening is higher than that of DRV [4]. In the second case, the flow stress increases to a plateau, followed by a fairly steady stress. This indicates that a dynamic equilibrium between work hardening and DRV is achieved [4]. In the third case, the flow stress exhibits a distinct peak value and then decreases significantly. In general, the decline of flow stress can be associated with the coalescence of precipitates, enhanced DRV [17,21-24] and DDRX [5-9]. Under conditions of low Zener-Hollomon parameter, multiple peaks may be exhibited along with a continuous flow softening, which is also as a result of DDRX [4]. Cracking may also occur during hot deformation at high strain rates that could result in a decrease in the flow stress after reaching the peak stress [42,43]. In addition, the flow stress decrease can be caused by a severe deformation heating when deformation is performed at high strain rates [2,16-18].

A decline ratio of flow stress, R_d, is introduced to characterize the evolution of flow stress curves during hot deformation of the alloy. R_d is based on the decline level in flow stress at the end of the deformation with respect to the corresponding peak stress, and is defined in Equation 3.1. The lower the value of R_d, the more decline the flow stress relative to the peak stress.

$$R_d(\%) = \frac{\sigma_s - \sigma_p}{\sigma_p} \times 100 \tag{3.1}$$

where σ_s is the value of flow stress at the end of the deformation (at a true strain of 0.8 in our study) and σ_p is the value of peak stress.

According to the experimental data obtained under deformation at temperatures of 300 to 450 °C and at strain rates of 0.001 to 10 s^{-1}, the decline ratio map of flow stresses at various deformation conditions for the 7150 alloy is presented in Fig. 3.3b. Generally, with increasing strain rate, the value of decline ratio increased, indicating an enhanced work hardening effect and a decreasing level of dynamic softening. However, at the strain rate of 10 s^{-1}, the decline ratio value again decreased. This map can be divided into five deformation domains:

Domain I illustrates a significant decrease in flow stress after the peak stress with the values of R_d between -13% and -6%, when the deformation was performed at a high strain rate of 10 s^{-1}.

Domain II represents the deformation conditions at temperatures of 300 to 400 °C with strain rates of 0.1 to 1 s^{-1}, as well as at higher temperatures of 400 to 450 °C with a strain rate of 1 s^{-1}. Either slight decrease or continuous increase in flow stress after the peak stress is observed, and the values of R_d vary between -8% and 17%.

Domain III represents the deformation performed at temperatures of 300 to 400 °C with low strain rates of 0.001 to 0.01 s^{-1}. A significant decline in flow stress is observed with the values of R_d between -28% and -10%.

Domain IV is characterized by a large decrease of flow stress with the value of R_d approximately -12%, during the deformation at a high temperature of 450 °C with strain rates of 0.01 to 0.1 s^{-1}. It is of interest to notice that only a single peak followed a steady-state flow

was observed in the flow stress curves of Domains III and IV (Fig. 3.2). However, Yamagata [5,6] has reported that multiple peaks followed by a continuous flow softening could also be induced as a result of DDRX in pure aluminum at those deformation conditions. In both cases, the values of R_d could be in the same range, though the softening mechanisms resulting in such features might be different.

Domain V shows a slight decrease of flow stress under the deformation at a high temperature of 450 °C with a low strain rate of 0.001 s^{-1}, and the value of R_d is around -5%.

It is observed that the R_d is generally a function of temperature and strain rate, rather than a unique value. The changes of the values of R_d in the Al-Zn-Mg-Cu alloy under different deformation domains correspond to various softening mechanisms [2,4-9,17,21-24,42,43], which will be discussed in the following sections.

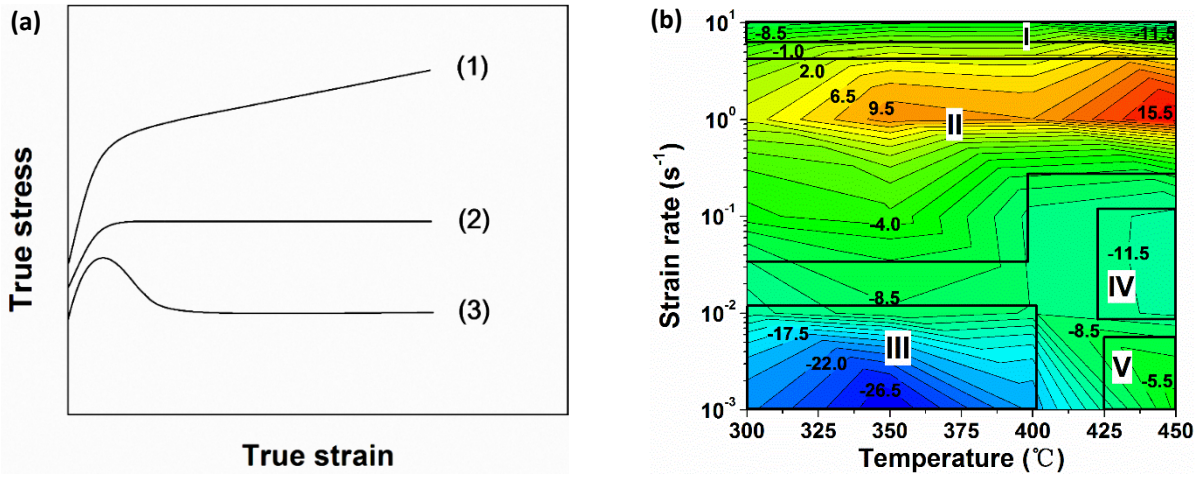

Fig. 3.3 (a) Schematic illustration of evolution of true stress-true strain curves in three cases; (b) decline ratio map of flow stresses, $R_d(\%)$, as a function of deformation temperature and strain rate.

3.3.4 Microstructural evolution

The microstructures of deformed samples in different deformation domains were examined using the optical microscope. Besides, in an attempt to gain more insight into microstructural evolution during hot deformation, orientation imaging maps were generated at the same deformation conditions as those in optical micrographs. In an orientation imaging map, the boundary misorientation angles of both grains and subgrains can be distinguished by the colors: white lines: 1-5°; blue lines: 5-15°; thin black lines: 15-30° and thick black lines: (> 30°). Fig. 3.4 illustrates the initial grain structure of the homogenized sample, which is composed of uniform equiaxed grains that originates from the casting. The average grain size was 127 μm, and the grain boundaries are characterized by high angle boundaries, typically with misorientation angles between 30 and 60°.

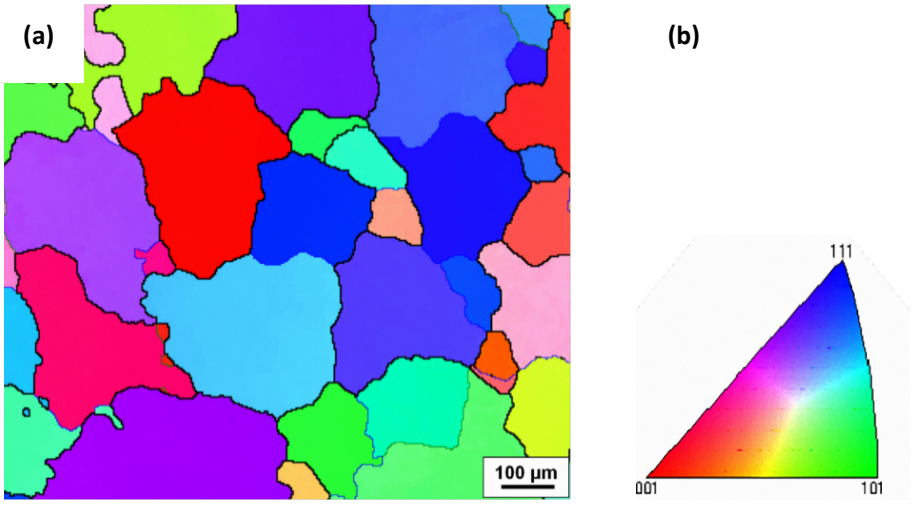

Fig. 3.4 (a) Grain structure of the alloy after homogenization treatment; (b) representation of the color code used to identify the crystallographic orientations on standard stereographic projection (red: [001]; blue: [111]; green: [101]).

During hot compression, the original grains were plastically elongated perpendicular to the compression direction (Fig. 3.5). In Domain I, when the alloy was deformed at 300 °C and 10 s^{-1}, the original grains were severely torn and broke into irregular deformation bands (DBs, see the arrow in Fig 3.5a), due to deformation occurring on different slip systems [33]. Shear bands (SBs, see the arrow) were also observed through several grains, as a result of a highly localized plastic deformation. Fig 3.5b shows several deformation bands with high angle transition boundaries inside the elongated grains, which oriented along the elongation direction. Moreover, a large amount of low angle boundaries were observed with misorientation angles largely between 1° and 5°, indicating a high density of cell and subgrain structures.

As the deformation temperature increased to 450 °C with a strain rate of 10 s^{-1}, Fig. 3.5c, d reveals that, besides the major recovered structure, strings of equiaxed grains with high angle boundaries (>15°) have been developed along the original grain boundaries, and in regions which were associated with the large intermetallic particles (>1μm). The dark green regions in Fig. 3.5d, e represent the intermetallic particles, where no indexing of the EBSD pattern of aluminum occurs. This indicates that the formation of those recrystallized grains was closely related with the particle stimulated nucleation by large intermetallic particles [2,4,12]. Furthermore, the newly formed grains are distinguished by a free of internal substructure (cell and subgrain structures). This suggests that they were formed as a result of static recrystallization during the quenching process. This phenomenon was also observed in

AA1100 and AA5083 aluminum alloys during quenching after deformation at high temperatures and high strain rates due to considerable stored energy for static recrystallization [44,45].

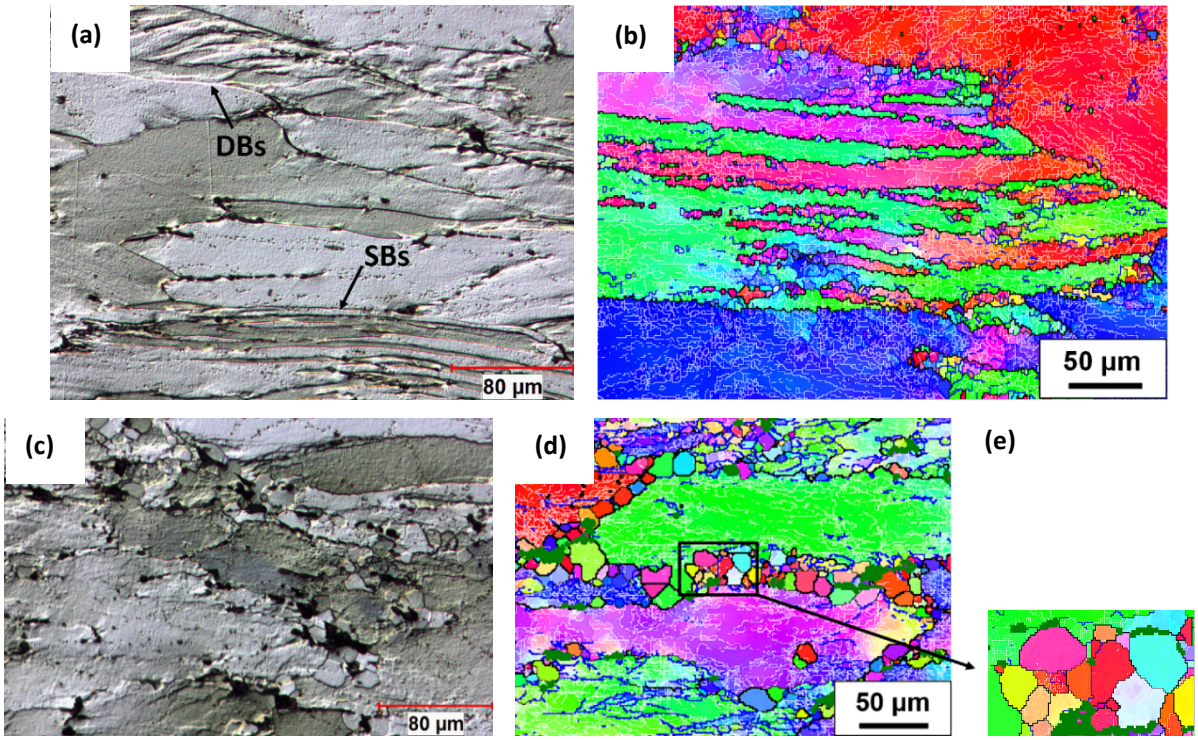

Fig. 3.5 Optical micrographs and orientation imaging maps showing deformed microstructures under different deformation conditions: (a) (b) 300°C, 10 s^{-1}; and (c) (d) (e) 450°C, 10 s^{-1}.

In Domain II, under the deformation condition at 350 °C and 0.1 s^{-1}, Fig 3.6a shows that the deformation became more homogeneous compared to that in Fig. 3.5a, with fewer deformation bands visible under the optical microscope. This is the result of an increase in the number of operating slip systems and an increased level of DRV as the temperature increased [4]. Fig. 3.6b reveals that the density of low angle boundaries was significantly reduced, and subgrains with higher angle boundaries (5-15°) were found along the grain

boundaries, thus indicating a further recovered structure. In Domain III, the grain boundaries of deformed samples remained planar and deformation bands were not noticeable, as an example shown by the sample deformed at 350 °C and 0.001 s^{-1}. Moreover, a strong recovered microstructure was observed inside the elongated grains (Fig 3.6c). EBSD result shows that the substructure became better organized, and a number of larger subgrains were formed with neatly arranged boundaries, which were characterized by misorientation angles between 5 and 15° (Fig 3.6d). This suggests an increased level of DRV as strain rate decreased, involving the annihilation and rearrangement of dislocations.

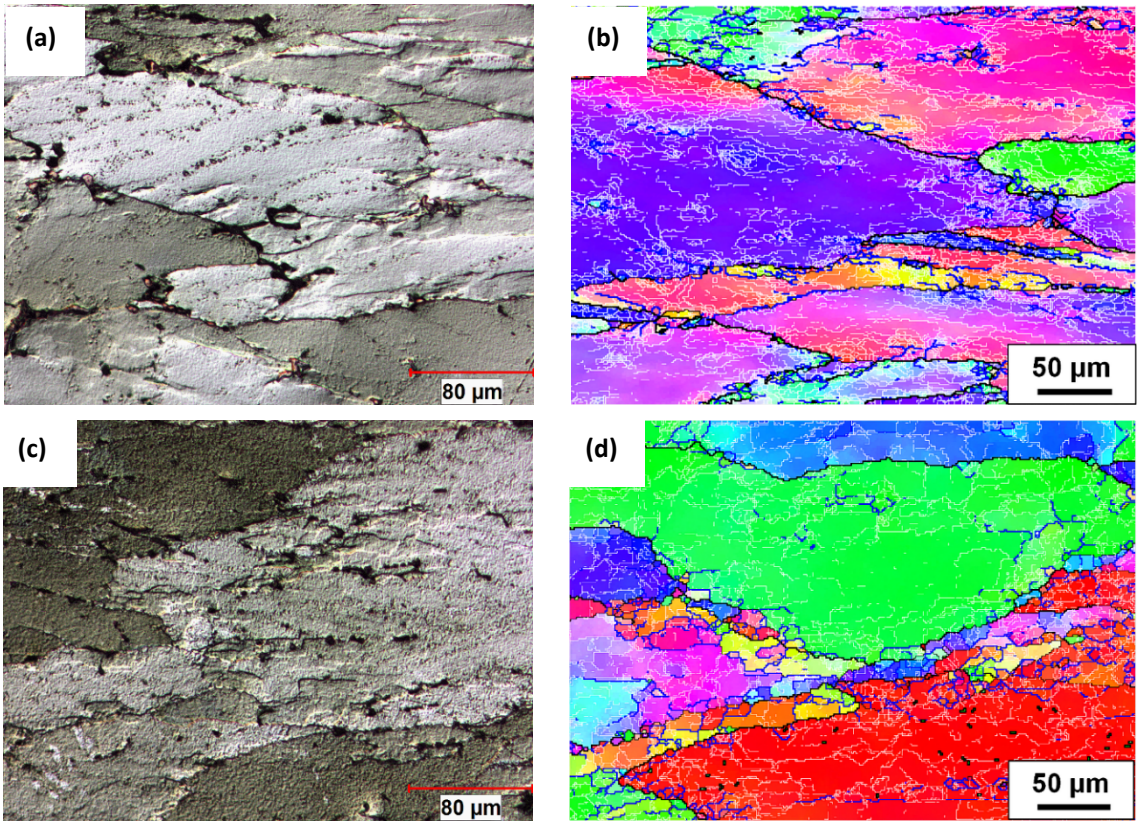

Fig. 3.6 Optical micrographs and orientation imaging maps showing deformed microstructures of under different deformation conditions: (a) (b) 350°C, 0.1 s^{-1}; and (c) (d) 350°C, 0.001 s^{-1}.

In Domain IV, during the deformation at 450 °C and 0.01 s^{-1}, the bulging of original grain boundaries was frequently observed and small equiaxed grains were found along the serrated grain boundaries (see the arrows in Fig 3.7a), indicating a partially recrystallized microstructure. An example is given by a misorientation profile of along V1 (Fig. 3.7b, c), where a bridging medium angle boundary (8°) has been developed behind a bulged section of boundary of an original grain (54°). Furthermore, as deformation processed, a bulged section has been completely pinched off and became a refined grain, which contained substructure and possessed a similar orientation to its parent grain (V2 in Fig. 3.7b, d). The average size of the recrystallized grains is approximately 14 μm. It is approximately 2 times the sizes of subgrains (5-7 μm) reported in 7050 and 7075 aluminum alloys at the same deformation condition, in which DRV solely operated as the softening mechanism [22,46]. This result is in agreement with the study in 5083 aluminum alloy during hot torsion by McQueen et al. [44], in which the size of dynamic recrystallized grain is 2-3 times the subgrain size. Therefore, partial DRX occurred during the hot deformation, and little grain rotation was involved in the formation of those recrystallized grains.

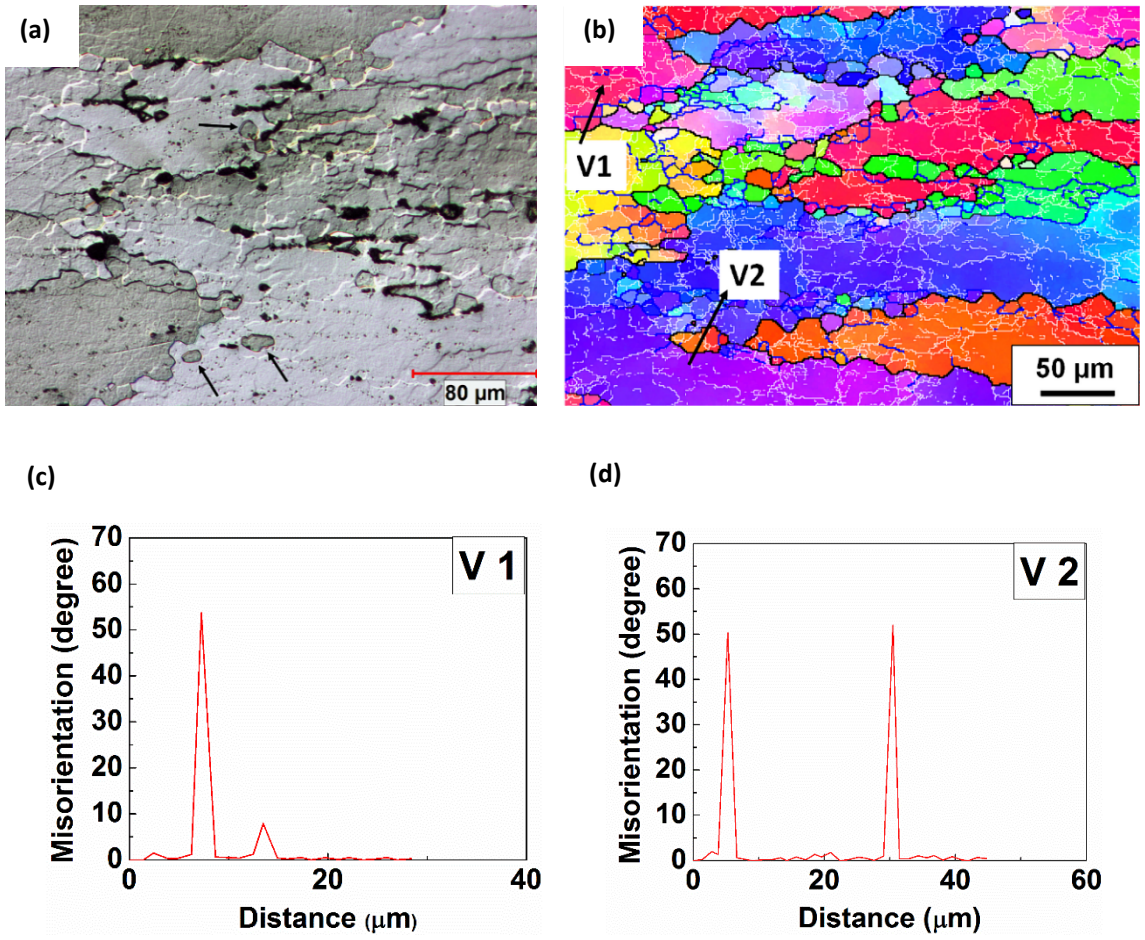

Fig. 3.7 Deformed microstructures under deformation condition at 450°C, 0.01 s^{-1}: (a) optical micrograph; (b) orientation imaging map; (c) a misorientation profile along the vector V1; and (d) a misorientation profile along the vector V2.

In Domain V, when the deformation was performed at 450 °C and 0.001 s^{-1}, new grains with high angle boundaries containing substructures were presented along the elongated original grain boundaries (see the arrows in Fig. 3.8a), and a large number of subgrains were observed inside the original grains as well, which illustrated a strong dynamic recovered microstructure mixed with dynamic recrystallized microstructure (Fig. 3.8a, b). The microstructure of the recrystallized grain consists of partially the original grain boundaries (30-60°) and the newly formed high angle boundaries (15-30°), as illustrated by V3 in Fig.

3.8b, c. Besides, a misorientation profile, V4 in Fig. 3.8b, d, demonstrates that a subgrain was progressively increasing in misorientation and being transformed into a dynamically recrystallized grain. Moreover, those recrystallized grains exhibited an average size of 33 μm, which is about 3 times the subgrain size (9.5 μm) solely observed in 7050 aluminum alloy during deformation at 450 °C and 0.0005 s^{-1} by Deng et al. [46].

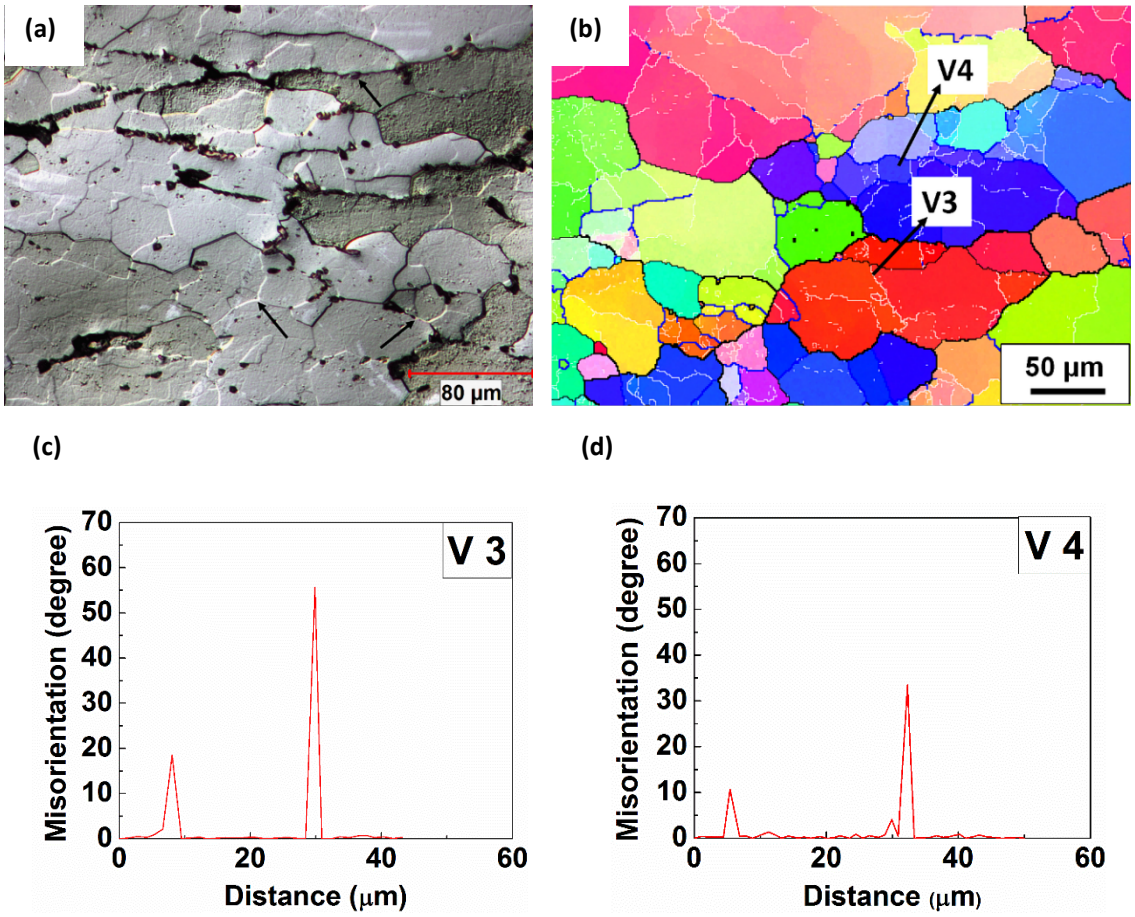

Fig. 3.8 Deformed microstructures under deformation condition at 450°C, 0.001 s^{-1}: (a) optical micrograph; (b) orientation imaging map; (c) a misorientation profile along the vector V3; and (d) a misorientation profile along the vector V4.

3.3.5 Quantitative analyses of grain boundaries

Based on the microstructure observation of samples deformed at various deformation conditions, DRV generally occurred during hot deformation in Domains I, II and III, and DRX took place when the deformation was conducted in Domains IV and V. For a further investigation of the dynamic softening mechanisms during the hot deformation processes, a quantitative measurement of misorientation angle distributions of boundaries for samples deformed at different deformation conditions was carried out using EBSD technique, and results are illustrated in Fig. 3.9. It is evident that at deformation temperatures between 300 and 400 °C, a continuous decrease in the fraction of low angle boundaries (1-5°), along with an increase in the fraction of medium angle boundaries (5-15°) was observed as the temperature increased and the strain rate decreased (see the deformation conditions from A to D). This implies an increased level of DRV, involving elimination of low angle boundaries and transformation into higher angle boundaries, which is consistent with the microstructural evolution observed in Fig 3.5 and 3.6. However, there is no indication of DRX occurring during the deformation at temperatures of 300 to 400 °C, due to the little variation in the fraction of high angle boundaries (>15°). On the other hand, as the temperature increased to 450 °C with different strain rates of 0.01 s^{-1} and 0.001 s^{-1} (deformation conditions E and F), the boundaries with misorientation angles between 1 and 15° decreased dramatically, and this was associated with a rapid increase in high angle boundaries. This result suggests that DRX occurred accompanied by an increasing fraction of high angle boundaries, as a result of the

formation of recrystallized grains. This is in good agreement with the microstructure observation in Fig 3.7 and 3.8.

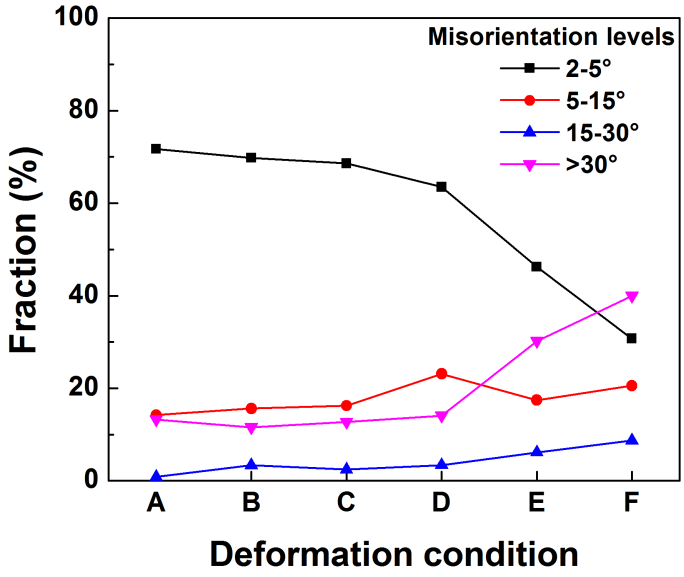

Fig. 3.9 Fractions of boundaries with different misorientation levels under different deformation conditions: A 300°C, 10 s^{-1}; B 300°C, 1 s^{-1}; C 350°C, 0.1 s^{-1}; D 400°C, 0.01 s^{-1}; E 450°C, 0.01 s^{-1}; and F 450°C, 0.001 s^{-1}.

3.4 Discussion

The decline ratio map of flow stress as a function of temperature and strain rate is divided into five domains, which can be utilized to study the relationship between flow stress behavior and various dynamic softening mechanisms in the Al-Zn-Mg-Cu alloy (7150) during hot deformation at different deformation temperatures and strain rates.

In Domain I, the microstructure observation confirms that DRV is the main dynamic softening mechanism during hot deformation (Fig. 3.5). Although deformed at high strain rates, no cracking in the deformed samples was observed. The continuous decline of the flow

stress after attaining the peak stress is likely associated with a severe deformation heat release. The variations of sample temperatures are shown in Fig. 3.10, which were monitored during the compression tests at the target temperatures from 300 to 450 °C with different strain rates. When the deformation was performed at the high strain rate of 10 s^{-1} (Domain I), the sample temperature rose continuously with increasing strain at each target deformation temperature. The maximum overheating temperature reached 22 °C at the target temperature of 450 °C, and increased as high as 35 °C at the target temperature of 300 °C. Those results suggest that the heat release during deformation at the high strain rate of 10 s^{-1} plays an important role in the decrease of flow stress, leading to a significant thermal softening, as confirmed by other researchers [16-18].

However, in other domains, when the deformation was carried out at low strain rates between 0.001 s^{-1} and 0.1 s^{-1}, the sample temperatures kept close to the target temperatures (within 2 °C). Thus, it is reasonable to consider that the deformation was under an isothermal process. Even at the intermediate strain rate of 1 s^{-1}, the temperature increase was generally limited within several degrees (4 to 8 °C). Therefore, it is believed that the thermal softening effect in this case plays a minor role in the flow softening.

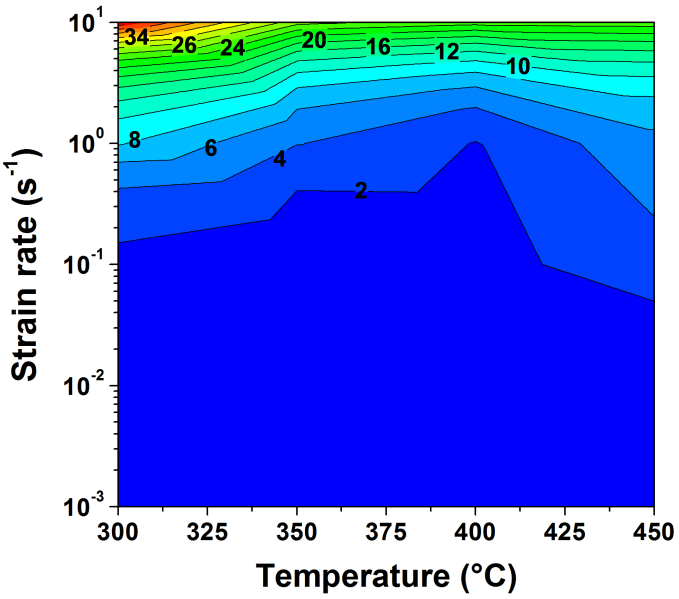

Fig. 3.10 Maximum increase of sample temperature (ΔT_{max}) measured during compression tests as a function of deformation temperature and strain rate.

Domain II represents a typical recovered structure (Fig. 3.6a, b), indicating that DRV is the sole dynamic softening mechanism. The flow stress curves showed a continuous increase of flow stress after the peak stress at a higher strain rate (1 s^{-1}) or a slight decrease at a lower strain rate (0.1 s^{-1}). It is evident that the effect of work hardening was dominant during hot deformation at the strain rate of 1 s^{-1}, whereas the dynamic softening slightly overcame the work hardening at the lower strain rate of 0.1 s^{-1}.

In Domain III, DRV still operated as the main dynamic softening mechanism (Fig. 3.6c, d). Differentiated from Domain II, a significant decline of the flow stress after the peak stress occurred. It was observed that the dynamic precipitation and coarsening took place during the hot compression process. Fig 3.11a shows a precipitate-free aluminum matrix after the

homogenization prior to the hot deformation. At the beginning of deformation (at a true strain of 0.1), as exemplified at the deformation condition at 350°C and $0.001s^{-1}$, a large number of spherical and rod-shaped precipitates with an average size of 60 nm appeared (Fig. 3.11b). The TEM-EDS result (Table 3.2) shows that the precipitates contain Mg, Zn and Cu, with a composition approaching stoichiometric $Mg(Zn,Cu)_2$ phase [47-49]. Those fine precipitates interacted with dislocations and exhibited a strong pinning effect on dislocation movement, leading to a high value of the peak stress at the initial stage of deformation. As the deformation progressed to a true strain of 0.8, the precipitates remarkably coarsened to an average size of 125 nm with a larger interparticle spacing (Fig. 3.11c). The coalescence of precipitates, accompanied by enhanced DRV, resulted in a significant flow stress softening. Similar behaviors have been observed in solution treated 7012, 7075 and 7085 as well as homogenized 2026 aluminum alloys during hot deformation at low strain rates [17,22,24].

It should be mentioned that the dynamic precipitation can also occur in Domain II. However, the coalescence of precipitates was not observed by TEM due to a relatively short deformation time at high strain rates. Those fine precipitates significantly increased the multiplication rate of dislocations [2,4], which resulted in a strong work hardening effect and a continuous increase of flow stress at strain rate $1\ s^{-1}$, as shown in Fig. 3.2.

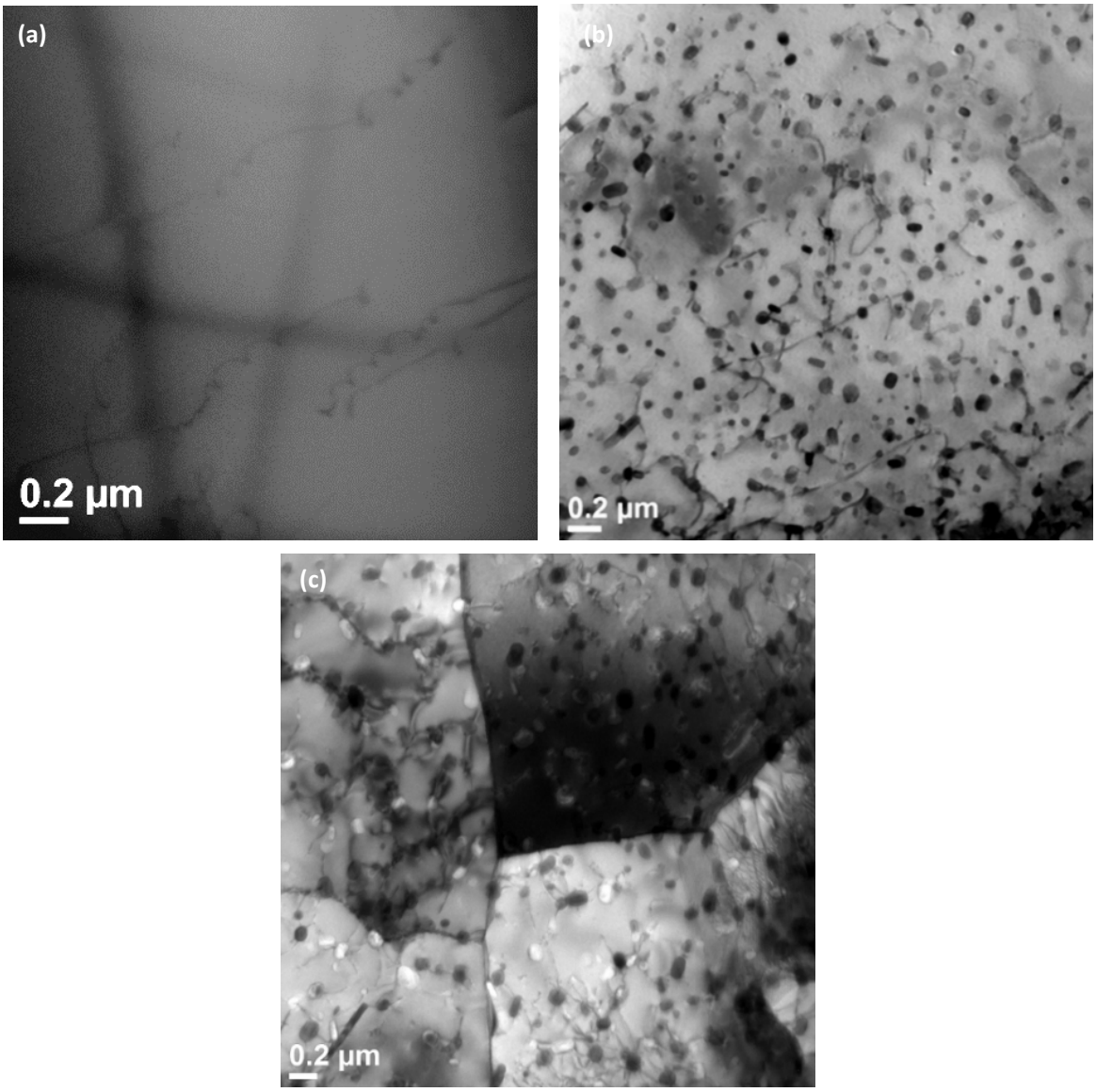

Fig. 3.11 Bright-field TEM micrographs showing as-homogenized microstructure prior to deformation (a); deformed microstructures at 350°C and 0.001s^{-1} with the true strain of 0.1 (b) and 0.8(c). The electron beam is parallel to [011] of α-Al.

Table 3.2 Results of TEM-EDS analysis of the precipitates shown in Fig. 3.11b, c.

Element	Mg	Cu	Zn	Al
Mole fraction (%)	26.58	18.82	25.67	28.94

Moreover, in Domain IV, the deformed microstructure reveals a partially recrystallized microstructure at the serrated grain boundaries (Fig. 3.7), which probably involves in the

discontinuous dynamic recrystallization (DDRX) by strain-induced boundary migration (SIBM). Fig. 3.12 illustrates an example of the formation of one dynamically recrystallized grain before pinching off from the original grain in the sample deformed at 450 °C and 0.01 s^{-1}. The STEM micrograph gives an overview of the recrystallized grain and its surroundings, and four bright-field TEM images show the enlarged views in the corresponding areas. The misorientation angles of boundary were determined by measuring the shift of Kikuchi line intersections on crossing boundary under TEM mode [2,23].

It can be seen that the recrystallized grain C comprised of partially bulged original grain boundary (Fig. 3.12a, c) and a bridging of low angle boundary (3-5°) with the grain B (Fig. 3.12a, b). This suggests a characteristic feature of SIBM, by which the grain C was gradually formed at the expense of the higher density of dislocations in the grain A and displayed a similar orientation to its parent grain B. Moreover, the grain C contains substructures of dislocations and dislocation networks (Fig. 3.12a, d, e). This provides a direct evidence that the new grain was formed dynamically during deformation and suffered a significant strain [2,7]. Furthermore, it was reported that a high content of solute atoms, Mg, Zn and Cu in the aluminum matrix of the homogenized sample, could reduce the dislocation mobility and retard dynamic recovery, thus leading to a high stored energy [2,4,12]. Therefore, the driving force for dynamic recrystallization was increased and DDRX took place during the hot deformation process at this deformation condition, resulting in an appreciable flow softening [2,12].

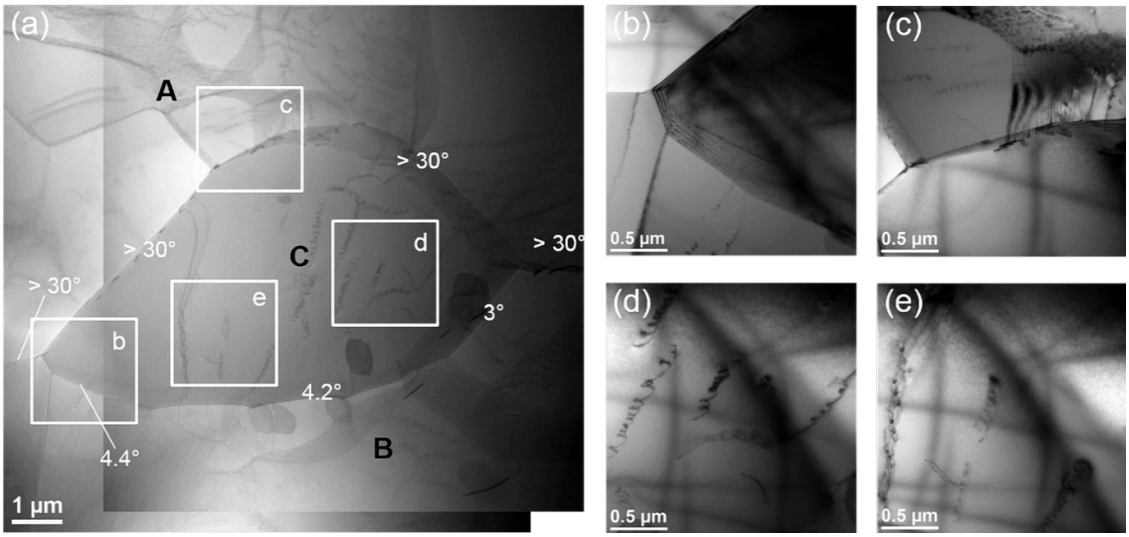

Fig. 3.12 Transmission electron micrographs of the alloy compressed at 450°C and 0.01 s^{-1} to a true strain of 0.8: (a) STEM image showing one dynamically recrystallized grain and its surroundings; and (b)-(e) bright-field TEM images illustrating the enlarged views of four locations in (a).

During the deformation at a high temperature of 450 °C and at a low strain rate of 0.001 s^{-1} in Domain V, bulging of grain boundaries and formation of recrystallized grains by DDRX were not observed in Fig 3.8. As a high level of DRV was induced during the slow straining process at the high temperature, accumulation rate of dislocations was considerably decreased. Hence, the driving force was not sufficient for nucleation and growth of recrystallized grains by DDRX. However, a number of newly formed grains with high angle boundaries can be clearly seen in the microstructure (Fig 3.8), in which it most probably involved a continuous dynamic recrystallization (CDRX). Fig 3.13 shows the evolution of substructure and misorientation distribution with increasing strain during the deformation at 450 °C and 0.001 s^{-1}. At a true strain of 0.3, subgrains were well developed inside the original grains (see the arrows in Fig 3.13a), and characterized mainly by low angle

boundaries between 1 and 5° (Fig. 3.13c). As the deformation processed to a true strain of 0.5, subgrains were presented with boundaries of increased misorientations (see the arrows in Fig. 3.13b). Besides, the fraction of subgrain boundaries with low misorientations (1-5°) was significantly reduced, while the number of boundaries with higher misorientations increased (Fig. 3.13d). When the true strain approached to 0.8, recrystallized grains with high angle boundaries could be observed (Fig. 3.8), and the fraction of high angle boundaries continuously increased, reaching more than 45% (Fig. 3.13e). This result indicates that the low angle boundaries (1-5°) were progressively converted into medium angle boundaries (5-15°), which in turn transformed into high angle boundaries during the slow deformation process (Domain V). Such evolution can be considered as a process of continuous dynamic recrystallization (CDRX) [10-12]. In this case, the flow stress curve attained a peak stress and then showed a slow decline upon further straining [50].

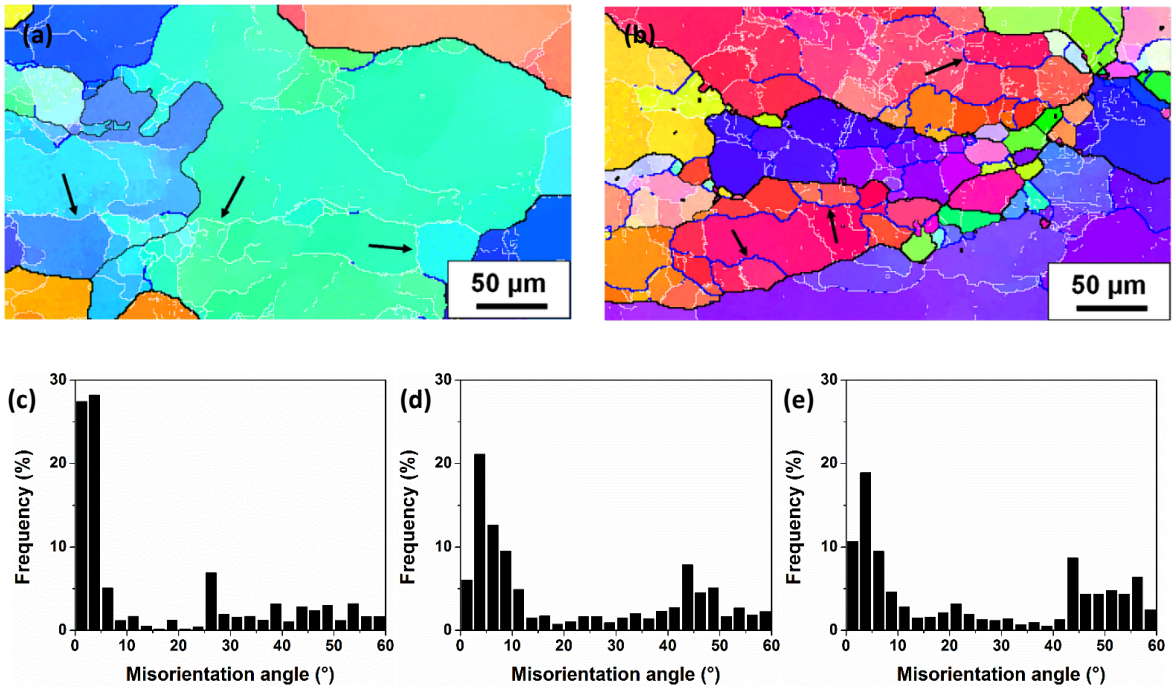

Fig. 3.13 Orientation imaging maps of the alloy deformed at 450°C and 0.001s^{-1} with the true strain of: (a) 0.3 and (b) 0.5; misorientation distribution at the true strain of: (c) 0.3; (d) 0.5; and (e) 0.8.

In brief, the decline ratio map of flow stress was utilized to study the relationship between flow stress behavior and various dynamic softening mechanisms in the Al-Zn-Mg-Cu alloy (7150) during hot deformation. Recovered structures are generally observed in the samples deformed in Domains I, II and III. In these cases, DRV is the sole dynamic softening mechanism during hot deformation, which is commonly reported in 7xxx aluminum alloys [2,22,46,51]. However, a partially recrystallized microstructure is presented in the deformed samples in Domains IV and V. It is proved using EBSD and TEM that DRX does take place during hot deformation at certain conditions in this alloy. Therefore, besides DRV, DRX plays an important role in flow stress softening at the high temperature. Furthermore, results reveal that two possible mechanisms of DRX operate during the hot

forming, in which DDRX is involved in Domain IV and CDRX is implied in Domain V. Finally, it should be emphasized that generation of decline ratio map of flow stress, accompanied with investigation on typical microstructures in each domain could provide a convenient approach to study the dynamic softening mechanisms of materials through hot processing.

Recently, several works have been done to optimize the hot working processes of 7xxx aluminum alloys using the processing maps [52-55]. Correlating various deformation mechanisms suggested from the decline ratio map with those processing maps, it is possible to predict the hot workability of the Al-Zn-Mg-Cu aluminum alloy studied. Results obtained in this study show that Domains II, IV and V correspond to the safe processing domains, due to DRV and DRX operating as the dynamic softening mechanisms [42,52-55]. Furthermore, the optimum hot working parameters for the alloy are considered to be in Domains IV and V, i.e. at the temperature of 450 °C and strain rates of 0.001-0.1 s^{-1}, where DRX occurs during hot deformation, leading to softening and reconstituting the microstructure [42]. This is in agreement with results obtained from 7xxx aluminum alloys by other researchers [52-55]. On the other hand, the deformation in Domain I should be avoided, due to the flow instability and formation of adiabatic shear bands [42,54,55]. The coarse dynamic precipitates generated in Domain III may lead to the deep inter-granular corrosion and large areas of denudation layer, which are detrimental to the properties of the deformed material [54].

3.5 Conclusions

1. The hot deformation behavior of 7150 aluminum alloy (Zr free) is systematically investigated at temperatures of 300 to 450 °C and strain rates of 0.001 to 10 s^{-1}. The level of flow stress decreases with increasing deformation temperature and with decreasing strain rate.

2. The decline ratio map of flow stresses is proposed and further divided into five deformation domains, in which the flow stress behavior is correlated with different microstructures and dynamic softening mechanisms at various deformation conditions.

3. The dynamic recovery is the sole softening mechanism of the alloy when the hot deformation is performed at temperatures of 300 to 400 °C with various strain rates, as well as at temperatures of 400 to 450°C with strain rates between 1 and 10 s^{-1}. The level of dynamic recovery increases with increasing temperature and with decreasing strain rate.

4. At the high strain rate of 10 s^{-1}, the heat release during deformation plays an important role in the decrease of flow stress, leading to a significant thermal softening. At low strain rates of 0.001 to 0.01 s^{-1} and temperatures of 300 to 400 °C, the coalescence of dynamic precipitation, accompanied by enhanced dynamic recovery, results in a considerable decline in flow stress.

5. The dynamic recrystallization takes place when the deformation is conducted at the high deformation temperature of 450 °C with strain rates of 0.001 to 0.1 s^{-1}, providing an alternative softening mechanism. Results reveal that two kinds of DRX may operate at the high temperature, in which DDRX is involved at the higher strain rates and CDRX is implied at the lower strain rates.

References

[1] E.A. Starke, J.T. Staley, Prog. Aerosp. Sci. 32 (1996) 131-172.

[2] H.J. McQueen, S. Spigarelli, M. Kassner, E. Evangelista, Hot Deformation and Processing of Aluminum Alloys, CRC Press, Florida, 2011, pp. 87-233.

[3] E. Cerri, E. Evangelista, H.J. McQueen, High Temp. Mat. Proc. 18 (1999) 227-240.

[4] F.J. Humphreys, M. Hatherly, Recrystallization and Related Annealing Phenomena, second ed., Elsevier Ltd., Oxford, 2004, pp. 169-450.

[5] H. Yamagata, Scripta Metall. Mater. 27 (1992) 727-732.

[6] H. Yamagata, Scripta Metall. Mater. 30 (1992) 411-416.

[7] T. Sheppard, M.G. Tutcher, Met. Sci. 14 (1980) 579-589.

[8] H.J. McQueen, E. Evangelista, J. Bowles, G. Crawford, Met. Sci. 18 (1984) 395-402.

[9] F.J. Humphreys, P.N. Kalu, Acta Metall. Mater. 35 (1987) 2815-2829.

[10] C. Perdrix, M.Y. Perrin, F. Montheillet, Mém. Sci. Rev. Metall. 78 (1981) 309-320.

[11] S. Gourdet, E.V. Konopleva, H.J. McQueen, F. Montheillet, Mat. Sci. Forum 217 (1996) 441-446.

[12] S. Gourdet, F. Montheillet, Mat. Sci. Eng. A 283 (2000) 274-288.

[13] S.J. Hales, T.R. McNelley, H.J. McQueen, Metal. Trans. 22A (1991) 1037-1047.

[14] G.I. Taylor, H. Quinney, Proc. R. Soc. Lond. A 143 (1934) 307-326.

[15] A. Marchand, J. Duffy, J. Mech. Phys. Solids 36 (1988) 251-283.

[16] R.E.D. Mann, R.L. Hexemer Jr., I.W. Donaldson, D.P. Bishop, Mater. Sci. Eng. A 528 (2011) 5476-5483.

[17] X. Huang, H. Zhang, Y. Han, W. Wu, J. Chen, Mater. Sci. Eng. A 527 (2010) 485-490.

[18] M. Rajamuthamilselvan, S. Ramanathan, J. Alloys Compd. 509 (2011) 948-952.

[19] C.M. Sellars, W.J. McTegart, Met. Rev. 17 (1972) 1-24.

[20] E. Cerri, E. Evangelista, A. Forcellese and H.J. McQueen, in L. Arnberg, O. Lohne, E. Nes and N. Ryum (eds.), Aluminium Alloys, Physical and Mechanical Properties (ICAA3), Vol. 2, NTH-SINTEF, Trondheim, 1992, pp. 139-144.

[21] A. Espedal, H. Gjestland, N. Ryum, Scand. J. Met. 18 (1989) 131-136.

[22] E. Cerri, E. Evangelista, A. Forcellese, H.J. McQueen, Mater. Sci. Eng. A 197 (1995)

181-198.

[23] G. Avramovic-Cingara, D.D. Perovic, H.J. McQueen, Met. Mat. Trans A 27A (1996) 3478-3490.

[24] S.Y. Chen, K.H. Chen, G.S. Peng, X.H. Chen, Q.H. Ceng, J. Alloys Comp. 537 (2012) 338-345.

[25] M.R. Rokni, A. Zarei-Hanzaki, A.A. Roostaei, A. Abolhasani, Mater. Des. 32 (2011) 4955-4960.

[26] J. Li, F. Li, J. Cai, R. Wang, Z. Yuan, F. Xue, Mater. Des. 42 (2012) 369-377.

[27] N. Jin, H. Zhang, Y. Han, W. Wu, J. Chen, Mater. Charact. 60 (2009)5 30-536.

[28] H. Zhang, N.P. Jin, J.H. Chen, Trans. Nonferrous Met. Soc. China 21 (2011) 437-442.

[29] Y. Li, Z. Liu. L. Lin, J. Peng, A. Ning, J. Mater. Sci. 46 (2011) 3708-3715.

[30] M.R. Rokni, A. Zarei-Hanzaki, A.A. Roostaei, H.R. Abedi, Mater. Des. 32 (2011) 2339-2344.

[31] J.J. Jonas, X. Quelennec, L. Jiang, E. Martin, Acta Mater. 57(2009) 2748-2756.

[32] M.A. Mostafaei, M. Kazeminezhad, Mater. Sci. Eng. A 544 (2012) 88-91.

[33] H.J. McQueen, Metall. Sci. Technol. 28 (2010) 12-21.

[34] S. Mitsche, P. Poelt, C. Sommitsch, J. Microsc. 227 (2007) 267-274.

[35] H. Mirzadeh, J.M. Cabrera, A. Najafizadeh, P.R. Calvillo, EMater. Sci. Eng. A 538 (2012) 236-245.

[36] F.J. Humphreys, J. Mater. Sci, 36 (2001) 3833-3854.

[37] H. Jazaeri, F.J. Humphreys, J. Microsc. 213 (2004) 241-246.

[38] C. Mondal, A.K. Mukhopadhyay, Mater. Sci. Eng. A 391 (2005) 367-376.

[39] J.D. Robson, Mater. Sci. Eng. A 382 (2004) 112-121.

[40] R.W.K. Honeycombe, The plastic deformation of metals, second ed., Edward Arnold Ltd. Maryland, 1984, pp. 33-128.

[41] D. Caillard, J.L. Martin, Thermally Activated Mechanisms in Crystal Plasticity, Pergamon Press, Oxford, 2003, pp. 1-280.

[42] Y.V.R.K. Prasad, S. Sasidhara, Hot working guide - a compendium of processing maps; ASM Intl., Ohio, USA, 1997, pp. 1-24.

[43] H.R. Ezatpour, S.A. Sajjadi; M. Haddad-Sabzevar, G.R. Ebrahimi, Mater. Sci. Eng. A 550 (2012)152-159.

[44] W. Blum, Q. Zhu, R. Merkel, H.J. McQueen, Mater. Sci. Eng. A 205 (1996) 23-30.

[45] H.J. McQueen, J.E. Hockett, Met. Trans. 1 (1970) 2997-3004.

[46] Y. Deng, Z. Yin, J. Huang, Mater. Sci. Eng. A 528 (2011) 1780-1786.

[47] G. Sha, A. Cerezo, Surf. Interface Anal. 36 (2004) 564-568.

[48] M. Conserva, P. Fiorini, Metall. Trans. 4 (1973) 857-862.

[49] L.K. Berg, J. Gjønnes, V. Hansen, X.Z. Li, M. Knutson-Wedel, G. Waterloo, D. Schryvers, L.R. Wallenberg, Acta Mater. 49 (2001) 3443-3451.

[50] A.G. Beer, M.R. Barnett, Metall. Mater. Trans. A 38A (2007) 1856-1867.

[51] P. Leo, E. Cerri, H.J. McQueen, A. Taurino, in J. Hirsch, B. Skrotzki and G. Gottstein (eds.), Aluminium Alloys, Their Physical and Mechanical Properties (ICA11), Wiley-VCH (DE), 2008, pp. 1868-1874.

[52] A. Jenab; A. Karimi Taheri, Int. J. Mech. Sci. 78 (2014) 97-105.

[53] J. Luo, M.Q. Li, B. Wu, Mater. Sci. Eng. A 530 (2011) 559-564.

[54] Y.C. Lin, L.T. Li, Y.C. Xia, Y.Q. Jiang, J. Alloys Compd. 550 (2013) 438-445.

[55] Y. Yang, Z. Zhang, X. Li, Q. Wang, Y. Zhang, Mater. Des. 51 (2013) 592-597.

CHAPTER IV

EFFECT OF ZR ADDITION ON HOT DEFORMATION BEHAVIOR AND MICROSTRUCTURAL EVOLUTION OF 7150 ALUMINUM ALLOY

Chapter IV Effect of Zr addition on hot deformation behavior and microstructural evolution of 7150 aluminum alloy

Abstract

The hot deformation behavior of homogenized 7150 aluminum alloys containing different Zr contents (0 to 0.19 wt%) was studied. The results reveal no significant variation in the peak flow stress or activation energy between the 7150 base alloy and the alloy containing 0.04 wt% Zr. With a further increase in the Zr content to 0.19 wt%, the values of peak flow stress and activation energy increased significantly. The materials constants and activation energy for hot deformation were determined from the experimental compression data obtained for all alloys studied. The solved constitutive equations yielded good predictions of the peak flow stress over wide temperature and strain-rate ranges for 7150 alloys with different Zr contents. The dynamic recovery level of the materials was reduced after being alloyed with Zr, which was associated with a decrease in the mean misorientation angle of boundaries and a decrease in subgrain size. The addition of Zr promoted the retardation of dynamic recovery and the inhibition of dynamic recrystallization during hot deformation due to the pinning effect of Al_3Zr dispersoids on dislocation motion and to restrained dynamic restoration.

The content of this chapter has been published as: C. Shi, X.-G. Chen, Effect of Zr addition on hot deformation behavior and microstructural evolution of 7150 aluminum alloy, Materials Science and Engineering A, 596 (2014) 183-193.

4.1 Introduction

7xxx series aluminum alloys are very attractive materials for their applications in the automotive and aerospace industries due to their excellent combination of properties such as high strength-to-density ratio, high fracture toughness and resistance to stress corrosion cracking [1]. These aluminum alloys are generally subjected to hot forming processes such as rolling, extrusion and forging. The mechanical properties of the alloys are affected by their chemical composition, strain history and resulting microstructure from thermomechanical processing [2,3]. The addition of micro-alloying elements, such as Zr, Sc, Sn, In, Cd and Ag, has also been reported to increase the material strength of the alloys and afford reasonably high toughness [4-7]. To optimize the mechanical properties and processability of hot formed alloys, a better understanding of the effect of micro-alloying elements on deformation behavior and microstructural evolution during hot deformation is required.

Dynamic recovery (DRV) and dynamic recrystallization (DRX) are the typical softening mechanisms active in aluminum alloys during deformation at elevated temperatures [8-11]. Previous investigations have shown that micro-alloying has significant effects on these softening mechanisms during hot deformation [12-15]. Hu et al. [12] suggested that the softening mechanism of 7050 aluminum alloy shifted from DRV to DRX with decreasing Z (Zener-Hollomon parameter). A minor addition of Sn (0.02 to 0.1 wt%) to Al-Cu-Mg alloy resulted in an increase in peak flow stress and deformation activation energy in a study reported by Banerjee et al. [13]. McQueen et al. investigated the hot torsion behavior of 8090

alloy containing 0.1 wt% Zr and observed that dynamic recovery occurred as the sole softening mechanism [14]. However, dynamic recrystallized grains were observed in extruded Al-5 wt%Mg-0.8 wt%Mn alloy due to the stimulation of nucleation by Al_6Mn particles [15].

The addition of Zr is well known to increase the recrystallization resistance of aluminum alloys by forming fine, coherent Al_3Zr dispersoids [4,16]. The presence of these dispersoids promotes the formation of a stable and refined subgrain structure during the hot deformation process, which promotes additional substructure strengthening [17]. In commercial practice, Al_3Zr dispersoids are generally precipitated during the homogenization of cast billets [4,16]. The effectiveness of the dispersoids depends on their size, number density and distribution [18], which are strongly influenced by the homogenization treatment [19]. To date, several studies have focused on investigating the effect of Zr addition on the static recrystallization of aluminum alloys during solution treatment because the fracture toughness is closely related to the amount of recrystallized structure [4,16,20-22]. A few studies have been conducted on the hot deformation of aluminum alloys containing Zr, in which a pinning effect of Al_3Zr dispersoids on dislocations and grain boundaries has been reported [14,23,24]. However, a systematical investigation of the effect of different Zr contents on the hot deformation behavior of 7150 aluminum alloys has not been found in the literature. The evolution of the deformed microstructure of 7150 aluminum alloy after adding various contents of Zr must be understood.

In the present study, the hot deformation behavior of homogenized 7150 alloys with different Zr contents (ranging from 0 to 0.19 wt%) was studied by hot compression tests at various temperatures and strain rates. The constitutive equations correlating the peak flow stress, deformation temperature, strain rate and activation energy were analyzed for these alloys. The microstructural evolution of the alloys during hot deformation was investigated to understand the effect of Zr addition on the dynamic softening mechanisms that occur under various deformation conditions.

4.2 Experimental

Experiments were conducted on 7150 alloys with different contents of added Zr ranging from 0 to 0.19% (all alloy compositions in wt% unless otherwise indicated). The alloys were designated Alloy-A to Alloy-F based on their Zr contents, and their chemical compositions are analyzed by an optical emission spectrometer and presented in Table 4.1. Approximately 3 kg of material was melted in an electrical resistance furnace and held at 750 °C for 30 min under mechanical stirring, and then cast into a rectangular permanent steel mold measuring 30 x 40 x 80 mm^3. The cooling rate in the liquid state is approximately ~12 ºC s^{-1}. When the content of added Zr exceeded 0.19%, large primary intermetallics of Al_3Zr were observed in the as-cast microstructure, which is not the interest in the present study. The cast ingots of these alloys were homogenized at 465 °C for 24 h, followed by direct water quenching. Cylindrical samples measuring 10 mm in diameter and 15 mm long were machined from the homogenized ingots. Uniaxial compression tests were conducted on a Gleeble 3800

thermomechanical simulation unit at strain rates of 0.001, 0.01, 0.1, 1 and 10 s^{-1} and deformation temperatures of 300, 350, 400 and 450 °C, respectively. During the tests on the Gleeble 3800 unit, the samples were heated to the desirable deformation temperature at a heating rate of 10 °C/s and held for 3 min to ensure a homogeneous temperature distribution throughout the samples. The samples were deformed to a total true strain of 0.8 and then immediately water-quenched to retain the microstructure at the deformation temperature.

The microstructure of the as-homogenized materials was etched by Keller's solution prior to hot deformation. All deformed samples were sectioned parallel to the compression axis along the centerline and then metallographically prepared for electron backscattered diffraction (EBSD) analysis under a scanning electron microscope (SEM, JEOL JSM-6480LV). In EBSD analysis, the boundaries of both grains and subgrains are defined as low-angle boundaries (LABs), medium-angle boundaries (MABs) and high-angle boundaries (HABs) with misorientation angles of 1-5°, 5-15° and greater than 15°, respectively [25]. The step size between the scanning points was set to 1.0 μm for the grain structure of the samples. For the quantitative measurement of the misorientation distribution of boundaries, EBSD line scanning was carried out [26,27], and a sample surface area of approximately 2.73 mm^2 with a scanning step size of 1.0 μm was selected. In addition, EBSD analysis was performed to measure the subgrain size of the deformed samples using the linear intercept method [26]; a surface area of approximately 0.42 mm^2 with a scanning step size of 0.1 μm was selected. Samples for TEM observation were mechanically ground to a thicknesses of 35-60 μm and

followed by electropolishing in a twin-jet polishing unit, which was operated at 15 V and -20 °C using a 30% nitric acid and 70% methanol solution. The samples were observed under a transmission electron microscope (TEM, JEM-2100) operated at 200 kV. To observe the distribution of Al_3Zr, electropolished TEM foils of an as-homogenized sample containing 0.12% Zr were examined using a field-emission gun SEM (Hitachi SU-70) operated at 10 kV with a working distance of 10 mm in the backscattered mode.

Table 4.1 Chemical composition of the alloys studied (wt%).

Alloy	Zn	Mg	Cu	Si	Fe	Ti	Zr	Al
Alloy-A (base alloy)	6.44	2.47	2.29	0.16	0.15	0.009	-	Bal.
Alloy-B (0.04 Zr)	6.27	2.14	2.23	0.11	0.14	0.008	0.04	Bal.
Alloy-C (0.07 Zr)	6.36	2.31	2.29	0.16	0.15	0.008	0.07	Bal.
Alloy-D (0.12 Zr)	6.35	2.22	2.34	0.16	0.15	0.008	0.12	Bal.
Alloy-E (0.15 Zr)	6.16	2.15	2.16	0.11	0.14	0.008	0.15	Bal.
Alloy-F (0.19 Zr)	6.04	2.08	1.97	0.11	0.14	0.008	0.19	Bal.

4.3 Results

4.3.1 Flow stress behavior

The hot compression tests of 7150 alloys containing different Zr contents were carried out at deformation temperatures ranging from 300 to 450 °C and at strain rates ranging from 0.001 to 10 s^{-1}. A series of typical true stress-true strain curves obtained during hot deformation are presented in Fig. 4.1. In general, all of the curves exhibit a peak flow stress at a certain strain, followed by dynamic flow softening to the end of straining. Significant flow softening beyond the peak stress was observed at the highest strain rate of 10 s^{-1}, which was attributed to severe adiabatic deformation heating. This phenomenon was reported in our

previous study [28], in which the deformation temperature considerably rose during the compression process. Under other deformation conditions, the flow stress curves remained fairly constant or decreased to some extent beyond the peak stresses, demonstrating a dynamic equilibrium between work hardening and dynamic softening. In addition, it is evident that the level of flow stress and peak stress increased with increasing strain rate and decreasing deformation temperature, which is in general agreement with the results reported in previous studies on metallic alloys [12-15,23,24]. However, the flow stress and peak stress levels increased remarkably with an increase in Zr content.

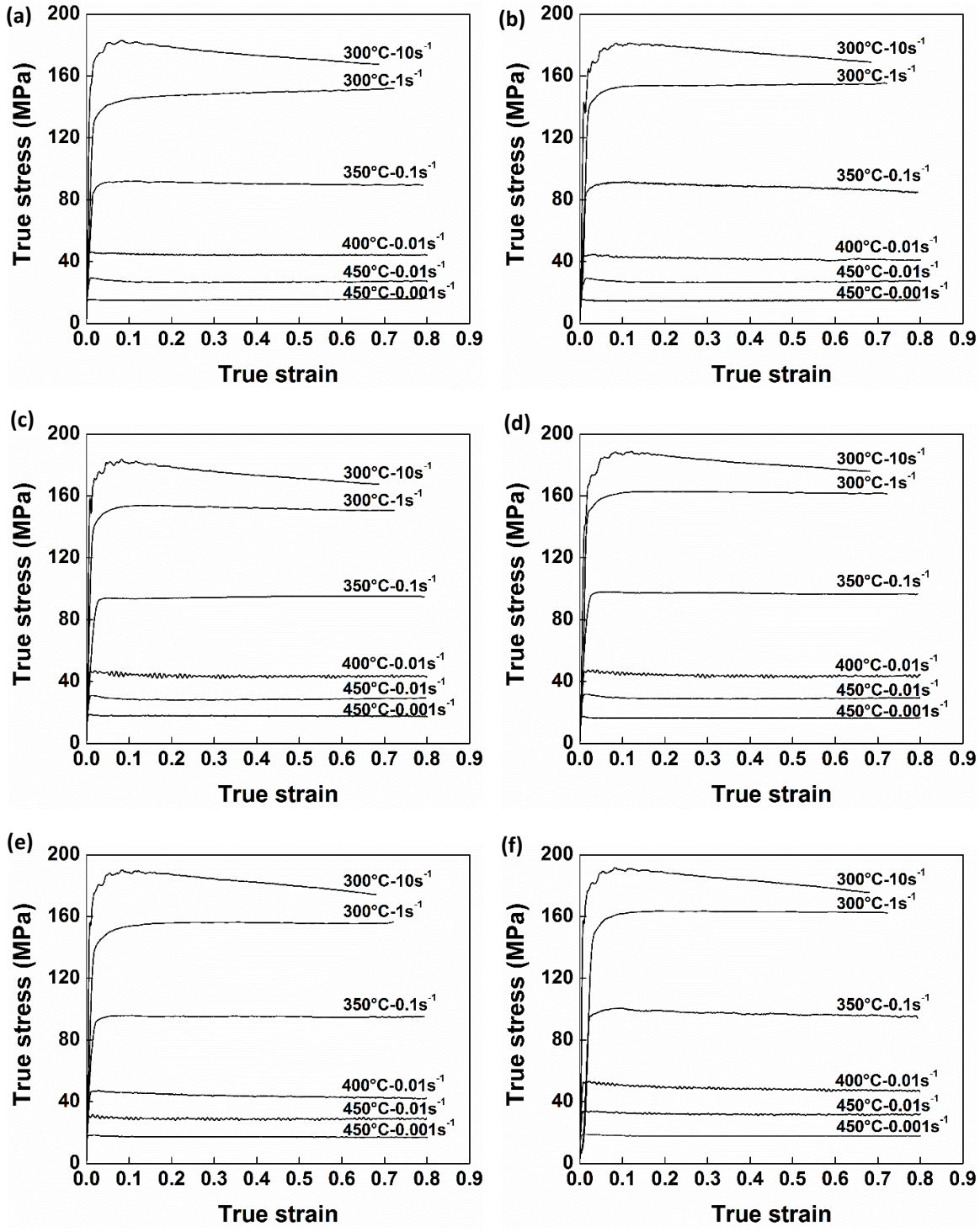

Fig. 4.1 Typical true stress-true strain curves during hot compression deformation: (a) Alloy-A (base alloy); (b) Alloy-B (0.04 Zr); (c) Alloy-C (0.07 Zr); (d) Alloy-D (0.12 Zr); (e) Alloy-E (0.15 Zr); and (f) Alloy-F (0.19 Zr).

Fig. 4.2 illustrates the evolution of the peak flow stresses of the alloys with different Zr contents as a function of strain rate at various deformation temperatures. Under a given deformation condition, no significant variation could be observed in the peak stress between the base alloy (Alloy-A) and Alloy-B with 0.04% Zr. With the further addition of Zr, increasing the content from 0.07 to 0.19%, the peak stress levels increased significantly. The values of peak stress showed a gradual rise with increasing content of Zr under the same deformation condition. For example, when hot deformation was performed at 300 °C and 0.1 s^{-1}, the peak stress of the base alloy was 130.4 MPa, which increased to 136.3 MPa and 139.7 MPa after the material was alloyed with 0.12 and 0.19% Zr, respectively. As the deformation temperature increased to 450 °C at the same strain rate of 0.1 s^{-1}, the peak stresses of the alloys containing 0.12% and 0.19% Zr increased to 55.68 MPa and 59.22 MPa, representing 6.2% and 13% increases, respectively, relative to the peak stress in the base alloy. The results indicate that micro-alloying with a Zr content greater than 0.04% could remarkably retard the dynamic softening of the base material and enhance its deformation resistance during deformation at elevated temperatures.

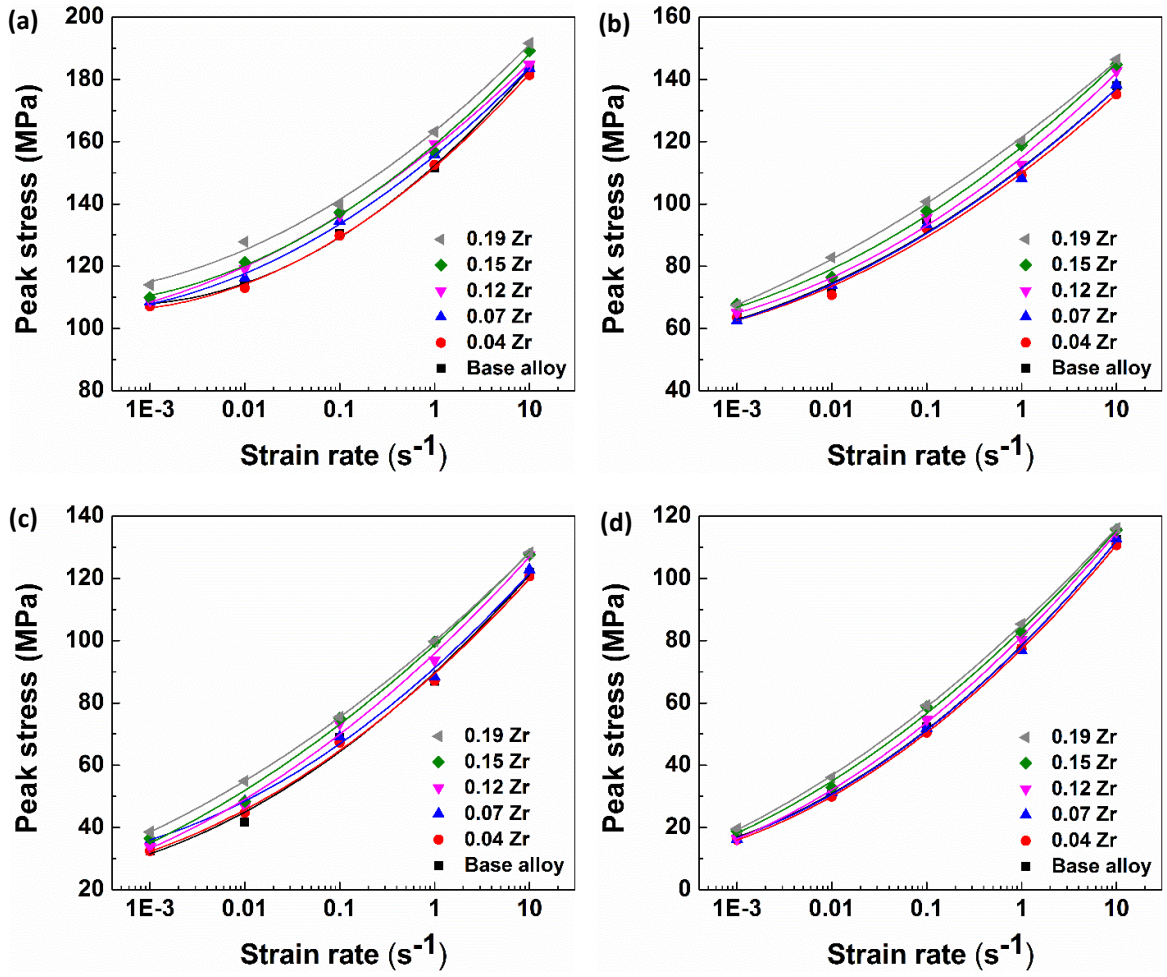

Fig. 4.2 The evolution of peak stresses of alloys A-F during hot deformation at (a) 300 °C; (b) 350 °C; (c) 400 °C; and (d) 450 °C.

4.3.2 Constitutive analyses

Constitutive equations are generally developed to model the hot deformation behavior of materials and to demonstrate the effects of deformation conditions on the state of the flow stress. The hyperbolic-sine equation, proposed by Sellars and McTegart [29], is widely employed to describe the relationship between the strain rate, deformation temperature and flow stress, especially over a wide range of stresses [2,29],

$$Z = \dot{\varepsilon} \exp(\frac{Q}{RT}) = A[\sinh(\alpha\sigma)]^n \quad (4.1)$$

where Z is the Zener-Hollomon parameter, n and A are material constants, α is the stress multiplier, σ is the flow stress (MPa), Q is the activation energy for hot deformation (kJ/mol), R is the universal gas constant (8.314 J/mol K) and T is the deformation temperature (K).

In this study, the experimental data obtained for Alloy-D, containing 0.12% Zr, were used as an example to derive the activation energy Q and material constants for all materials studied. The peak flow stress σ_p is used to proxy for σ, which is generally utilized in aluminum alloys and refers to the dynamic equilibrium between work hardening and dynamic restoration [30,31]. The data obtained at a strain rate of 10 s^{-1} were not taken into account due to the flow instability derived from the significant rise in deformation temperature. The stress multiplier α can be defined as $\alpha = \beta / n_1$ [29], where β and n_1 are evaluated from the mean slopes of the plots of $\ln(\dot{\varepsilon})$ - σ_p and $\ln(\dot{\varepsilon})$ - $\ln(\sigma_p)$, respectively, for the range of temperatures studied. From Fig. 4.3, the values of β and n_1 were calculated and the value of α for Alloy-D was determined to be 0.011.

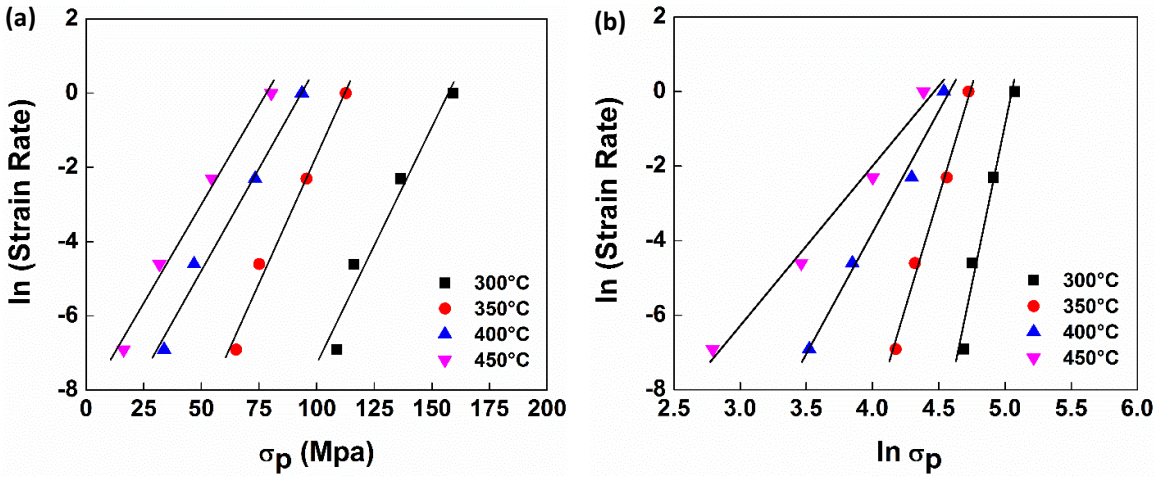

Fig. 4.3 Relationships between (a) $\ln\dot{\varepsilon}$ **and** σ_p **and (b)** $\ln\dot{\varepsilon}$ **and** $\ln\sigma_p$**.**

Differentiating Eq. (4.1) yields:

$$Q = R[\frac{\partial \ln\dot{\varepsilon}}{\partial \ln[\sinh(\alpha\sigma_p)]}]_T[\frac{\partial \ln[\sinh(\alpha\sigma_p)]}{\partial(1/T)}]_{\dot{\varepsilon}} = RnS \tag{4.2}$$

where n is the mean slope of plots of $\ln\dot{\varepsilon}$ - $\ln[\sinh(\alpha\sigma_p)]$ at different temperatures and S is the mean slope of plots of $\ln[\sinh(\alpha\sigma_p)]$ - $1/T$ at various strain rates. The relationship between $\ln\dot{\varepsilon}$ and $\ln[\sinh(\alpha\sigma_p)]$, which was derived from the measured peak stresses (Fig. 4.2), is shown in Fig. 4.4(a). The mean value of the slopes at four deformation temperatures, n, was then calculated. Additionally, the relationship between $\ln[\sinh(\alpha\sigma_p)]$ and $1/T$, which was derived from experimental peak stress data (Fig. 4.2), is plotted in Fig. 4.4(b). The mean value of the slopes at different strain rates, S, was obtained. The activation energy Q could then be determined directly from Eq. (4.2).

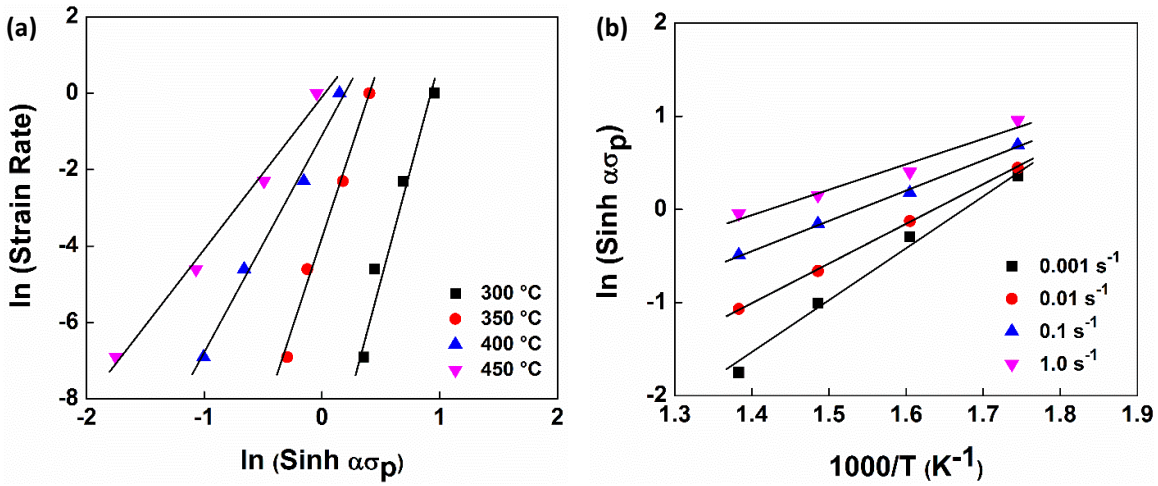

Fig. 4.4 Relationships between (a) $\ln \dot{\varepsilon}$ **and** $\ln[\sinh(\alpha\sigma_p)]$ **and (b)** $\ln[\sinh(\alpha\sigma_p)]$ **and** $1000/T$**.**

Taking the natural logarithm of both sides of Eq. (4.1) yields:

$$\ln Z = \ln(A) + n\ln[\sinh(\alpha\sigma_p)] \tag{4.3}$$

where $\ln(A)$ is obtained from the intercept of the plot of $\ln Z$ - $\ln[\sinh(\alpha\sigma_p)]$, as shown in Fig. 4.5. Likewise, the material constants A, n and α and the activation energies Q for all alloys were calculated according to Eq. (4.1), (4.2) and (4.3). Table 4.2 presents the values of these constants and activation energies corresponding to all alloys studied. As shown, α remains fairly constant, whereas the values of n and A increase with increasing Zr content. For example, the value of n increases from 7.02 for the base alloy to 8.08 for the alloy containing 0.19% Zr, whereas the value of A increases from 1.01 x 10^{17} for the base alloy to 2.08 x 10^{19} for the alloy containing 0.19% Zr.

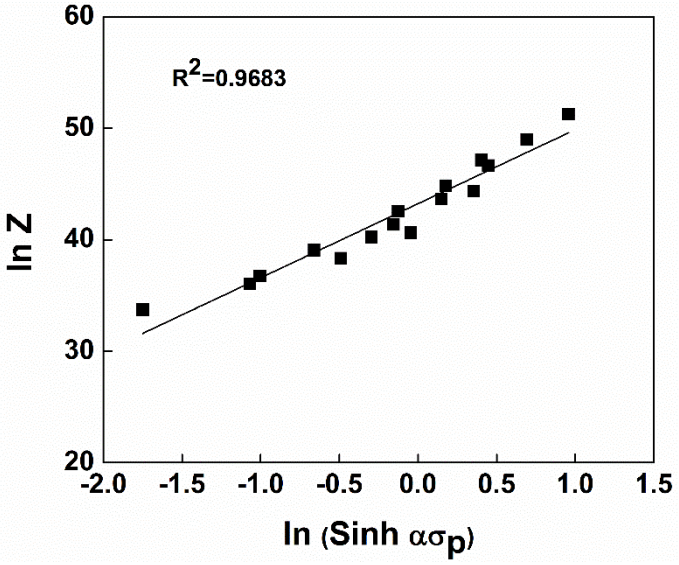

Fig. 4.5 Relationship between $\ln Z$ and $\ln[\sinh(\alpha\sigma_p)]$.

Table 4. 2 Values of material constants and activation energies for the alloys studied.

Alloy	α (MPa^{-1})	n	A (s^{-1})	Q (kJ mol^{-1})
Alloy-A (base alloy)	0.012	7.02	1.01×10^{17}	229.4
Alloy-B (0.04 Zr)	0.011	7.00	8.92×10^{16}	226.5
Alloy-C (0.07 Zr)	0.011	7.36	7.65×10^{17}	235.7
Alloy-D (0.12 Zr)	0.011	7.51	5.96×10^{18}	247.2
Alloy-E (0.15 Zr)	0.010	7.65	8.59×10^{18}	249.4
Alloy-F (0.19 Zr)	0.010	8.08	2.08×10^{19}	255.2

Fig. 4.6(a) plots the variation in the hot deformation activation energy, Q, as a function of Zr content. Q is an important physical parameter serving as an indicator of the degree of difficulty of plasticity deformation. The activation energy of 229.4 kJ/mol obtained for the base alloy is in general agreement with the values reported for similar alloys, such as 7150, 7050 and 7075 alloys [12,32,33]. Alloy-B, containing 0.04% Zr, exhibited a similar but slightly lower value of 226.5 kJ/mol compared with that of the base alloy. With an increase in Zr content to 0.19%, Q showed a distinctly increasing tendency and reached 255.2 kJ/mol for Alloy-F, which contained 0.19% Zr. These results suggest that the addition of

more than 0.04% Zr can significantly increase the resistance of the 7150 aluminum alloy to deformation during the hot working process.

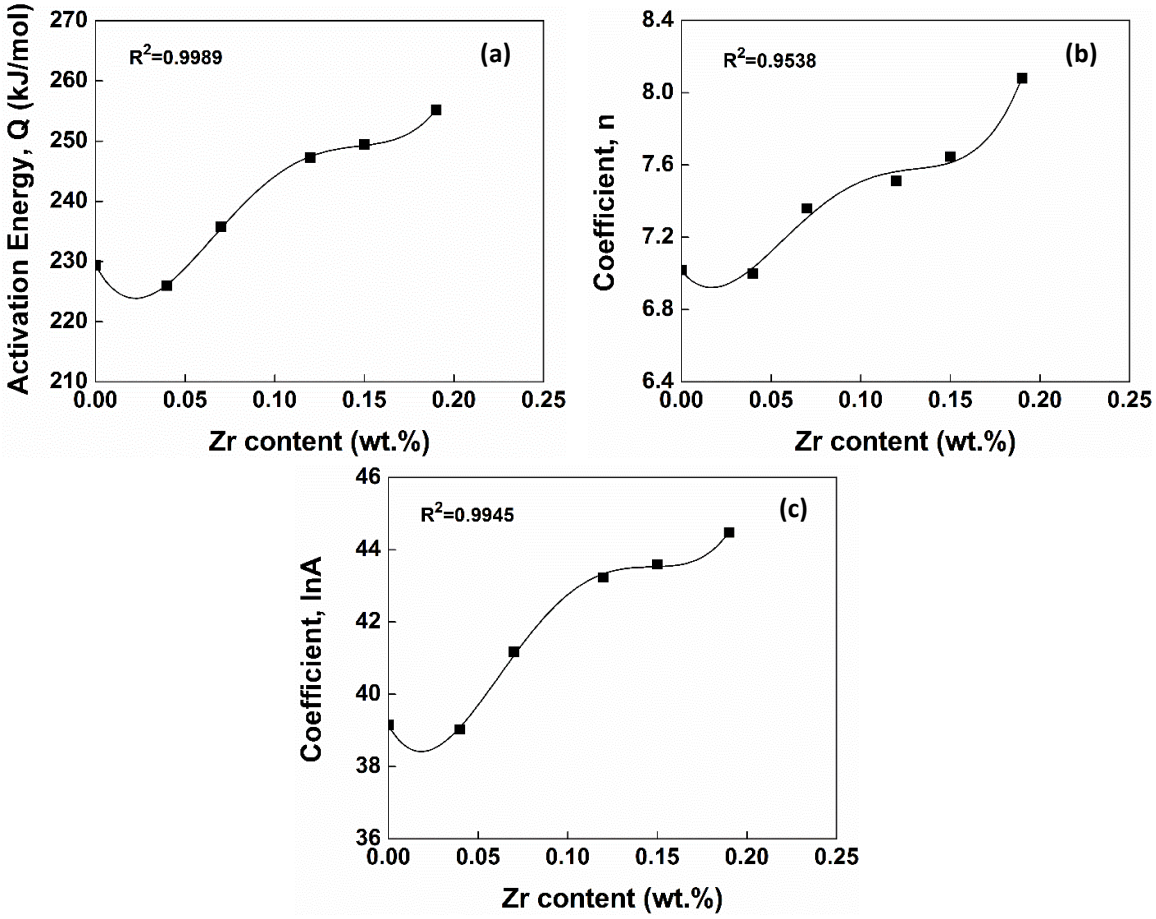

Fig. 4.6 Relationships between (a) Q, (b) n and (c) lnA and Zr content with polynomial fit.

Based on the above-described analysis, it is evident that the values of the activation energy and material constants are closely related with the variation in the Zr content. Relatively good polynomial relationships between the activation energy Q, material constants n and A and the Zr content were obtained (Fig. 4.6), as shown in Eq. (4.4). The coefficients of the polynomial are presented in Table 4.3. In addition, it is shown that the value of α remained nearly constant at different Zr contents (Table 4.2); thus, the average

value of 0.011 was adopted for the alloys studied.

$$\begin{cases} Q = B_0 + B_1 Zr + B_2 Zr^2 + B_3 Zr^3 + B_4 Zr^4 \\ n = C_0 + C_1 Zr + C_2 Zr^2 + C_3 Zr^3 + C_4 Zr^4 \\ \ln A = D_0 + D_1 Zr + D_2 Zr^2 + D_3 Zr^3 + D_4 Zr^4 \\ \alpha = 0.011 \end{cases} \quad (4.4)$$

where Zr in Eq. (4.4) is the Zr content in wt%.

Table 4. 3 Coefficients of polynomial fit for Q, n and lnA.

Q		n		lnA	
B_0	229.39	C_0	7.01	D_0	39.14
B_1	-546.099	C_1	-11.92	D_1	-85.96
B_2	15902.69	C_2	444.49	D_2	2940.14
B_3	-117270.53	C_3	-3765.92	D_3	-22601.70
B_4	276129.49	C_4	10068.03	D_4	54153.35

From Eq. (4.1), the peak flow stress, σ_p, can be expressed as a function of the deformation temperature, strain rate, activation energy and material constants (Eq. (4.5)). Through Eqs. (4.4) and (4.5), the peak flow stress related to the change in Zr content at any given temperature and strain rate can be predicted. The predicted values of the peak stresses versus the measured ones for the 7150 alloys with different Zr contents are plotted in Fig. 4.7. As demonstrated, there is excellent agreement between the predicted and experimental results.

$$\sigma_p = \frac{1}{\alpha}\sinh^{-1}\left[\frac{\dot{\varepsilon}\exp(\frac{Q}{RT})}{A}\right]^{1/n} \quad (4.5)$$

Furthermore, to evaluate the accuracy of the developed constitutive equations (Eq. (4.4)), the error between the predicted peak flow stress (σ_p) and the measured stress (σ_M) can be expressed as follows:

$$error\% = \left| \frac{\sigma_p - \sigma_M}{\sigma_M} \right| \times 100 \tag{4.6}$$

The mean error for the 7150 alloys with Zr contents ranging from 0 to 0.19%, under the various deformation conditions studied, was determined to be 5.32%, which indicates good agreement between the predicted and measured peak stresses. Therefore, the developed constitutive equations offer excellent prediction of the hot deformation behavior of 7150 aluminum alloy with a variation in Zr content and can be used to analyze problems associated with the hot working process.

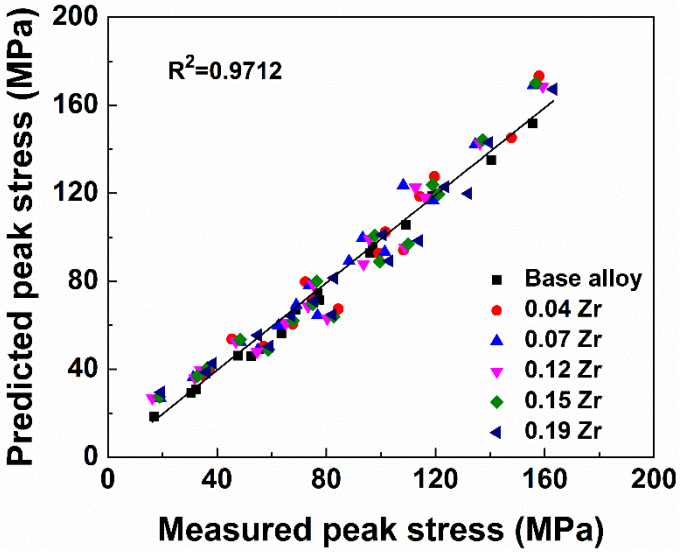

Fig. 4.7 Correlation between predicted and experimental peak flow stress.

4.3.3 Microstructure evolution

4.3.3.1 Initial microstructure

To investigate the microstructural evolution of the alloys studied when alloyed with Zr, Alloy-A (base alloy), Alloy-D (0.12% Zr) and Alloy-F (0.19% Zr) were selected for further study. Fig. 4.8 shows optical micrographs of these alloys after the homogenization treatment. The homogenized structures of the three alloys were composed of uniform equiaxed grains formed during casting. The average grain size of Alloy-A was 127 μm. The grain structures of the alloys containing Zr were much coarser. The average grain sizes were approximately 547 μm and 485 μm for Alloy-D and F, respectively. This is due to the poisoning effect of Zr, through which the added Zr reacts with iron and silicon in the melt, reducing the growth restriction of grains [34]. Moreover, the EBSD analysis results revealed that the grain boundaries of all three alloys were characterized by high-angle boundaries, typically with misorientation angles between 30 and 60°.

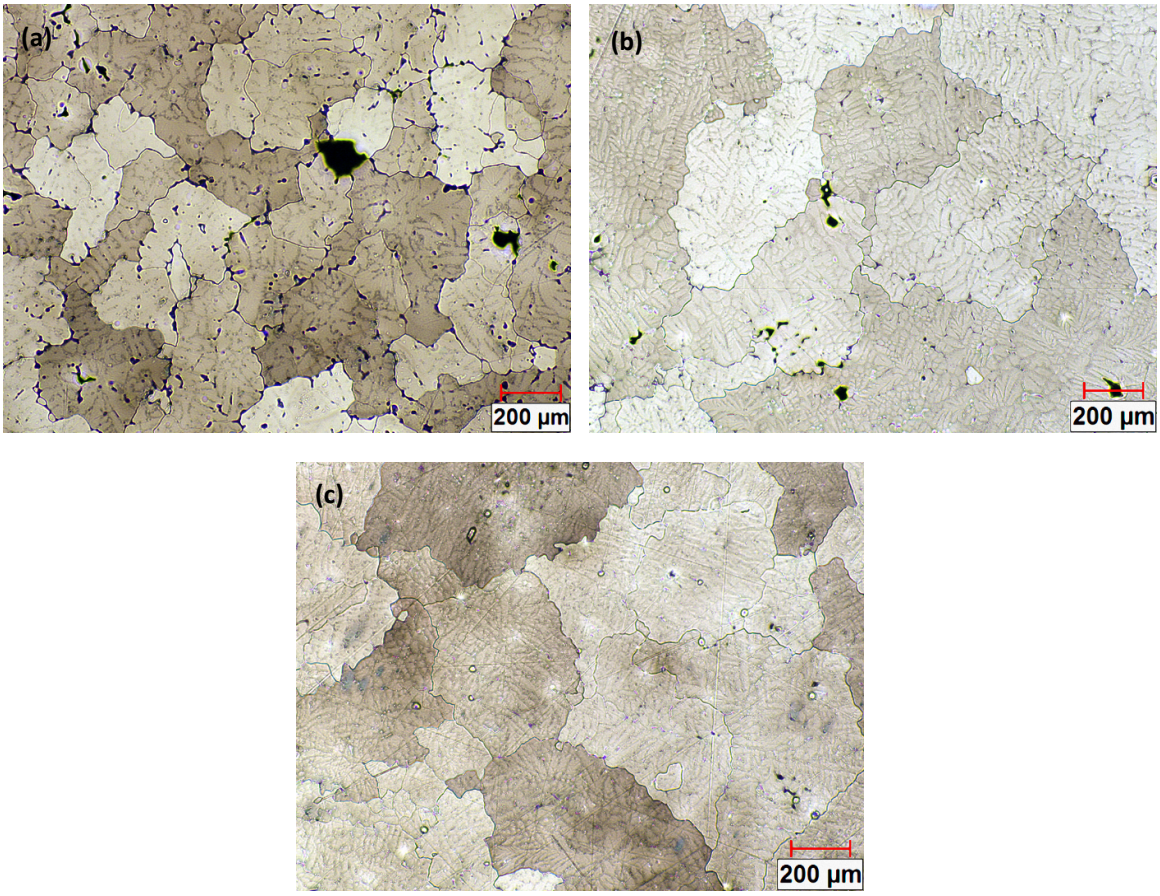

Fig. 4.8 Optical micrographs showing the grain structures after homogenization: (a) Alloy-A (base alloy); (b) Alloy-D (0.12 Zr); and (c) Alloy-F (0.19 Zr).

After homogenization at 465 °C for 24 h, the precipitation of Al_3Zr dispersoids was clearly observed in the materials micro-alloyed with Zr contents ranging from 0.07 to 0.19%. Fig. 4.9 shows an example of Alloy-D containing 0.12% Zr. The dark-field TEM micrograph shows that a large number of spheroidal and coherent Al_3Zr dispersoids with an average size of 14.5 nm were precipitated in the aluminum matrix (Fig. 4.9(a)), indicating a strong pinning effect on dislocation movement during hot deformation. However, the distribution of Al_3Zr dispersoids was not homogeneous, and dispersoid-free bands were observed in the interdendritic region (Fig. 4.9(b)) and near grain boundaries (Fig. 4.9(c)). During casting,

zirconium tended to segregate in the dendrite centers, which resulted in a high concentration of Zr and hence a sufficiently high level of supersaturation that allowed for the precipitation of a large number of Al_3Zr dispersoids. On the other hand, the matrix toward the edge of the dendrites and in the area adjacent to the grain boundaries contained an insufficient Zr concentration, leading to a relatively dispersoid-free zone [16,35]. In the samples with low Zr contents (0.04%), almost no Al_3Zr dispersoids could be found, indicating that the added Zr mainly existed as the solute atoms in the aluminum matrix. The role of these fine Al_3Zr dispersoids in hot deformation will be discussed in the following sections.

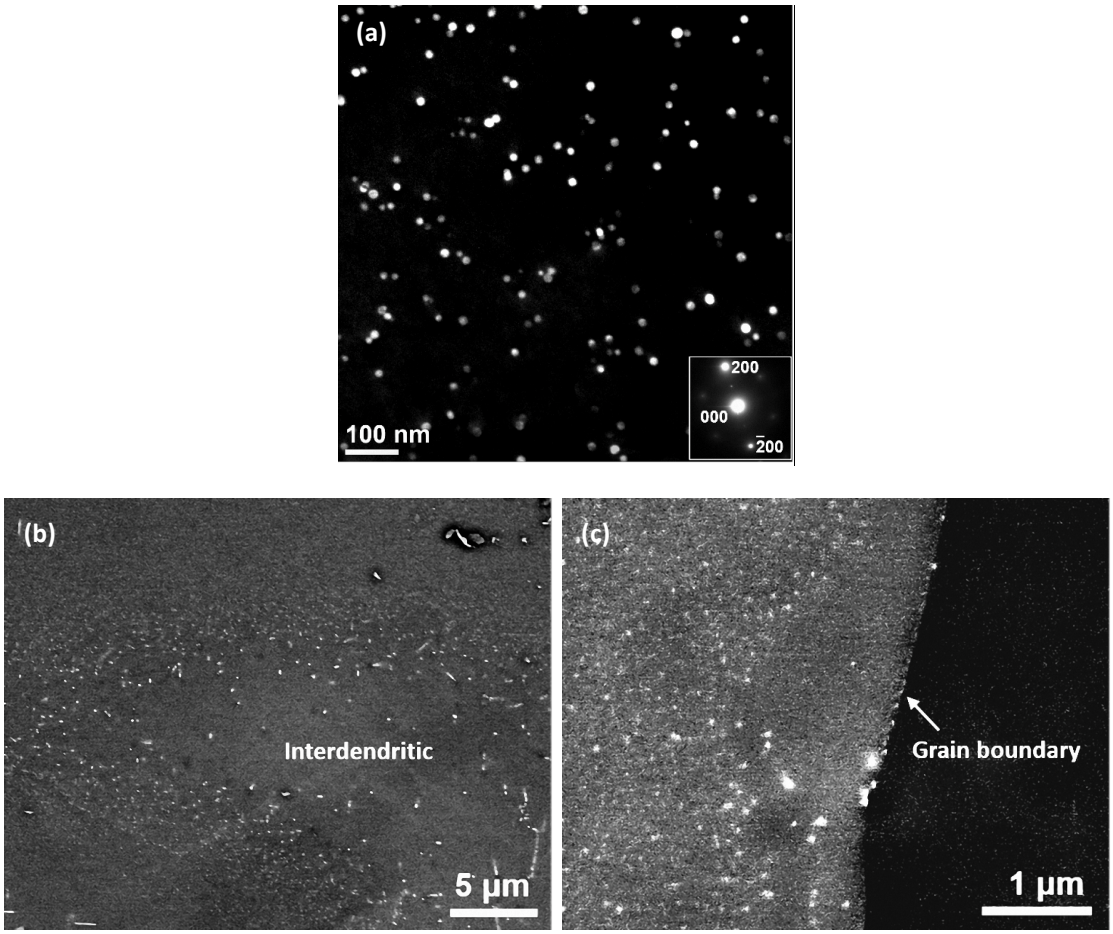

Fig. 4.9 TEM and FEG-SEM micrographs displaying precipitation of Al_3Zr dispersoids in Alloy D (0.12 Zr) after homogenization at 465 for 24 h. (a) A dark-field TEM image recorded near the [011]α zone axis by using the (100) superlattice reflections of Al_3Zr ($L1_2$). The inset image is the corresponding diffraction pattern. (b) FEG-SEM images across an interdendritic region and (c) near a grain boundary.

4.3.3.2 Hot deformed microstructure

To investigate the microstructures during hot deformation, orientation imaging maps of the deformed samples of Alloy-A, D and F were generated under different deformation conditions using the EBSD technique (Fig. 4.10). In orientation imaging maps, the boundary misorientation angles of both grains and subgrains can be distinguished as follows: white

lines: 1-5°; blue lines: 5-15°; thin black lines: 15-30° and thick black lines: (> 30°).

When the deformation was performed at 300 °C and 1 s^{-1}, the original grains of the three alloys were severely torn and broke into irregular deformation bands (Fig. 4.10(a), (d) and (g)). A large amount of low-angle boundaries of 1-5° were observed, indicating a high density of cell and subgrain structures. For the deformation processes conducted at higher temperatures and lower strain rates, the evolution of the substructures of all three alloys showed a similar tendency: the deformation became more homogeneous (Fig. 4.10(b), (e) and (h)). The substructures became better organized, and larger subgrains were formed with neatly arranged boundaries between 1° and 15° (Fig. 4.10(c), (f) and (i)). The rise of this organized structure was due to the increase in the number of operating slip systems and the increase in the dynamic recovery level as the temperature increased and strain rate decreased [2].

It should be emphasized that, in the base alloy deformed at 450 °C and 1 s^{-1}, a large number of subgrains with higher angle boundaries (5-15°) existed along the serrated grain boundaries (Fig. 4.10(b)), indicating a strong dynamically recovered structure [2,18]. On the other hand, in the alloys containing 0.12 and 0.19% Zr, the serration of the grain boundaries disappeared and the recovered substructures were mainly characterized by low-angle boundaries (1-5°). This result demonstrates that the dynamic recovery was remarkably restricted when alloying with Zr.

Furthermore, as the strain rate was lowered to 0.01 s^{-1} at 450 °C, in addition to the

development of a recovered structure, partially dynamic recrystallization occurred during the deformation of the base alloy. Small equiaxed grains with high-angle boundaries (>15°) that contained substructures were observed along the bulged grain boundaries (see the arrows in Fig. 4.10(c)). However, only dynamically recovered microstructures were observed in the alloys containing 0.12 and 0.19% Zr (Fig. 4.10(f) and (i)). Subgrains with boundaries of misorientation angles between 5 and 15° were observed along the elongated grain boundaries. Hence, the addition of Zr was observed to inhibit dynamic recrystallization.

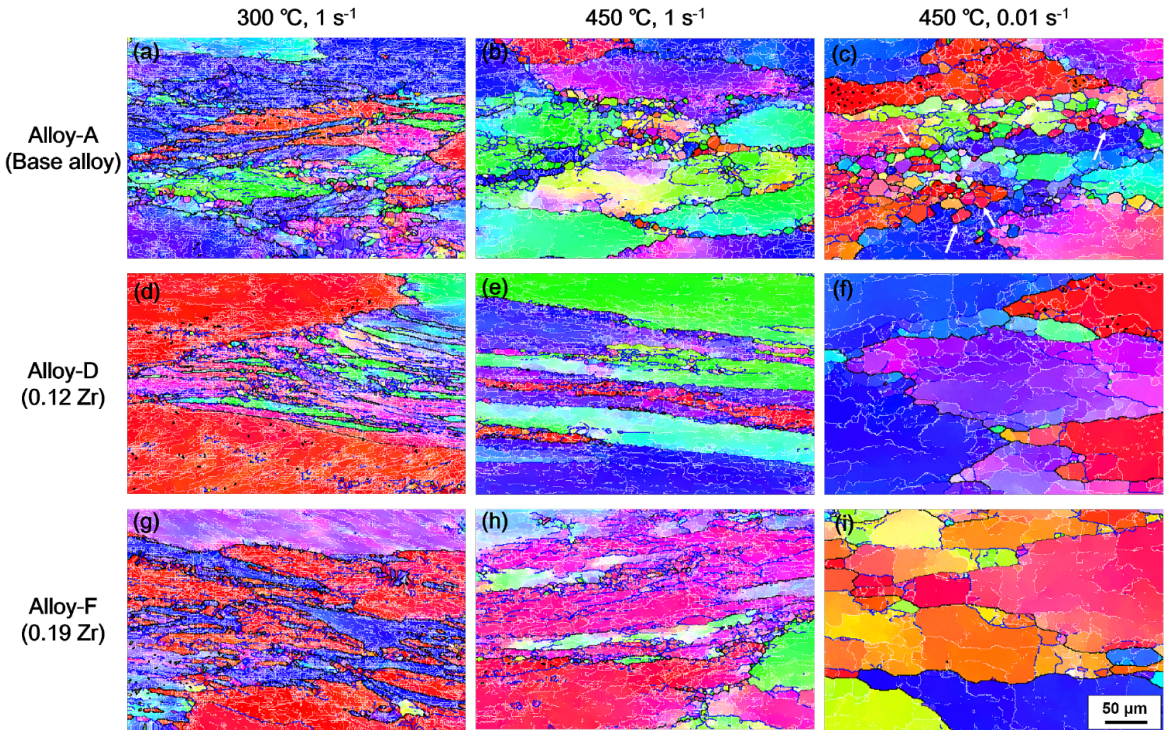

Fig. 4.10 Orientation imaging maps of Alloy-A (base alloy), Alloy-D (0.12 Zr) and Alloy-F (0.19 Zr) under different deformation conditions. The crystallographic orientations illustrated on standard stereographic projection (red: [001]; blue: [111]; green: [101]).

4.3.3.3 Quantitative characterization of substructure

To further study the effects of deformation temperature, strain rate and Zr addition on dynamic softening, the misorientation angles of boundaries as well as subgrain sizes under different deformation conditions were quantitatively analyzed for the deformed samples of Alloy-A, D and F using the EBSD technique. As the temperature increased from 350 to 450 °C and the strain rate decreased from 0.1 to 0.01 s^{-1}, the mean misorientation angle of boundaries was continuously increased in the three alloys (Fig. 4.11). This result suggests an increased level of dynamic restoration with increasing temperature and decreasing strain rate [18], which is consistent with the microstructural observations shown in Fig. 4.10. On the other hand, under the same deformation conditions, the mean misorientation angle of boundaries was largely reduced with the addition of Zr. Alloy-F, which contained the highest Zr content, exhibited the lowest mean misorientation angles.

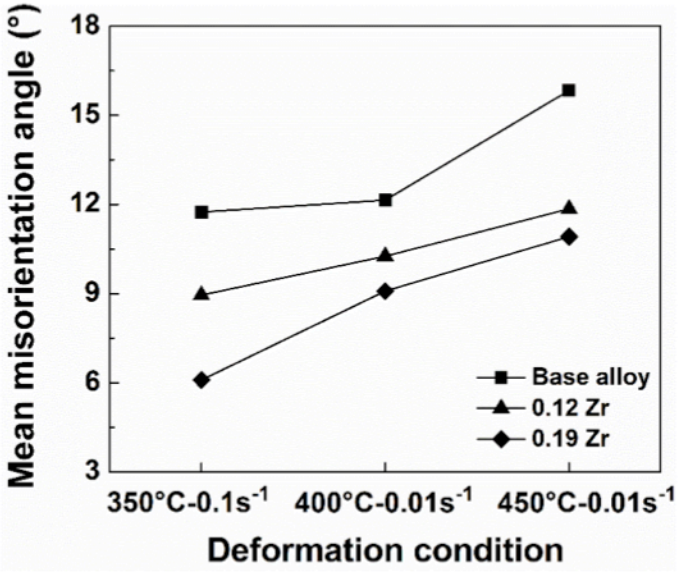

Fig. 4.11 Evolution of mean misorientation angles of boundaries in Alloy-A (base alloy), Alloy-D (0.12 Zr) and Alloy-F (0.19 Zr) under different deformation conditions.

Fig. 4.12 shows an example of the misorientation angle distributions of three alloys deformed at 450 °C and $0.01s^{-1}$. The deformed structures of those alloys were characterized by high fractions of subgrains with boundary misorientation angles between 1 and 15°. Generally, among the three alloys, the fraction of high-angle boundaries (>15°) in the base alloy was clearly observed to be higher, approximately 34.4%. This high fraction is attributed to the formation of dynamically recrystallized grains with high-angle boundaries, as shown in Fig 4.10(c). However, no increase in the number of high-angle boundaries was observed when alloying with Zr (Fig. 4.12(b) and (c)), indicating an inhibition of dynamic recrystallization, which is in agreement with the solely recovered structures in Fig. 4.10(f) and (i). Furthermore, with the increase in Zr content from 0.12 to 0.19%, the fraction of boundaries with higher misorientation angles (5-15°) declined, which is associated with an increase in the fraction of low-angle boundaries (1-5°), as shown in Fig. 4.12(b) and (c). This result indicates a decrease in dislocation polygonization and subgrain coalescence with increasing Zr content [2,18]. Therefore, the addition of Zr significantly restrained dynamic recovery during hot deformation, and the level of dynamic recovery decreased with increasing Zr content.

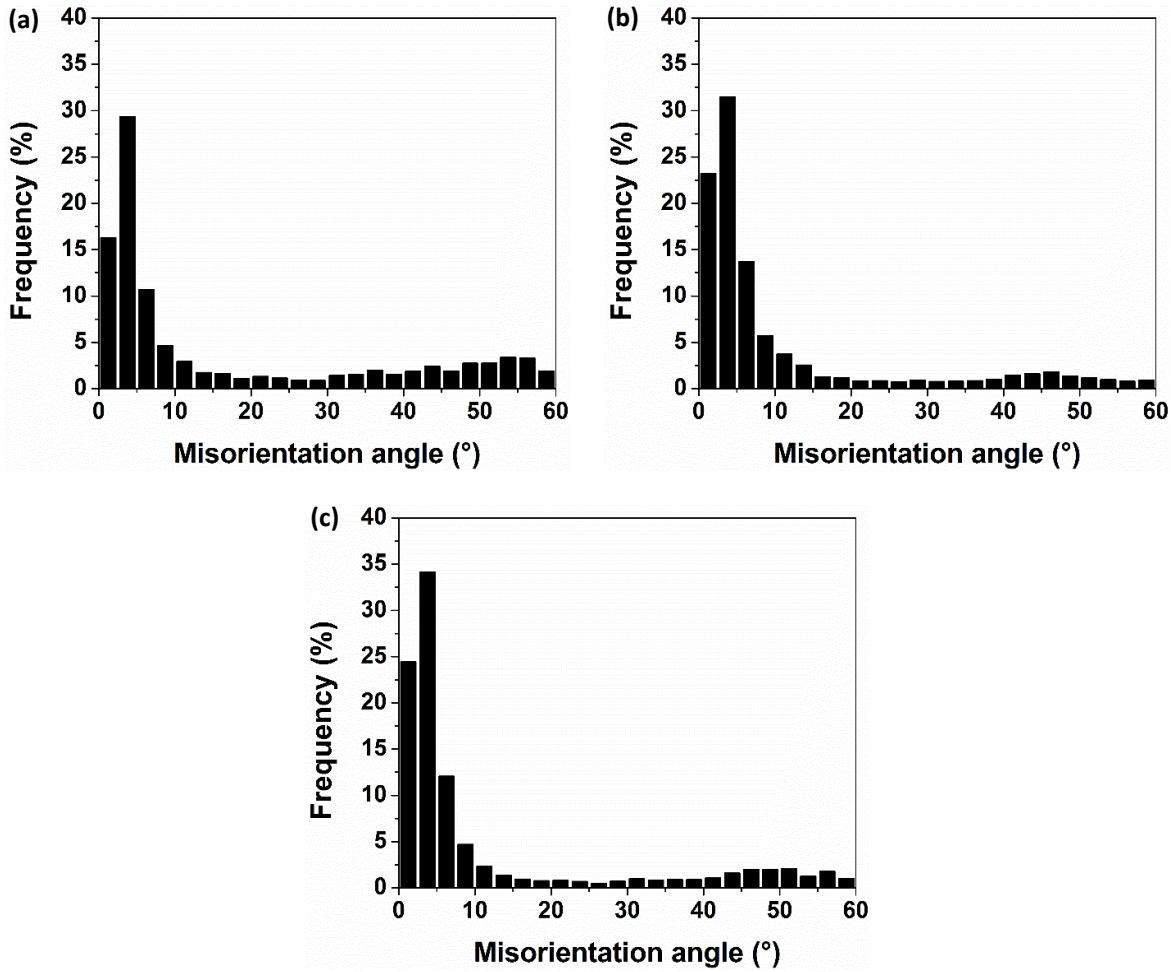

Fig. 4.12 Evolution of misorientation angle distribution of boundaries under deformation at 450 °C and 0.01s^{-1} for (a) Alloy-A (base alloy); (b) Alloy-D (0.12 Zr) and (c) Alloy-F (0.19 Zr).

Fig. 4.13(a) shows the change in subgrain sizes with deformation condition in three alloys. The average subgrain sizes of all of those alloys increased with increasing temperature and decreasing strain rate. The increase in subgrain size was due to an increase in the rate of subgrain formation and growth as the temperature increased, and the time required for subgrain coalescence increased as the strain rate decreased [18]. Under a given deformation condition, the subgrain size decreased as the Zr content increased (Fig. 4.13(a)). Alloy-F,

containing 0.19% Zr, exhibited the smallest subgrain sizes among the three alloys, indicating a slowing of dynamic recovery with increased Zr addition [2,18]. Moreover, the decrease in subgrain size after alloying with Zr was observed to increase in magnitude at higher deformation temperatures (Fig. 4.13(a)). This trend was probably because the high rate of subgrain coalescence at elevated temperatures was effectively constrained by adding Zr.

Fig. 4.13(b) illustrates the relationship between the steady-state flow stress at a true strain of 0.8, σ_s, with the subgrain size, d, in Alloy-A, Alloy-D and Alloy-F. It is clear that the steady-state flow stress increased with decreasing subgrain size, and a good linear relationship between the flow stress and reciprocal subgrain size was established, as described by Eq. (4.7):

$$\sigma_s = 384.61 d^{-1} - 53.52 \tag{4.7}$$

This relationship agrees well with that reported for aluminum alloys under hot compression, torsion and extrusion by McQueen et al. and Jonas et al. [14,36,37]. It is believed that the deformation conditions (temperature and strain rate) define the steady-state subgrain size, which in turn determines the flow stress [2]. As temperature decreased and strain rate increased, a higher flow stress was induced as a result of a finer subgrain size generated during hot deformation [2]. Furthermore, when adding Zr, the level of dynamic recovery was considerably reduced, leading to a finer subgrain structure (Fig. 4.13(a)). Hence, the flow stress was higher compared with that of the 7150 base alloy under the same deformation condition.

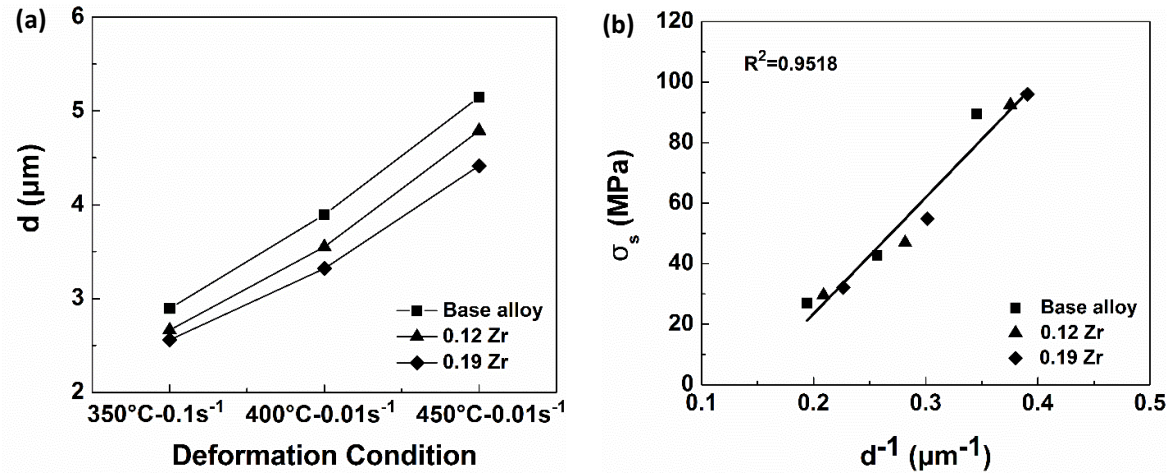

Fig. 4.13 (a) Evolution of subgrain diameters under different deformation conditions and (b) relationship between steady-state flow stress and reciprocal subgrain size for Alloy-A (base alloy), Alloy-D (0.12 Zr) and Alloy-F (0.19 Zr).

4.4 Discussion

The hot deformation behavior of 7150 aluminum alloys with a systematic variation in Zr content was studied. When alloyed with Zr of 0.04%, the alloys showed very little precipitation of Al_3Zr dispersoids because the Zr concentration just approached the solubility of Zr (approximately 0.04%) in the aluminum matrix at the homogenization temperature of 465 °C [38,39]. With the increase in Zr content from 0.07 to 0.19%, the precipitation of Al_3Zr dispersoids became more evident (Fig. 4.9), and the amount of Al_3Zr dispersoids remarkably increased as the Zr content increased. However, when the content of added Zr exceeded 0.19%, large primary intermetallics of Al_3Zr appeared, and the supersaturation of Zr in the aluminum matrix could increase no further. The presence of those large intermetallic particles is also known to promote recrystallization and to reduce the strength and fracture toughness of the material [16,21,40]. Therefore, the content of added Zr was

limited to 0.19% to investigate the effect of Zr on the hot deformation of 7150 aluminum alloy.

No significant variation could be observed in the peak flow stress or activation energy between the 7150 base alloy and the alloy containing 0.04% Zr. However, with a further increase in the Zr content from 0.07 to 0.19%, the peak flow stress and activation energy increased significantly. The addition of Zr promoted the retardation of dynamic recovery and the inhibition of dynamic recrystallization during the hot deformation process.

In general, the level of dynamic recovery of the base alloy, as well as that of the alloys containing Zr, increased with increasing temperature and decreasing strain rate (Fig. 4.10, 4.11 and 4.13), which was characterized by an increase in mean misorientation angle of boundaries and an increase in subgrain size (Fig. 4.11 and 4.13). On the other hand, the level of dynamic recovery was observed to decrease after alloying with Zr (Fig. 4.10, 4.11 and 4.13). When Zr was added, the precipitation of Al_3Zr dispersoids during homogenization played an important role in dynamic softening. Fig. 4.14 shows the interaction of Al_3Zr dispersoids with deformed substructures as exemplified in Alloy-D, containing 0.12% Zr, under deformation performed at 450 °C and $0.01s^{-1}$. Fig. 4.14(a) shows the edge dislocations bowing at the points where they encountered Al_3Zr dispersoids, indicating a strong pinning effect of Al_3Zr dispersoids on dislocation slip [14,23,24]. Moreover, it is observed that the low-angle subgrain boundaries were strongly pinned by those dispersoids (Fig. 4.14(b)), and thus, the ability for subgrain rotation to lead to coalescence was reduced [2,14,18]. Hence,

dynamic recovery in the alloys containing Zr was restrained due to the pinning effect of Al_3Zr dispersoids on dislocation motion and subgrain rotation [2,18]. When a higher content of Zr was added, the increased amount of Al_3Zr dispersoids generated a stronger effective pinning effect on substructures and resulted in a further decrease in the dynamic recovery level, which was associated with a decrease in the mean misorientation angle of boundaries and a decrease in subgrain size (Fig. 4.11 and 4.13).

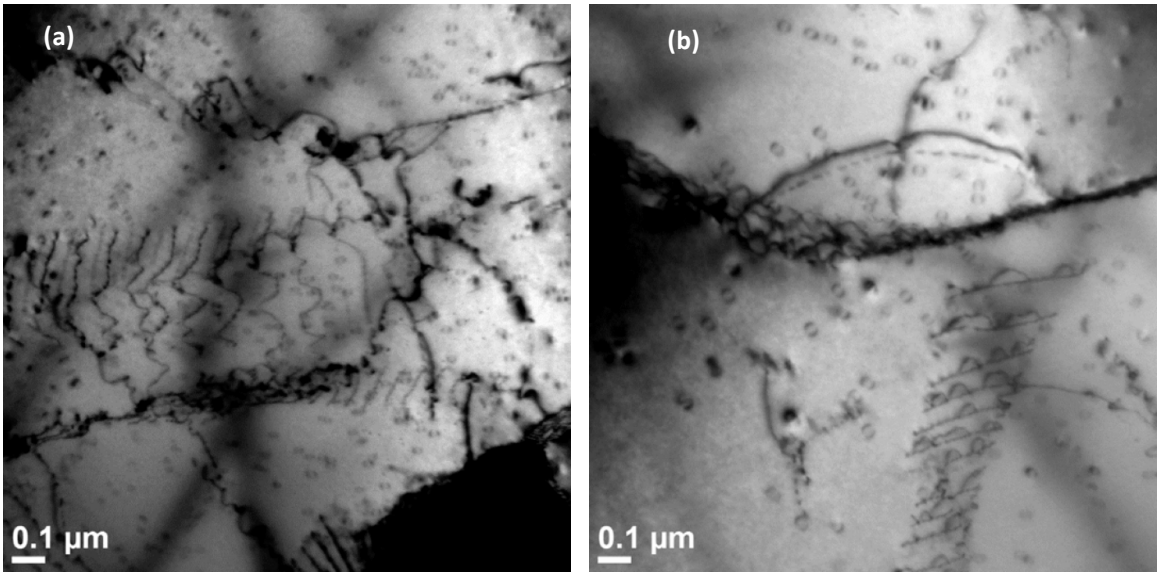

Fig. 4.14 Bright-field TEM images (with the g=(200) reflection at [011]α) of Alloy-D deformed at 450 °C and 0.01s^{-1} showing the interaction of Al_3Zr dispersoids with (a) dislocations and (b) subgrain boundaries.

It is worth noting that, when alloyed with Zr, coarse grain structures were induced as a result of the poisoning effect of Zr (Fig. 4.8). However, the increase in flow stress due to the change in grain size could be neglected. In aluminum alloys, grain boundary sliding becomes pronounced above 300 °C, which reduces the effectiveness of grain boundary strengthening [2]. McQueen et al. [2] indicated that a decrease in grain size has a relatively small effect on

increasing flow stress during high-temperature deformation. On the other hand, with the addition of Zr, the pinning effect of Al_3Zr dispersoids on dislocation slip and restrained dynamic recovery resulted in a significant increase in the peak flow stress and activation energy of 7150 aluminum alloy.

4.5 Conclusions

1. No significant variation in peak flow stress was observed between the 7150 base alloy (Zr free) and the alloy containing 0.04% Zr. With a further increase in the Zr content from 0.07 to 0.19%, the peak flow stress increased significantly.

2. The materials constants and activation energy for hot deformation were determined from the experimental compression data gathered for all alloys studied. The solved constitutive equations yielded good predictions of the peak flow stress over wide temperature and strain-rate ranges for 7150 alloys with different Zr contents.

3. With increasing Zr content, the hot deformation activation energy of the 7150 alloys progressively increased from 229.4 kJ/mol for the base alloy to 255.2 kJ/mol for the alloy containing 0.19% Zr.

4. The level of dynamic recovery was reduced after alloying with Zr, which was associated with a decrease in the mean misorientation angle of boundaries and a reduction in subgrain size.

5. The addition of Zr promoted the retardation of dynamic recovery and the inhibition of

dynamic recrystallization in the 7150 alloys during hot deformation due to the pinning effect of Al_3Zr dispersoids on dislocation motion and due to restrained dynamic restoration. Dynamic recovery is the sole dynamic softening mechanism in the alloys containing Zr.

References

[1] E.A. Starke, J.T. Staley, Prog. Aerosp. Sci. 32 (1996) 131-172.

[2] H.J. McQueen, S. Spigarelli, M. Kassner, E. Evangelista, Hot Deformation and Processing of Aluminum Alloys, CRC Press, Florida, 2011, pp. 87-233.

[3] E. Cerri, E. Evangelista, H.J. McQueen, High Temp. Mat. Proc. 18 (1999) 227-240.

[4] J.D. Robson, Acta Mater. 52 (2004) 1409-1421.

[5] S. Hirosawa, T. Sato, A. Kamio, H.M. Flower, Acta Mater. 48 (2000) 1797-1806.

[6] G.B. Schaffer, S.H. Huo, J. Drennan, G.J. Auchterlonie, Acta Mater. 49 (2001) 2671-2678.

[7] J.M. Silcock, H.M. Flower, Scripta Mater. 46 (2002) 389-394.

[8] W.V. Geertruyden,W.Z. Misiolek, P.T.Wang, Mater. Sci. Eng. A419 (2006) 105-114.

[9] J.Q. Su, T.W. Nelson, C.J. Sterling, Mater. Sci. Eng. A 405 (2005) 277-286.

[10] R. Kaibyshev, O. Sitdikov, A. Goloborodko, Mater. Sci. Eng. A 344 (2003) 348-356.

[11] S. Gourdet, F. Montheillet, Mater. Sci. Eng. A 283 (2000) 274-288.

[12] H.E. Hu, L. Zhen, L. Yang, W.Z. Shao, B.Y. Zhang, Mater. Sci. Eng. A 488 (2008) 64-71.

[13] S. Banerjee, P.S. Robi, A. Srinivasan, L.P. Kumar, Mater. Sci. Eng. A 527 (2010) 2498-2503.

[14] G. Avramovic-Cingara, D.D. Perovic, H.J. McQueen, Met. Mat. Trans. A. 27 (1996) 3478-3490.

[15] T. Sheppard, M.G. Tutcher, Met. Sci. 14 (1980) 579-589.

[16] J.D. Robson, P.B. Prangnell, Acta Mater. 49 (2001) 599-613.

[17] Y.V. Milman, A.I. Sirko, D.V. Lotsko, D.B. Miracle, O.N. Senkov, Mater. Sci Forum, 396-402 (2002) 1217-1222.

[18] F.J. Humphreys, M. Hatherly, Recrystallization and Related Annealing Phenomena, second ed., Elsevier Ltd., Oxford, 2004, pp. 169-450.

[19] X. LU, E. Guo, P. Rometsch, L. Wang, Trans. Nonferrous Met. Soc. China 22 (2012) 2645-2651.

[20] B. Morere, R. Shahani, C. Maurice, J. Driver, Metall. Mater. Trans. A 32 (2001) 625-632.

[21] J.D. Robson, Mater. Sci. Eng. A 338 (2002) 219-229.

[22] A.R. Eivani, H. Ahmed, J. Zhou, J. Duszczyk, Mater. Sci. Eng. A 527 (2010) 2418-2430.

[23] Y. Li, Z. Liu, L. Lin, J. Peng, A. Ning, J. Mater. Sci. 46 (2011) 3708-3715.

[24] L. Zou, Q. Pan, Y. He, W. Liang, C. Wang, Mater. Sci. 44 (2008) 120-125.

[25] H.J. McQueen, E. Evangelista Metall. Sci. Technol. 28 (2010) 12-21.

[26] F.J. Humphreys, J. Mater. Sci, 36 (2001) 3833-3854.

[27] H. Jazaeri, F.J. Humphreys, J. Microsc. 213 (2004) 241-246.

[28] C. Shi, J. Lai, X.-G. Chen, Microstructural evolution and dynamic softening mechanisms of Al-Zn-Mg-Cu alloy during hot compressive deformation, Materials (2013), submitted for publication.

[29] C.M. Sellars, W.J. McTegart, Mem. Sci. Rev. Met. 63 (1966) 731-746.

[30] H.J. McQueen, N.D. Ryan, Mater. Sci. Eng. A 322 (2002) 43-63.

[31] S.F. Medina, C.A. Hernandez, Acta Metall. 44 (1996) 137-148.

[32] E. Cerri, E. Evangelista, A. Forcellese, H.J. McQueen, Mater. Sci. Eng. A 197 (1995) 181-198.

[33] N.P. Jin, H. Zhang, Y. Han, W.X. Wu, J.H. Chen, Mater. Charact. 60 (2009) 530-536.

[34] A.M. Bunn, P. Schumacher, M.A. Kearns, C.B. Boothroyd, A.L. Greer, Mater. Sci. Technol. 15 (1999) 1115-1123.

[35] K. E. Knipling, D. C. Dunand, D. N. Seidman, Acta Mater. 56 (2008) 114-127.

[36] H.J. McQueen, J.E. Hockett, Met. Trans. 1 (1970) 2997-3004.

[37] J. J. Jonas, D. R. Axelrad, J. L. Uvira, Trans. Japan Inst. Met. 9 (1968) 257-267.

[38] J. Murray, A. Peruzzi, J.P. Abriata, J. Phase Equilibria 13 (1992) 277-291.

[39] N. Saunders, Z. Metallkde, 80 (1989) 894-903.

[40] F.R. Castro-Fernandez, C.M. Sellars, Mat. Sci. Tech. 4 (1988) 621-627.

CHAPTER V

EFFECT OF V ADDITION ON HOT DEFORMATION AND MICROSTRUCTURAL EVOLUTION OF 7150 ALUMINUM ALLOY

Chapter V Effect of V addition on hot deformation and microstructural evolution of 7150 aluminum alloy

Abstract

The hot deformation behavior of 7150 aluminum alloys containing different V contents (0.01 to 0.19 wt%) was studied. The results reveal the peak flow stresses of the 7150 alloy significantly increased when V was added. The alloys containing 0.03-0.05 wt% V displayed higher values of peak flow stress than those with 0.11-0.19 wt% V at low temperatures, whereas they displayed comparable values at higher temperatures. The materials constants and activation energies for hot deformation were determined from the experimental compression data for all alloys studied. The activation energy for hot deformation increased from 229 kJ/mol for the base alloy to approximately 270 kJ/mol for the alloys containing 0.03-0.05 wt% V. With further increases in V contents up to 0.19 wt%, the activation energy returned to approximately 250 kJ/mol. The vanadium-solute diffusion acted as the deformation rate-controlling mechanism for the alloys containing up to 0.05 wt% V, resulting in enhanced work hardening and improved subgrain strengthening effects. The precipitation of $Al_{21}V_2$ dispersoids in the alloys containing 0.11 to 0.19 wt% V promoted the retardation of dynamic recovery and the inhibition of dynamic recrystallization due to their pinning effect on dislocation motion and subgrain rotation.

The content of this chapter has been published as: C. Shi, X.-G. Chen, Effect of vanadium on hot deformation and microstructural evolution of 7150 aluminum alloy, Materials Science and Engineering A, 613 (2014) 91-102.

5.1 Introduction

Al-Zn-Mg-Cu (7xxx) aluminum alloys with a high strength-to-density ratio and excellent mechanical properties have been widely used for aircraft and vehicles [1]. These alloys are generally subjected to thermomechanical processing at elevated temperatures, such as rolling, extrusion and forging. The microstructure evolution during hot deformation can significantly affect the strength and fracture toughness of the materials [2,3]. Recently, a number of studies on the hot deformation behavior and microstructural evolution of 7xxx alloys have been reported [4-6]. Shi et al. [4] proposed a decline ratio map of flow stresses for the 7150 alloy in which the flow stress behavior was correlated with different microstructures and dynamic softening mechanisms. Hu et al. [5] reported that the main deformation mechanism of the 7050 alloy was the grain boundary slip at high Z values and the grain boundary sliding at low Z values. Chen et al. [6] found that dynamic precipitation and coarsening were responsible for the flow softening in the 7085 alloy at low temperatures, whereas dynamic recovery and dynamic recrystallization were the softening mechanisms at high temperatures.

Dynamic recovery (DRV) and dynamic recrystallization (DRX) are the typical softening mechanisms active in aluminum alloys during deformation at elevated temperatures. Previous investigations have demonstrated that the hot deformation behavior of aluminum alloys is significantly affected by alloying elements [2,7-14]. Solute addition can lead to decreasing grain boundary mobility, impeding dislocation movement and accelerating dislocation multiplication [2,7,8]. Cerri et al. [9] observed that the addition of 5.2 wt% Mg

caused the solute drag effect during the hot torsion of the aluminum, leading to the decrease in subgrain size. Sherby et al. [10] found that the diffusion of solute atoms within the subgrain boundary determined the rate-controlling creep process and observed a decreasing creep rate of the pure aluminum after the trace addition of 0.054 wt% Fe. On the other hand, the presence of dispersoids has a strong pinning effect on dislocation motion and migration of grain boundary, as well as stabilizing the substructure [2,11]. McQueen et al. investigated the effect of 0.1 wt% Zr addition on the hot torsion of an Al-Li-Cu-Mg-Zr (8090) alloy and observed dynamic recovery was significantly restricted by the Al_3Zr dispersoids [12]. Li et al. [13] reported that the dynamic precipitation of Al_3Zr and $Al_{20}Cu_2Mn_3$ dispersoids inhibited dynamic recrystallization and increased the activation energy of the Al-Cu-Mg-Mn-Zr alloy. However, dynamic recrystallized grains were observed in the extruded Al-5 wt%Mg-0.8 wt%Mn alloy due to the stimulation of nucleation by Al_6Mn particles [14].

Vanadium is known to maintain high-temperature strength in aluminum alloys by forming thermally stable dispersoids of $Al_{11}V$ [15,16]. The presence of these dispersoids can retard dynamic softening and raise the recrystallization temperature during hot working processes [17]. Previous studies have mainly focused on investigating the precipitation of $Al_{11}V$ dispersoids in aluminum alloys containing V using rapid solidification technique [15,18-21]. Ning and Li [21] studied the age hardening response of a rapid solidified Al-3.9V-0.1Zr alloy, and found that the precipitation of $Al_{11}V$ dispersoids at 450 °C was responsible for the peak age hardening. Kazakova et al. [15] suggested that addition of

vanadium in the Al-Fe alloys caused the precipitation hardening by forming Al_3Fe and $Al_{11}V$ dispersoids during annealing. Recently, Wang et al. [22] reported that the addition of 0.045 wt% V in the 5083 aluminum alloy resulted in a restriction of the growth of recrystallized grains and yielded a refined fibrous structure in the rolling sheet. However, a systematic investigation of the effect of different V contents on the hot deformation behavior of 7xxx aluminum alloys cannot currently be found in the literature. The evolution of the deformed microstructure of 7xxx aluminum alloys after adding various contents of V should be better understood.

In the present study, the hot deformation behavior of homogenized 7150 alloys with different V contents (ranging from 0 to 0.19 wt%) was studied by hot compression tests at various temperatures and strain rates. The constitutive equations correlating the peak flow stress, deformation temperature, strain rate and activation energy were analyzed for these alloys. The microstructural evolution of the alloys during hot deformation was investigated to understand the effect of V addition on the deformation and dynamic softening mechanisms that occur under various deformation conditions.

5.2 Experimental

Experiments were conducted on 7150 alloys (Zr free) with different V contents ranging from 0.01 to 0.19% (all alloy compositions are in wt% unless otherwise indicated). The alloys were designated Alloy-A to Alloy-F based on their V contents, and their chemical compositions are analyzed by an optical emission spectrometer and provided in Table 5.1.

For each V content, approximately 3 kg of material was batched in an electrical resistance furnace and held at 750 °C for 30 min under mechanical stirring, and then cast into a rectangular permanent steel mold measuring 30 x 40 x 80 mm^3 with a cooling rate of approximately ~12 ºC s^{-1} in the liquid state. The cast ingots of these alloys were homogenized at 465 °C for 24 h, followed by water quenching to room temperature. Cylindrical samples measuring 10 mm in diameter and 15 mm in length were machined from the homogenized ingots. Uniaxial compression tests were conducted on a Gleeble 3800 thermomechanical simulation unit at strain rates of 0.001, 0.01, 0.1, 1 and 10 s^{-1} and deformation temperatures of 300, 350, 400 and 450 °C, respectively. During the tests on the Gleeble 3800 unit, the samples were heated to the desirable deformation temperature at a heating rate of 10 °C/s and held for 3 min to ensure a homogeneous temperature distribution throughout the samples. The samples were deformed to a total true strain of 0.8 and then immediately water-quenched to retain the microstructure at the deformation temperature.

The microstructure of the as-homogenized materials was etched by Keller's solution prior to hot deformation. All deformed samples were sectioned parallel to the compression axis along the centerline and then metallographically prepared for electron backscattered diffraction (EBSD) analysis under a scanning electron microscope (SEM, JEOL JSM-6480LV). The step size between the scanning points was set to 1.0 μm for the grain structure of the samples. For the quantitative measurement of the misorientation distribution of boundaries, EBSD line scanning was performed [23,24], and the same sample surface

areas of approximately 2.73 mm^2 with a scanning step size of 1.0 μm were selected for all the alloys under any given deformation condition. In addition, EBSD analysis was performed to measure the subgrain size of the deformed samples using the linear intercept method [23]; a surface area of approximately 0.42 mm^2 with a scanning step size of 0.1 μm was selected. Samples for TEM observation were mechanically ground to a thicknesses of 35-60 μm, followed by electropolishing in a twin-jet polishing unit, which was operated at 15 V and -20 °C using a 30% nitric acid and 70% methanol solution. The samples were observed under a transmission electron microscope (TEM, JEOL JEM-2100) operated at 200 kV. To observe the distribution of V-containing dispersoids, TEM foils of the homogenized sample containing 0.11% V were examined using a field-emission gun SEM (Hitachi SU-70) operated at 10 kV with a working distance of 10 mm in backscattered mode.

Table 5.1 Chemical composition of the alloys studied (wt%).

Alloy	Zn	Mg	Cu	Si	Fe	Ti	V	Al
Alloy-A (base alloy)	6.44	2.47	2.29	0.16	0.15	0.009	0.01	Bal.
Alloy-B (0.03 V)	6.24	2.10	2.17	0.16	0.13	0.008	0.03	Bal.
Alloy-C (0.05 V)	6.21	2.18	2.20	0.16	0.14	0.009	0.05	Bal.
Alloy-D (0.11 V)	6.31	2.30	2.24	0.16	0.14	0.008	0.11	Bal.
Alloy-E (0.15 V)	6.16	2.10	2.15	0.16	0.13	0.008	0.15	Bal.
Alloy-F (0.19 V)	6.25	2.17	2.27	0.16	0.14	0.009	0.19	Bal.

5.3 Results

5.3.1 Effect of V on flow stress behavior

The hot compression tests of the 7150 alloys containing different V contents were conducted at deformation temperatures ranging from 300 to 450 °C and at strain rates

ranging from 0.001 to 10 s^{-1}. Fig. 5.1 presents a series of typical true stress-true strain curves obtained during hot deformation. A peak flow stress was generally exhibited at a certain strain, followed by dynamic flow softening to the end of straining. Significant flow softening beyond the peak stress existed at the highest strain rate of 10 s^{-1}, which was also observed during hot deformation of 7150 alloys containing Zr in our previous studies [4,25]. This was a result of severe adiabatic deformation heating, which considerably increased the deformation temperature during the compression process. Under other deformation conditions, the flow stress curves remained fairly constant or decreased to some extent beyond the peak flow stresses, demonstrating a dynamic equilibrium between work hardening and dynamic softening. It is evident that the level of flow stress and peak flow stress increased with increasing strain rate and decreasing deformation temperature. Moreover, the flow stress and peak flow stress levels increased significantly with the addition of V.

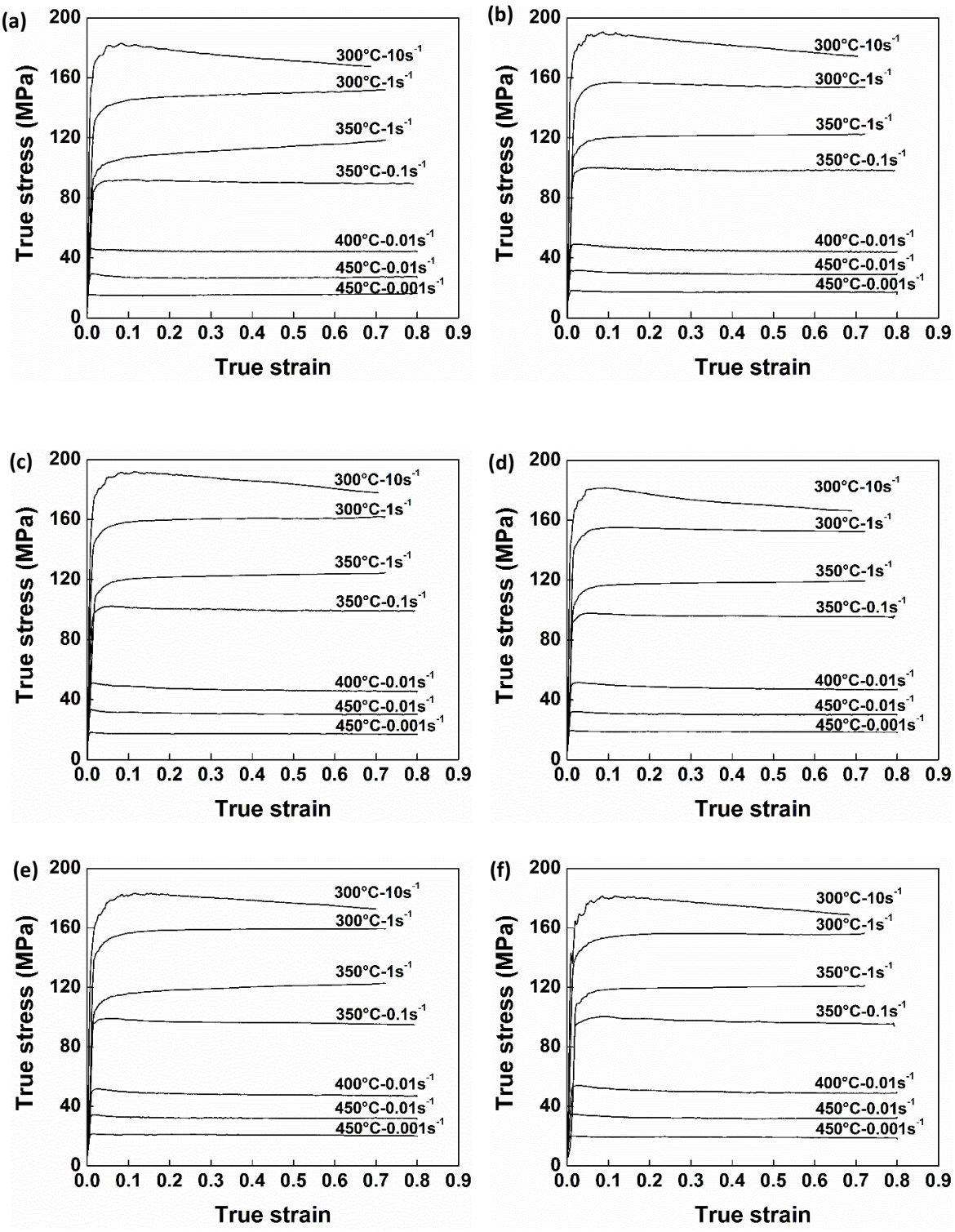

Fig. 5.1 Typical true stress-true strain curves during hot compression deformation: (a) Alloy-A (base alloy); (b) Alloy-B (0.03% V); (c) Alloy-C (0.05% V); (d) Alloy-D (0.11% V); (e) Alloy-E (0.15% V); (f) Alloy-F (0.19% V).

Fig. 5.2 illustrates the evolution of the peak flow stresses of the alloys with different V contents as a function of strain rate at various deformation temperatures. Under a given deformation condition, the peak stress levels of the 7150 alloys increased significantly when V was added. However, the increase of peak stress varied depending on the V content and the deformation condition.

Alloy-B and Alloy-C, containing 0.03 and 0.05% V, displayed dramatic increases of peak stress relative to the base alloy. With increasing V contents to 0.11 and 0.15% (Alloy-D and Alloy-E), an increase of peak stress was also observed. However, with a further increase in V content to 0.19% (Alloy-F), instead of a progressive rise, the values of peak stress slightly decreased compared with those of the alloy with 0.15% V at all deformation conditions.

Moreover, it is of interest to note that at low deformation temperatures (300-350 °C), Alloy-B and Alloy-C (0.03 and 0.05% V) illustrated much higher values of peak stress compared with those observed in Alloy-D and Alloy-E (0.11 and 0.15% V) under the same deformation condition (Fig. 5.2a and b). However, as the deformation temperature increased to 400 and 450 °C, the peak stresses of Alloy-B and Alloy-C demonstrated comparable values with Alloy-D. Alloy-E exhibited even higher peak stresses than those of Alloy-B and Alloy-C during deformation at 400-450°C (Fig. 5.2c and d). For example, when hot deformation was performed at 300 °C and 0.1 s^{-1}, the peak stresses of the alloys with 0.03 and 0.05% V were 144 MPa and 148 MPa, respectively, whereas the alloys containing 0.11 and 0.15% V displayed lower peak stresses of 138 MPa and 141 MPa, respectively. As the

deformation temperature increased to 400 °C at the same strain rate of 0.1 s^{-1}, the peak stresses of the alloys with 0.03% and 0.05% V were 72 MPa and 73 MPa, respectively, whereas, the peak stresses of the alloys containing 0.11 and 0.15% V were 73 MPa and 77 MPa, respectively.

The results indicate that the low V additions from 0.03 to 0.05% could remarkably enhance the deformation resistance, especially at low deformation temperatures of 300-350 °C. Alloying with V from 0.11 to 0.15% generally retarded the dynamic softening and significantly increased the flow stress during deformation at all temperature ranges investigated. Furthermore, when the V addition reached 0.19%, the effect on flow stress became less evident.

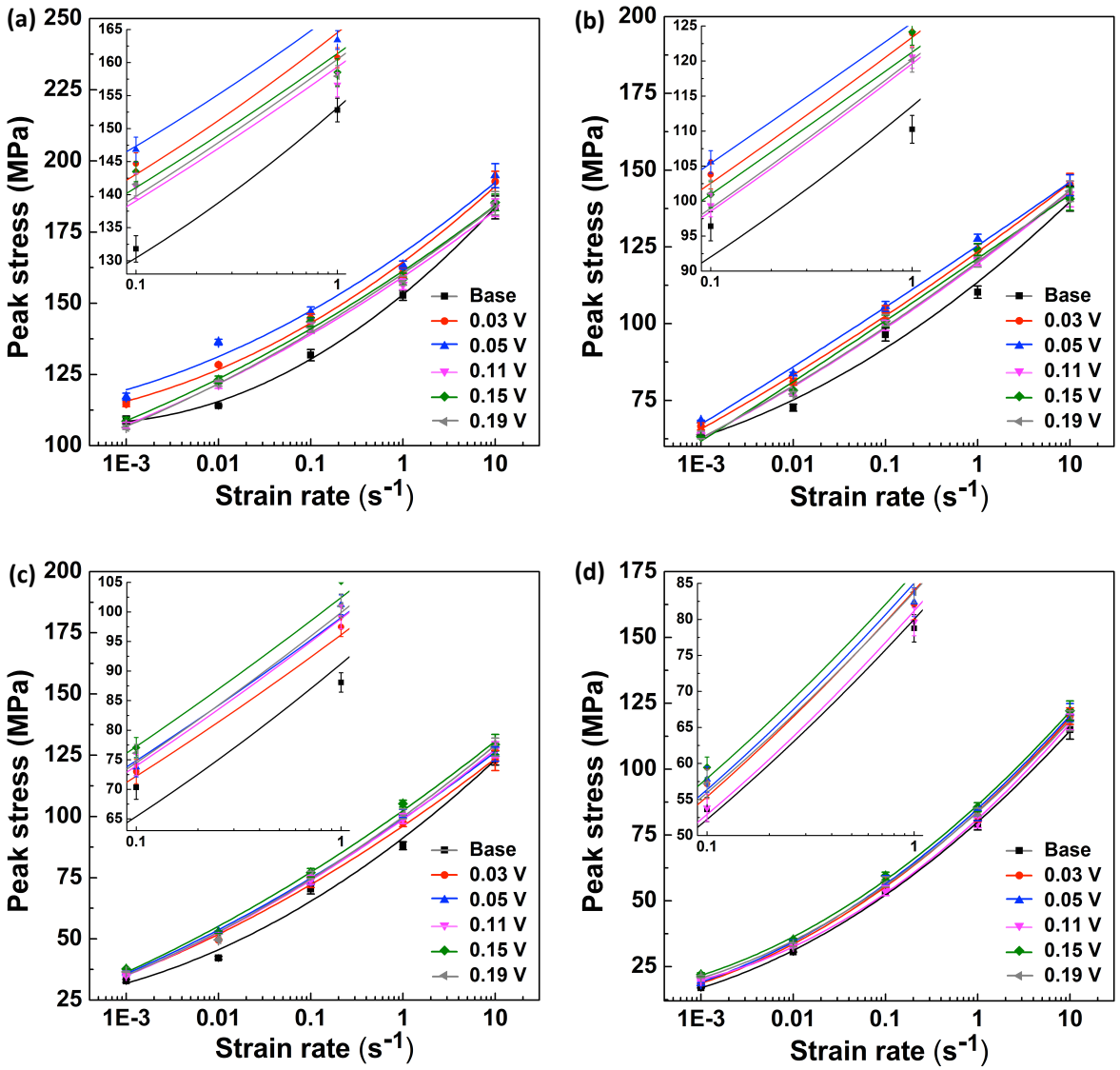

Fig. 5.2 The evolution of peak stresses of alloys A-F during hot deformation at (a) 300 °C; (b) 350 °C; (c) 400 °C; (d) 450 °C.

5.3.2 Constitutive analyses

The hyperbolic-sine equation, which was proposed by Sellars and McTegart [26], is widely employed to describe the relationship between the strain rate, deformation temperature and flow stress, especially over a wide range of stresses [2,26,27],

$$Z = \dot{\varepsilon} \exp(\frac{Q}{RT}) = A[\sinh(\alpha\sigma)]^n \quad (5.1)$$

where Z is the Zener-Hollomon parameter; n and A are material constants; α is the stress multiplier; σ is the flow stress (MPa); Q is the activation energy for hot deformation (kJ/mol); R is the universal gas constant (8.314 J/mol K); T is the deformation temperature (K).

In this study, the experimental data obtained for Alloy-D, which contains 0.11% V, were used as an example to derive the activation energy Q and material constants for all materials studied. The peak flow stress σ_p is used as a proxy for σ, which is generally utilized in aluminum alloys and refers to the dynamic equilibrium between work hardening and dynamic restoration [28,29]. The data obtained at a strain rate of 10 s^{-1} were not taken into account because of the flow instability derived from the significant rise in deformation temperature. The stress multiplier α can be defined as $\alpha = \beta / n_1$ [26], where β and n_1 are evaluated from the mean slopes of the plots of $\ln(\dot{\varepsilon})$ - σ_p and $\ln(\dot{\varepsilon})$ - $\ln(\sigma_p)$, respectively, for the range of temperatures studied. From Fig. 5.3, the values of β and n_1 were calculated, and the value of α for Alloy-D was determined to be 0.011.

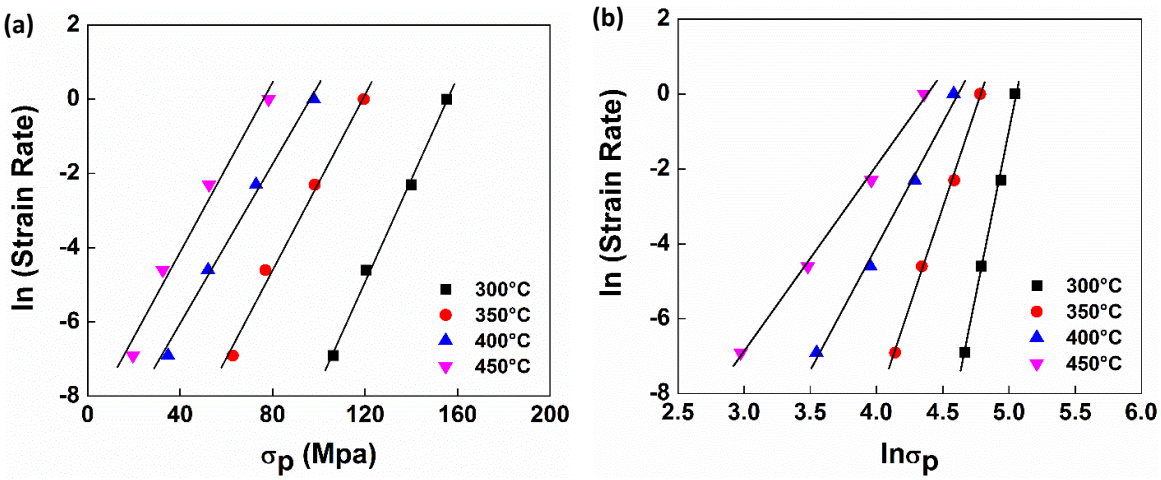

Fig. 5.3 Relationships between (a) $\ln\dot{\varepsilon}$ **and** σ_p **and (b)** $\ln\dot{\varepsilon}$ **and** $\ln\sigma_p$**.**

Differentiating Eq. (5.1) yields the following:

$$Q = R[\frac{\partial \ln\dot{\varepsilon}}{\partial \ln[\sinh(\alpha\sigma_p)]}]_T[\frac{\partial \ln[\sinh(\alpha\sigma_p)]}{\partial(1/T)}]_{\dot{\varepsilon}} = RnS \tag{5.2}$$

where n is the mean slope of plots of $\ln\dot{\varepsilon}$-$\ln[\sinh(\alpha\sigma_p)]$ at different temperatures, and S is the mean slope of plots of $\ln[\sinh(\alpha\sigma_p)]$-$1/T$ at various strain rates. The relationship between $\ln\dot{\varepsilon}$ and $\ln[\sinh(\alpha\sigma_p)]$, which was derived from the measured peak stresses (Fig. 5.2), is shown in Fig. 5.4(a). The mean value of the slopes at four deformation temperatures, n, was then calculated. In addition, the relationship between $\ln[\sinh(\alpha\sigma_p)]$-$1/T$, which was derived from experimental peak stress data (Fig. 5.2), is plotted in Fig. 5.4(b). The mean value of the slopes at different strain rates, S, was obtained. The activation energy Q could then be determined directly from Eq. (5.2).

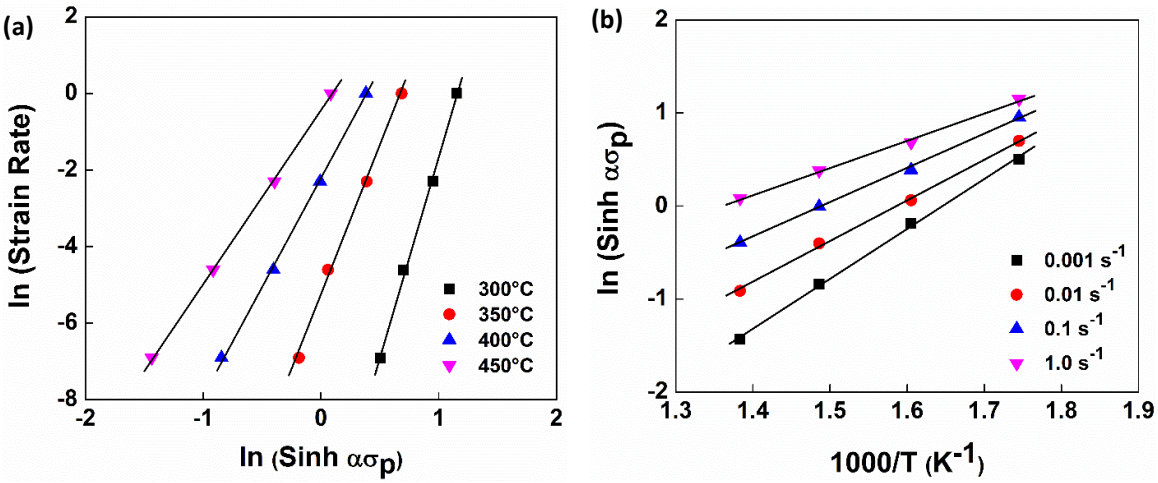

Fig. 5.4 Relationships between (a) $\ln \dot{\varepsilon}$ **and** $\ln[\sinh(\alpha\sigma_p)]$ **and (b)** $\ln[\sinh(\alpha\sigma_p)]$ **and** $1000/T$**.**

Taking the natural logarithm of both sides of Eq. (5.1) yields the following:

$$\ln Z = \ln(A) + n\ln[\sinh(\alpha\sigma_p)] \tag{5.3}$$

where $\ln(A)$ is obtained from the intercept of the plot of $\ln Z$ - $\ln[\sinh(\alpha\sigma_p)]$, as shown in Fig. 5.5. Likewise, the material constants A, n and α and the activation energies Q for all alloys were calculated according to Eqs. (5.1), (5.2) and (5.3). Table 5.2 presents the values of these constants and activation energies corresponding to all alloys studied. As shown, α remains fairly constant, whereas the values of n and A vary with increases in the V content.

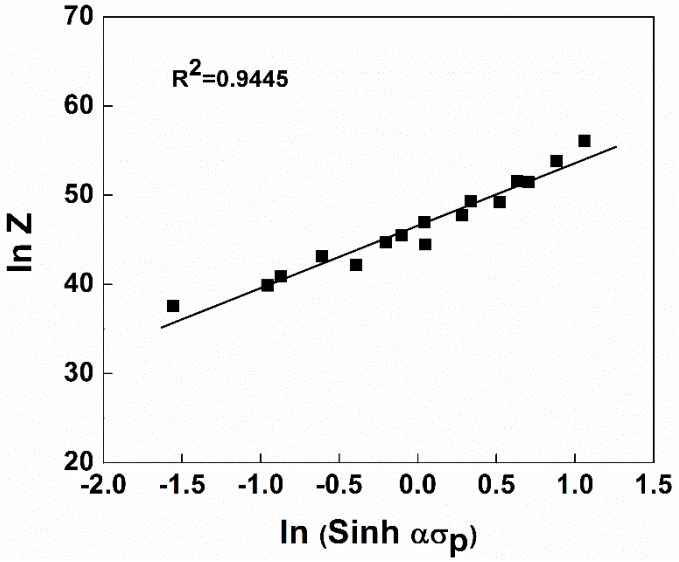

Fig. 5.5 Relationship between $\ln Z$ and $\ln[\sinh(\alpha\sigma_p)]$.

Table 5.2 Values of material constants and activation energies for the alloys studied.

Alloy	α (MPa^{-1})	n	A (s^{-1})	Q (kJ mol^{-1})
Alloy-A (base alloy)	0.012	7.020	1.01×10^{17}	229.4
Alloy-B (0.03 V)	0.011	7.762	1.79×10^{20}	270.6
Alloy-C (0.05 V)	0.011	7.764	2.35×10^{20}	272.7
Alloy-D (0.11 V)	0.011	7.113	6.15×10^{17}	242.0
Alloy-E (0.15 V)	0.012	7.301	5.26×10^{18}	254.9
Alloy-F (0.19 V)	0.011	7.212	2.68×10^{18}	248.3

Fig. 5.6 presents a plot of the variation in the hot deformation activation energy, Q, as a function of the V content. The activation energy of 229 kJ/mol obtained for the base alloy is in general agreement with the values reported for similar alloys, such as the 7050 and 7075 alloys [5,30]. However, it is much higher than that of pure aluminum (142 kJ/mol) [31]. This difference is attributed to the solute drag effect of Zn, Mg and Cu dissolved in the 7xxx aluminum matrix on the dislocation glide, resulting in increased deformation resistance [9,32]. The solute drag effect is suggested to be comparable for all the alloys studied, due to

the little variations in Zn, Mg and Cu contents as shown in Table 5.1. Moreover, Alloy-B and C, containing 0.03 and 0.05% V, exhibited distinct increases in activation energy, reaching approximately 270 kJ/mol. With the increase of the V content from 0.11 to 0.19%, the Q returned to the level of approximately 250 kJ/mol, which displayed higher values compared with that of the base alloy but lower values than those of the alloys with 0.03 and 0.05% V. In addition, the Q value displayed an increasing tendency when the V content increased from 0.11 to 0.15% and then decreased slightly after the V content reached 0.19%. The results suggest that the addition of V can significantly increase the deformation resistance of the 7150 aluminum alloy during the hot working process. However, various V contents played different roles in the hot deformation, which will be discussed in the following sections.

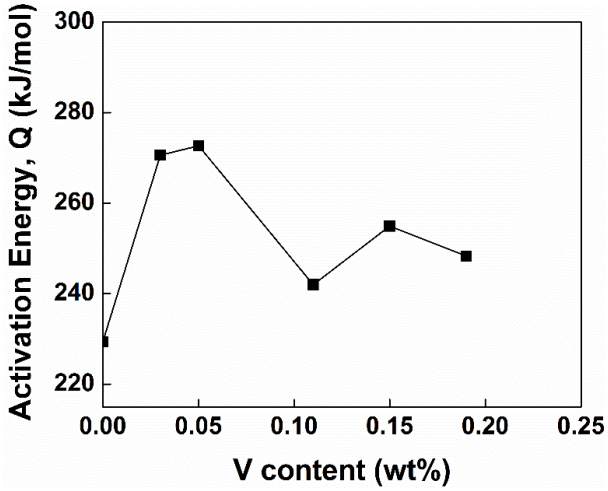

Fig. 5.6 The activation energy for hot deformation of 7150 alloys, Q, as a function of the V content.

5.3.3 Effect of V on microstructural evolution

5.3.3.1 Initial microstructures

To investigate the microstructural evolution of the alloys with different V contents, Alloy-A (base), Alloy-C (0.05% V), Alloy-D (0.11% V), Alloy-E (0.15% V) and Alloy-F (0.19% V) were selected for further study. Fig. 5.7 shows optical micrographs of these alloys after the homogenization treatment. The homogenized structures of all five alloys are characterized by uniform equiaxed grains originated from casting. The average grain size of the base alloy is 127 μm. The V addition appears to slightly coarsen the grain structure. The average grain sizes are approximately 157, 152, 133 and 131 μm for Alloy-C, D, E and F, respectively. After the homogenization, some intermetallic phases, including $Al_6(FeCu)$, Mg_2Si and Al_2CuMg, were only partially dissolved and retained in the interdendritic regions, which is consistent with our previous study [4]. EDX results indicate that the chemical compositions of these intermetallic phases were not effected by the alloying with V, while image analysis results suggest similar volume fractions of those phases for all the alloys studied. Up to a V addition of 0.15%, the base alloy and V-containing alloys have similar microstructures. However, when the V content reached 0.19% (Alloy-F), coarse primary V-bearing intermetallic particles with needle-like or block-like morphologies appeared and were randomly distributed in the matrix (see the arrows in Fig. 5.7e). After homogenization, those primary intermetallic particles were undissolved and remained in the matrix. Based on Al-V binary phase diagram, the precipitation of primary V-bearing intermetallic particles in

the alloy with 0.19% V occurs and the peritectic reaction has insufficient time to complete the transformation of those primary particles into the Al solid solution. Therefore, the primary V-bearing particles remained in the microstructure.

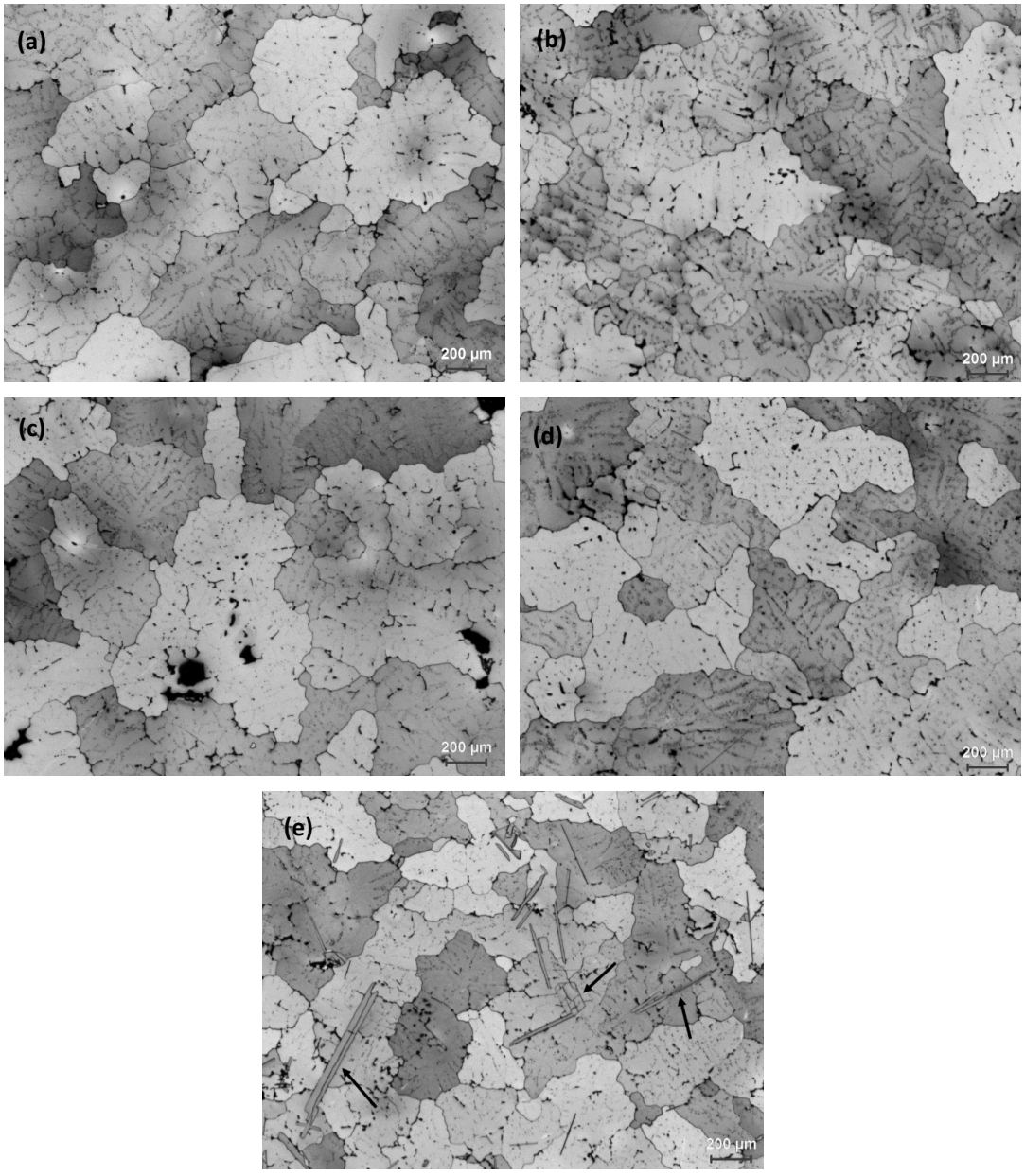

Fig. 5.7 Optical micrographs showing the grain structures after homogenization: (a) Alloy-A (base alloy); (b) Alloy-C (0.05% V); (c) Alloy-D (0.11% V); (d) Alloy-E (0.15% V); (e) Alloy-F (0.19% V).

After homogenization at 465 °C for 24 h, the precipitation of V-containing dispersoids was clearly observed in the alloys with V contents ranging from 0.11 to 0.19%. These dispersoids were identified as a $Al_{21}V_2$-type phase by TEM selected area electron diffraction [33,34], and these dispersoids are often designated as $Al_{11}V$ dispersoids in the literature [15,18-21]. Both $Al_{21}V_2$ and $Al_{11}V$ have the same face-centered cubic structure in the same space group of $Fd\bar{3}m$, and exhibit very close lattice parameters of 1.4492 and 1.4568 nm respectively. Fig. 5.8 gives an example of Alloy-D and Alloy-E containing 0.11 and 0.15% V, respectively. The STEM micrographs show that a large number of spheroidal $Al_{21}V_2$ dispersoids were precipitated in the aluminum matrix (Fig. 5.8a and b), with average sizes of 51 and 52 nm for Alloy-D and Alloy-E, respectively. These dispersoids were distributed homogeneously in the centers of dendrites, whereas precipitate-free zones were observed in the interdendritic regions and near grain boundaries. To reveal the distribution of V-containing dispersoids in the dendrite structure, the TEM foils of Alloy-D were examined under a field-emission gun SEM. Because of a relatively low V concentration in the dispersoids, the contrast of $Al_{21}V_2$ dispersoids was rather poorer than the similar Al_3Zr dispersoids in 7xxx alloys [25]. By careful analysis of FE-SEM images, the distribution feature of $Al_{21}V_2$ dispersoids across the intersection of dendrites can be outlined (Fig. 5.8c). As a consequence of the peritectic reaction during solidification [34], vanadium tended to be enriched in the dendrite centers, which resulted in a high degree of supersaturation at the as-cast condition and allowed the precipitation of a large number of $Al_{21}V_2$ dispersoids in the dendritic cores during homogenization. Conversely, the matrix toward the edge of the

dendrites and the area adjacent to the grain boundaries were depleted in V, leading to precipitate-free zones. These results are consistent with the observations reported in other similar peritectic systems, such as the precipitation of Al_3Zr dispersoids in the Al-Zr alloy [35,36]. However, when 0.19% V was added to the alloy, the distribution of $Al_{21}V_2$ dispersoids became more heterogeneous even at the macro scale, and the precipitate-free zones were often observed in the dendrite centers. The formation of coarse primary intermetallic particles largely consumed the V atoms and led to a depletion of V concentration in the vicinity of those particles. Therefore, the precipitate-free zones were not only observed in the interdendritic regions but also in the dendrite centers near the primary intermetallic particles. In the samples with low V contents (0.03 and 0.05%), almost no $Al_{21}V_2$ dispersoids could be found, indicating that the added V mainly existed as the solute atoms in the aluminum matrix. In the samples with low V contents (0.03 and 0.05%), almost no $Al_{21}V_2$ dispersoids could be found, indicating that the added V mainly existed as the solute atoms in the aluminum matrix. The influences of the $Al_{21}V_2$ dispersoids and the V solute atoms on hot deformation will be discussed later.

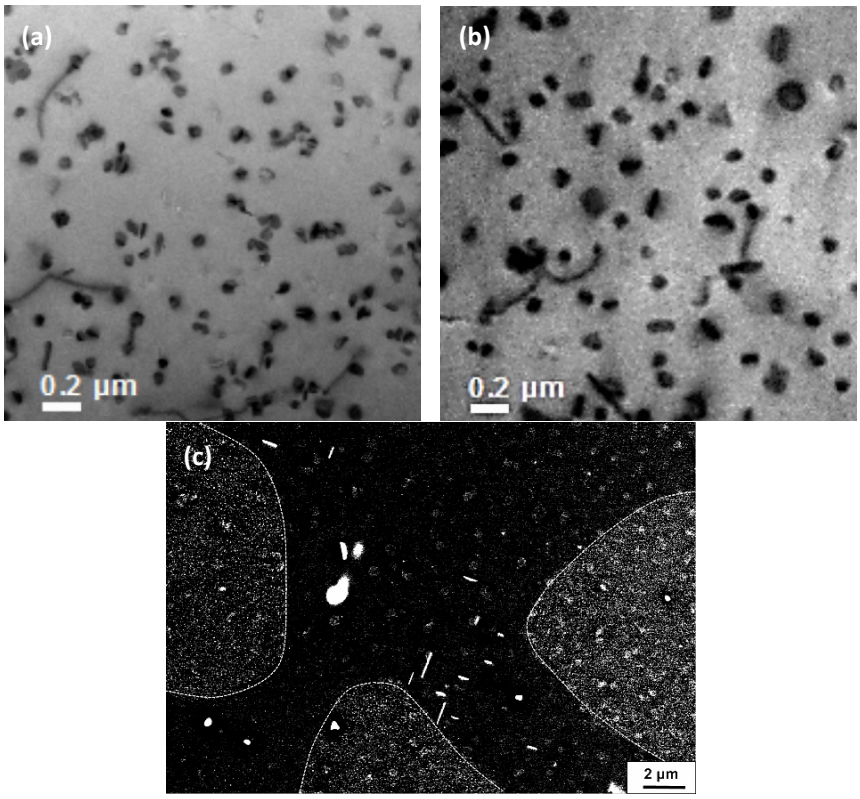

Fig. 5.8 STEM and FE-SEM micrographs showing the precipitation of $Al_{21}V_2$ dispersoids after homogenization at 465 °C for 24 h in (a) Alloy-D (0.11% V); (b) Alloy-E (0.15% V); (c) FE-SEM image across an intersection of dendrites in Alloy-D.

5.3.3.2 Hot deformed microstructures

Fig. 5.9 shows orientation imaging maps of the deformed samples of Alloys A, C, D and E generated under different deformation conditions using the EBSD technique. In orientation imaging maps, the misorientation angles of both grains and subgrains can be distinguished as follows: white lines: 1-5°; red lines: 5-15°; thin black lines: 15-30° and thick black lines: (>30°). In addition, in an attempt to gain more insight into microstructural evolution, the misorientation angle distributions of boundaries for these alloys were measured at the same deformation conditions as those in the orientation imaging maps, and the results are

illustrated in Fig. 5.10.

Under the deformation condition at 350 °C and 0.1 s^{-1}, large numbers of low-angle boundaries of 1-5° were mainly observed inside the elongated grains of the four alloys, indicating high densities of dislocation cells and subgrains (Fig. 5.9a, d, g and j). The deformed samples of the four alloys were all characterized by recovered structures, whereas the level of the dynamic recovery varied with the V contents. Compared to Alloy-A (base), Fig. 5.10a shows that the alloys containing V present a decrease in the fraction of boundaries between 5° and 15°, which is associated with the increase in the fraction of low-angle boundaries (1-5°). This implies a reduced level of dynamic recovery after the V addition [2,37]. Furthermore, the addition of 0.05% V resulted in the highest increase in the fraction of low-angle boundaries (1-5°) among the three V-containing alloys (Fig. 5.10a), which suggests a strong restriction on dynamic recovery.

With the increasing deformation temperature and the decreasing strain rate, the evolution of substructures in all four alloys exhibited a similar tendency: the serration of original grain boundaries was frequently observed. The substructures became better organized, and larger subgrains were formed with neatly arranged boundaries between 1° and 15° (Fig. 5.9), which corresponds to increasing fractions of medium-angle boundaries (5-15°) and decreases in low-angle ones (1-5°) (Fig. 5.10b and c). This suggests an increasing level of dynamic recovery as the temperature increased and the strain rate decreased [2,37]. As the deformation temperature increased to 450 °C at 0.1 s^{-1}, in addition to the development of a

recovered structure, small equiaxed grains with high-angle boundaries (>15°) that contained substructures were observed along the bulged grain boundaries in the base alloy and Alloy-C (0.05% V) (see the arrows in Fig. 5.9b and e). Thus, partially dynamic recrystallization occurred during the deformation, which was characterized by a significant increase in the fraction of high-angle boundaries compared with those deformed at 350 °C and 0.1 s^{-1} (Fig. 5.10a and b). However, only dynamically recovered microstructures were observed in the alloys containing 0.11% and 0.15% V (Fig. 5.9h and k), which is consistent with the low level of high-angle boundaries shown in Fig. 5.10b. It is evident that the addition of higher V levels (0.11% and 0.15%) could inhibit the dynamic recrystallization.

Furthermore, with a lower strain rate of 0.01 s^{-1} at 450 °C, an increased amount of dynamically recrystallized grains were observed in Alloy-A and Alloy-C compared with those formed at 450 °C and 0.1 s^{-1} (see the arrows in Fig. 5.9c and f). This is due to the longer time for the growth of those recrystallized grains as the strain rate decreased. Moreover, it was observed that a larger size of recrystallized grains and a higher fraction of high-angle boundaries were presented in Alloy-C than those in the base alloy (Fig. 5.9f and 5.10c). This indicates an improved degree of dynamic recrystallization with the 0.05% V addition. On the other hand, the deformed samples of Alloy-D and Alloy-E still exhibited solely dynamically recovered microstructures (Fig. 5.9i and l) with much lower levels of high-angle boundaries (Fig. 5.10c).

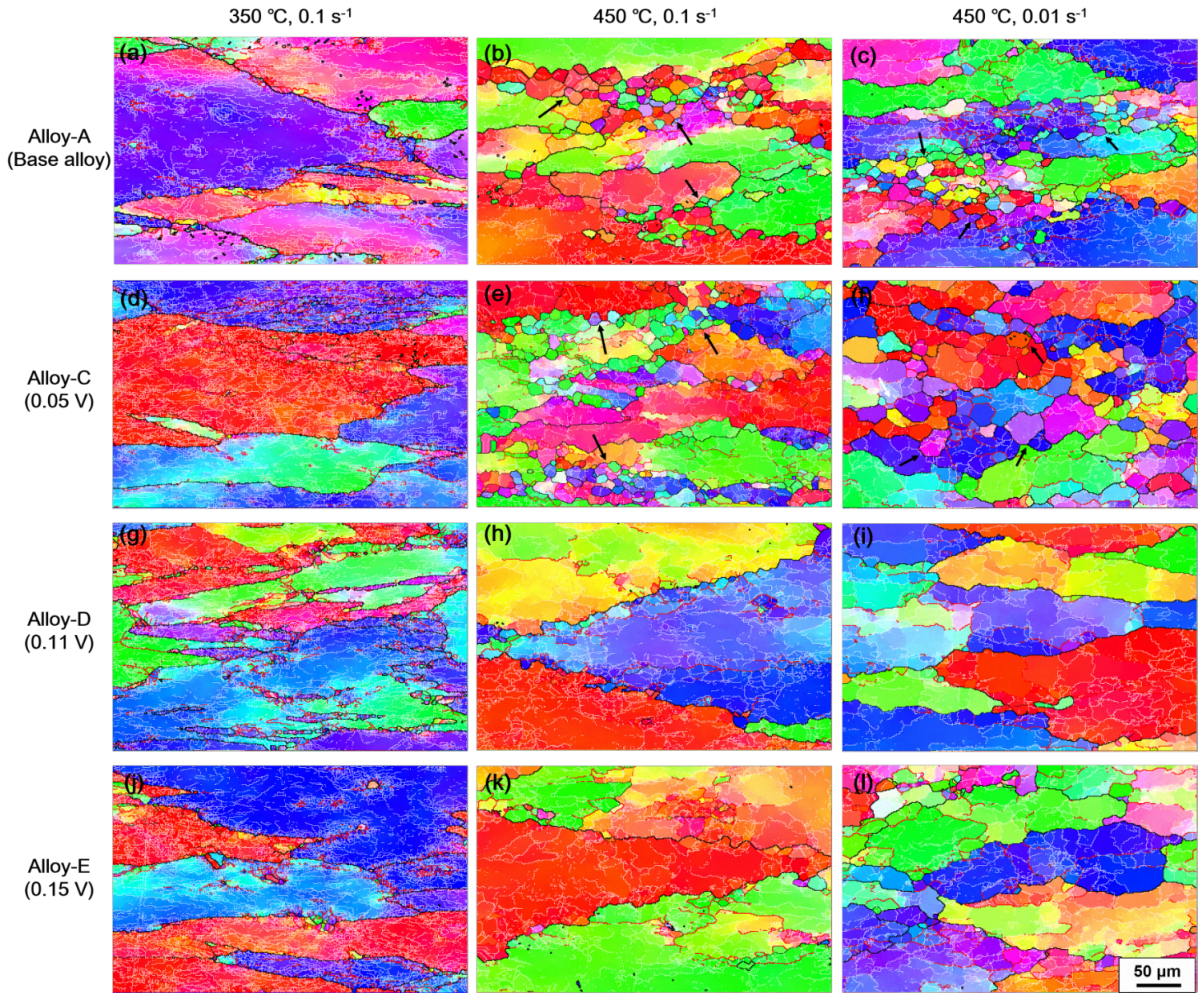

Fig. 5.9 Orientation imaging maps of Alloy-A (base alloy), Alloy-C (0.05% V), Alloy-D (0.11% V) and Alloy-E (0.15% V) under different deformation conditions.

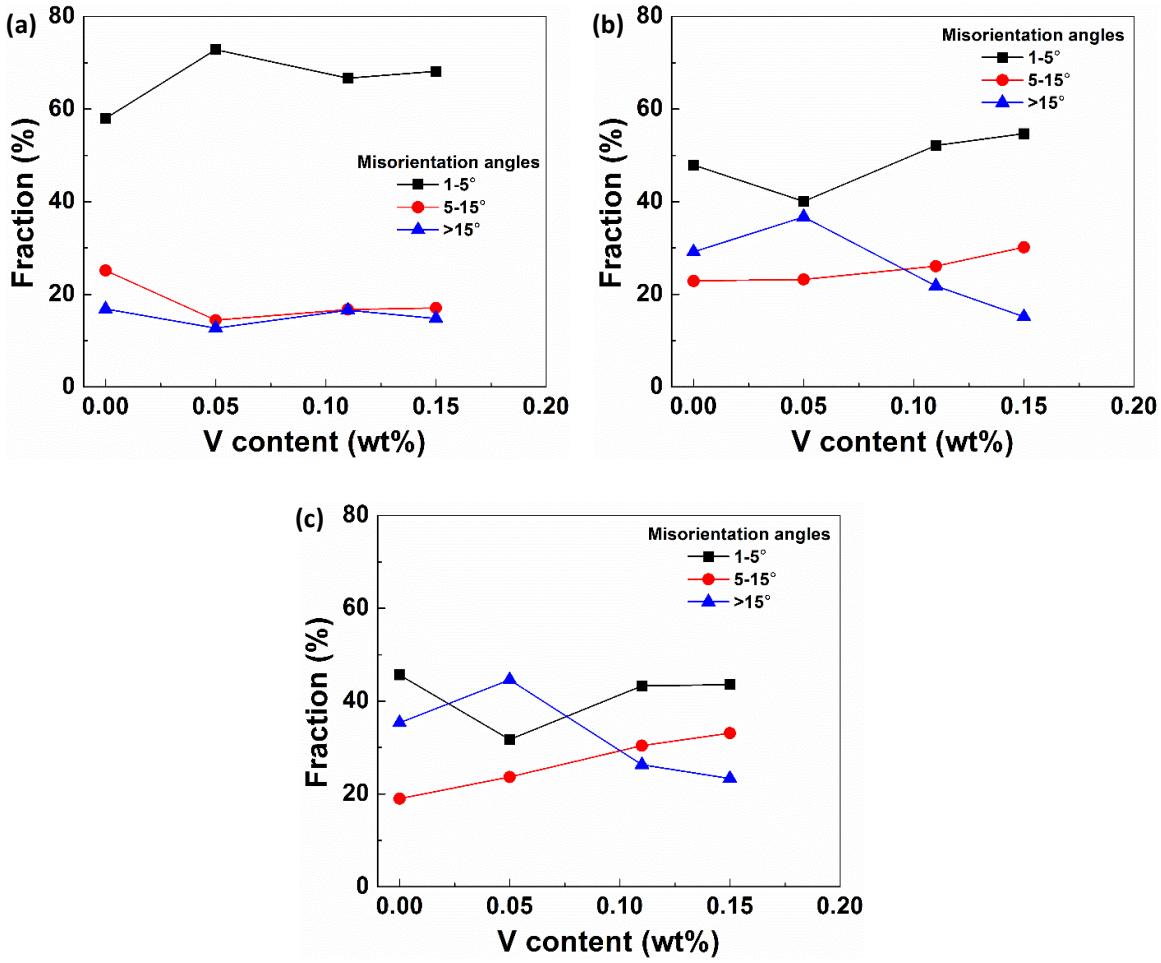

Fig. 5.10 Evolution of misorientation angle distribution of boundaries as a function of V content under different deformation conditions: (a) 350 °C and 0.1 s^{-1}; (b) 450 °C and 0.1 s^{-1} and (c) 450 °C and 0.01 s^{-1}.

5.3.3.3 Quantitative characterization of substructures

To further investigate the effects of deformation temperature, strain rate and V addition on dynamic softening, the mean misorientation angles of boundaries as well as subgrain sizes under different deformation conditions were quantitatively analyzed for the deformed samples of Alloys A, C, D and E using the EBSD technique. As the temperature increased from 350 to 450 °C, and the strain rate decreased from 0.1 to 0.01 s^{-1}, the mean

misorientation angles of boundaries were continuously increased in the four alloys (Fig. 5.11). This result implies an increased level of dynamic restoration with increasing temperature and decreasing strain rate [37], which is consistent with the microstructural observations shown in Fig. 5.9.

For the higher V levels (0.11 and 0.15%), the mean misorientation angles were consistently lower than that of the base alloy at any given deformation condition, indicating a retardation of dynamic recovery and the inhibition of dynamic recrystallization. On the other hand, at a low V level (Alloy-C with 0.05% V), the mean misorientation angle was remarkably reduced and displayed the lowest value among four alloys at a low temperature (350°C). However, as the temperature increased to 450 °C, the mean misorientation angles of Alloy-C sharply increased at both strain rates of 0.1 and 0.01 s^{-1} and displayed even higher values than those of the base alloy at the same deformation conditions. This is a result of a higher level of dynamic recrystallization in Alloy-C relative to the base alloy, as observed in Fig. 5.9.

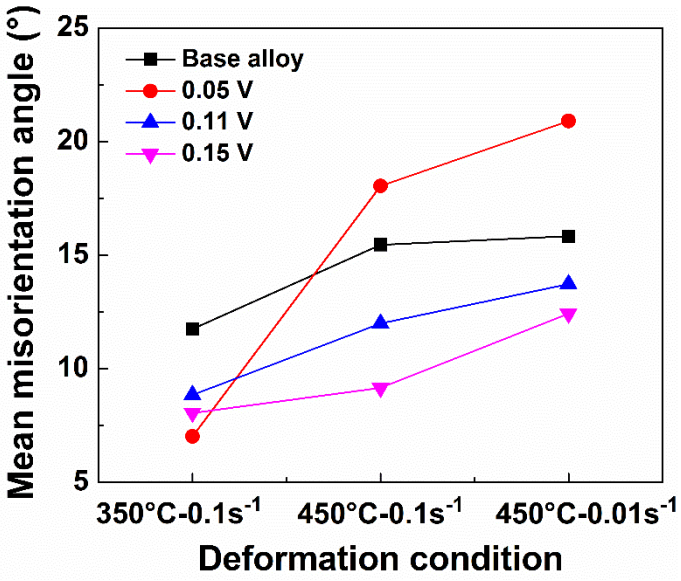

Fig. 5.11 Evolution of mean misorientation angles of boundaries in Alloy-A (base alloy), Alloy-C (0.05% V), Alloy-D (0.11% V) and Alloy-E (0.15% V) under different deformation conditions.

Fig. 5.12a shows the changes in subgrain sizes with deformation conditions in four alloys. The average subgrain sizes of all of those alloys increased with increasing temperature and decreasing strain rate. Under a given deformation condition, the subgrain size was reduced when V was added (Fig. 5.12a). When the deformation was performed at 350 °C and 0.1 s^{-1}, Alloy-C (0.05% V) exhibited the smallest subgrain sizes among four alloys, indicating a significant restriction of dynamic recovery [2,37]. However, as the temperature increased to 450 °C at both strain rates of 0.1 and 0.01 s^{-1}, the subgrain sizes of Alloy-C became larger than those of Alloy-E (0.15% V), which suggests a higher rate of subgrain coalescence in Alloy-C at higher deformation temperatures.

The relationship between the steady-state flow stress at a true strain of 0.8, σ_s, with the subgrain size, d, in Alloys A, C, D and E, is shown in Fig. 5.12b. It is evident that the

steady-state flow stress increased with decreasing subgrain size, and a good linear relationship between the flow stress and reciprocal subgrain size was established, as described by Eq. (5.4):

$$\sigma_s = 317.81d^{-1} - 37.98 \quad (5.4)$$

This relationship agrees well with that reported for aluminum alloys under hot compression, torsion and extrusion [12,25,38,39]. It is believed that the deformation conditions (temperature and strain rate) define the steady-state subgrain size, which, in turn, determines the flow stress [2]. When adding V, the level of dynamic recovery was considerably reduced, leading to a finer subgrain structure (Fig. 5.12a). Hence, the flow stress was higher compared with that of the base alloy under the same deformation conditions.

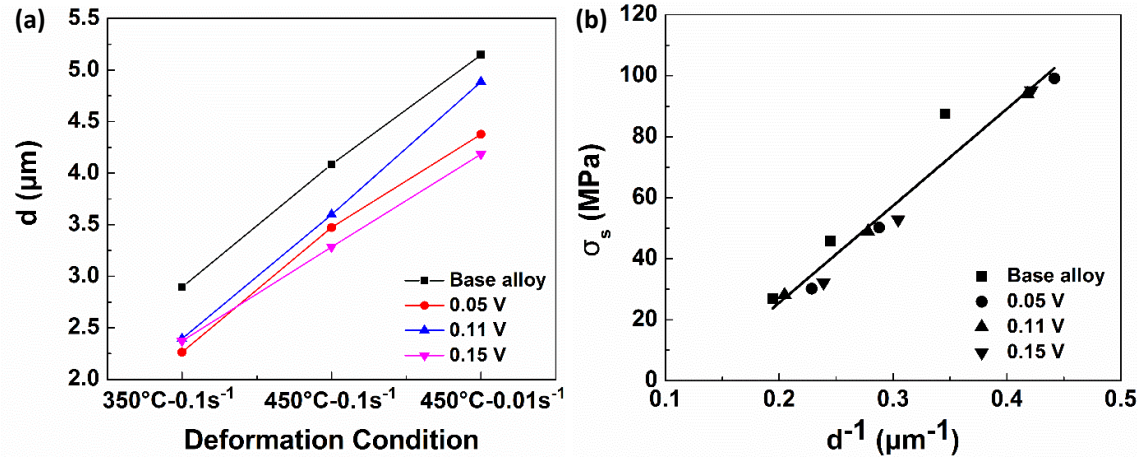

Fig. 5.12 (a) Evolution of subgrain diameters under different deformation conditions and (b) relationship between steady-state flow stress and reciprocal subgrain size for Alloy-A (base alloy), Alloy-C (0.05% V), Alloy-D (0.11% V) and Alloy-E (0.15% V).

5.4 Discussion

The hot deformation behavior of 7150 aluminum alloys with a systematic variation in V contents was studied. When alloyed with low V levels (0.03-0.05%), the alloys had almost no precipitation of $Al_{21}V_2$ dispersoids, and the V existed as solute atoms in the aluminum matrix. With the increase of V content from 0.11 to 0.15%, the precipitation of $Al_{21}V_2$ dispersoids became predominant (Fig. 5.8), and the amount of $Al_{21}V_2$ dispersoids increased as the V content increased. However, when the V content reached 0.19%, large primary V-bearing intermetallic particles appeared in the microstructure, and the amount of the $Al_{21}V_2$ dispersoids could not increase, with their distribution becoming more heterogeneous. In addition, the presence of those large intermetallic particles is also known to promote recrystallization and reduce the strength and fracture toughness of the material [40,41].

5.4.1 Effect of the V solute atoms

When the materials were alloyed with low V levels (0.03-0.05%), significant increases in peak flow stress and activation energy were observed (Figs. 5.2 and 5.6). The results might be attributed to the vanadium-solute-diffusion-controlled hot deformation proposed in a dislocation climb model by Sherby et al. [10,42]. The vanadium solutes could segregate at subgrain boundaries during hot deformation to lower the energy of dislocation. In the initial stage, the pile-up of dislocations at a subgrain boundary occurs under the applied shear stress. Then, the opposing stress fields from subgrain boundaries and from piled-up dislocations during deformation are cyclically relaxed through the vanadium solute diffusion. Thereby,

the lead dislocation from the pile-up is allowed to glide or climb, and then deformation of the material occurs [10,42].

Fig. 5.13 shows that the diffusivity of vanadium in aluminum is much lower than the aluminum self-diffusion at a given temperature [43]. Due to a very low diffusion rate of vanadium solutes, the pile-up dislocations were strongly pinned at the subgrain boundaries [10,42]. This resulted in a high multiplication rate of dislocations (Fig. 5.9), which acted as barriers to further dislocation movement, leading to an enhanced work hardening effect. In addition, the dynamic recovery, which involved rearrangement and annihilation of dislocations, was restrained, developing a finer subgrain structure, as observed in Fig. 5.12a. The fine substructure was stabilized by the solutes of vanadium, which acted as effective barriers to dislocation motion [8,10,42]. Therefore, low diffusivity of vanadium, enhanced work hardening and increased subgrain strengthening led to the significant increases of the flow stress during the hot deformation process.

It should be mentioned that during the deformation at a high temperature of 450 °C, an increased level of dynamic recrystallization was observed in the alloy with 0.05% V compared to the base alloy (Fig. 5.9 and 5.10). Due to the higher multiplication rate of dislocations and the restrained dynamic recovery with vanadium solutes, the driving force for dynamic recrystallization is increased [2,37], whereas the drag effect of solute atoms on mobility of high-angle boundaries becomes limited because of the higher diffusion rate of solutes at high temperature [7,9]. Thus, dynamic recrystallization steadily occurred by

bulging of grain boundaries and caused a higher degree of recrystallized structure. However, the experimental results suggest that the increased level of dynamic recrystallization in Alloy-C (0.05% V) could not completely offset the raised strengthening effects induced by the vanadium solutes at higher temperatures and resulted in an increase in flow stresses during hot deformation even at higher temperatures compared to the base alloy. Furthermore, Alloy-B and Alloy-C (0.03 and 0.05% V) displayed similar activation energy values for hot deformation, 271 kJ/mol and 273 kJ/mol, respectively, which are close to the activation energy for vanadium solute diffusion in aluminum of 303 kJ/mol [16,43]. This finding implies that the hot deformation process involved the vanadium solute diffusion, which acted as the deformation rate-controlling mechanism [10,42]. Similar results were reported during the high temperature creep of aluminum alloys containing dilute solutes, such as 0.054% Fe, 1.0% Mn and 0.068% Cu [10,42,44].

In our previous study [25], no remarkable change in the peak flow stress and activation energy was observed between the 7150 base alloy and an alloy containing 0.04% Zr in which the Zr mainly existed as a solute in the aluminum matrix. The activation energy for zirconium solute diffusion in aluminum is 242 kJ/mol [16,43], whereas the 7150 base alloy exhibits an activation energy for hot deformation of 229 kJ/mol, indicating a similar energy barrier to dislocation motion for the base alloy and the alloy containing 0.04% Zr. Therefore, the similar deformation resistance leads to the comparable values of peak flow stress and activation energy for hot deformation between the base alloy and the alloy with 0.04% Zr.

Moreover, the zirconium solute has a lower diffusion activation energy and higher diffusivity than does the vanadium solute in aluminum (Fig. 5.13), resulting in a weaker solute strengthening and a reduced flow stress relative to the alloys containing V in solution.

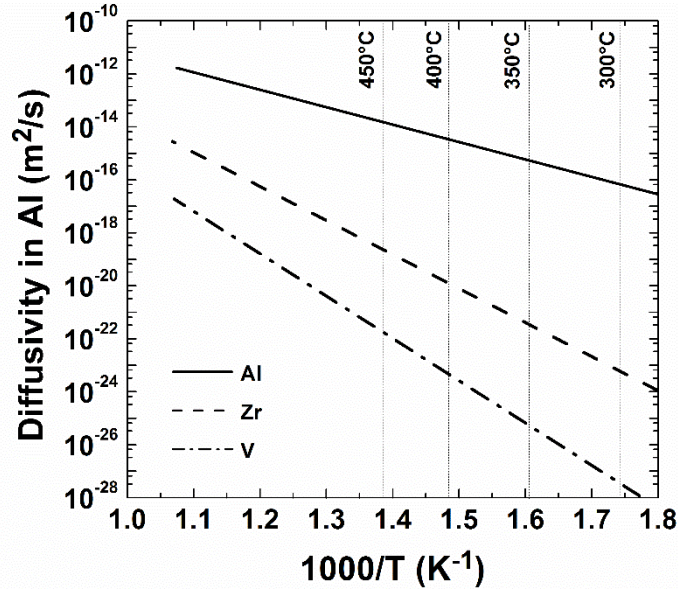

Fig. 5.13 The diffusivity of aluminum, zirconium and vanadium in aluminum as a function of the reciprocal temperature [43].

5.4.2 Effect of the V-containing dispersoids

With a further increase of V contents from 0.11 to 0.19%, the peak flow stress and activation energy increased considerably compared with those of the base alloy (Figs. 5.2 and 5.6). The addition of V resulted in the precipitation of a large number of $Al_{21}V_2$ dispersoids during homogenization, which promoted the retardation of dynamic recovery and the inhibition of dynamic recrystallization during hot deformation processes (Figs. 5.9 and 5.10). Fig. 5.14 shows the interaction of $Al_{21}V_2$ dispersoids with deformed substructures as exemplified in Alloy-D (0.11% V) under the deformation condition at 450 °C and 0.01 s^{-1}.

Fig. 5.14a reveals the edge dislocations bowing at the points where they encountered the dispersoids, indicating a strong pinning effect of dispersoids upon dislocation slip. Moreover, it was observed that the low-angle subgrain boundaries were strongly pinned by those dispersoids (Fig. 5.14b), and the ability for subgrain rotation to lead to coalescence was thus reduced [2,12,37]. Hence, dynamic recovery in the alloy containing 0.11% V was restrained because of the pinning effect of the dispersoids on dislocation motion and subgrain rotation. When a higher V content of 0.15% was added, the increased amount of $Al_{21}V_2$ dispersoids generated a stronger pinning effect on substructures and resulted in a further decrease both in the mean misorientation angle and subgrain size (Figs. 5.11 and 5.12), leading to a decrease in the dynamic recovery and an increase in the peak flow stress and activation energy. Conversely, when alloyed with 0.19% V, the peak flow stress and activation energy exhibited a decreasing trend, most likely attributed to the heterogeneous distribution of the dispersoids caused by the formation of coarse primary V-bearing intermetallic particles.

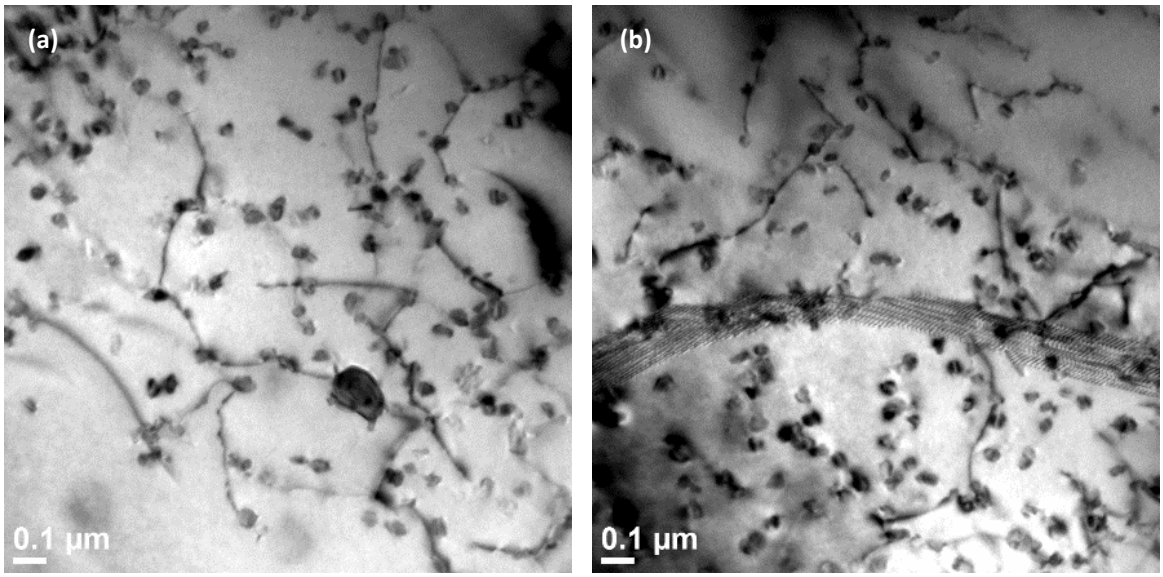

Fig. 5.14 Bright-field TEM images (with the g=(200) reflection at [011]α) of Alloy-D deformed at 450 °C and 0.01 s^{-1} showing the interaction of $Al_{21}V_2$ dispersoids with (a) dislocations and (b) subgrain boundaries.

It is interesting to notice that the 7150 alloys containing 0.11-0.19% V, and the alloys containing 0.12-0.19% Zr [25] displayed almost the same values of activation energy for hot deformation, being 242-255 kJ/mol and 247-255 kJ/mol, respectively. The alloys containing the same range of V and Zr levels exhibited the similar size and amount of $Al_{21}V_2$ and Al_3Zr dispersoids that resulted in strong pinning effects on the substructures during the hot deformation, leading to the equivalent increases in the hot deformation activation energy relative to that of the base alloy.

It is worth noting that under the deformation conditions at low temperatures of 300-350 °C and at a given strain rate, the alloys containing V in solution (0.03-0.05% V) demonstrated higher peak stresses compared with those of the alloys containing $Al_{21}V_2$ dispersoids (0.11-0.19% V), as shown in Fig. 5.2, indicating a stronger solute strengthening.

Similar results were observed by Sherby et al. [10] during the creep process of Al-Fe alloys at 200-250 °C, where the Al-0.04% Fe alloy exhibited a higher creep strength than the Al-0.45% Fe alloy containing Al_3Fe dispersoids. Conversely, when the deformation was performed at higher temperatures (400-450 °C), the peak stresses of the alloys containing V in solution displayed comparable values to those alloys containing dispersoids, which suggests a decreased strengthening effect by the solutes as the temperature increased. At higher temperatures, the diffusion rate of vanadium in the aluminum matrix increased significantly, as illustrated in Fig. 5.13, which could reduce the pinning ability on the dislocation slip and increase the dynamic recovery. In addition, a partial dynamic recrystallization occurred at higher deformation temperature (450 °C), and the dislocation density was thus considerably reduced to facilitate further dislocation motion.

Furthermore, higher values of activation energy for the alloys containing 0.03-0.05% V were observed relative to the alloys with 0.11-0.19% V (Fig. 5.6). It should be mentioned that the activation energy for hot deformation calculated from Eq. (2) is an average value at all temperatures studied. Our previous study [27] demonstrated that the hot deformation activation energy decreases remarkably with increasing temperature at a given strain rate. For example, the activation energy for hot deformation of the 7150 base alloy reached 500 kJ/mol under the condition of 300 °C and 0.001 s^{-1} and decreased to 206 kJ/mol under the condition of 450 °C and 0.001 s^{-1}. The activation energies at lower temperatures contribute a much larger portion to the average value of the activation energy than at higher temperatures.

For a given strain rate, the higher peak stress levels in the alloys containing 0.03-0.05% V involved in a significant rise of hot deformation activation energy at low temperatures compared to the alloys with 0.11-0.19% V, whereas at high temperatures, the former alloys had comparable values of hot deformation activation energy with the latter alloys. Therefore, higher average activation energy values are observed for the alloys containing 0.03-0.05% V compared with the alloys with 0.11-0.19% V (Table 5.2 and Fig. 5.6).

5.5 Conclusions

1. The hot deformation behavior of 7150 aluminum alloys (Zr free) containing different V levels (0 to 0.19 wt%) was studied at various temperatures (300 to 450 °C) and strain rates (0.001 to 10 s^{-1}). The materials constants and activation energies for hot deformation were determined from the experimental compression data gathered for all alloys studied.

2. The peak flow stresses of the 7150 alloy significantly increased when V was added. The alloys containing 0.03-0.05% V displayed higher values of peak stresses than the alloys containing 0.11-0.19% V at low temperatures of 300-350 °C, whereas they displayed comparable values at high temperatures of 400-450 °C.

3. The activation energy for hot deformation in 7150 alloys increased from 229 kJ/mol for the base alloy to approximately 270 kJ/mol for the alloys containing 0.03-0.05% V. With a further increase in V content up to 0.19%, the activation energy for hot deformation returned to approximately 250 kJ/mol.

4. For the alloys with low V levels (0.03-0.05%), the V mainly existed as solute atoms in the aluminum matrix. The vanadium-solute-diffusion acted as the deformation rate-controlling mechanism for these alloys and resulted in the enhanced work hardening and the improved subgrain strengthening effects.

5. At high V levels (0.11-0.19%), the precipitation of a large number of $Al_{21}V_2$ dispersoids occurred during homogenization, which promoted the retardation of dynamic recovery and the inhibition of dynamic recrystallization because of their pinning effect on dislocation motion and subgrain rotation.

References

[1] E.A. Starke, J.T. Staley, Prog. Aerosp. Sci. 32 (1996) 131-172.

[2] H.J. McQueen, S. Spigarelli, M. Kassner, E. Evangelista, Hot Deformation and Processing of Aluminum Alloys, CRC Press, Florida, 2011, pp. 87-233.

[3] D. Dumont, A. Deschamps, Y. Brechet, Mater. Sci. Eng. A 356 (2003) 326-336.

[4] C. Shi, J. Lai, X.-G. Chen, Materials 7 (2014) 244-264.

[5] H.E. Hu, L. Zhen, L. Yang, W.Z. Shao, B.Y. Zhang, Mater. Sci. Eng. A 488 (2008) 64-71.

[6] S. Chen, K. Chen, G. Peng, X. Chen, Q. Ceng, J. Alloys Comp. 537 (2012) 338-345.

[7] R.L. Gall, J.J. Jonas, Acta Mater. 47 (1999) 4365-4374.

[8] C.O. Schmidt, Int. J. Eng. Sci. 22 (1984) 1055-1063.

[9] E. Cerri, E. Evangelista, H.J. McQueen, High Temp. Mat. Proc. 18 (1999) 227-240.

[10] O.D. Sherby, A. Goldberg, O.A. Ruano, Philoso. Magazine 84 (2004) 2417-2434.

[11] T. G. Nieh, R. Kaibyshev, L. M. Hsiung, N. Nguyen, J. Wadsworth, Scripta Mater. 36 (1997) 1011-1016.

[12] G. Avramovic-Cingara, D.D. Perovic, H.J. McQueen, Met. Mat. Trans. A. 27 (1996) 3478-3490.

[13] Y. Li, Z. Liu, L. Lin, J. Peng, A. Ning, J. Mater. Sci. 46 (2011) 3708-3715.

[14] T. Sheppard, M.G. Tutcher, Met. Sci. 14 (1980) 579-589.

[15] E.F. Kazakova, Y.I. Rusnyak, Met. Sci. Heat Treat. 51 (2009) 436-439.

[16] K.E. Knipling, D.C. Dunand, D.N. Seidman, Z. Metallkd. 97 (2006) 246-265.

[17] J.R. Davis, ASM Specialty Handbook: Aluminum and Aluminum Alloys, American Society for Metals, Metals Park, OH, USA, 1993, pp. 23-58.

[18] A.K. Srivastava, S. Ranganathan, J. Mater. Res. 16 (2001) 2103-2117.

[19] M. Moss, Acta Metall. 16 (1968) 321-326.

[20] Y.W. Kim, F.H. Froes, Mater. Sci. Eng. 98 (1988) 207-211.

[21] Y. Ning, Y. Li, Chin. J. Met. Sci. Technol. 6 (1990) 103-105.

[22] X. Wang, F. Cong, Q. Zhu, J. Cui, Sci China Technol. Sci. 55 (2012) 510-514.

[23] F.J. Humphreys, J. Mater. Sci, 36 (2001) 3833-3854.

[24] H. Jazaeri, F.J. Humphreys, J. Microsc. 213 (2004) 241-246.

[25] C. Shi, X.-G. Chen, Mater. Sci. Eng. A 596 (2014) 183-193.

[26] C.M. Sellars, W.J. McTegart, Mem. Sci. Rev. Met. 63 (1966) 731-746.

[27] C. Shi, W. Mao, X.-G. Chen, Mater. Sci. Eng. A 571 (2013) 83-91.

[28] H.J. McQueen, N.D. Ryan, Mater. Sci. Eng. A 322 (2002) 43-63.

[29] S.F. Medina, C.A. Hernandez, Acta Metall. 44 (1996) 137-148.

[30] E. Cerri, E. Evangelista, A. Forcellese, H.J. McQueen, Mater. Sci. Eng. A 197 (1995) 181-198.

[31] O.D. Sherby, R.H. Klundt, A.K. Miller, Metall. Trans. A 8 (1977) 843-850.

[32] R. Carmona, Q. Zhu, C.M. Sellars, J.H. Beynon, Mater. Sci. Eng. A 393 (2005) 157-163.

[33] J. Lai, C. Shi, X.-G. Chen, Effect of V addition on recrystallization resistance of hot-deformed 7150 aluminum alloy, Mater. Charact. 2014, in revision.

[34] H. Okamoto, Phase Diagrams of Dilute Binary Alloys. ASM International, Materials Park, OH, 2002.

[35] K. E. Knipling, D. C. Dunand, D. N. Seidman, Acta Mater. 56 (2008) 114-127.

[36] K.E. Knipling, D.C. Dunand, D.N. Seidman, Metall. Mater. Trans. A 38 (2007) 2552-2563.

[37] F.J. Humphreys, M. Hatherly, Recrystallization and Related Annealing Phenomena, second ed., Elsevier Ltd., Oxford, 2004, pp. 169-450.

[38] H.J. McQueen, J.E. Hockett, Met. Trans. 1 (1970) 2997-3004.

[39] J. J. Jonas, D. R. Axelrad, J. L. Uvira, Trans. Japan Inst. Met. 9 (1968) 257-267.

[40] J.D. Robson, P.B. Prangnell, Acta Mater. 49 (2001) 599-613.

[41] F.R. Castro-Fernandez, C.M. Sellars, Mat. Sci. Tech. 4 (1988) 621-627.

[42] O.D. Sherby, O.A. Ruano, Mater. Sci. Eng. A 410-411 (2005) 8-11.

[43] G. Neumann, C. Tuijn, Self-diffusion and Impurity Diffusion in Pure Metals: Handbook of Experimental Data, Elsevier Ltd., New York, 2009, pp. 121-148.

[44] C.H. Perdix, M.Y. Perrin, F. Montheillet, Mem. Etudes Sci. 78 (1981) 309-320.

CHAPTER VI

HOT WORKABILITY AND PROCESSING MAPS OF 7150 ALUMINUM ALLOYS WITH ZR AND V ADDITIONS

Chapter VI Hot workability and processing maps of 7150 aluminum alloys with Zr and V additions

Abstract

The hot workability and processing maps of 7150 aluminum alloys with different Zr additions (0 to 0.15 wt%) and V additions (0.01 to 0.15 wt%) were investigated using uniaxial compression tests conducted at various temperatures (300 to 450 °C) and strain rates (0.001 to 10 s^{-1}). The results reveal that the processing map of the 7150 base alloy exhibits a single domain (Domain I) associated with dynamic recovery and partially dynamic recrystallization. With increasing Zr and V additions, Domain I shrinks towards higher temperatures and higher strain rates and exhibits decreases in efficiency of power dissipation due to a restrained level of dynamic recovery caused by the pinning effect of Al_3Zr and $Al_{21}V_2$ dispersoids. When the added Zr and V contents reach 0.15 wt%, another domain (Domain II) is formed, corresponding to cavity formation in the microstructure. Flow instability during hot deformation of 7150 alloys is attributed to the formation of adiabatic shear bands and deformation bands. The instability region extends toward lower strain rates when alloyed with Zr and V. The optimum hot-working parameters for those alloys are determined to be a deformation temperature of 450 °C and a strain rate of 0.01 s^{-1}.

The content of this chapter is submitted as: C. Shi, X.-G. Chen, Hot workability and processing maps of 7150 aluminum alloys with Zr and V additions, Journal of Materials Engineering and Performance, 2014.

6.1 Introduction

In recent years, aluminum alloys have been progressively used in aircraft and transportation industries due to their remarkable physical and mechanical properties. Among all, the 7xxx series (Al-Zn-Mg-Cu) aluminum alloys are utilized extensively due to their high fracture toughnesses, good corrosion resistance, and heat treatability properties [1]. These aluminum alloys are generally subjected to hot forming processes such as rolling, extrusion and forging; it is thus necessary to optimize the parameters of these processes for maximum efficiency and workability of the product metals. The hot workability is usually defined as the ease with which a material can be shaped by plastic deformation without the onset of fracture or reaching other undesirable conditions and is influenced by thermomechanical processing parameters and the alloying elements used [2,3]. A clear understanding of the effects of the alloying elements used on the hot workability of the alloy is required to establish optimum processing conditions and improve mechanical properties.

Zirconium addition is well known to increase the recrystallization resistance of aluminum alloys by forming fine, coherent Al_3Zr dispersoids [4,5]. The presence of these dispersoids promotes the formation of a stable and refined subgrain structure during hot working, which provides additional substructure strengthening [6]. Morere et al. [7] investigated the effects of Zr addition on the static recrystallization of AA7010 aluminum alloys during solution treatment. A few studies have been conducted on the hot deformation of aluminum alloys containing Zr, in which a pinning effect of Al_3Zr dispersoids on dislocations and grain

boundaries has been reported [8,9]. In the author's recent work [10], the effects of various Zr additions (0-0.19 wt%) on the microstructural evolution during hot compression of 7150 aluminum alloys was studied, and it was found that the dynamic recovery level was reduced after being alloyed with Zr due to the pinning effects of Al_3Zr dispersoids on dislocation motion and also due to restrained dynamic restoration.

Vanadium addition has been reported to maintain the high temperature strength of the aluminum alloy by forming thermally stable dispersoids of $Al_{11}V$ [11,12]. The presence of these dispersoids could retard dynamic softening and raise the recrystallization temperature during hot working processes [13]. Wang et al. [14] found that the addition of 0.045 wt% V into the 5083 aluminum alloy exhibited a restriction on the growth of recrystallized grains and yielded a refined fibrous structure in the rolling sheet. With the addition of 0.15 wt% V, Cui et al. observed the precipitation of V-containing dispersoids in AA2091 (2.15Li-2.04Cu-1.5Mg-0.14Zr) alloy [15]. The effect of different V additions (0.01-0.19 wt%) on the hot deformation behavior of 7150 aluminum alloy was reported in the author's previous work [16]; it was suggested that vanadium-solute diffusion acted as the deformation rate controlling mechanism for alloys containing up to 0.05 wt% V, whereas the precipitation of $Al_{21}V_2$ dispersoids in the alloys containing 0.11 to 0.19 wt% V promoted the retardation of dynamic recovery and the inhibition of dynamic recrystallization.

Processing maps were developed on the basis of the dynamic materials model (DMM) and have been used to design hot working schedules for a wide variety of materials [3]. The

maps explicitly represent local peak efficiencies of power dissipation and regions of flow instability, which are associated with specific deformation mechanisms [3,17]. With the help of processing maps, the deformation temperature and the strain rate corresponding to local peak efficiencies of power dissipation in the safe domain is chosen as the optimum processing parameters for the hot working of materials. Hot working should not be performed in the regions of flow instability to prevent the occurrence of microstructure defects [18]. Recently, processing maps had been widely used to optimize the processing parameters during the hot working of aluminum alloys. Luo et al. [19] developed the processing maps of 7050 aluminum alloys at different strains and obtained the optimum processing parameters at a strain of 0.7 with an efficiency of 42%. Various microstructural defects generated during hot deformation in 2124 aluminum alloys were studied using a processing map; the flow instability was found to be caused by the adiabatic shear band, and matrix cracking was observed [20]. Ganesan et al. [21] developed the processing map for 6061 Al/15 vol% SiCp using the flow stresses predicted from a neural network model, and the safe domains of hot working were identified and validated through microstructural investigations. A 4D process map was developed by Bhimavarapu et al. [22], illustrating the contours of power dissipation and flow instability with respect to the strain rate, temperature and strain. However, most of these studies focused on the influence of thermomechanical parameters on the processing map of an individual material. Studies that investigate the effects of micro-alloying elements on the processing maps for hot working of aluminum alloys are not common.

In the present study, the effects of different Zr concentrations (0.04 to 0.15 wt%) and V additions (0.05 to 0.15 wt%) on the processing maps of homogenized 7150 alloys were studied by hot compression tests at various temperatures and strain rates. The microstructural evolution of the alloys during hot deformation was investigated to understand the effects of Zr and V additions on the processing maps and dynamic deformation mechanisms that occurred under various deformation conditions.

6.2 Experimental

Experiments were conducted on 7150 base alloy (Zr free) and alloys with Zr contents from 0.04 to 0.15% and V contents from 0.05 to 0.15%. All alloy compositions are in wt% unless otherwise indicated. The chemical compositions of these alloys are provided in Table 6.1. Approximately 3 kg of each material was melted in an electrical resistance furnace and then cast into a rectangular permanent steel mold measuring 30 x 40 x 80 mm^3. The cast ingots of these alloys were homogenized at 465 °C for 24 h, followed by direct water quenching to room temperature. Cylindrical samples measuring 10 mm in diameter and 15 mm long were machined from the homogenized ingots. Uniaxial compression tests were conducted on a Gleeble 3800 thermomechanical simulation unit at strain rates of 0.001, 0.01, 0.1, 1 and 10 s^{-1} and deformation temperatures of 300, 350, 400 and 450 °C, respectively. During the tests, the samples were heated to the desirable deformation temperature at a heating rate of 10 °C/s and held for 3 min to ensure a homogeneous temperature distribution throughout the samples. The samples were deformed to a total true strain of 0.8 and then

immediately water-quenched to retain the microstructure at the deformation temperature.

The microstructure of the homogenized materials was etched by Keller's solution prior to hot deformation. All deformed samples were sectioned parallel to the compression axis along the centerline, and then polished and etched in the Keller solution for optical microscope observation. Additionally, some deformed samples were selected for electron backscattered diffraction (EBSD) analysis under a scanning electron microscope (SEM, JEOL JSM-6480LV). The step size between the scanning points was set to 1.0 μm. Samples for TEM observation were mechanically ground to a thicknesses of 35-60 μm and followed by electropolishing in a twin-jet polishing unit, which was operated at 15 V and -20 °C using a 30% nitric acid and 70% methanol solution. The samples were observed under a transmission electron microscope (TEM, JEOL JEM-2100) operated at 200 kV.

Table 6.1 Chemical composition of the alloys studied (wt%).

Alloy	Zn	Mg	Cu	Si	Fe	Ti	Zr	V	Al
7150 base alloy	6.44	2.47	2.29	0.16	0.15	0.009	-	0.01	Bal.
7150-0.04%Zr	6.27	2.14	2.23	0.11	0.14	0.008	0.04	0.01	Bal.
7150-0.12%Zr	6.35	2.22	2.34	0.16	0.15	0.008	0.12	0.01	Bal.
7150-0.15%Zr	6.16	2.15	2.16	0.11	0.14	0.008	0.15	0.01	Bal.
7150-0.05%V	6.21	2.18	2.20	0.16	0.14	0.009	-	0.05	Bal.
7150-0.11%V	6.31	2.30	2.24	0.16	0.14	0.008	-	0.11	Bal.
7150-0.15%V	6.16	2.10	2.15	0.16	0.13	0.008	-	0.15	Bal.

6.3 Results

6.3.1 Flow stress behavior

The flow stress behavior of the 7150 alloys with Zr additions from 0.04 to 0.19% and

those with V additions from 0.03 to 0.19% was investigated in the author's previous studies [10,16]. Fig. 6.1 presents a series of typical true stress-true strain curves obtained during hot deformation for the alloys containing different Zr and V contents. It is evident that the flow stresses increase rapidly at the beginning of deformation and then either remain fairly constant or decrease to some extent after attaining a peak stress. The level of flow stress increases with increasing strain rate and decreasing deformation temperature, which is a general trend in hot deformation [2]. Previous results [10,16] revealed that under a given deformation condition, no significant variation in flow stress was observed between the base alloy and the alloy containing 0.04% Zr. However, the values of flow stress show a gradual rise with increasing content of Zr from 0.04 to 0.19%. Conversely, the alloys containing 0.03-0.05% V display dramatic increases of flow stress relative to the base alloy, especially at low deformation temperatures of 300-350 °C. With increasing V contents from 0.11 and 0.15%, the flow stress is increased significantly during deformation at all temperature ranges investigated. Furthermore, when the V addition reaches 0.19%, the effect on flow stress becomes less evident. To study the effects of Zr and V additions on the processing map for hot deformation of 7150 alloy, seven alloys including the base alloy (Table 6.1) were selected in the present work.

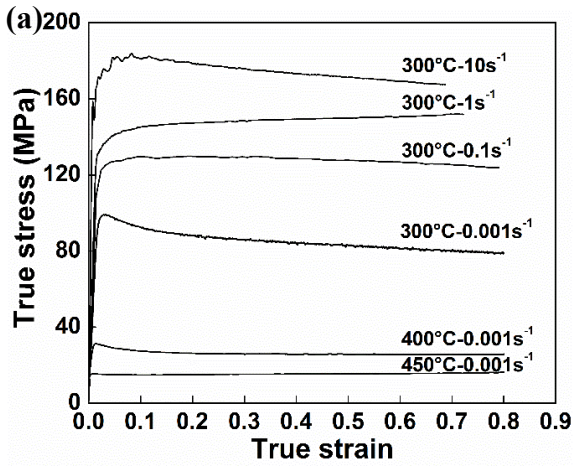
(a)
True stress (MPa)
True strain
300°C-10s-1
300°C-1s-1
300°C-0.1s-1
300°C-0.001s-1
400°C-0.001s-1
450°C-0.001s-1

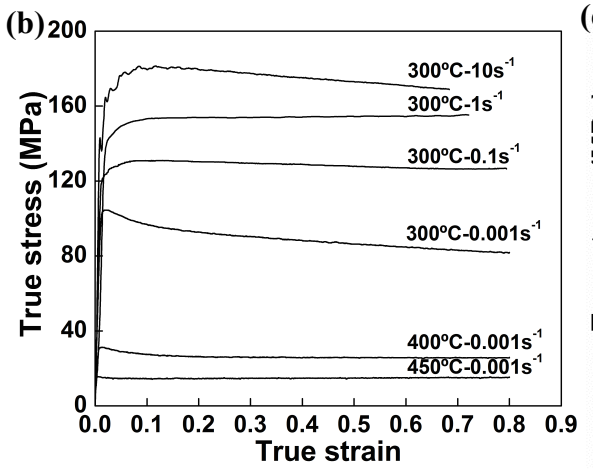
(b)
True stress (MPa)
True strain
300°C-10s-1
300°C-1s-1
300°C-0.1s-1
300°C-0.001s-1
400°C-0.001s-1
450°C-0.001s-1

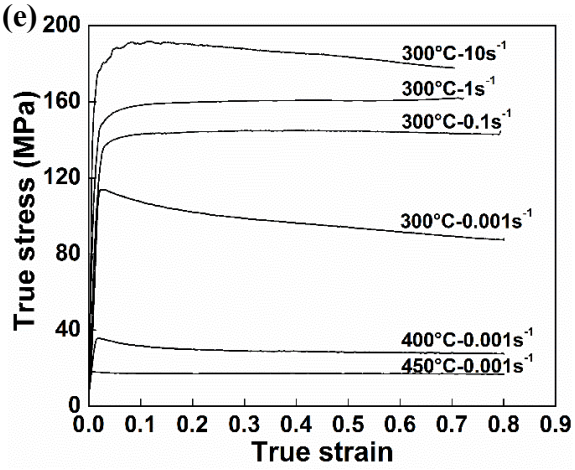
(e)
True stress (MPa)
True strain
300°C-10s-1
300°C-1s-1
300°C-0.1s-1
300°C-0.001s-1
400°C-0.001s-1
450°C-0.001s-1

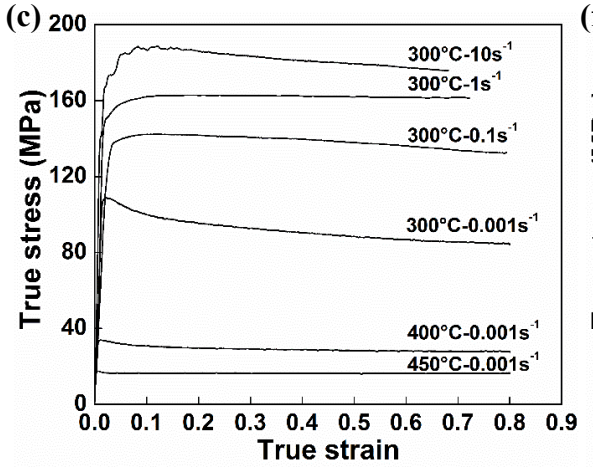
(c)
True stress (MPa)
True strain
300°C-10s-1
300°C-1s-1
300°C-0.1s-1
300°C-0.001s-1
400°C-0.001s-1
450°C-0.001s-1

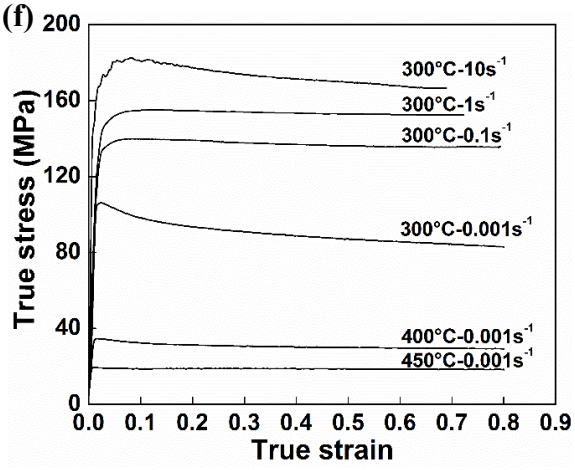
(f)
True stress (MPa)
True strain
300°C-10s-1
300°C-1s-1
300°C-0.1s-1
300°C-0.001s-1
400°C-0.001s-1
450°C-0.001s-1

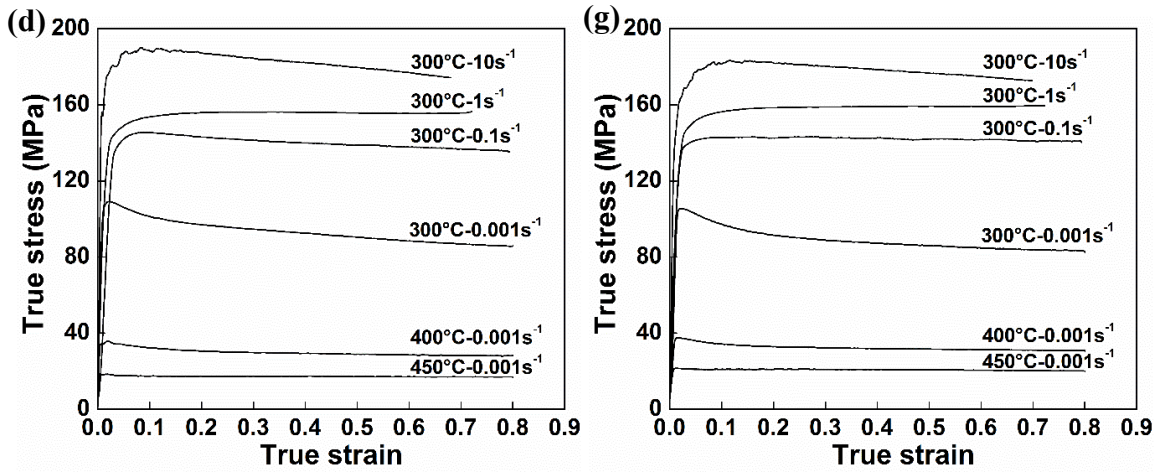

Fig. 6.1 Typical true stress-true strain curves during hot compression deformation: (a) base alloy and the alloys with (b) 0.04% Zr ; (c) 0.12% Zr ; (d) 0.15% Zr (e) 0.05%V; (f) 0.11% V and (g) 0.15% V.

6.3.2 Initial microstructure

Fig. 6.2 gives an example of the microstructural evolution of the 7150 alloys with 0.12% Zr and 0.11% V addition after homogenization. The homogenized structures of all three alloys are composed of uniform equiaxed grains formed during casting. The average grain size of the base alloy is determined to be 127 μm. The alloys containing Zr exhibit much coarser grain structures. The average grain sizes are approximately 586, 547 and 524 μm for the alloys with 0.04, 0.12 and 0.15% Zr, respectively. This is due to the poisoning effect of Zr, through which the added Zr reacts with iron and silicon in the melt, reducing the growth restriction of grains [23]. The V addition appears to slightly coarsen the grain structure. The average grain sizes are approximately 157, 152 and 133 μm for the alloys containing 0.05, 0.11 and 0.15% V, respectively. In addition, the EBSD analysis results reveal that the grain boundaries of all of the alloys are characterized by high-angle boundaries, typically with misorientation angles between 30 and 60°.

After homogenization at 465 °C for 24 h, the precipitation of Al_3Zr dispersoids was clearly observed in the alloys with 0.12 and 0.15% Zr. The dark-field TEM micrograph in Fig. 6.3a shows an example of the precipitation of spheroidal and coherent Al_3Zr dispersoids with an average diameter of 15 nm in the alloy containing 0.12% Zr. When V was added into the alloy, the precipitation of V-containing dispersoids was found in the alloys containing 0.11 and 0.15% V. These dispersoids were determined to be in the $Al_{21}V_2$-type phase by TEM selected area electron diffraction in the author's previous studies [24]. The STEM micrograph (Fig. 6.3b) shows that a large number of spheroidal $Al_{21}V_2$ dispersoids with an average diameter of 51 nm were precipitated in the alloy containing 0.11% V. In the samples with lower contents of Zr (0.04%) and V (0.05%), almost no Al_3Zr and $Al_{21}V_2$ dispersoids were observed, indicating that the added Zr and V mainly existed as the solute atoms in the aluminum matrix.

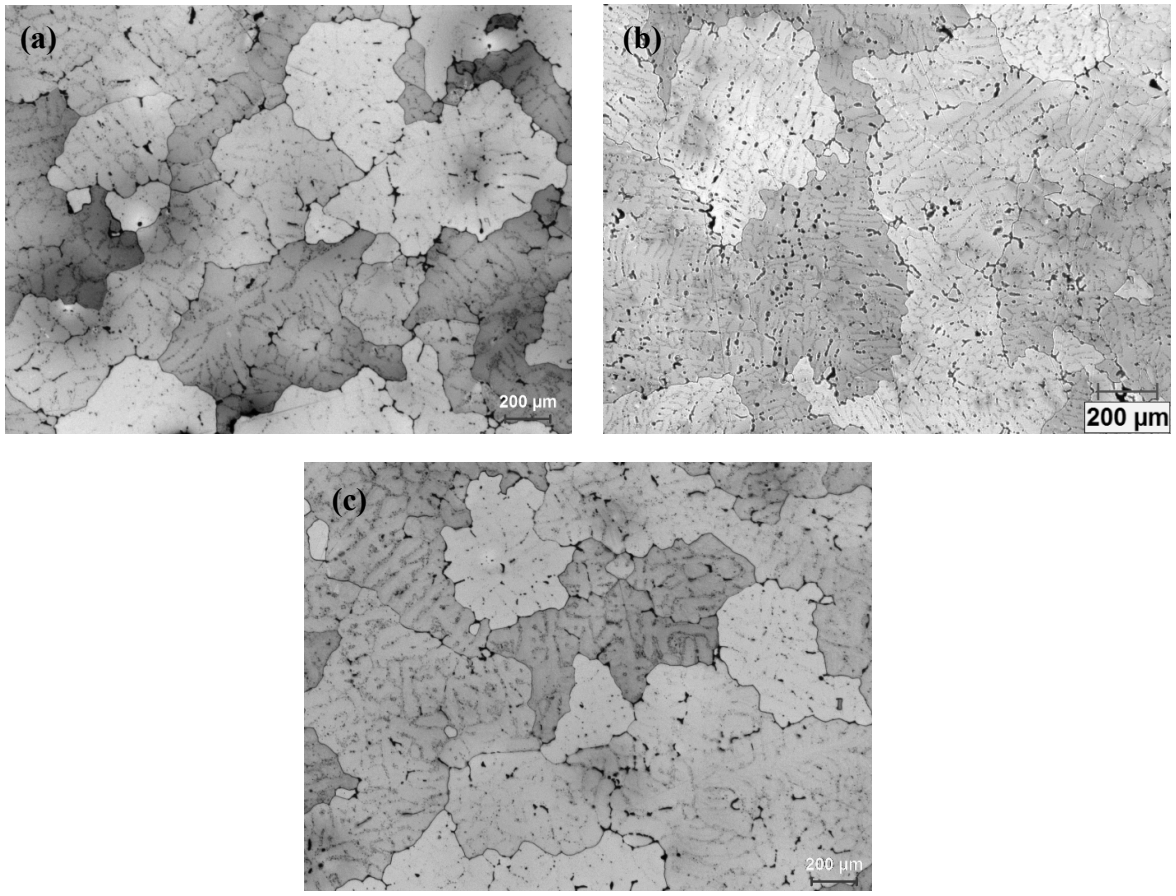

Fig. 6.2 Optical micrographs showing the grain structures after homogenization: (a) the base alloy and alloys with (b) 0.12% Zr and (c) 0.11% V.

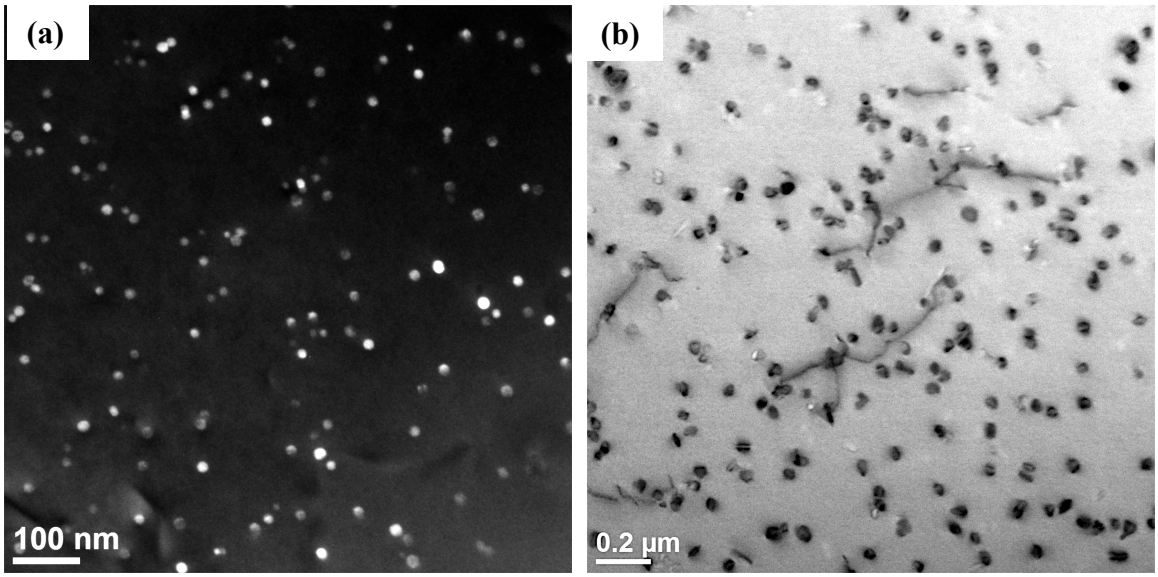

Fig. 6.3 The precipitation of Al_3Zr and $Al_{21}V_2$ dispersoids after homogenization at 465 °C for 24 h: (a) Dark-field TEM micrograph displaying Al_3Zr dispersoids in alloy with 0.12% Zr, recorded near the [011]α zone axis by using the (100) superlattice reflections of Al_3Zr ($L1_2$); (b) STEM image showing $Al_{21}V_2$ dispersoids in alloy with 0.11% V.

6.3.3 Effects of Zr and V on processing map

Processing maps have been widely used to understand the hot workability of materials in terms of various dynamic deformation mechanisms operating at different deformation conditions, which were developed on the basis of the dynamic materials model by Prasad [3,17]. In this method, the efficiency of power dissipation, η, represents the energy dissipated through the microstructural evolution and is given in Eq. (6.1):

$$\eta = \frac{2m}{2m+1} \tag{6.1}$$

where m is the strain rate sensitivity of the material given by $\frac{\partial \ln \sigma}{\partial \ln \dot{\varepsilon}}$.

The contour plot of the iso-efficiency η values as a function of temperature and strain

rate constitutes the power dissipation map. Different domains in the power dissipation map imply specific microstructural manifestations, such as dynamic recrystallization, dynamic recovery, wedge cracking and void formation [3,17]. However, during the deformation process, flow instability may occur and lead to deformation defects in the microstructure, including flow localization, adiabatic shear deformation, flow rotation and kinking [3]. The criterion to evaluate the flow instabilities is expressed as:

$$\xi = \frac{\partial \ln[m/(m+1)]}{\partial \ln \dot{\varepsilon}} + m < 0 \tag{6.2}$$

The material may exhibit the deformation defects when ξ is negative [3]. Hence, the instability map can be generated based on the variation of ξ with the temperature and strain rate. Finally, the processing map is obtained by superimposing the instability map on the power dissipation map.

Fig. 6.4 shows the typical processing maps developed for the base alloy and alloys containing different Zr and V contents at the true strain of 0.8. The contour numbers represent the efficiency of power dissipation and the shaded zones correspond to the flow instability region. It can be seen that in the base alloy, the efficiency of power dissipation generally increases with increasing deformation temperature, indicating an increased level of energy dissipated through the dynamic deformation mechanisms [3]. A single domain (Domain I) is observed at the temperatures of 402-450 °C and the strain rates of 0.001-0.4 s^{-1}, reaching a peak efficiency of 42% at 450 °C and 0.01 s^{-1} (Fig. 6.4a).

At a lower Zr content of 0.04% (Fig. 6.4b), the alloy exhibits a similar processing map to the base alloy, in which only one domain is present and is located in the same range of temperatures and strain rates as the base alloy; an identical peak efficiency of 42% is also reached at 450 °C and 0.01 s^{-1}. This is as a result of little variation in flow stress from the base alloy (Fig. 6.1).

At higher Zr contents (0.12 to 0.15%), Al_3Zr dispersoids begin to precipitate, influencing the processing map. Domain I appears to shrink towards higher temperatures and higher strain rates, and a decrease of the efficiency value in this domain is observed at a given deformation condition compared with the base alloy (Fig. 6.4c and d). In addition, under the deformation conditions at 350-400 °C and 0.001-0.003 s^{-1} in the alloy with 0.12% Zr, the efficiency level is increased relative to that of the base alloy (Fig. 6.4c). When a higher Zr content of 0.15% is added (Fig. 6.4d), another domain (Domain II) appears between 378-412 °C and 0.001-0.005 s^{-1}, which is associated with a significant increase in efficiency. It is apparent that the processing map of the alloy with 0.12% Zr still exhibits a single domain between 406-450 °C and 0.003-0.2 s^{-1} with a peak efficiency of 39% at 450 °C and 0.01 s^{-1}, while two domains occur in the alloy containing 0.15% Zr. Domain I is located between 420-450 °C and 0.008-0.15 s^{-1} with a peak efficiency of 38% at 450 and 0.01 s^{-1}, and Domain II is situated between 378-412 °C and 0.001-0.005 s^{-1} with a peak efficiency of 37% at 400 and 0.001 s^{-1}, respectively (Fig. 6.4d).

Compared with the base alloy, the processing map of the alloy containing 0.05% V (Fig.

6.4e) displays higher efficiency values at lower temperatures (350-410 °C) and lower strain rates (0.001-0.003 s^{-1}). A single domain is observed in the same range of temperatures and strain rates as the base alloy, but with a slightly lower peak efficiency of 40% at 450 °C and 0.01 s^{-1}.

Conversely, the precipitation of $Al_{21}V_2$ dispersoids is observed in the alloys with V from 0.11 to 0.15%, as shown in Fig. 6.3. The evolution of the processing map of these alloys displays a similar trend to that of the alloys containing Al_3Zr dispersoids. Compared with the base alloy, Domain I narrows at higher temperatures and higher strain rates (Fig. 6.4f and g). With increasing V addition to 0.15%, Domain II gradually forms with a high degree of power dissipation efficiency, as shown in Fig. 6.4g. The processing map of the alloy with 0.11% V exhibits only one domain between 428-450 °C and 0.004-0.1 s^{-1} with a peak efficiency of 37% at 450 °C and 0.01 s^{-1}. For the alloy with 0.15% V, two domains are observed: Domain I between 422-450 °C and 0.008-0.12 s^{-1} with a peak efficiency of 36% at 450 and 0.01 s^{-1}, and Domain II between 375-415 °C and 0.001-0.005 s^{-1} with a peak efficiency of 36% at 400 °C and 0.001 s^{-1}, respectively.

Moreover, a large region of flow instability is observed in the base alloy at the strain rates above 0.1 s^{-1} in the temperature range studied. After alloyed with Zr (0.04-0.15%) and V (0.05-0.15%), the evolution of the flow instability regions in all six alloys exhibits a similar tendency: the flow instability region expands towards lower strain rates. For the alloys containing Al_3Zr or $Al_{21}V_2$ dispersoids, the instability region extends up to the strain rate of

0.01 s^{-1}, particularly at lower temperatures between 300 and 350 °C. It is evident that the flow instability regions in all alloys present lower values of power dissipation efficiencies, compared with the adjacent stable regions. For example, the efficiency values are approximately 2-28% when the deformation is conducted at the strain rates of 1-10 s^{-1}; however, they increase up to 36-42% under the deformation conditions in Domain I. Therefore, the processing parameters should not be chosen in the instability region of those alloys to obtain good hot workability and to prevent the occurrence of deformation defects.

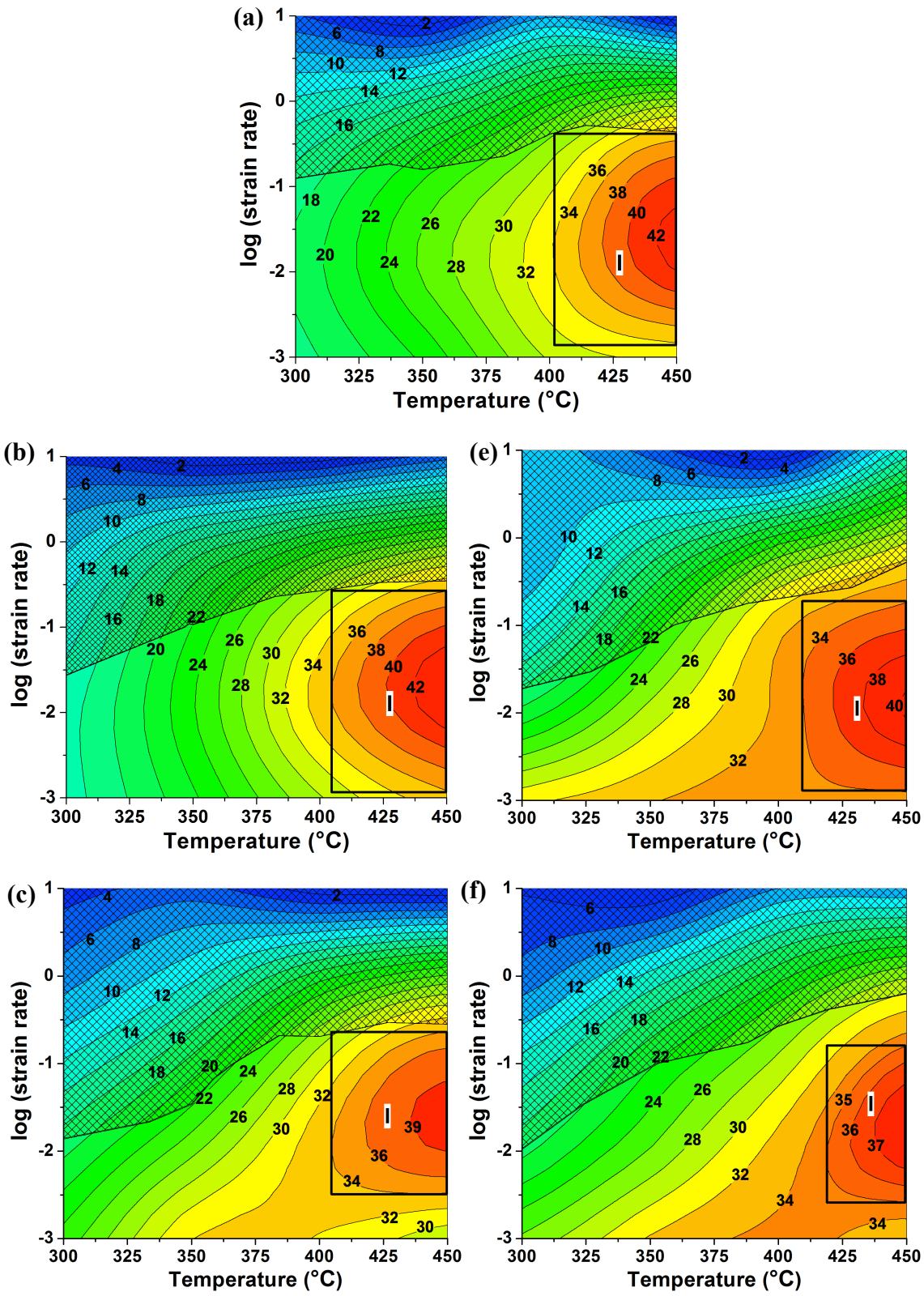
(a)
(b)
(c)
(e)
(f)
log (strain rate)
Temperature (°C)
I

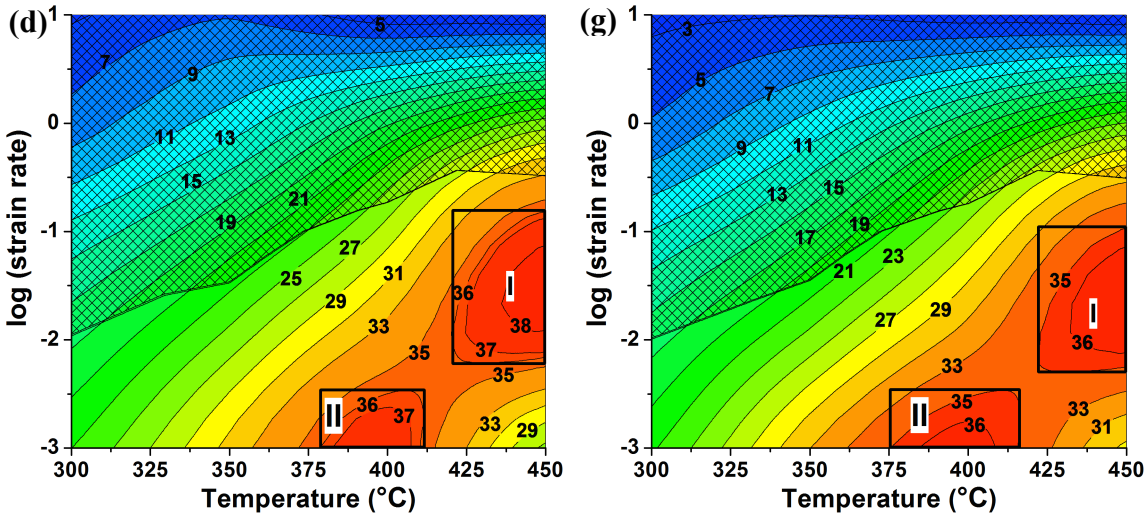

Fig. 6.4 The processing maps developed at the true strain of 0.8 for (a) base alloy and the alloys with (b) 0.04% Zr; (c) 0.12% Zr; (d) 0.15% Zr; (e) 0.05%V; (f) 0.11% V and (g) 0.15% V.

6.3.4 Microstructural evolution of deformed samples

To understand the effects of Zr and V additions on the dynamic deformation mechanisms operating in each domain and on the manifestations of flow instability, the deformed samples of the base alloy and alloys containing 0.15% Zr, 0.05% V and 0.15% V under different deformation conditions at the true strain of 0.8 were selected for microstructure examination using the optical microscope and the EBSD technique. In EBSD analysis, the misorientation angles of both grains and subgrains are distinguished as follows: white lines: 1-5°; red lines: 5-15°; thin black lines: 15-30° and thick black lines: (>30°).

6.3.4.1 Domain I

Fig. 6.5 shows the orientation imaging maps of the deformed samples of the four alloys under the deformation condition at 450 °C and 0.01 s^{-1}, which corresponds to the peak efficiencies of power dissipation in Domain I (Fig. 6.4). In the base alloy, small equiaxed

grains with high angle boundaries (>15°) containing substructures are formed along the bulged grain boundaries (see the arrows in Fig. 6.5a). A large number of subgrains with low and medium angle boundaries (1-15°) are observed inside the deformed grains. These results indicate a strong dynamic recovered microstructure mixed with partially dynamic recrystallization. However, only dynamically recovered microstructures are observed in the alloys containing Al_3Zr or $Al_{21}V_2$ dispersoids (0.15% Zr and 0.15% V), and the subgrains were formed with neatly arranged boundaries between 1° and 15° (Fig. 6.5b and d). In this case, dynamic recrystallization is inhibited as a result of the pinning effect of the dispersoids on the migration of high-angle boundaries [10,16]. Conversely, the alloy containing 0.05% V in solution displays a partially recrystallized structure and a larger number of recrystallized grains is presented, compared with that in the base alloy (see the arrows in Fig. 6.5c), showing an increasing level of dynamic recrystallization. A previous study [16] reveals that the V solutes in the 7150 alloy can cause a higher multiplication rate of dislocations and restrain dynamic recovery, thereby leading to an improved driving force for dynamic recrystallization [2,25], whereas the drag effect of solute atoms on the mobility of high-angle boundaries becomes limited due to the higher diffusion rate of solutes at high temperature [26]. Hence, dynamic recrystallization steadily occurs and causes a higher degree of recrystallized structure. Therefore, during the deformation in Domain I, the dynamic recovery and partially dynamic recrystallization act as the deformation mechanisms in the base alloy and the alloy containing 0.05% V. For the alloys with 0.15% V and 0.15% Zr, the mechanism is solely dynamic recovery.

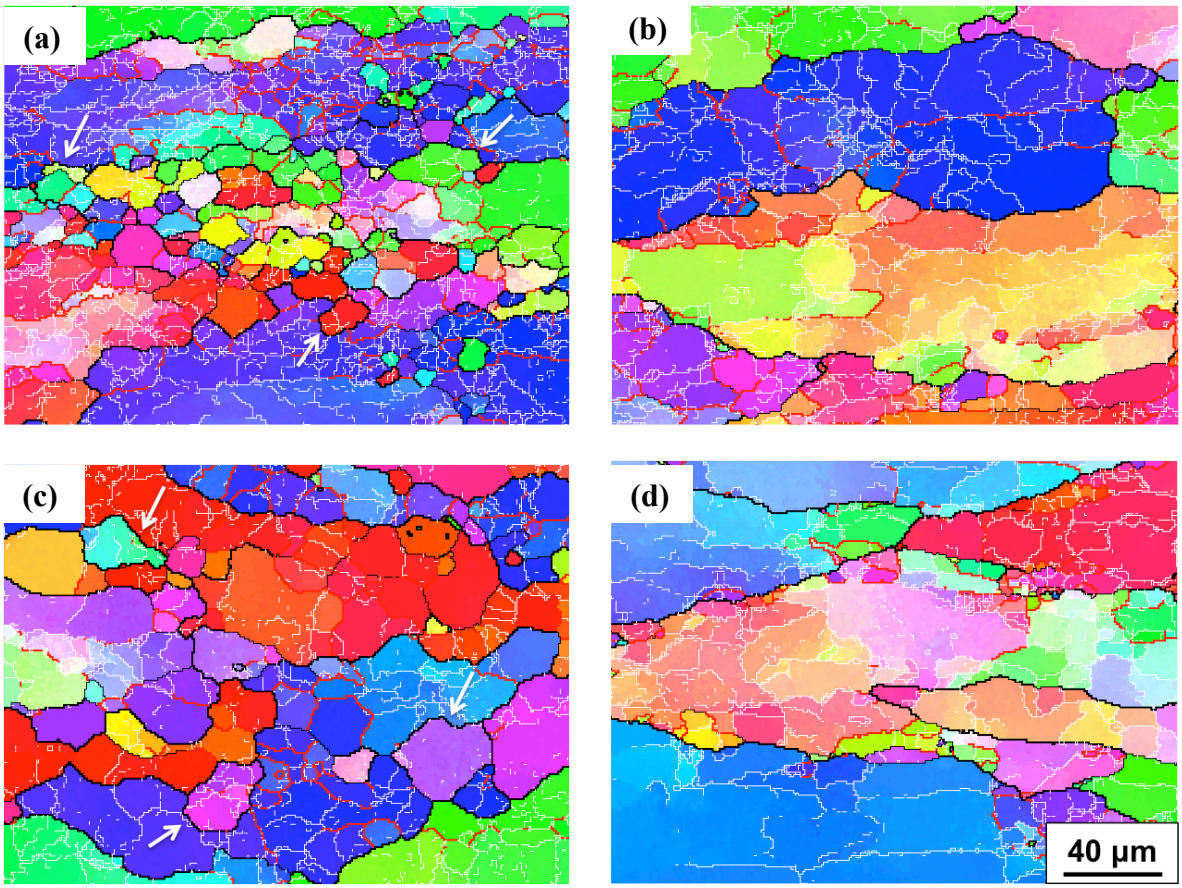

Fig. 6.5 Orientation imaging maps under the deformation condition at 450 °Cand 0.01 s^{-1} with the true strain of 0.8, (a) the base alloy and the alloys with (b) 0.15% Zr; (c) 0.05% V; and (d) 0.15% V.

6.3.4.2 Domain II

When the deformation is conducted at 400 °C and 0.001 s^{-1}, both the alloys with 0.15% Zr and 0.15% V display high values of peak efficiency in Domain II, and a remarkable increase in the efficiency is also observed after the 0.05% V addition, compared with the base alloy (Fig. 6.4). As shown in Fig. 6.6, cracking is observed in the deformed microstructures of the micro-alloyed Zr and V materials. However, no obvious cracks are found in the base alloy.

During a slow strain rate deformation and creep process at elevated temperatures, microcracks are usually observed in the deformed microstructure of metals, which is generally reported to occur in two modes: wedge cracking and cavity formation [3,20,27-30]. Wedge cracks are produced at triple junctions of grain boundaries to relieve stress concentrations, when grain boundary sliding occurs under shear stress [3,27]. Conversely, cavities are frequently observed along grain boundaries due to the stress concentration arising from dislocation pile-up against the grain boundary and the intermetallic particles at grain boundaries; this process involves the Zener-Stroh mechanism [27,29].

The deformed sample of the base alloy displays a high occurrence of dynamically recovered structures, in which the dislocation density is largely decreased and the subgrains are well organized with higher angle boundaries of 5-15° (Fig. 6.7a). The formation of subgrains and the continuous increase in subgrain boundary misorientation effectively lead to grain refinement near the original grain boundaries. The dispersed fine subgrains subsequently accommodate the stress concentration at triple junctions of original grain boundaries by the subgrain boundary sliding during hot deformation, leading to a homogenous deformation without cracking [31].

When the deformation is conducted in the alloys containing Al_3Zr or $Al_{21}V_2$ dispersoids (0.15% Zr and 0.15% V), the formation of cavities along the grain boundaries is observed (Fig. 6.6a and b). EBSD results show that the deformed structure is characterized by a large number of low-angle boundaries of 1-5° along the grain boundaries (Fig. 6.7b and d),

indicating a low level of dynamic recovery and a high density of dislocation tangle and cell structures. Thus, the deformation cannot be accommodated through subgrain boundary sliding, as occurred in the base alloy. During hot deformation, dislocation pile-up generally occurs at the grain boundaries under the applied shear stress. However, the slip and climb of the dislocations are strongly pinned by the dispersoids, resulting in a high concentration of dislocations accumulated at the grain boundaries (Fig. 6.7b and d). Subsequently, cavities can be initiated to release high energies induced by the dislocation pile-up, and then grow rapidly by the vacancy diffusion along the grain boundaries [27,29]. With further straining, the propagation of the cavities could lead to intercrystalline cracking, which was widely observed during hot deformation at low strain rates ranging from 0.003 to 0.001 s^{-1} in different alloys, including Ni-20Cr, Mg-11.5Li-1.5Al alloy and cast TXA321 magnesium alloy [3,32]. Conversely, wedge cracking is rarely found at the triple junction of grain boundaries because grain boundary sliding is effectively pinned by the dispersoids [25].

The formation of cavities along grain boundaries are also present in the deformed sample of the alloy with 0.05% V (Fig. 6.6c). Fig. 6.7c illustrates a much less recovered microstructure with numerous dislocation substructures along grain boundaries, which is similar to those observed in alloys containing dispersoids (Fig. 6.7b and d), due to the V solute drag effect on dislocation motion and subgrain coalescence [16]. High stress concentrations resulting from dislocation pile-up at grain boundaries stimulates the formation of cavities. However, wedge cracking at the triple junctions of grain boundaries is also

observed (Fig. 6.6c). Due to the limited drag effect of V solutes on the boundary mobility at high temperatures [16,26], original grain boundary sliding occurs during deformation, leading to accumulated stress at triple junctions and the formation of wedge cracks [20,27,28].

Cavity formation is also observed in the alloys with 0.11% V and 0.12% Zr at 400°C and 0.001 s^{-1}; this likely causes the comparable increase in efficiency with the alloy containing 0.05% V (Fig. 6.4). Therefore, the presence of microcracks in alloys with 0.12-0.15% Zr and 0.05-0.15% V likely results in significant increases in the efficiency of power dissipation under deformation conditions at low strain rates of 0.001-0.003 s^{-1} in the temperature range of 350 to 410°C.

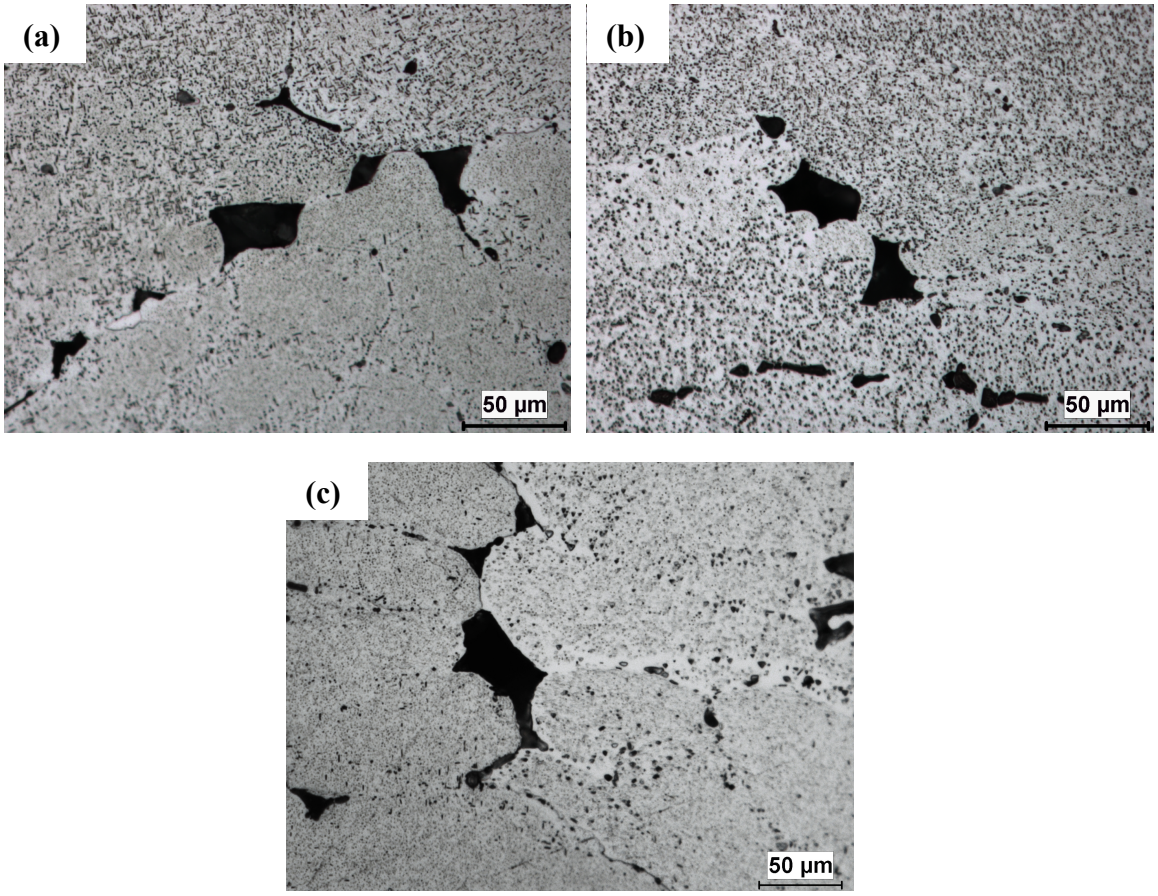

Fig. 6.6 Optical micrographs under deformation condition at 400 °C and 0.001 s^{-1} with the true strain of 0.8, (a) 0.15% Zr; (b) 0.15% V and (c) 0.05% V.

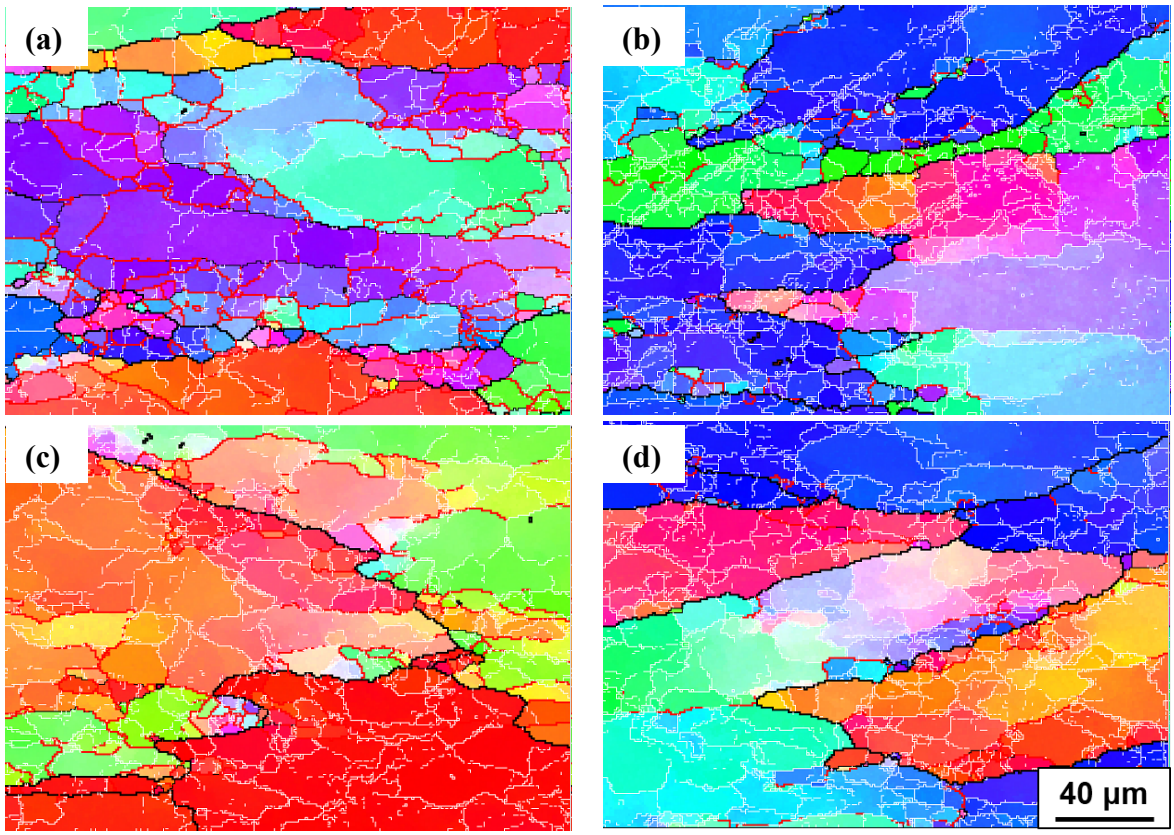

Fig. 6.7 Orientation imaging maps under deformation condition at 400 °C and 0.001 s^{-1} with the true strain of 0.8, (a) base alloy; (b) 0.15% Zr; (c) 0.05% V and (d) 0.15% V.

6.3.4.3 Flow instability region

Fig. 6.8 shows the microstructure of four alloys under deformation conditions at 300 °C and 1 s^{-1}, which is located in the flow instability region (Fig. 6.4). The original grains of all four alloys are severely torn and broke into irregular deformation bands (DBs), which are often found in individual grains as a result of either inhomogeneous stresses transmitted by neighboring grains or the intrinsic instability of the grains during deformation [25]. Adiabatic shear bands (ASBs) are also observed and extend through several grains, implying highly localized plastic deformation. EBSD analyses indicate that these deformation bands are characterized by high-angle transition boundaries (>15°), and contain a large amount of

low-level recovered substructures. Hence, the formation of deformation bands and adiabatic shear bands are the major mechanism causing the flow instability during hot deformation of the alloys.

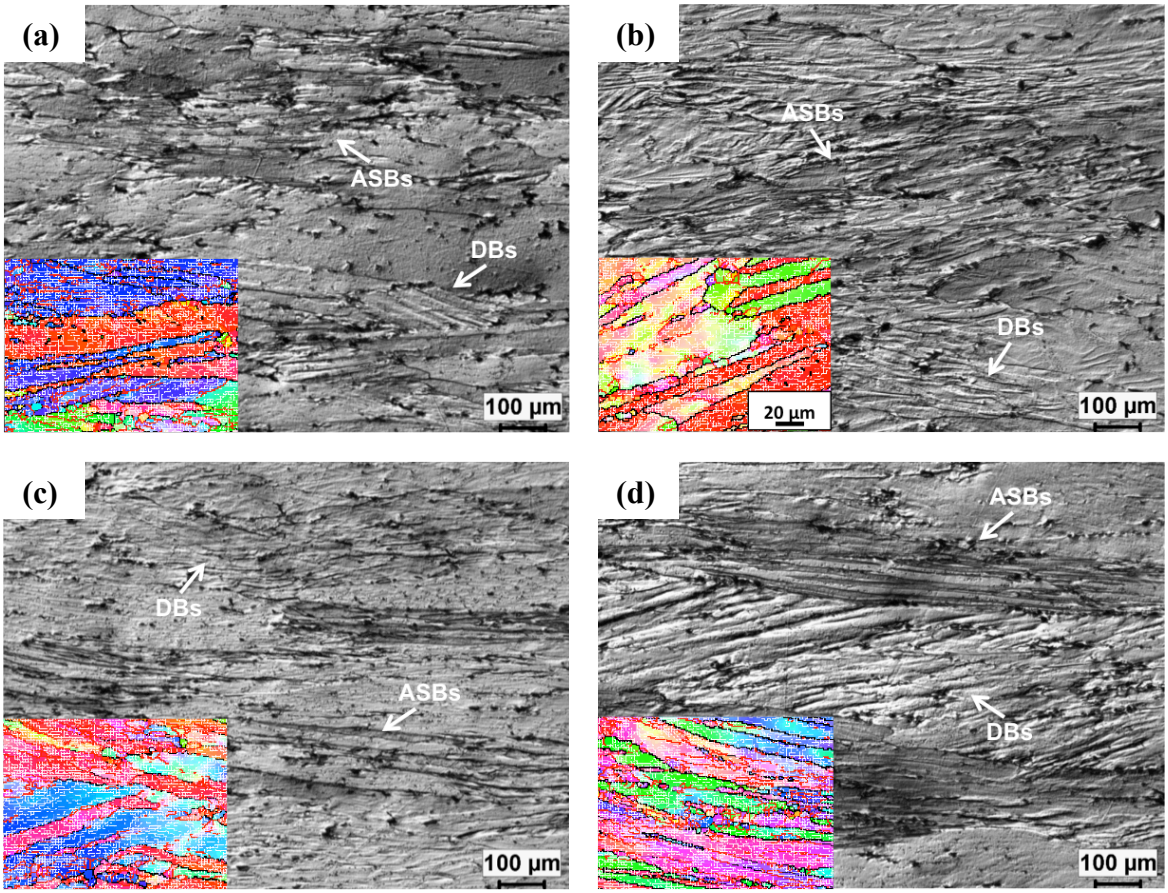

Fig. 6.8 Optical micrographs under deformation condition at 300 °C and 1 s-1 with the true strain of 0.8, (a) base alloy; (b) 0.15% Zr; (c) 0.05% V and (d) 0.15% V. The inset image represents the corresponding orientation imaging map of deformation bands.

6.3.5 Effect of strain on processing map

In commercial 7150 aluminum alloys, Zr is added at 0.08-0.15% to inhibit recrystallization by forming Al_3Zr dispersoids during homogenization treatment. To understand the effect of strain on processing map of 7150 alloys, the alloy with 0.15% Zr was

selected for study. Fig. 6.9 shows the evolution of the processing map of the alloy containing 0.15% Zr with increasing strain. At the early stage of deformation (i.e., a true strain of 0.2), dynamic recovery occurs as the deformation mechanism in the flow stable region and leads to the increase in efficiency of power dissipation as the temperature increases [3,25], as illustrated in Fig. 6.9a. As true strain increases from 0.2 to 0.6, the region with higher efficiencies gradually shifts to higher temperatures and higher strain rates, and Domain I is formed between 405-450 °C and 0.005-0.3 s^{-1} with a peak efficiency of 37% at 450 °C and 0.01 s^{-1} (Fig. 6.9b and c). In addition, another domain (Domain II) begins to form at the lower temperatures of 330-385 °C and lower strain rates of 0.001-0.003 s^{-1} with a peak efficiency of 33% at 350 °C and 0.001 s^{-1} (Fig. 6.9c). As the deformation strain further increases from 0.6 to 0.8, the dislocation density continuously rises; however, the movement of dislocations is strongly pinned by the Al_3Zr dispersoids, leading to a restrained dynamic recovery. A higher level of energy dissipated through dynamic recovery can only be achieved when the deformation temperature and strain rate increase [25,33], thereby resulting in Domain I with high efficiencies appearing at higher temperatures and higher strain rates (Fig. 6.4d). Conversely, Domain II is completely formed between 378-412 °C, which can be primarily attributed to the formation and propagation of cavities along grain boundaries. Compared to the true strain of 0.6, Domain II is observed to shift towards higher temperatures and displays an increased value of peak efficiency (from 33 to 37%), as illustrated in Fig. 6.9c and 6.4d. The continuously increased density of dislocations with increasing strain stimulates the initiation of cavities at grain boundaries, which quickly grow as the temperature increases

due to the increased diffusion rate of vacancy [27,29], contributing to an improved peak efficiency in Domain II.

At the lower true strain of 0.2, flow instability regions initiate at two high strain rate corners, namely one at the strain rates of 0.1-10 s^{-1} with lower temperatures (300-350 °C) and another at the strain rates of 1-10 s^{-1} with higher temperatures (400-450 °C). This is attributed to the formation of adiabatic shear bands and deformation bands in the microstructure, which are commonly reported during the deformation of aluminum alloys at high strain rates [3]. With increasing strain, the two instability regions are gradually connected (Fig. 6.9b and c), and then extend towards a lower strain rate of 0.01 s^{-1}, particularly at low temperatures of 300-350 °C (Fig. 6.4d).

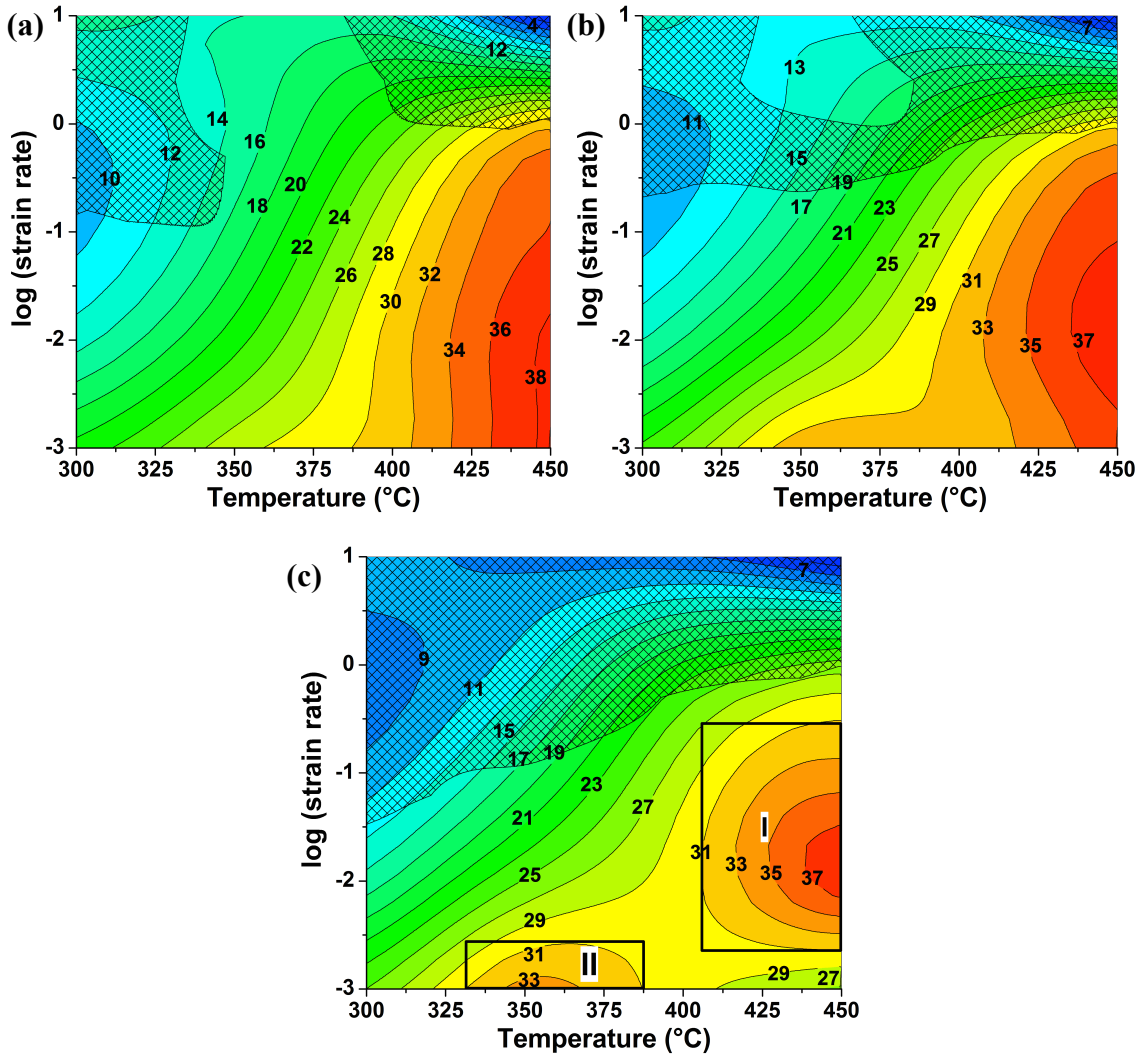

Fig. 6.9 The processing maps of 7150 aluminum alloy with 0.15% Zr at the true strains of (a) 0.2; (b) 0.4 and (c) 0.6. For the true strain of 0.8 see Fig. 6.4d.

6.4 Discussion

To understand the effects of micro-alloying with Zr and V on the processing map, the evolution of processing map during hot deformation of 7150 aluminum alloys with Zr addition ranging from 0-0.15% and V addition ranging from 0.01-0.15% was studied. The effects of Zr and V additions on the dynamic deformation mechanisms operating in different deformation domains and on manifestations of flow instability were investigated.

6.4.1 Effects of Zr and V on Domain I

In Domain I, microstructural observations reveal that dynamic recovery and partially dynamic recrystallization are the deformation mechanisms of the base alloy (Fig. 6.5a), leading to a high degree of dislocation annihilation and the high efficiencies of power dissipation [3], as shown in Fig. 6.4a. When alloyed with higher Zr contents from 0.12 to 0.15%, dynamic recrystallization is inhibited, and only dynamic recovery takes place, which is less efficient at dissipating stored deformation energy than dynamic recrystallization [3]. This results in a lower efficiency value at a given deformation condition in Domain I compared to the base alloy (Fig. 6.4c and d). With increasing Zr addition from 0.12 to 0.15%, Domain I shrinks towards higher temperatures and higher strain rates. With increasing temperature, the level of dynamic recovery can be improved [2,25]. Conversely, with increasing strain rate, the applied external force increases and leads to an augmented shear stress to activate the motion of dislocations, which favors dynamic recovery [34,35]. In addition, the dislocation multiplication rate increases with increasing strain rate, which increases the rate of dynamic recovery [25]. Therefore, in alloys containing Al_3Zr dispersoids, a high degree of power dissipation efficiency can be achieved as the temperature and strain rate increase, which offsets the restriction of dynamic recovery caused by the dispersoids and thereby resulting in a narrow Domain I. Similarly, in alloys containing $Al_{21}V_2$ dispersoids (0.11-0.15% V), dynamic recovery operates as the deformation mechanism, leading to decreases in efficiency compared to the base alloy in Domain I (Fig. 6.4f and g). Domain I

also narrows towards higher temperatures and higher strain rates, as observed in the alloys containing Al_3Zr dispersoids.

For the alloy containing a lower V content of 0.05% in which V mainly exists as solutes in the aluminum matrix, Domain I displays slightly lower efficiencies relative to the base alloy (Fig. 6.4e). A high level of dynamic recrystallization is observed after the 0.05% V addition (Fig. 6.5c), which contributes to a large portion of power dissipation. However, the V solute drag effect on dislocation motion and restrained dynamic recovery leads to a significant restriction of power dissipation. Hence, the overall efficiency of power dissipation of the alloy with 0.05% V displays a slightly lower value than that of the base alloy at a given condition in Domain I. Conversely, the alloy containing 0.04% Zr in solution demonstrates an identical variation in efficiency with temperature and strain rate in Domain I compared with the base alloy (Fig. 6.4b), indicating a limited solute drag effect. Zirconium solute has a lower diffusion activation energy and higher diffusivity than does the vanadium solute in aluminum [36], resulting in weaker solute strengthening.

The evolution of peak efficiencies in Domain I of the 7150 alloys with different Zr and V additions is shown in Fig. 6.10. It is evident that the peak efficiency continuously decreases with increasing Zr and V additions. This indicates that the material flow becomes more difficult as the Zr and V contents increase, leading to a decrease in hot workability [17]. With the same addition of Zr and V, the alloys containing V exhibit an even lower peak efficiency relative to the alloys containing Zr, which may be attributed to a higher level of solution or

dispersoid strengthening of V alloying. These results are in good agreement with those reported in the author's previous studies [10,16]: the flow stresses and activation energy for hot deformation of the 7150 alloy significantly increase when alloyed with Zr and V, and the alloys containing V result in higher flow stresses and activation energies compared with the same level of Zr addition.

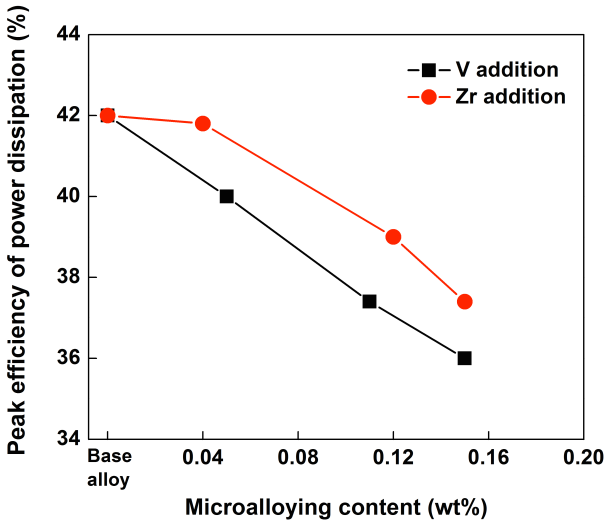

Fig. 6.10 The evolution of peak efficiency of power dissipation in Domain I as a function of Zr and V content.

6.4.2 Effects of Zr and V on Domain II

When the deformation is performed at low strain rates between 0.001-0.003 s^{-1} in the temperature range of 350 to 410 °C, a fine subgrain structure with medium-angle boundaries is formed in the base alloy; plastic deformation is then accommodated by subgrain boundary sliding, resulting in a homogenous deformation without cracking (Fig. 6.7a). However, for the alloys containing Al_3Zr and $Al_{21}V_2$ dispersoids (0.12-0.15% Zr and 0.11-0.15% V), pile-up dislocations at grain boundaries are strongly pinned by dispersoids, and cavities are

formed along grain boundaries to release the high induced energy (Fig. 6.6a and b), which contributes to a significant increase in efficiency of power dissipation relative to the base alloy [3], as illustrated in Fig. 6.4c, d, f and g. It should be emphasized that at higher contents of Zr and V of 0.15%, Domain II with relatively higher values of peak efficiency are formed (Fig. 6.4d and g). This is likely associated with a number of cavities formed due to the higher stress concentrations induced by the stronger pinning effect as the Zr and V contents increase. Conversely, at the lower V content of 0.05%, higher efficiencies of power dissipation are also observed at temperatures between 350-410 °C with low strain rates between 0.001-0.003 s^{-1} (Fig. 6.4e), which are mostly correlated with cavity formation due to the V solute drag effect on dislocation motion as well as with wedge cracking by grain boundary sliding (Fig. 6.6c). However, no obvious cracks are found in the alloy containing 0.04% Zr, which is attributed to the much weaker Zr solute strengthening and a high level of dynamic recovery.

6.4.3 Effects of Zr and V on flow instability region

The flow instability during hot deformation of 7150 alloys is caused by the formation of adiabatic shear bands and deformation bands (Fig. 6.8). When Zr and V are added and Al_3Zr and $Al_{21}V_2$ dispersoids form in the material, the instability regions exhibit a clear trend to extend towards lower strain rates, particularly at low temperatures of 300-350 °C (Fig. 6.4), which may cause some deformation defects in those conditions. Duckham et al. [37] suggested that a decrease in dynamic recovery during deformation led to greater development of shear bands. Due to the restriction of dynamic recovery after Zr and V additions, instable

flow may take place in the originally flow stable area adjacent to the instability region as shown in the base alloy, resulting in enlargements of flow instability regions towards lower strain rates. In addition, decreases in dynamic recovery and the number of active dislocation slipping systems with decreasing temperature give rise to more heterogeneous deformation [25,37,38], attributing to extension of instability regions particularly at lower temperatures.

However, the calculated values of the instability factor, ξ, are between -0.02 and 0.05 for all alloys containing Zr and V under the deformation conditions at temperatures between 300 and 350 °C and strain rates between 0.01 and 0.1 s^{-1}. These values are near zero, indicating a low susceptibility of unstable deformation occurring under those conditions [3,39], compared to the base alloy. Although the area of instability region enlarges, the flow instability of 7150 alloys may not be substantially influenced by micro-alloying of Zr and V.

In summary, the large strain deformation of 7150 aluminum alloys with Zr and V additions is preferred under the deformation conditions in Domain I, which is associated with high efficiencies of power dissipation for good hot workability and the safe deformation mechanisms of dynamic recrystallization or dynamic recovery. Dynamic recrystallization yields good workability by simultaneous softening the material and reconstituting the microstructure [3]. In addition, dynamic recovery provides a stable flow and a well-defined subgrain structure [2,3]. Deformation is avoided at low strain rates between 0.001-0.003 s^{-1} in the temperature range of 350-410 °C for the 7150 alloys containing more than 0.12% Zr or

0.05% V due to the occurrence of cavities and cracking. Furthermore, processing parameters should not be chosen in the unstable flow regions to obtain good hot workability and to prevent deformation defects. Therefore, the optimum hot-working parameters for these alloys at a strain of 0.8 are determined to be a deformation temperature of 450 °C and a strain rate of 0.01 s^{-1}, which are correlated with the peak efficiencies of power dissipation in the safe Domain I.

6.5 Conclusions

1. The processing map of the 7150 base alloy (Zr free) at a true strain of 0.8 exhibits a single domain (Domain I), in which dynamic recovery and partially dynamic recrystallization operate as the deformation mechanism.

2. With increasing Zr and V additions, Domain I shrinks towards higher temperatures and higher strain rates and exhibits decreases in efficiency of power dissipation as a result of restrained dynamic recovery caused by the pinning effect of Al_3Zr and $Al_{21}V_2$ dispersoids.

3. When the added Zr and V contents reach 0.15%, another domain (Domain II) is formed, corresponding to the occurrence of cavities along the grain boundaries in the microstructure.

4. Flow instability during hot deformation of 7150 alloys is attributed to the formation of adiabatic shear bands and deformation bands. The instability regions are enlarged towards lower strain rates after being alloyed with Zr and V.

5. The optimum hot-working parameters for all 7150 alloys are a deformation temperature of 450 °C and a strain rate of 0.01 s^{-1}.

References

[1] Starke EA, Staley JT. Application of modern aluminum alloys to aircraft. Prog Aerosp Sci 1996;32:131-72.

[2] McQueen HJ, Spigarelli S, Kassner M, Evangelista E. Hot Deformation and Processing of Aluminum Alloys. Florida: CRC Press; 2011. p. 87-233.

[3] Prasad YVRK, Sasidhara S. Hot Working Guide: A Compendium of Processing Maps, OH: ASM International, Materials Park; 1997. p. 1-177.

[4] Robson JD. A new model for prediction of dispersoid precipitation in aluminium alloys containing zirconium and scandium. Acta Mater 2004;52:1409-21.

[5] Robson JD, Prangnell PB. Dispersoid precipitation and process modelling in zirconium containing commercial aluminium alloys. Acta Mater 2001;49:599-613.

[6] Milman YV, Sirko AI, Lotsko DV, Miracle DB, Senkov ON, Microstructure and mechanical properties of cast and wrought Al-Zn-Mg-Cu alloys modified with Zr and Sc. Mater Sci Forum 2002;396-402:1217-22.

[7] Morere B, Shahani R, Maurice C, Driver J. The influence of Al_3Zr dispersoids on the recrystallization of hot-deformed AA 7010 alloys. Metall Mater Trans A 2001;32:625-32.

[8] Li Y, Liu Z, Lin L, Peng J, Ning A. Deformation behavior of an Al-Cu-Mg-Mn-Zr alloy during hot compression. J Mater Sci 2011;46:3708-15.

[9] Zou L, Pan Q, He Y, Liang W, Wang C. Microstructures and tensile properties of Al-Zn-Cu-Mg-Zr alloys modified with scandium. Mater Sci 2008;44:120-5.

[10] Shi C, Chen XG. Effect of Zr addition on hot deformation behavior and microstructural evolution of AA7150 aluminum alloy. Mater Sci Eng A 2014;596:183-93.

[11] Kazakova EF, Rusnyak YI. A study of rapidly hardened aluminum alloys with iron and vanadium. Met Sci Heat Treat 2009;51:436-9.

[12] Knipling KE, Dunand DC, Seidman DN. Criteria for developing castable, creep-resistant aluminum-based alloys-A review. Z Metallkd 2006;97:246-65.

[13] Davis JR. ASM Specialty Handbook: Aluminum and Aluminum Alloys. OH: American Society for Metals, Metals Park; 1993. p. 23-58.

[14] Wang X, Cong F, Zhu Q, Cui J. Effect of trace element vanadium on superplasticity of 5083 aluminium alloy sheets. Sci China Technol Sci 2012;55:510-4.

[15] Cui Q, Itoh G, Kanno M, Tsuji Y, Kobayashi K. Effects of vanadium and chromium

addition on S'-phase precipitation in a 2091 aluminium alloy. J Japan Inst Metals 1995;59:251-7.

[16] Shi C, Chen XG. Effect of vanadium on hot deformation and microstructural evolution of 7150 aluminum alloy. Mater Sci Eng A 2014;613:91-102.

[17] Prasad YVRK, Gegel HL, Doraivelu SM, Malas JC, Morgan JT, Lark KA, et al. Modeling of dynamic material behavior in hot deformation: Forging of Ti-6242. Metall Trans A 1984;15A:1883-92.

[18] Robi PS, Dixit US, Application of neural networks in generating processing map for hot working. J Mater Process Technol 2003;142:289-94.

[19] Luo J, Li MQ, Wu B. The correlation between flow behavior and microstructural evolution of 7050 aluminum alloy. Mater Sci Eng A 2011;530:559-64.

[20] Ramanathan S, Karthikeyan R, Deepak Kumar V, Ganesan G. Hot deformation behavior of 2124 Al alloy. J Mater Sci Technol 2006;22:611-25.

[21] Ganesan G, Raghukandan K, Karthikeyan R. Development of processing map for 6061 Al/15% SiC_p through neural networks. J Mater Process Technol 2005;166:423-9.

[22] Bhimavarapu SB, Maheshwari AK, Bhargava D, Narayan SP. Compressive deformation behavior of Al 2024 alloy using 2D and 4D processing maps. J Mater Sci 2011;46:3191-9.

[23] Bunn AM, Schumacher P, Kearns MA, Boothroyd CB, Greer AL. Grain refinement by Al-Ti-B alloys in aluminium melts: a study of the mechanisms of poisoning by zirconium. Mater Sci Technol 1999;15:1115-23.

[24] Lai J, Shi C, Chen XG. Effects of V addition on recrystallization resistance of 7150 aluminum alloy after simulative hot deformation, Mater Charact 2014;96:126-34.

[25] Humphreys FJ, Hatherly M. Recrystallization and Related Annealing Phenomena, second ed., Oxford: Elsevier Ltd.; 2004. p. 169-450.

[26] Gall RL, Jonas JJ. Solute drag effect during the dynamic recrystallization of Nickel. Acta Mater 1999;47:4365-74.

[27] Kassner ME, Hayes TA. Creep cavitation in metals. Int J Plasticity 2003;19:1715-48.

[28] Tanaka M, Iizuka H. On the initiation of wedge-type cracks at grain-boundary triple junctions during high-temperature creep. J Mater Sci 1985;20:9-16.

[29] Fan H, Sun YM, Xiao ZM. Contact zone in an interfacial zone Zener-Stroh crack. Mech Mater 1998;30:151-9.

[30] Rajamuthamilselvan M, Ramanathan S. Hot deformation behaviour of 7075 alloy. J Alloy compd 2011;509:948-52.

[31] Soer WA, Chezan AR, De Hosson JThM. Deformation and reconstruction mechanisms in coarse-grained superplastic Al–Mg alloys. Acta Mater 2006;54:3827-33.

[32] Dharmendra C, Rao KP, Prasad YVRK, Hort N, Kainer KU. High temperature deformation and microstructural features of TXA321 magnesium alloy: correlations with processing map. Adv Eng Mater 2013;15:761-6.

[33] Shi C, Mao W, Chen XG. Evolution of activation energy during hot deformation of AA7150 aluminum alloy. Mater Sci Eng A 2013;571:83-91.

[34] Caillard D, Martin JL. Thermally activated mechanisms in crystal plasticity. Oxford: Pergamon Press; 2003. p. 1-280.

[35] Honeycombe RWK. The plastic deformation of metals, second ed. Maryland: Edward Arnold Ltd.; 1984. p. 33-128.

[36] Neumann G, Tuijn C. Self-diffusion and impurity diffusion in pure metals: handbook of experimental data. New York: Elsevier Ltd.; 2009. p. 121-48.

[37] Duckham A, Knutsen RD, Engler O. Influence of deformation variables on the formation of copper-type shear bands in Al-lMg. Acta Mater 2001;49:2739-49.

[38] Ridha AA, Hutchinson WB. Recrystallisation mechanisms and the origin of cube texture in copper. Acta Metall 1982;30:1929-39.

[39] Han Y. Liu GW, Zou DN, Liu R, Qiao GJ. Deformation behavior and microstructural evolution of as-cast 904L austenitic stainless steel during hot compression. Mater Sci Eng A 2013;565:342- 50.

CHAPTER VII

EVOLUTION OF ACTIVATION ENERGY DURING HOT DEFORMATION OF 7150 ALUMINUM ALLOY

Chapter VII Evolution of activation energy during hot deformation of 7150 aluminum alloy

Abstract

The hot deformation behavior of a homogenized 7150 aluminum alloy was studied in compression tests conducted at various temperatures (573~723 K) and strain rates (0.001~10 s^{-1}). The flow stress behavior and microstructural evolution were observed during the hot deformation process. A revised Sellars' constitutive equation was proposed, which considered the effects of the deformation temperature and strain rate on the material variables and which provided an accurate estimate of the hot deformation behavior of the 7150 aluminum alloy. The results revealed that the activation energy for the hot deformation of the 7150 aluminum alloy is not a constant value but rather varies as a function of the deformation conditions. The activation energy for hot deformation decreased with increasing deformation temperature and with increasing strain rate. The peak flow stresses under various deformation conditions were predicted by a revised constitutive equation and correlated with the experimental data with excellent accuracy.

The content of this chapter has been published as: C. Shi, W.M. Mao, X.-G. Chen, Evolution of activation energy during hot deformation of 7150 aluminum alloy, Materials Science and Engineering A, 571 (2013) 83-91.

7.1 Introduction

The 7xxx aluminum alloys with a high strength-to-density ratio and excellent mechanical fracture toughness have been widely used in the aircraft and aerospace industries [1]. These aluminum alloys are generally subjected to hot-forming processes such as rolling, forging and extrusion. Mechanical properties are affected by the chemical composition, strain history and microstructure resulting from thermomechanical processing. The flow behavior of aluminum alloys during hot deformation is of great importance for the design of metal-forming processes due to its effective role in the required deformation energy as well as in the kinetics of metallurgical transformations, such as dynamic recovery (DRV) and dynamic recrystallization (DRX) [2-3]. Furthermore, the flow behavior is influenced by thermomechanical factors such as the degree of deformation, strain rate and deformation temperature [2].

A constitutive relation is generally used to describe the plastic flow properties of metals and alloys, which are correlated with the flow stress, strain rate and deformation temperature. Several models have been proposed to describe the hot deformation behavior, including physical-based, phenomenological and artificial neural network models and equations [4-13]. Sellars and McTegart [4] developed a hyperbolic-sine constitutive law to describe the hot working and creep behavior of aluminum, nickel, copper and steel materials. Johnson and Cook [5] proposed a phenomenological model, which Lin et al. [6] then modified to evaluate the hot compressive behavior of a 7075 aluminum alloy by considering the effects of strain

rate and the deformation temperature. Chai et al. [7] conducted a comparative study on the capability of a back propagation neural network model and a strain-compensated, Arrhenius-type constitutive equation to represent the elevated temperature flow behavior of XC45 steel. Lin et al. [8] proposed a revised Arrhenius constitutive equation to describe the effect of strain on material constants and on the flow behavior of 42CrMo steel. In addition, some researchers have applied these constitutive models and equations to evaluate the hot deformation behavior of various metals and alloys [9-13].

With various constitutive models and equations available, the hyperbolic-sine law, proposed by Sellars and McTegart [4], has been proven to be most applicable over a wide range of stresses. The activation energy of a material for hot deformation derived from this relation is usually used as an indicator of the degree of difficulty of the hot deformation process. It may provide a guideline for optimizing the hot working process and also furnish additional information on the microstructure and flow stress evolution in successive deformation processes. In the majority of research on the hot deformation behavior of materials [4-13], the activation energy has been treated as a constant value for all applied hot deformation conditions. In fact, the activation energy of an aluminum alloy for hot deformation represents mainly the free energy barrier to dislocation slipping on slip planes. As the energy required for dislocation slipping is affected by the temperature and external stress during hot-forming processes [2, 14], the activation energy for hot deformation cannot remain constant, but should instead be a function of the main deformation parameters,

including deformation temperature and strain rate. However, the effects of deformation temperature and strain rate on the evolution of activation energy have rarely been reported. Moreover, the thermodynamic mechanism of the evolution of the activation energy under different deformation conditions has not been clarified.

In the present paper, the hot deformation behavior of a homogenized 7150 alloy is studied using hot compression tests performed at various temperatures and strain rates. Considering the effect of deformation temperature and strain rate, a revised Sellars' constitutive equation is proposed to predict the hot deformation behavior of an 7150 aluminum alloy. The evolution of the activation energy for hot deformation under various deformation conditions is described.

7.2 Experimental

The experiments were conducted on a 7150 aluminum alloy (Zr free), which was taken as the starting material in the form of cylindrical DC cast billets. Approximately 3 kg of materials was remelted in an electrical resistance furnace and then cast into a rectangular permanent steel mold measuring 30 x 40 x 80 mm. The chemical composition of the alloy used is given in Table. 7.1. The cast ingots were homogenized at 738 K for 24 h, followed by a direct water quench. Small cylindrical samples 10 mm in diameter and 15 mm long were machined from the homogenized ingots. Uniaxial compression tests were conducted on a Gleeble 3800 thermomechanical simulation unit at strain rates of 0.001 s^{-1} to 10 s^{-1} and deformation temperatures of 573 K to 723 K. During the tests on the Gleeble unit, the

samples were heated to the desirable deformation temperature at a heating rate of 10 K/s and held at that temperature for 3 min prior to compression. The samples were deformed to a total true strain of 0.8 and then immediately water-quenched.

All deformed samples were sectioned parallel to the compression axis along the centerline and then polished and etched in Keller solution for observation under an optical microscope. The microstructure of the as-homogenized material was also examined prior to hot deformation. Additionally, some samples were selected for analysis using the electron backscattered diffraction (EBSD) technique with a scanning electron microscope (SEM, JEOL JSM-6480LV). In EBSD analysis, the boundaries of both the grains and subgrains are defined as low angle boundaries (LAB), medium angle boundaries (MAB) and high angle boundaries (HAB) for which the angles of boundary misorientation occur in the ranges of 1-5°, 5-15° and greater than 15°, respectively [15]. The step size between the scanning points was set to 1.0 μm for the deformed grain structure. In addition, EBSD analysis was performed to measure the grain size of the as-homogenized sample using the linear intercept method [16]; a surface area of approximately 10 mm^2 with a scanning step size of 5.0 μm was selected for the sample.

Table 7.1 Chemical composition of the 7150 aluminum alloy (Zr free) studied.

Material	Chemical compositions, wt%						
	Zn	Mg	Cu	Si	Fe	V	Al
7150 alloy	6.44	2.47	2.29	0.16	0.15	0.01	Bal.

7.3 Results

7.3.1 Flow stress behavior

The true stress-true strain curves obtained during hot compression of the 7150 aluminum alloy at strain rates of 0.001~10 s^{-1} and at deformation temperatures of 573~723 K are presented in Fig. 7.1. In general, the flow stresses increased rapidly at the beginning of deformation and then either remained fairly constant or decreased to some extent after attaining the peak stress. At the early stages of deformation, dislocations multiplied dramatically, and the work hardening process was predominant, thereby leading to a rapid increase in the flow stress. As the dislocation density increased, dynamic softening occurred, which can offset the effect of work hardening; thus, the flow stress increased at a decreasing rate until the peak stress was reached. Subsequently, the flow stress either decreased with increasing strain or remained steady. The former behavior is observed when the rate of dynamic softening is higher than that of work hardening. In this case, the peak stress is defined as the maximum value of the flow stress curve at which a distinct peak appears (indicated by an arrow in Fig. 7.1(a)). The latter behavior occurs as a result of a dynamic equilibrium between work hardening and dynamic softening, in which the peak stress was identified as the tangent point on the flow curve by the extension of a line along the steady-state flow stresses (indicated by an arrow in Fig. 7.1(b). It is evident that the level of both the peak stress and the flow stress increased with increasing strain rate and with decreasing deformation temperature. The peak stress was the highest (189 MPa) at a strain

rate of 10 s^{-1} and at a deformation temperature of 573 K, whereas the lowest peak stress (18 MPa) was obtained at a strain rate of 0.001 s^{-1} and at a temperature of 723 K. For a given strain rate, the driving force for dynamic softening which counteracts work hardening was reduced with decreasing temperature [2], thereby leading to an increase in both the peak stress and the overall flow stress. On the other hand, for a given temperature, the greater the strain rate, the higher the peak stress and the flow stress. It has been reported that the higher multiplication of dislocations and the formation of tangled dislocation structures, as barriers to dislocation movement, were caused by an increase in the strain rate [2]. These observations are in good agreement with earlier reports on 7xxx alloys [6, 17-19].

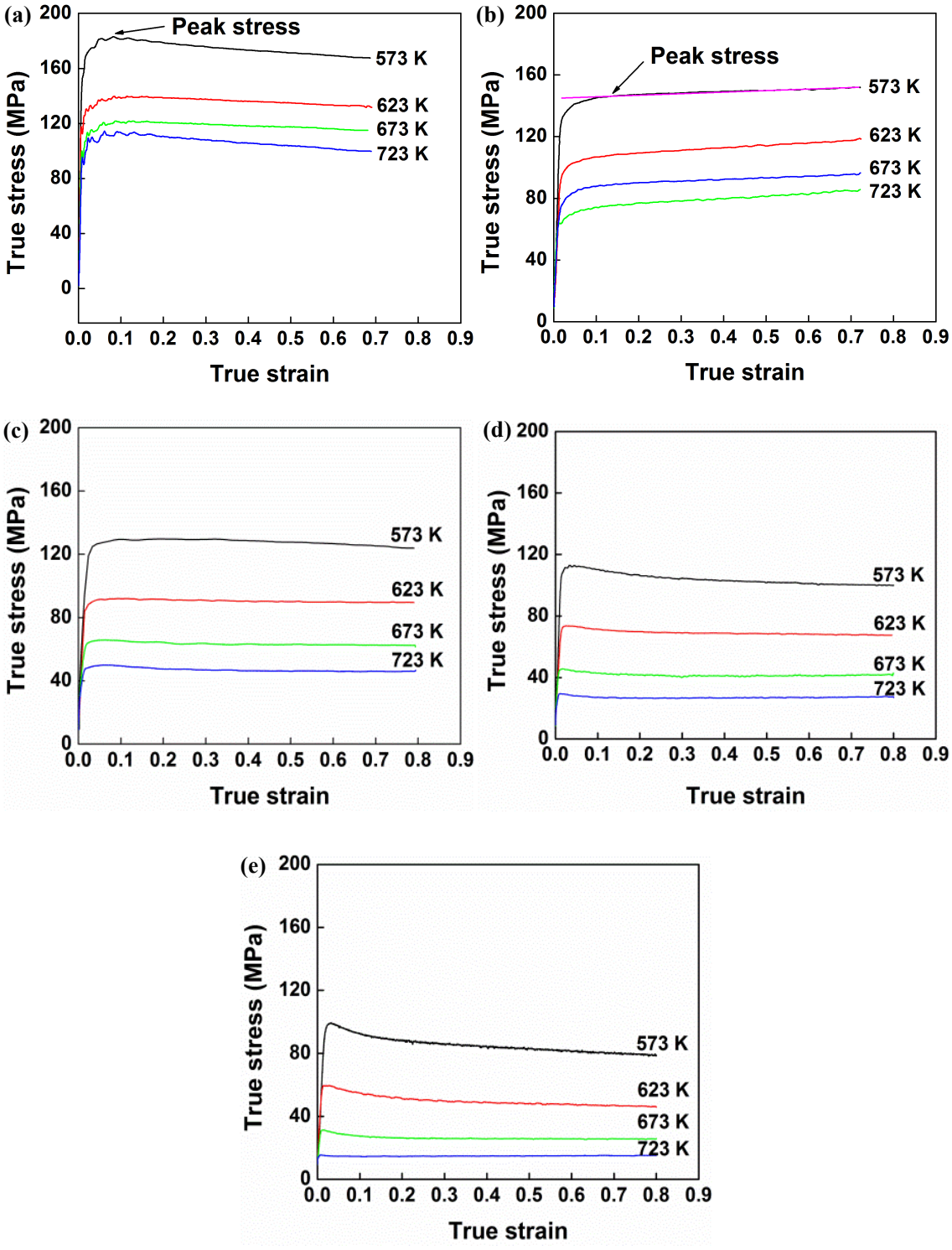

Fig. 7.1 True stress-true strain curves of 7150 aluminum alloy during hot compression deformation: (a) $\dot{\varepsilon}$ =10 s^{-1}; (b) $\dot{\varepsilon}$ =1 s^{-1}; (c) $\dot{\varepsilon}$ =0.1 s^{-1}; (d) $\dot{\varepsilon}$ =0.01 s^{-1}; (e) $\dot{\varepsilon}$ =0.001 s^{-1}.

7.3.2 Microstructural evolution

Fig. 7.2 illustrates the initial grain structure of the homogenized 7150 alloy prior to hot compression, as well as some representative microstructures deformed under various conditions. Fig. 7.2(a) reveals that the homogenized alloy is composed of uniform equiaxed grains that originate from the casting. The average grain size was 127 μm. During hot compression, the original grains were plastically elongated perpendicular to the compression direction. When the alloy was deformed at 573 K and 10 s^{-1} (Fig. 7.2(b)), the original grains were severely torn and broke into irregular deformation bands due to deformation occurring on different slip systems [15]. As the deformation temperature increased to 673 K with a strain rate of 10 s^{-1} (Fig. 7.2(c)), the deformation became more homogeneous, with fewer large-scale deformation bands visible under the optical microscope, which was the result of an increase in the number of operating slip systems and an increasing level of dynamic recovery as the temperature increased [20]. Moreover, when the strain rate was lowered to 0.01 s^{-1} at 673 K, the original grain boundaries became serrated along which subgrains became visible (Fig. 7.2(d)). This morphology is related to the migration of high angle grain boundaries in response to both the boundary tensions of the substructure and to variations in dislocations, which indicates a stronger dynamic recovered structure compared with the microstructure resulting from deformation at 673 K with higher strain rates.

In an attempt to gain more insight into microstructural evolution during the hot compression process, orientation imaging maps were generated under different deformation

conditions, as shown in Fig. 7.3. The results from EBSD analysis indicate that the original grain boundaries of the homogenized 7150 alloy are characterized by high angle boundaries, especially those with misorientation angles between 30° and 60°. When the alloy was deformed at 573 K and 10 s^{-1}, several irregular deformation bands with high angle transition boundaries were observed inside the elongated grains and oriented along the elongation direction. A large amount of low angle boundaries were observed with misorientation angles largely between 1° and 5°, indicating a high density of cell and subgrain structures (Fig. 7.3(a)). As the deformation temperature increased to 673K with a strain rate of 10 s^{-1}, fewer deformation bands were present in certain grains that exhibited more homogeneous deformation, and the density of low angle boundaries was reduced due to further polygonization (Fig. 7.3(b)). Moreover, as the strain rate was lowered to 0.01 s^{-1} at 673 K, the substructure became better organized, and larger subgrains were formed with neatly arranged boundaries, which were characterized by low and medium angle boundaries between 1° and 15° (Fig. 7.3(c)). This suggests an increased level of dynamic recovery, involving the annihilation and rearrangement of dislocations.

It is observed that the deformed 7150 alloy possessed a recovered grain structure during the hot compression process, indicating that the main softening mechanism of a 7150 alloy during hot deformation is dynamic recovery, which is consistent with previously reported studies [17, 18]. It is a general trend that the level of dynamic recovery increased with increasing temperature and with decreasing strain rate, thus resulting in a decrease in both the

peak stress and flow stresses.

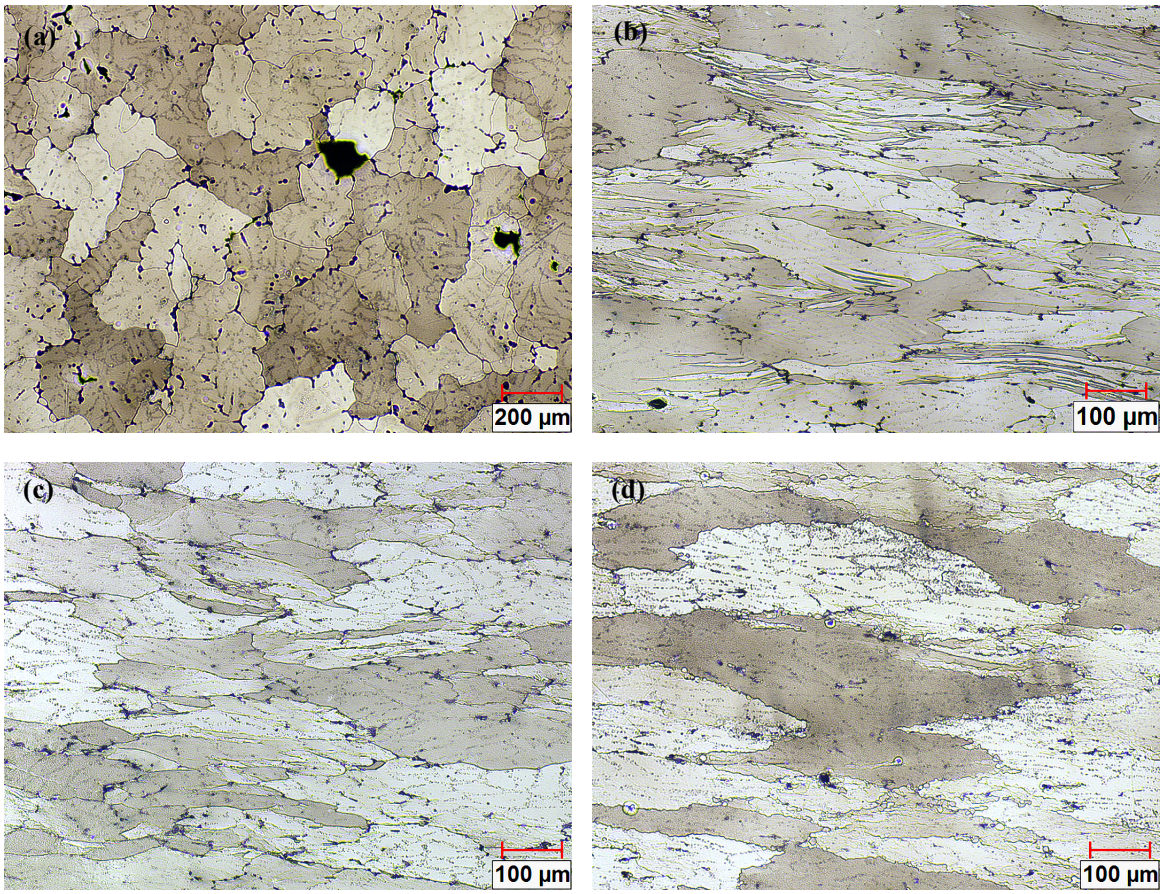

Fig. 7.2 Optical micrographs of the 7150 aluminum alloy: (a) as-homogenized grain structure; and deformed microstructures under different conditions: (b) 573 K, 10 s^{-1}; (c) 673 K, 10 s^{-1}; (d) 673 K, 0.01 s^{-1}.

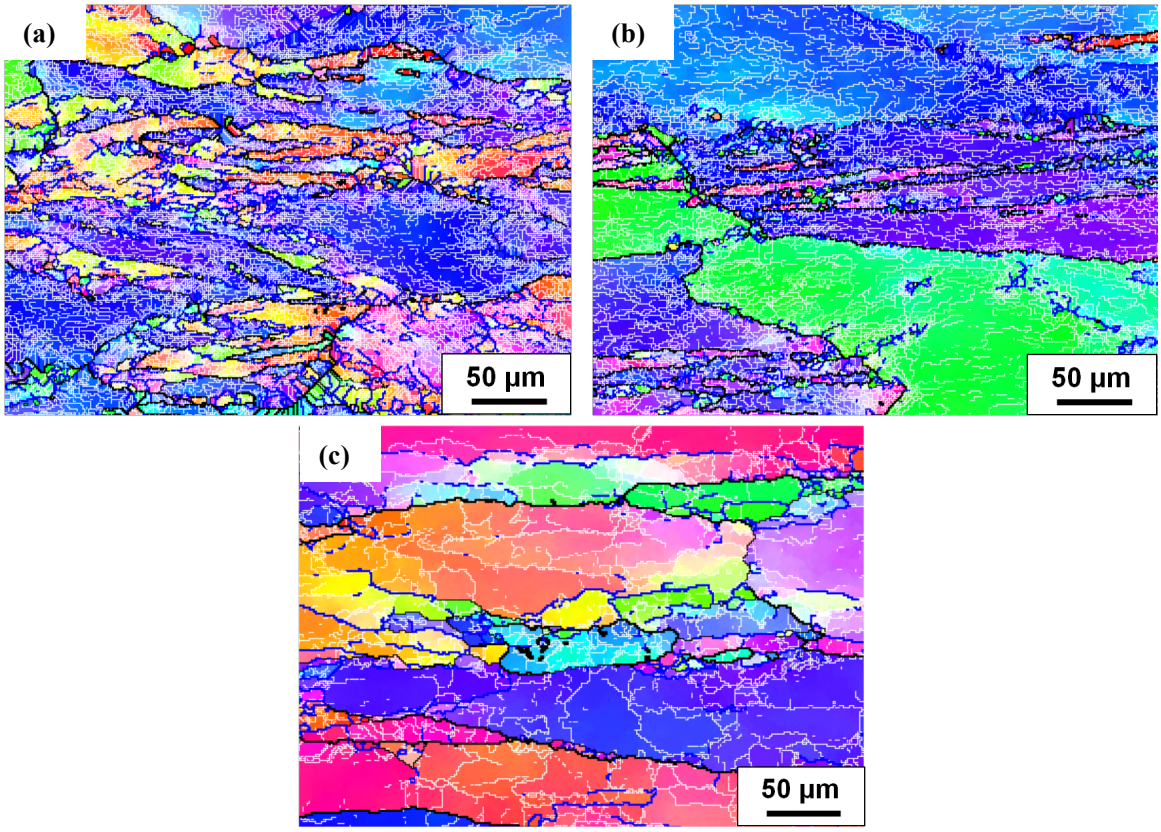

Fig. 7.3 Orientation imaging maps of the 7150 aluminum alloy under different deformation conditions: (a) 573 K, 10 s^{-1}; (b) 673 K, 10 s^{-1}; (c) 673 K, 0.01 s^{-1}. Boundary misorientation as indicated by the following: white lines: 1-5°; blue lines: 5-15°; thin black lines: 15-30°; thick black lines: (> 30°).

7.3.3 Constitutive analyses

7.3.3.1 Sellars' constitutive equation

In general, constitutive equations are developed to model the hot deformation behavior of the materials and to demonstrate the effects of the deformation conditions on the state of the flow stress [4-13]. The hyperbolic-sine equation, proposed by Sellars and McTegart [4], is widely employed to describe the relationship between the strain rate, deformation temperature and flow stress, especially over a wide range of stresses [2, 4, 21],

$$\dot{\varepsilon} = A[\sinh(\alpha\sigma)]^n \exp(-\frac{Q}{RT}) \tag{7.1}$$

where n and A are material constants, α is the stress multiplier, σ is the flow stress (MPa), Q is the activation energy for hot deformation (kJ/mol), R is the universal gas constant (8.314 J/mol K), and T is the deformation temperature (K).

Here, the peak stress σ_p is used as the σ term, which is generally utilized in aluminum alloys, and refers to a dynamic equilibrium between work hardening and dynamic restoration [22,23]. The stress multiplier α can be defined as $\alpha = \beta / n_1$ [4], where β and n_1 are evaluated from the slopes of the plots of $\ln(\dot{\varepsilon})$ - σ_p and $\ln(\dot{\varepsilon})$ - $\ln(\sigma_p)$, respectively, for the range of temperatures studied; thus, the value of α in our study for the homogenized 7150 alloy was calculated to be 0.011.

Differentiating Eq. (7.1) gives,

$$Q = R[\frac{\partial \ln \dot{\varepsilon}}{\partial \ln[\sinh(\alpha\sigma_p)]}]_T [\frac{\partial \ln[\sinh(\alpha\sigma_p)]}{\partial(1/T)}]_{\dot{\varepsilon}} = RnS \tag{7.2}$$

where n is the mean slope of plots of $\ln\dot{\varepsilon}$ - $\ln[\sinh(\alpha\sigma_p)]$ at different temperatures and S is the mean slope of plots of $\ln[\sinh(\alpha\sigma_p)]$ - $1/T$ at various strain rates. The relationship between $\ln\dot{\varepsilon}$ and $\ln[\sinh(\alpha\sigma_p)]$, which was derived from the measured true stress-true stain curves (Fig. 7.1), is shown in Fig. 7.4(a). The mean value of the slopes at four deformation temperatures, n, was then calculated. Likewise, the relationship between $\ln[\sinh(\alpha\sigma_p)]$ and $1/T$, which was derived from experimental true stress-true stain data (Fig. 7.1), is plotted in Fig. 7.4(b). The mean value of the slopes at each strain rate, S, is

obtained. The activation energy Q can then be determined directly from Eq. (7.2).

Taking the natural logarithm of both sides of Eq. (7.1) gives,

$$\ln \dot{\varepsilon} + \frac{Q}{RT} = \ln(A) + n \ln[\sinh(\alpha \sigma_p)] \tag{7.3}$$

where, $\ln(A)$ is obtained from the intercept of $(\ln \dot{\varepsilon} + \frac{Q}{RT})$ - $\ln[\sinh(\alpha \sigma_p)]$ plot. Consequently, the material constants A, n, α and the activation energy Q for the 7150 aluminum alloy were extracted and are presented in Table. 7.2.

Table 7.2 Values of material constants and activation energy for the 7150 aluminum alloy.

A (s^{-1})	n	α (MPa^{-1})	Q ($kJmol^{-1}$)
1.42×10^{17}	6.47	0.011	227

The activation energy of 227 kJ/mol obtained in the present study is comparable to the value for a homogenized 7150 alloy (229.75 kJ/mol) reported by Jin et al. [19]. However, it is much higher than either that of an aged 7150 alloy (158.8~161.4 kJ/mol) [24] or that of a precipitated and overaged 7075 alloy (143~156 kJ/mol) [17]. This result indicates that the activation energy for hot deformation is closely correlated with the material composition and the temper state. However, with this approach, the effects of applied thermomechanical factors, such as the deformation temperature and strain rate, on the evolution of the activation energy are not considered.

In the original Sellars' equation [4], both n and A were always considered to be material constants, likely due to simplifications. To calculate the activation energy Q of a material based on the experimental data, only the mean values of n and S were taken.

Therefore, the activation energy Q derived from Eqs. (7.1) and (7.2) became a constant value that was independent of the deformation conditions (T and $\dot{\varepsilon}$). In fact, the values of n, namely the slopes of the $\ln\dot{\varepsilon}$ - $\ln[\sinh(\alpha\sigma_p)]$ curves at each temperature, are considerably different in our experiment (Fig. 7.4(a)) and other studies [4-13, 16, 17, 21], thus indicating that n is obviously temperature dependent. Likewise, the values of S, namely the slopes of the $\ln[\sinh(\alpha\sigma_p)]$ - $1/T$ curves at each strain rate, are also remarkably different in our experimental data (Fig. 7.4(b)) and other studies [4-13, 17, 18, 22], showing that the S is dependent on strain rate. Moreover, it is generally recognized that the hot deformation of alloys occurs mainly by dislocation slipping, which is a thermally activated process [2]. The activation energy of dislocation slips is reduced by applied external stress, and the deformation difficulty is affected by temperature [14]. Dorn *et al.* [25, 26] have studied the evolution of activation energy for high-purity aluminum during creep at constant stress and concluded that the activation energy is temperature dependent. The hot deformation conditions for aluminum alloys generally vary over a wide range of temperatures and strain rates. It is obvious that hot deformation is a complex process that involves dislocation slip [2, 27, 28], and the effects of thermomechanical factors on the evolution of the activation energy should be considered. Therefore, the original Sellars' equation cannot adequately represent the hot deformation behavior of aluminum alloys.

7.3.3.2 A revised Sellars' constitutive equation

Based on the experimental data of the hot compressive deformation (Fig. 7.4), the

material constants in the original equation, n and A, should be treated as material variables. It is assumed that n is a function of deformation temperature while A is a function of both deformation temperature and strain rate. Thus, the activation energy Q becomes temperature and strain rate dependent. To overcome the shortcomings of the original Sellars' equation, the following expression is proposed:

$$\dot{\varepsilon} = A(T,\dot{\varepsilon})[\sinh(\alpha\sigma_p)]^{n(T)} \exp(-\frac{Q(T,\dot{\varepsilon})}{RT}) \tag{7.4}$$

where σ_p is peak stress. The material variables n, A, and activation energy Q are functions of the deformation temperature and the strain rate.

Determination of $n(T)$

Taking the natural logarithm of both sides of Eq. (7.4) gives,

$$\ln\dot{\varepsilon} = [\ln A(T,\dot{\varepsilon}) - \frac{Q(T,\dot{\varepsilon})}{RT}] + n(T)\ln[\sinh(\alpha\sigma_p)] \tag{7.5}$$

The values of n at each deformation temperature can be obtained from the slopes of the $\ln\dot{\varepsilon}$ - $\ln[\sinh(\alpha\sigma_p)]$ plots (Fig. 7.4(a)). By linear fitting, a good linear relationship between n and the deformation temperature is obtained, as illustrated in Fig. 7.5(a). It is evident that n is not a material constant, but rather decreases linearly with increasing temperature, which indicates an obvious dependency on deformation temperature. The variation of n with the deformation temperature has also commonly been observed in many studies on various metals and alloys [4-13, 17, 18, 22].

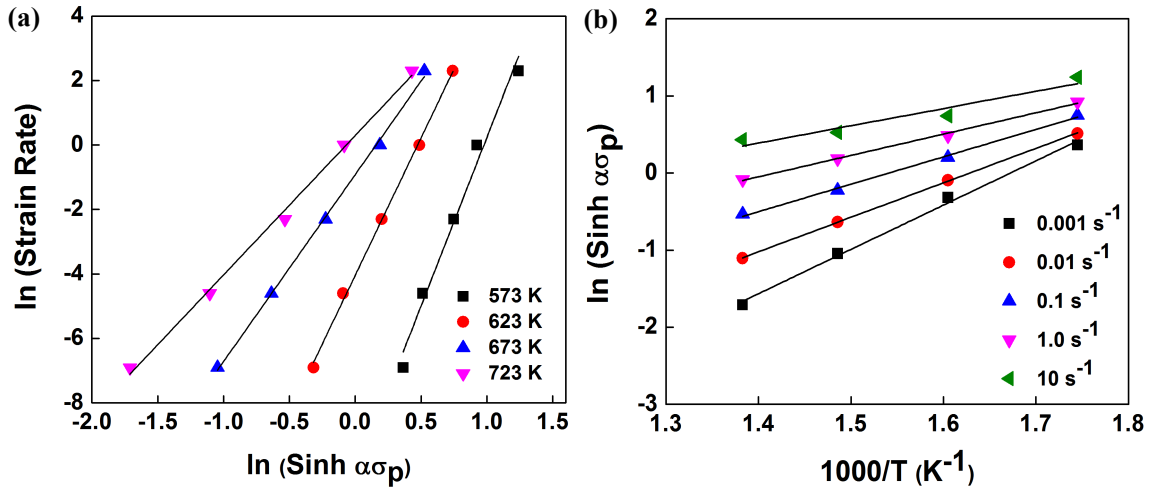

Fig. 7.4 Relationships between: (a) $\ln\dot{\varepsilon}$ **and** $\ln[\sinh(\alpha\sigma_p)]$**; (b)** $\ln[\sinh(\alpha\sigma_p)]$ **and** $1000/T$**.**

Determination of $Q(T,\dot{\varepsilon})$

At a constant strain rate, partial **differentiation** of Eq. (7.4) gives,

$$Q(T,\dot{\varepsilon}) = Rn(T)[\frac{\partial \ln[\sinh(\alpha\sigma_p)]}{\partial(1/T)}]_{\dot{\varepsilon}} + \{R\ln[\sinh(\alpha\sigma_p)][\frac{\partial n(T)}{\partial(1/T)}]_{\dot{\varepsilon}} + R[\frac{\partial \ln A(T,\dot{\varepsilon})}{\partial(1/T)}]_{\dot{\varepsilon}} - \frac{1}{T}[\frac{\partial Q(T,\dot{\varepsilon})}{\partial(1/T)}]_{\dot{\varepsilon}}\}$$

(7.6)

We define the terms in the braces as P, which was commonly assumed to be zero [4, 6-13, 17, 18, 22]. We assumed that $P\approx 0$ is valid as well. The validity of this assumption will be verified in the following discussion.

$$P = \{R\ln[\sinh(\alpha\sigma_p)][\frac{\partial n(T)}{\partial(1/T)}]_{\dot{\varepsilon}} + R[\frac{\partial \ln A(T,\dot{\varepsilon})}{\partial(1/T)}]_{\dot{\varepsilon}} - \frac{1}{T}[\frac{\partial Q(T,\dot{\varepsilon})}{\partial(1/T)}]_{\dot{\varepsilon}}\} \qquad (7.7)$$

Hence, after above assumption, the Eq. (7.6) can be simplified as

$$Q(T,\dot{\varepsilon}) = Rn(T)[\frac{\partial \ln[\sinh(\alpha\sigma_p)]}{\partial(1/T)}]_{\dot{\varepsilon}} = Rn(T)S(\dot{\varepsilon}) \quad (7.8)$$

Based on the measured true stress-true strain data, the values of S at each of the strain rates can be determined from the slopes of the $\ln[\sinh(\alpha\sigma_p)]$ - $1/T$ plots (Fig. 7.4(b)). From regression fitting, an excellent polynomial relationship between S and strain rate is found (Fig. 7.5(b)), which is expressed in Eq. (7.9). Based on the known $n(T)$ and $S(\dot{\varepsilon})$ functions, the activation energy $Q(T,\dot{\varepsilon})$ can be evaluated in Eq. (7.10).

$$S(\dot{\varepsilon}) = 2.767 - 0.281(\ln\dot{\varepsilon}) + 0.023(\ln\dot{\varepsilon})^2 \quad (7.9)$$

$$Q(T,\dot{\varepsilon}) = 797.986 - 0.973T + 0.098T(\ln\dot{\varepsilon}) - 0.008T(\ln\dot{\varepsilon})^2 - 80.319(\ln\dot{\varepsilon}) + 6.289(\ln\dot{\varepsilon})^2 \quad (7.10)$$

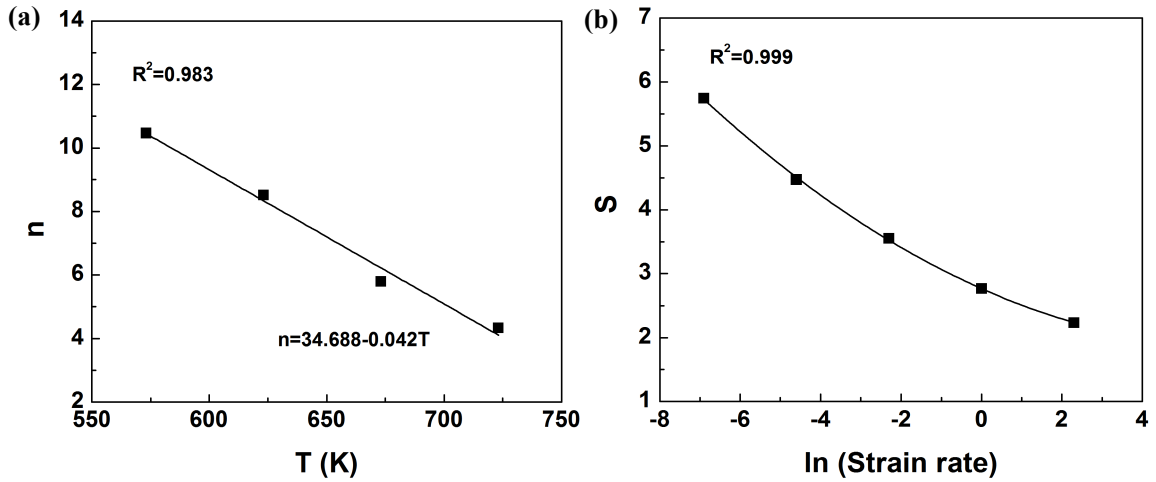

Fig. 7.5 Relationships between: (a) n and T; (b) S and $\dot{\varepsilon}$.

Fig. 7.6(a) shows the evolution of Q values calculated from the **experimental** data by substituting the values of n at each deformation temperature and S at each strain rate into Eq. (8). It can be seen that the activation energy for hot deformation tends to decrease with increasing temperature and strain rate. The activation energy reached 500 kJ/mol under the most severe condition (573 K and 0.001 s^{-1}) and declined by 84% (81 kJ/mol) under the

easiest condition (723 K and 10 s^{-1}). Interestingly, if the average value of Q is calculated at all deformation conditions, it is equal to 227 kJ/mol, which is the same value as that derived from the original Sellars' equation (in Table. 7.2). However, the results in Fig. 7.6(a) indicate that as the hot deformation varies over a wide range of temperature and strain rate, so also do the values of the activation energy for hot deformation. It is evident that the activation energy for hot deformation is quite sensitive to the deformation conditions, and plastic deformation occurs more easily as the temperature and strain rate increase. Furthermore, the predicted values of Q derived from Eq. (7.10) are shown in Fig. 7.6(b), which demonstrate excellent agreement with those obtained from the experimental data (Fig. 7.6(a)).

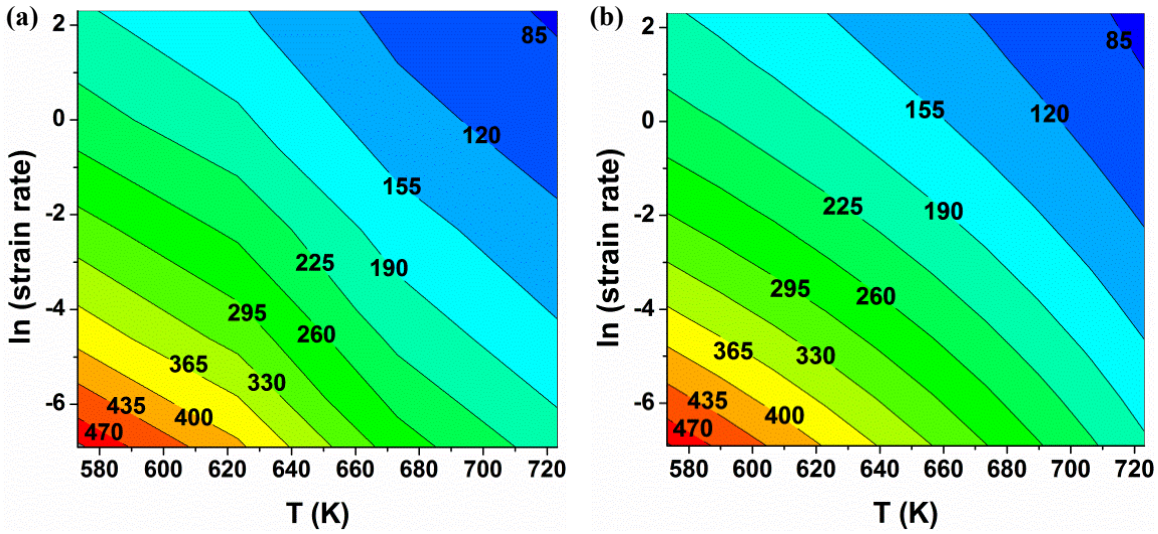

Fig. 7.6 The evolution of Q value (kJ/mol) as a function of deformation temperature and strain rate: (a) experimental results; (b) predicted results.

Determination of $A(T,\dot{\varepsilon})$

The values of $[\ln A(T,\dot{\varepsilon}) - \frac{Q(T,\dot{\varepsilon})}{RT}]$ at different deformation temperatures can be

determined from the intercepts of the $\ln\dot{\varepsilon} - \ln[\sinh(\alpha\sigma_p)]$ plots according to Eq. (7.5), as illustrated in Fig. 7.4(a). Subsequent substitution of Q and the $\ln A$ at each deformation temperature and strain rate can be obtained, and the results are shown in Fig. 7.7. It is found that the value of $\ln A$ decreases with increasing temperature and strain rate. Because the term $[\ln A(T,\dot{\varepsilon}) - \frac{Q(T,\dot{\varepsilon})}{RT}]$ is equal to a constant at each temperature, the relation of $\ln A$ to temperature and strain rate is expected to be similar to that of $Q(T,\dot{\varepsilon})$. By regression fitting, a good polynomial relationship between $\ln A$ and T, $\dot{\varepsilon}$, is calculated in Eq. (7.11) with a coefficient of $R^2 = 0.992$.

$$\ln A(T,\dot{\varepsilon}) = 133.774 - 0.163T + 0.023T(\ln\dot{\varepsilon}) - 0.002T(\ln\dot{\varepsilon})^2 - 18.3661(\ln\dot{\varepsilon}) + 1.4381(\ln\dot{\varepsilon})^2 \quad (7.11)$$

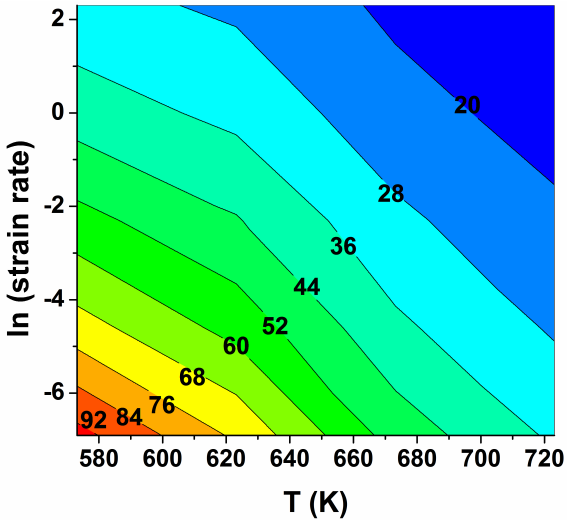

Fig. 7.7 The evolution of $\ln A$ (s^{-1}) as a function of strain rate and deformation temperature.

Verification of the revised constitutive equation

Based on the analysis above, it is apparent that there are relatively good linear or polynomial relationships among the material variables, n, A, the activation energy Q and thermomechanical factors, T and $\dot{\varepsilon}$. Therefore, a revised Sellars' constitutive equation to evaluate the hot deformation of the 7150 aluminum alloy can be expressed as,

$$\begin{cases} \sigma_p = \dfrac{1}{\alpha}\sinh^{-1}\left[\dfrac{\dot{\varepsilon}\exp(\dfrac{Q}{RT})}{A}\right]^{1/n} \\ \alpha = 0.011 \\ n = 34.688 - 0.0423T \\ Q = 797.986 - 0.973T + 0.0981T(\ln\dot{\varepsilon}) - 0.008T(\ln\dot{\varepsilon})^2 - 80.319(\ln\dot{\varepsilon}) + 6.289(\ln\dot{\varepsilon})^2 \\ \ln A = 133.774 - 0.163T + 0.023T(\ln\dot{\varepsilon}) - 0.002T(\ln\dot{\varepsilon})^2 - 18.3661(\ln\dot{\varepsilon}) + 1.4381(\ln\dot{\varepsilon})^2 \end{cases} \tag{7.12}$$

It is noteworthy that, according to Eq. (7.12), the values of the P term in Eq. (7.7) can be obtained at different deformation conditions. The ratios of the P value to the Q value are determined to lie between 0.0078 and 0.0562, which are quite small. Therefore, it is reasonable to simplify Eq. (7.6) by neglecting the P term for convenient calculation of the Q value.

Furthermore, to verify the validity of the revised constitutive equation for prediction of the deformation behavior of the 7150 aluminum alloy at elevated temperatures (Eq. (7.12)), the measured and predicted values of the peak stresses are plotted in Fig. 7.8 as a function of

deformation temperature and strain rate. As demonstrated, there is excellent agreement between the experimental and predicted results.

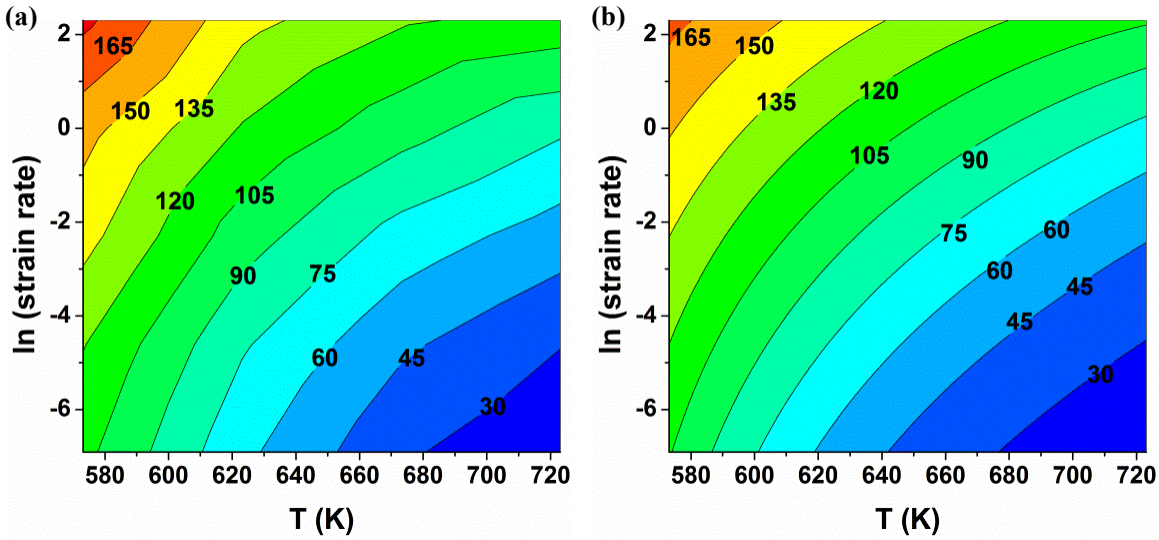

Fig. 7.8 The evolution of peak stresses (MPa) as a function of strain rate and deformation temperature: (a) experimental results; (b) predicted results.

In addition, for better comparison, the error between the predicted peak flow stress (σ_p) and the measured stress (σ_M) can be expressed as [11, 29],

$$error\% = \left| \frac{\sigma_p - \sigma_M}{\sigma_M} \right| \times 100 \tag{7.13}$$

The mean error under the deformation conditions studied is determined to be 3.41%, which shows good agreement between the predicted and measured peak stresses. Therefore, the revised constitutive equations reflects an excellent prediction of the deformation behavior for 7150 aluminum alloys at elevated temperatures and can be used to analyze the problems during hot working process.

7.4 Discussion

A revised Sellars' constitutive equation was proposed after considering the effects of thermomechanical factors on the hot deformation of materials in which the material variables, n, A and the activation energy for hot deformation Q, depend on the deformation temperature and the strain rate. The results show that the activation energy decreases with increasing deformation temperature and with increasing strain rate. This is closely correlated with the thermodynamic mechanism of dislocation movement. Plastic deformation in aluminum alloys mainly occurs as a result of dislocation slipping on slip planes [2, 27 ,28]. Dislocations can move randomly when the energy barrier, i.e., an activation energy, is overcome, which is a thermally activated process [14]. Furthermore, dislocations can move when an external shear stress is applied in the direction of slip on the slip plane, which must exceed a minimum stress, the Peierls-Nabarro stress [28]; the energy barrier can also be overcome for dislocations that are free to move. [28].

Thermal activation, which favors overcoming the energy barrier to dislocation motion, increases with increasing deformation temperature [14], while the activation energy does not change. However, the level of dynamic restoration is improved with increasing temperature, such that the dislocation density is reduced to facilitate further dislocation motion [2, 20]. Hence, increasing the deformation temperature could substantially reduce the resistance to dislocation slipping and, thus, decrease the activation energy for hot deformation.

On the other hand, the applied external force increases with increasing strain rate, thus

leading to an augmented shear stress to activate the motion of dislocations [14, 28], while the thermal energy needed to overcome the energy barrier is reduced. In addition, the dislocation multiplication rate increases with increasing strain rate, thereby resulting in an increase in the rate of dynamic restoration, which facilitates further movement of dislocations [2, 20, 28]. However, increasing the strain rate might induce more tangled dislocation structures as barriers to dislocation movement [2] and might decrease the level of dynamic restoration due to the relatively lesser amount of time for dislocation polygonization. Therefore, the influence of the first two aspects is expected to decrease the activation energy of dislocation movement and favors plastic deformation, whereas the effect of the last aspect increases the activation energy and the difficulty of the plastic deformation. The experimental results suggest that the first two effects are predominant during the hot deformation process and result in a decrease in activation energy with increasing strain rate.

The evolution of the activation energy for hot deformation indicates that the processing of deformation depends on the thermal activation, which is substantially influenced by deformation temperature and strain rate. Understanding the thermomechanical dependency of the activation energy could help to reveal more details of hot deformation and of corresponding microstructural changes under various deformation conditions, which could not be addressed solely based on a constant value of the activation energy. Furthermore, the revised Sellars' constitutive equation allows for excellent predictions of the deformation behavior for 7150 aluminum alloys at elevated temperatures. The predicted peak flow

stresses at different deformation temperatures and strain rates agree well with experimental data, and the solved constitutive equation can be used to analyze problems encountered during hot working processes.

7.5 Conclusions

1. Both the peak stress and flow stress decreased with increasing deformation temperature and decreasing strain rate. The peak stress of 7150 aluminum alloy (Zr free) varied from the highest value of 189 MPa at 573 K with a strain rate of 10 s^{-1} to the lowest value of 18 MPa at 723 K with a strain rate of 0.001 s^{-1}.

2. The deformed 7150 alloy exhibited a recovered grain structure during the hot compression process; the softening mechanism of the homogenized 7150 aluminum alloy during hot compression is mainly dynamic recovery.

3. The activation energy for hot deformation is a function of the deformation conditions, and it decreased with increasing temperature and increasing strain rate. The activation energy for the 7150 aluminum alloy reached 500 kJ/mol under the severest deformation condition (573 K and 0.001 s^{-1}) and decreased to 81 kJ/mol under the easiest condition (723 K and 10 s^{-1}).

4. The revised Sellars' constitutive equation provides excellent predictions of the deformation behavior of 7150 aluminum alloys at elevated temperatures.

References

[1] E.A. Starke, J.T. Staley, Prog. Aerosp. Sci. 32 (1996) 131-172.

[2] H.J. McQueen, S. Spigarelli, M. Kassner, E. Evangelista, Hot Deformation and Processing of Aluminum Alloys, CRC Press, Florida, 2011, pp. 87-233.

[3] M. Haas, J.T.M. Hosson, J. Mater. Sci. 37 (2002) 5065-5073.

[4] C.M. Sellars, W.J. McTegart, Mem. Sci. Rev. Met. 63 (1966) 731-746.

[5] G.R. Johnson, W.H. Cook, Eng. Fra. Mech.21 (1985), 31-48.

[6] Y. C. Lin, L.T. Li, Y.X. Fu, Y.Q. Jiang, J. Mater. Sci. 47 (2012) 1306-1318.

[7] R.X Chai, C. G, L. Yu, Mater. Sci. Eng. A 534 (2012) 101-110.

[8] Y.C. Lin, M.S. Chen, J. Zhong, Comput. Mater. Sci. 42 (2008) 470-477.

[9] S. Mandal, V. Rakesh, P.V. Sivaprasad, S. Venugopal, K.V. Kasiviswanathan,. Mater. Sci. Eng. A 500 (2009) 114-121.

[10] D. Samantaray, S. Mandal, A.K. Bhaduri, Mater. Des. 31 (2010) 981-984.

[11] Y.C. Lin, Y.C. Xia, X.M. Chen, M.S. Chen, Comput. Mater. Sci. 50 (2010) 227-233.

[12] C.L. Gan, Y.D. Xue, M.J. Wang, Mater. Sci. Eng. A 528 (2011) 4199-4203.

[13] G.L. Ji, F.G. Li, Q.H. Li, H.Q. Li, Z. Li, Mater. Sci. Eng. A 528 (2011) 4774- 4782.

[14] D. Caillard, J.L. Martin, Thermally Activated Mechanisms in Crystal Plasticity, Pergamon Press, Oxford, 2003, pp. 1-280.

[15] H.J. McQueen, Metall. Sci. and Technol. 28 (2010) 12-21.

[16] F.J. Humphreys, J. Mater. Sci, 36 (2001) 3833-3854.

[17] E. Cerri, E. Evangelista, A. Forcellese, H.J. McQueen, Mater. Sci. Eng. A 197 (1995) 181-198.

[18] Y. Deng, Z.M. Yin, J.W. Huang, Mater. Sci. Eng. A 528 (2011) 1780-1786.

[19] N.P. Jin, H. Zhang, Y. Han, W.X. Wu, J.H. Chen, Mater. Charact. 60 (2009) 530-536.

[20] F.J. Humphreys, M. Hatherly, Recrystallization and Related Annealing Phenomena, second ed., Elsevier Ltd., Oxford, 2004, pp. 169-450.

[21] C.M. Sellars, W.J. McTegart, Acta Metall. 14 (1996) 1136-1138.

[22] H.J. McQueen, N.D. Ryan, Mater. Sci. Eng. A 322 (2002) 43-63.

[23] S.F. Medina, C.A. Hernandez, Acta Metall. 44 (1996) 137-148.

[24] T. Sheppard, A. Jackson, Mater. Sci. Technol. 13 (1997) 203-209.

[25] O.D Sherby, J.L Lytton, J.E Dorn, Acta Metall. 5 (1957) 219–227.

[26] J.E. Dorn, J. Mech. Phys. Solids 8 (1954) 85-116.

[27] W.M. Mao, in: G.E. Totten, D.S. MacKenzie (Eds.), Handbook of Aluminum: Vol. 1: Physical Metallurgy and Processes, Marcel Dekker, Inc. New York, 2003, pp. 211-216.

[28] R.W.K. Honeycombe, The plastic deformation of metals, second ed., Edward Arnold Ltd. Maryland, 1984, pp. 33-128.

[29] A. Khamei, K. Dehghani, J. Alloys Comp. 490 (2010) 377-381.

CHAPTER VIII

GENERAL CONCLUSIONS AND RECOMMENDATIONS

Chapter VIII General Conclusions and Recommendations

8.1 General Conclusions

The hot deformation behavior of 7150 aluminum alloy (Zr free) is systematically investigated at temperatures of 300 to 450 °C and strain rates of 0.001 to 10 s^{-1}. A decline ratio map of flow stresses is developed and further divided into several deformation domains, in which the flow stress behavior is correlated with various dynamic softening mechanisms at different deformation conditions.

When micro-alloyed with Zr, no significant variation in peak flow stress or hot deformation activation energy occurs between the 7150 base alloy and the alloy with 0.04 wt% Zr. As the added Zr increases from 0.07 to 0.19 wt%, the peak flow stress and activation energy increased significantly. The level of dynamic recovery was decreased after alloying with Zr, which was associated with a decrease in the mean misorientation angle of boundaries and a reduction in subgrain size. The addition of Zr promoted the retardation of dynamic recovery and the inhibition of dynamic recrystallization due to the pinning effect of Al_3Zr dispersoids on dislocation motion and due to restrained dynamic restoration.

When V was added, the peak flow stresses of the 7150 alloy significantly increased. The alloys containing 0.03-0.05 wt% V displayed higher values of peak stresses than the alloys containing 0.11-0.19 wt% V at low temperatures of 300-350 °C, whereas they displayed comparable values at high temperatures of 400-450 °C. The hot deformation activation

energy increased from 229 kJ/mol for the base alloy to approximately 270 kJ/mol for the alloys containing 0.03-0.05 wt% V. With a further increase in V content up to 0.19 wt%, the activation energy returned to approximately 250 kJ/mol. The vanadium-solute diffusion acted as the deformation rate-controlling mechanism for the alloys containing up to 0.05 wt% V. The precipitation of $Al_{21}V_2$ dispersoids in the alloys containing 0.11 to 0.19 wt% V promoted the retardation of dynamic recovery and the inhibition of dynamic recrystallization.

The precipitation of Al_3Zr dispersoids with an average diameter of ~15 nm and $Al_{21}V_2$ dispersoids with an average size of ~50 nm in 7150 alloys with 0.12 to 0.19 wt% Zr and 0.11 to 0.19 wt% V were observed during homogenization at 465 °C for 24 h respectively. Both dispersoids were mainly distributed in supersaturated dendrite cells, whereas the precipitate-free zones were located in the interdendritic regions and near grain boundaries. Zirconium solute in the alloy containing 0.04 wt% Zr has a lower diffusion activation energy and higher diffusivity than does the vanadium solute in aluminum, resulting in a weaker solute strengthening relative to the alloys containing V in solution (0.03-0.05 wt% V).

The processing map of the 7150 base alloy exhibits a single domain (Domain I), associated with dynamic recovery and partially dynamic recrystallization. With increasing Zr and V additions, Domain I shrinks towards higher temperatures and higher strain rates with decreases in efficiency of power dissipation. When the added Zr and V contents reach 0.15 wt%, another domain (Domain II) is formed, corresponding to the cavity formation in microstructure. The flow instability during hot deformation of 7150 alloys is attributed to the

formation of adiabatic shear bands and deformation bands. The instability region extends toward lower strain rates when alloyed with Zr and V. The optimum hot-working parameters for those alloys are determined to be the deformation temperature of 450 °C and strain rate of 0.01 s^{-1}.

A revised Sellars' constitutive equation was proposed, which provided an accurate estimate of the hot deformation behavior of the 7150 aluminum alloy. The activation energy for the hot deformation is not a constant value but rather varies as a function of the deformation conditions. The activation energy for hot deformation decreased with increasing deformation temperature and with increasing strain rate.

8.2 Recommendations

The effect of Zr and V addition on hot deformation and microstructural evolution of the 7150 aluminum alloy were systematically investigated. Furthermore, the influence of Zr and V addition on the hot workability of the 7150 aluminum alloy were investigated using processing map. Based on the present study, following recommendations can be drawn for future work in this field:

- Dynamic precipitation behavior during hot deformation of 7150 aluminum alloy should be quantitatively studied to further understand the relationship between the evolution of flow stress and dynamic precipitation under different deformation conditions.

- The precipitation evolution of $Al_{21}V_2$ dispersoids in the aluminum alloy should be systematically investigated under different isothermal or isochronal aging schedules.
- The effects of grain refinement and multiple microalloying in 7150 aluminum alloy on microstructure, hot deformation behavior and mechanical property are suggested to study.
- Hot extrusion process can be designed by finite element modeling, and then be validated by simulated hot compression tests at different deformation conditions, in order to control the microstructure during hot extrusion process.